U.S. Department
of Transportation
Federal Railroad
Administration

Office of Research,
Development and Technology
Washington, DC 20590

# Side Impact Test and Analyses of a DOT-113 Surrogate Tank Car with Cryogenic Lading


DOT/FRA/ORD-22/33

Final Report | September 2022

NOTICE

This document is disseminated under the sponsorship of the Department of Transportation in the interest of information exchange. The United States Government assumes no liability for its contents or use thereof. Any opinions, findings and conclusions, or recommendations expressed in this material do not necessarily reflect the views or policies of the United States Government, nor does mention of trade names, commercial products, or organizations imply endorsement by the United States Government. The United States Government assumes no liability for the content or use of the material contained in this document.

NOTICE

The United States Government does not endorse products or manufacturers. Trade or manufacturers' names appear herein solely because they are considered essential to the objective of this report.

# REPORT DOCUMENTATION PAGE

*Form Approved*
*OMB No. 0704-0188*



| **1. REPORT DATE** *(DD-MM-YYYY* | **2. REPORT TYPE** | **3. DATES COVERED** *(From - To)* |
|---|---|---|
| September 2022 | Technical Report | July 2021 |

**4. TITLE AND SUBTITLE**
Side Impact Test and Analyses of a DOT-113 Surrogate Tank Car with Cryogenic Lading

**5a. CONTRACT NUMBER**
DTFR53-11-D-00008
TTCI-11-033

**5b. GRANT NUMBER**

**5c. PROGRAM ELEMENT NUMBER**

**6. AUTHOR(S)**
Steve Belport* – 0000-0002-8212-9873
Michael Carolan** – 0000-0002-8758-5739
Shawn Trevithick* – 0000-0001-6155-5526
Shaun Eshraghi** – 0000-0002-8152-0838
Aswani Krishnamurthy** – 0000-0003-3116-7797

**5d. PROJECT NUMBER**

**5e. TASK NUMBER**
Task Order 008
Task Order 345

**5f. WORK UNIT NUMBER**

**7. PERFORMING ORGANIZATION NAME(S) AND ADDRESS(ES)**
*Transportation Technology Center, Inc.
55500 DOT Road, Pueblo, CO 81001-0130
**Volpe National Transportation Systems Center
55 Broadway, Cambridge, MA 02142

**8. PERFORMING ORGANIZATION REPORT NUMBER**

**9. SPONSORING/MONITORING AGENCY NAME(S) AND ADDRESS(ES)**
U.S. Department of Transportation
Federal Railroad Administration
Office of Railroad Policy and Development
Office of Research, Development, and Technology
Washington, DC 20590

**10. SPONSOR/MONITOR'S ACRONYM(S)**

**11. SPONSOR/MONITOR'S REPORT NUMBER(S)**
DOT/FRA/ORD-22/33

**12. DISTRIBUTION/AVAILABILITY STATEMENT**
This document is available to the public through the FRA website.

**13. SUPPLEMENTARY NOTES**
COR: Francisco González, III

**14. ABSTRACT**

The Federal Railroad Administration (FRA) conducted a side impact test of a surrogate DOT-113 tank car at the Transportation Technology Center, Inc. (TTCI) to evaluate the performance of the tank car under dynamic impact conditions and to provide data for the verification and refinement of a computational model. The tank car surrogate was filled with liquid nitrogen at -320 °F to achieve a 5 percent outage. The targeted pressure range for this test was 15 to 35 psig. During the test, the pressure in the tank car was 30 psig. The tank car was impacted by a 297,200-pound ram car traveling at 18.3 mph fitted with a 12-inch by 12-inch impactor. The ram car impacted the tank car 32 inches off-center toward the A-End. The tank car was not punctured.

The Volpe National Transportation Systems Center (Volpe) performed pre-test finite element (FE) modeling to estimate the overall response of the tank to the impact. The goal of the DOT-113 side impact test series is to analyze the side impact performance of a DOT-113 tank car carrying liquefied natural gas (LNG) under typical service conditions. Once confidence in the FE model is achieved, this model will be used to estimate the puncture resistance of a DOT-113 tank car carrying LNG.

**15. SUBJECT TERMS**
Impact test, surrogate DOT-113 tank car, tank car performance, transportation safety, tank car, hazardous materials, rolling stock, test

| **16. SECURITY CLASSIFICATION OF:** | | | **17. LIMITATION OF ABSTRACT** | **18. NUMBER OF PAGES** | **19a. NAME OF RESPONSIBLE PERSON** |
|---|---|---|---|---|---|
| **a. REPORT** | **b. ABSTRACT** | **c. THIS PAGE** | | | Francisco González, III |
| Unclassified | Unclassified | Unclassified | | 206 | **19b. TELEPHONE NUMBER** *(Include area code)* 202-493-6076 |

**Standard Form 298** (Rev. 8/98)
Prescribed by ANSI Std. Z39.18

# METRIC/ENGLISH CONVERSION FACTORS

| ENGLISH TO METRIC | METRIC TO ENGLISH |
|---|---|
| **LENGTH (APPROXIMATE)** | **LENGTH (APPROXIMATE)** |
| 1 inch (in) = 2.5 centimeters (cm) | 1 millimeter (mm) = 0.04 inch (in) |
| 1 foot (ft) = 30 centimeters (cm) | 1 centimeter (cm) = 0.4 inch (in) |
| 1 yard (yd) = 0.9 meter (m) | 1 meter (m) = 3.3 feet (ft) |
| 1 mile (mi) = 1.6 kilometers (km) | 1 meter (m) = 1.1 yards (yd) |
| | 1 kilometer (km) = 0.6 mile (mi) |
| **AREA (APPROXIMATE)** | **AREA (APPROXIMATE)** |
| 1 square inch (sq in, $in^2$) = 6.5 square centimeters ($cm^2$) | 1 square centimeter ($cm^2$) = 0.16 square inch (sq in, $in^2$) |
| 1 square foot (sq ft, $ft^2$) = 0.09 square meter ($m^2$) | 1 square meter ($m^2$) = 1.2 square yards (sq yd, $yd^2$) |
| 1 square yard (sq yd, $yd^2$) = 0.8 square meter ($m^2$) | 1 square kilometer ($km^2$) = 0.4 square mile (sq mi, $mi^2$) |
| 1 square mile (sq mi, $mi^2$) = 2.6 square kilometers ($km^2$) | 10,000 square meters ($m^2$) = 1 hectare (ha) = 2.5 acres |
| 1 acre = 0.4 hectare (he) = 4,000 square meters ($m^2$) | |
| **MASS - WEIGHT (APPROXIMATE)** | **MASS - WEIGHT (APPROXIMATE)** |
| 1 ounce (oz) = 28 grams (gm) | 1 gram (gm) = 0.036 ounce (oz) |
| 1 pound (lb) = 0.45 kilogram (kg) | 1 kilogram (kg) = 2.2 pounds (lb) |
| 1 short ton = 2,000 pounds (lb) = 0.9 tonne (t) | 1 tonne (t) = 1,000 kilograms (kg) = 1.1 short tons |
| **VOLUME (APPROXIMATE)** | **VOLUME (APPROXIMATE)** |
| 1 teaspoon (tsp) = 5 milliliters (ml) | 1 milliliter (ml) = 0.03 fluid ounce (fl oz) |
| 1 tablespoon (tbsp) = 15 milliliters (ml) | 1 liter (l) = 2.1 pints (pt) |
| 1 fluid ounce (fl oz) = 30 milliliters (ml) | 1 liter (l) = 1.06 quarts (qt) |
| 1 cup (c) = 0.24 liter (l) | 1 liter (l) = 0.26 gallon (gal) |
| 1 pint (pt) = 0.47 liter (l) | |
| 1 quart (qt) = 0.96 liter (l) | |
| 1 gallon (gal) = 3.8 liters (l) | |
| 1 cubic foot (cu ft, $ft^3$) = 0.03 cubic meter ($m^3$) | 1 cubic meter ($m^3$) = 36 cubic feet (cu ft, $ft^3$) |
| 1 cubic yard (cu yd, $yd^3$) = 0.76 cubic meter ($m^3$) | 1 cubic meter ($m^3$) = 1.3 cubic yards (cu yd, $yd^3$) |
| **TEMPERATURE (EXACT)** | **TEMPERATURE (EXACT)** |
| [(x-32)(5/9)] °F = y °C | [(9/5) y + 32] °C = x °F |

## QUICK INCH - CENTIMETER LENGTH CONVERSION

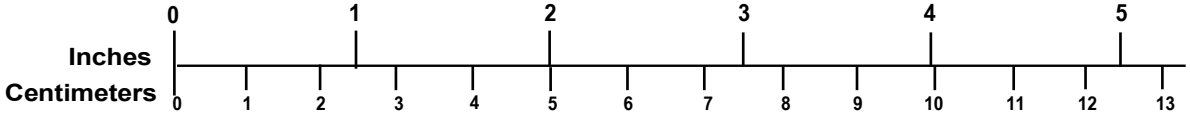


## QUICK FAHRENHEIT - CELSIUS TEMPERATURE CONVERSIO

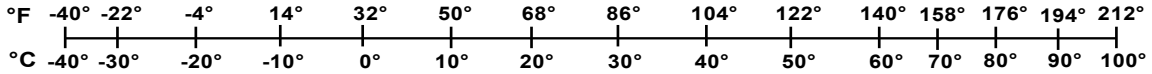


For more exact and or other conversion factors, see NIST Miscellaneous Publication 286, Units of Weights and Measures. Price $2.50 SD Catalog No. C13 10286

Updated 6/17/98

## Acknowledgements

The authors gratefully acknowledge the cooperation and assistance of Hector Villarreal and Devangkumar Patel of Taylor-Wharton Americas in providing engineering drawings and design information for the surrogate DOT-113 tank car used in this test. The authors also gratefully acknowledge the assistance provided by Trinity Rail in obtaining design information for the outer tank of the tank car surrogate used in this test.

The authors acknowledge the cooperation and assistance of John Burgess and Scott Tuttle of Airgas regarding the filling procedures and post-test procedures for testing with liquid nitrogen. The authors gratefully acknowledge the technical discussions held with Pat Brady, the Assistant Director of Hazmat, BNSF Railway, and Tim O'Brien, the Director Hazardous Materials, Union Pacific Railroad, on post-test safety procedures associated with cryogenic liquids in tank cars.

The authors gratefully acknowledge the work done by John N. Schwartzberg, P.E. from Rocky Mountain Engineering and Materials Technology, Inc. in planning and performing these material tests.

The authors recognize Benjamin Perlman, Senior Engineer at Volpe National Transportation Systems Center (Volpe) for their technical assistance. Volpe's Mechanical Engineer Wesley Peisch (former) assisted with developing and executing the finite element models. Additionally, inputs from Francisco González, III of the Federal Railroad Administration's (FRA) Office of Research, Development and Technology were valuable in developing this testing program. The authors also acknowledge technical discussions and assistance in developing the testing plan from Mark Maday of FRA's Office of Railroad Safety.

Dr. Phani Raj, of FRA's Office of Railroad Safety, developed the analyses described in Appendix G and Appendix I2.

## Contents

## Illustrations

## Tables

## Equations

## Executive Summary

This report documents the combined efforts of the Transportation Technology Center, Inc. and the Volpe National Transportation Systems Center (Volpe) to test and analyze the side impact puncture performance of a surrogate DOT-113 tank car filled with cryogenic liquid nitrogen (LN2). This was the third test in a planned four-test series on DOT-113 tank cars and tank car surrogates.

FRA conducted the impact test of the DOT-113 tank car surrogate on July 24, 2021, at the Transportation Technology Center (TTC) to evaluate the performance of the tank car and to provide data for the verification and refinement of a computational model. All test requirements were met. Volpe performed both pre-test and post-test analyses of the impact response to evaluate, validate, and improve the puncture modeling capabilities.

The tank car surrogate was initially filled with LN2 to achieve a 5 percent outage. The targeted pressure range for this test was 15 to 35 psig. The authors targeted a test speed of 17.7 mph $\pm$ 0.5 mph to be close to the threshold impact speed necessary to puncture both tanks of the tank car. Pre-test simulations indicated that puncture was a possibility at this speed. For comparison, the June 2020 DOT-113 surrogate test with water occurred at 17.3 mph and did not result in puncture; the November 2019 DOT-113 legacy test with water was at 16.7 mph and resulted in puncture. After filling, the lading continued to build pressure and increase in temperature. Researchers vented gaseous nitrogen (GN2) to auto-refrigerate the lading and reduce the pressure. After venting, the tank car was left approximately 91 percent full of LN2 by volume, and the remaining 9 percent of its volume (outage) was occupied by GN2 as determined by a static head pressure calculation. The pressure was approximately 30 psig.

The tank car surrogate was impacted by a 297,200-pound ram car fitted with a 12-inch by 12-inch ram head traveling at 18.3 mph. The impact resulted in a significant amount of deformation but did not puncture either the inner or outer tanks of the surrogate tank car. Pre-test finite element (FE) modeling was used to estimate the overall response of the tank to the impact for test planning. The pre-test simulations indicated that puncture depended on the ability of GN2 to build pressure during the impact before undergoing a phase change to LN2. After the test, the pre-test FE model was updated to represent the measured speed of the ram car. Additionally, the FE model was updated to simulate the effect of GN2 changing phase to LN2 through condensation at 70 psia (57.7 psig) and this resulted in good agreement with the measured test data.

The results of this test and lessons learned from comparing the FE model against the results of this test will be applied to the next test in the DOT-113 side impact test series which will feature a newly-constructed DOT-113C120W9 tank car filled with LN2. The overall goal of the DOT-113 side impact test series is to analyze the side impact performance of a DOT-113 tank car carrying liquefied natural gas (LNG) under typical service conditions. Due to safety concerns, a DOT-113 tank car with LNG lading cannot be directly tested in a full-scale side impact test. In lieu of a test with LNG, FRA has planned a series of four tests with DOT-113 tank cars and surrogate tank cars going from water to cryogenic LN2 with companion FE analyses. Once confidence in the FE model is achieved, this model will be used to estimate the puncture resistance of a DOT-113 tank car carrying LNG.

# 1. Introduction

This report documents the analyses and test results for a side impact test performed on a surrogate DOT-113 tank car surrogate filled with liquid nitrogen (LN2) that took place on July 24, 2021. The DOT-113 tank car is specially designed to transport cryogenic liquid commodities. The U.S. Department of Transportation (DOT)-113 surrogate described in this report included the features of a DOT-113 tank car essential to evaluate its impact response (e.g., typical tank materials, thicknesses, and diameters) but did not include tank car features such as couplers, brake rigging, and other tank car specific features that would not affect the impact response. Previously tested tank cars in the Federal Railroad Administration's (FRA) side impact testing program have typically had an exterior jacket that was much thinner than the commodity tank. The DOT-113 tank car surrogate used in this test featured an outer tank made of 0.608-inch carbon steel and an inner tank made of 1/4-inch stainless steel. This report documents the impact test and describes the FE model development and pre-test estimates, the comparisons of the test and analyses, and the subsequent post-test analyses.

## 1.1 Background

In the past decade, significant research has been conducted to analyze and improve the impact behavior and puncture resistance of railroad tank cars. Ultimately, the results of this research will be used by U.S. Department of Transportation Federal regulatory agencies—i.e., FRA and the Pipeline and Hazardous Materials Safety Administration (PHMSA)—to establish performance-based testing requirements and to develop methods to evaluate the crashworthiness and structural integrity of different tank car designs when subjected to a standardized shell impact scenario. A performance-based requirement for tank car head impact protection has already been defined within the current regulations [1], and an optional performance-based requirement for tank car shell impact resistance is applicable to DOT-117P tank cars [2].

FRA has a continuing research program to provide the technical basis for rulemaking on enhanced and alternative performance standards for tank cars and FRA also reviews any new and innovative designs that are developed by the tank car industry and other countries. In support of this ongoing research program, full-scale tests are necessary to provide the technical information to validate modeling efforts and to inform regulatory activities. These tests evaluate the crashworthiness performance of tank cars used in the transportation of hazardous materials under standardized, repeatable conditions.

The DOT-113 tank car is specially designed to transport cryogenic liquids.[1] A cryogenic liquid is "a refrigerated liquefied gas having a boiling point colder than -90 °C (-130 °F) at 101.3 kPa (14.7 psia) absolute."[2] DOT-113 tank cars are "tank-within-a-tank" cars, where the inner tank is in contact with the cryogenic material and resists the pressure exerted by the lading, and an outer tank surrounds the inner tank and insulating materials and carries the in-train forces. The DOT-113 tank car surrogate used in this test was constructed specifically for use in this shell impact

[1] PHMSA. Subpart F—Specification for Cryogenic Liquid Tank Car Tanks and Seamless Steel Tanks (Classes DOT-113 and 107A). Title 49 Code of Federal Regulations (CFR) § 179.302. Washington, DC: U.S. Department of Transportation.

[2] 49 CFR § 173.115(g)

test. The surrogate included design features representative of a specification DOT-113 tank car, including typical materials of construction for the inner and outer tanks, typical diameters for the inner and outer tank shells, typical thicknesses for the inner and outer tanks, and typical pressure relief valve (PRV) arrangements. The surrogate did not include features required of tank cars that would not have an effect on the puncture response during a shell impact, such as couplers, trucks, brake piping, or safety appliances. The terms "surrogate" and "tank car surrogate" are used interchangeably throughout this report.

The Hazardous Materials Regulations (HMR) permit the transportation of several cryogenic liquids via DOT-113 tank cars, including argon and ethylene. Refrigerated liquid methane (more commonly referred to as liquefied natural gas (LNG) was not authorized for transportation in a DOT-113 tank car prior to 2020. PHMSA and FRA published a Notice of Proposed Rulemaking (NPRM) in October 2019[3] that would permit LNG to be transported in DOT-113 tank cars. After Test 12, PHMSA and FRA published a second NPRM in November 2021[4] that would suspend the transportation of LNG in DOT-113 tank cars until further research could be conducted. Because the existing fleet of DOT-113 tank cars is small compared to the overall tank car fleet and limited accident data exist regarding the performance of these cars in derailments or collisions, a series of full-scale shell impact tests was planned to provide technical information on the puncture resistance of the DOT-113 tank car. The first test in this series was performed on November 19, 2019 [3]. The second test in this series was performed on June 11, 2020 [4]. After the second test, a series of finite element (FE) analyses was conducted to transition from testing and modeling a tank car filled with water to one filled with LN2 [5].

DOT-113 tank cars include several unique design features that are not found on unpressurized (e.g., DOT-117) or pressurized (e.g., DOT-105) tank cars because of the particular properties of cryogenic materials. The inner tank of a DOT-113 tank car will be exposed to cryogenic temperatures, and thus must be constructed of either ASTM A240 Type 304 or Type 304L stainless steel [6]. These grades of steel maintain desirable properties at cryogenic temperatures.

Since the inner tank and lading must be kept at cryogenic temperatures during transit, the inner tank must be surrounded by highly-effective insulation. This insulation may take the form of expanded perlite[5] (e.g., a granular, lightweight, and natural mineral) or multiple layers of "super" insulating materials (e.g., multi-layer insulation, [MLI]). Additionally, a vacuum is typically used in conjunction with either perlite or MLI to further reduce heat transfer into the inner tank. Specification Title 49 Code of Federal Regulations (CFR) Part 179 Subpart F defines a maximum rate of heat transfer that is permissible through the insulation system. The inner tank and insulation must be surrounded by an external tank to contain the insulation, maintain the vacuum, and carry the in-train forces.

---

[3] Pipeline and Hazardous Materials Safety Administration. *Hazardous Materials: Liquefied Natural Gas by Rail*. Federal Register/Vol 84, No. 206/Thursday, October 24, 2019.

[4] Pipeline and Hazardous Materials Safety Administration. *Hazardous Materials: Suspension of Hazardous Materials Regulations Amendments Authorizing Transportation of Liquefied Natural Gas by Rail*. Federal Register/Vol 86, No. 213/Monday, November 8, 2021.

[5] The DOT-113 car used in Test 10 was equipped with perlite insulation. All other tank cars and surrogates used in this test series were equipped with MLI.

## 1.2 Objectives

The objective of this test was to quantify the deformation mode, impact load-time history, and puncture resistance of a DOT-113 surrogate filled with LN2 in a side impact. Moreover, the development of impact conditions allowed the side impact test to be: 1) safe, 2) repeatable, and 3) analyzable. The test conditions were intended to be representative of planned service conditions, with the limitation that LNG could not be used in the test due to safety concerns. This test was intended to subject a new, surrogate DOT-113 tank car with a 0.608-inch-thick TC-128 outer tank to an impact with a rigid impactor having kinetic energy close to the puncture threshold for the tank car under the test conditions.

The pre- and post-test analyses provided estimates of the tank car impact responses for pre-test planning and for the validation of tank car impact and puncture modeling capabilities.

The lessons learned from the modeling efforts in this test will be applied to the next test in the series. Each test is planned to increase in both complexity and realism over the previous test in this series. This testing strategy will incrementally approach test conditions that represent the planned service conditions for DOT-113 tank cars.

## 1.3 Overall Approach

Prior to this test, FRA conducted similar shell impact tests on DOT-105, DOT-111, DOT-112, DOT-117, and DOT-113 tank cars. These previous tests were all accompanied by companion FE analysis. These previous tests covered a wide range of tank car designs (e.g., capacities, shell diameter, shell thickness, vintage, manufacturer, outage level, outage pressure, etc.) The goal of the tank car shell impact testing and modeling program is to understand how a particular tank car performs under a standardized impact scenario that is representative of typical service conditions.

The overall approach to understanding the behaviors of a DOT-113 tank car under impact conditions and the potential for improving its performance through design changes uses full-scale and laboratory testing with companion FE modeling of increasing complexity. This testing ultimately represents a DOT-113 tank car under LNG service conditions subjected to a shell impact that punctures both inner and outer tanks. The planned approach includes future tests and corresponding analyses to examine the influence of different materials/thicknesses used for the tank shell to 1) examine the effect(s) of modeling both the lading and the inner tank steel using properties at cryogenic conditions, and 2) ultimately model a DOT-113 tank car under "representative" conditions expected for LNG service.

Observations, lessons learned, and data collected during the first impact test of a DOT-113 tank car and the subsequent impact test of the surrogate were used as a starting point for modeling the DOT-113 surrogate in this test. The major difference is the use of LN2 in this test. An additional complexity for designs such as the DOT-113 is the consideration of puncture of one or both tanks. The desired outcome of this test was puncture of both the inner and outer tanks at a speed that minimized the post-puncture (residual) kinetic energy or speed of the impactor. Such a test would be an experimental demonstration of the impact energy required to puncture both tanks of a test article having the essential features of a DOT-113 tank car.

FRA collaborated with the authors before the test to determine the target test speed based on the model estimates, the desired outcome of the test, and such factors as ambient conditions (e.g., wind speed influencing actual impact speed) at the time of the test. After the test, material

coupon test data from both the inner and outer shells of the car, the measured internal pressure, and the measured test speed were used to update the pre-test model to reflect the actual test conditions. Finally, the post-test model results were compared to the test measurements.

## 1.4 Scope

This report describes the DOT-113 tank car surrogate and compares it with the test articles used in the previous two tests. . This report discusses the development and execution of FE models. The FE models include modeling the tank car steels and modeling the lading and gas phase outage within the tank. This report discusses the execution of the test, presents and summarizes the test results, and includes a discussion of the post-test modeling adjustments. Finally, the report presents a comparison between the test measurements and the model results.

This report does not include any results from further analyses using the DOT-113 tank car model, such as impact conditions outside of the conditions of the test. While this report refers to previously-performed shell impact tests on tank cars of different specifications [7, 8, 9, 10, 11, 12, 13, 14, 15], no comparison of results from those tests are included within the scope of this report. Research into the puncture resistance of DOT-113 tank cars is ongoing [3, 4, 5]. Further testing and simulations of the puncture responses of DOT-113 tank cars under varied impact conditions (e.g., varied outage level, varied impact speeds, varied tank thicknesses, cryogenic lading conditions, etc.) are planned will be documented in a future report.

## 1.5 Organization of the Report

Section 1 introduces the research and work conducted.

Section 2 details the tank car surrogate undergoing testing and analysis, and describes the shell impact test setup.

Section 3 describes the instrumentation used during the test and its placement. This description includes a discussion of the cameras used to capture the impact event.

Section 4 presents the results of the test. These results include a description of the actual conditions of the impact, a description of the test itself, and a summary of the measured test data.

Section 5 depicts the development of the FE models used in this program. This section describes the geometry used in the model, the different material models developed, and modeling techniques used in the pre-test and post-test models.

Section 6 presents test measurements alongside the corresponding estimates from the pre-test FE models.

Section 7 provides test measurements alongside the corresponding estimates from the post-test FE models.

Section 8 includes a summary of the report and concluding remarks.

Appendix A describes the positions of the cameras and targets used in the test.

Appendix B contains the full set of time history data measured during the test. The appendix also contains the material data measured during the tensile coupon tests for the TC-128 carbon steel making up the car's outer tank.

Appendix C consists of a full set of comparisons between test measurements and FE estimates. This appendix contains comparisons for pre-test models using three different outage modeling approaches and for the post-test model using the actual initial conditions.

Appendix D describes the geometry and mesh on each part used in the FE models.

Appendix E describes the modeling techniques that were used in both the pre-test and post-test FE models.

Appendix F depicts how each material behavior was developed in the FE models.

Appendix G contains the calculations used to determine the outage pressure and volume targeted for this test.

Appendix H contains a limited set of comparisons between the test measurements and FE models using the measured test pressure data as model input.

Appendix I summarizes the simplified heat transfer analyses conducted during the test planning phase.

# 2. Test Conditions

On July 24, 2021, FRA performed the side (shell) impact test at the Transportation Technology Center (TTC) in Pueblo, CO. The test was performed by sending a ram car into the side of a surrogate DOT-113 tank car that was mounted on skids and backed by a rigid impact barrier. The surrogate DOT-113 was partially filled with LN2. This section describes the tank car used and the overall test setup in the side impact testing program.

## 2.1 DOT-113 Tank Car Specification and Features

The DOT-113 tank car used in this test was a surrogate tank car designed to be similar to a DOT-113C120W9 tank car from a crashworthiness perspective. The commodity-carrying inner tank and insulation must be surrounded by an external tank to contain the insulation, maintain vacuum, and carry the in-train forces. The DOT-113C120W specification requires that the outer tank be made of a carbon steel or stainless steel that is approved for use in tank car construction [16], and be a minimum of 7/16 inches thick. For LNG transportation, the outer tank must be made of 9/16-inch-thick AAR TC-128, Grade B (TC-128) carbon steel.

Notably, the surrogate DOT-113 featured a 0.608-inch[6] TC-128 steel outer shell, compared to a 9/16-inch TC-128 steel outer shell in the previously tested (Test 11) DOT-113 surrogate tank car. The surrogate also featured a longer overall length compared to the previously tested DOT-113 surrogate. The surrogate tank car did not feature all the components, including couplers, running gear, safety appliances, etc., that would be included in a tank car meeting the full DOT-113 specification as defined in 49 CFR Part 179 Subpart F [17]. Since this surrogate was designed to hold LN2 during the test, it featured typical piping, valves, fittings, insulation, etc. that would be included in a complete DOT-113 tank car. Many of these design details were omitted from the DOT-113 surrogate used in the previous impact test using water within the tank [4]. Table 1 describes the alphanumeric code making up the DOT-113C120W specification.

**Table 1. Description of Specification DOT-113C120W Tank Car**

| DOT | 113 | C | 120 | W |
|---|---|---|---|---|
| Car built to meet a DOT specification | Specification 113 | Inner tank design service temperature of -260 °F | Inner tank test pressure of 120 psig | Welded tank |

### *2.1.1 DOT-113C120W9 Tank Car Specification and Features*

PHMSA promulgated a final rule (85 FR 44994)[7] on July 24, 2020, to authorize the transportation of methane, refrigerated liquid (more commonly referred to as liquefied natural gas (LNG)) by rail tank car [18]. In the final rule, enhanced outer tank requirements were

[6] A 0.608-inch outer tank was chosen over a 9/16-inch outer tank because it was available for manufacturing the DOT-113 surrogate in a timely manner for the target test date.

[7] Pipeline and Hazardous Materials Safety Administration (PHMSA). (2020). Hazardous Materials: Liquefied Natural Gas by Rail. Washington, DC: U.S. Department of Transportation.

specified for DOT-113C120W tank cars with the specification suffix "9" (DOT-113C120W9). This suffix denotes that the outer tank shall be 9/16 inches thick instead of 7/16 inches thick. Additionally, a specification DOT113C120W9 tank car must have its outer shell constructed of normalized TC-128 carbon steel. Table 2 summarizes the outer tank requirements from the final rule.

**Table 2. Summary of Tank Car Properties from Final Rule for LNG**

| Property | Final Rule |
|---|---|
| Tank Car Specification | DOT-113C120W9 |
| Minimum Wall Thickness of the Outer Tank Shell | 9/16 inches |
| Minimum Wall Thickness of the Outer Tank Heads | 9/16 inches |
| Required Outer Tank Steel Type(s) | AAR TC-128, Grade B normalized steel plate |

## 2.2 Description of DOT-113 Tank Car Surrogate Used in the Test

The surrogate DOT-113 tank car used in this test was constructed solely for the purpose of this side impact test.

The inner tank was made of American Society for Testing and Materials (ASTM) A240, Type 304 (T304) stainless steel having a nominal thickness of 0.25 inches [19]. The outer tank was made of Association of American Railroads (AAR) Specification TC-128, Grade B high strength carbon-manganese steel in the normalized condition with a nominal thickness of 0.608 inches [16].

The outer tank of the surrogate was manufactured to DOT specification 112A340. The tank car had an outside diameter of 117 1/8 inches, similar to the diameter of the outer tank of the DOT-113 tank car used in the November 2019 impact test (Test 10). As part of the fabrication processes, the DOT-112 tank car was put through a post-weld heat treatment (PWHT) process. After the completion of the manufacturing process, the tank car was cut apart circumferentially at two locations and a section of the shell was removed from the tank car. Removing the shell section reduced the length of the outer tank to 45 feet 8 1/2 inches over the heads. The inner tank was purpose-built for installation in the surrogate DOT-113. Its diameter, thickness, and material were consistent with the previously tested DOT-113C120W and DOT-113 surrogate tank cars (Test 10 and Test 11, respectively). The inner tank had a length over its heads of approximately 43 feet 7 inches. The inner tank had a nominal capacity of 17,864 gallons of water at room temperature.[8] The car was equipped with two pressure relief valves (PRVs) having start-to-discharge (STD) pressures of 75 and 90 psig.

The two tanks were nested together and separated by a 6-inch gap. This annular space contained MLI and was held under vacuum. Based on observations made during the previous test of a water-filled DOT-113 surrogate tank, the MLI was expected to have a negligible effect on the structural response of the surrogate during the impact.

[8] Due to thermal contraction, the inner tank would have a lower capacity of cryogenic material based on the temperature of that material.

The test was performed by sending a ram car into the side of the tank car, which was mounted on skids and backed by a rigid impact barrier as shown in Figure 1.


**Figure 1. DOT-113 Surrogate Tank Car Mounted on Support Skids**

### *2.2.1 Test Arrangement*

Figure 2 shows an overhead view of the test with annotations indicating: 1) the A-end and B-end of the tank car, 2) the east and west sides of the test site, and 3) the direction of travel of the ram car.

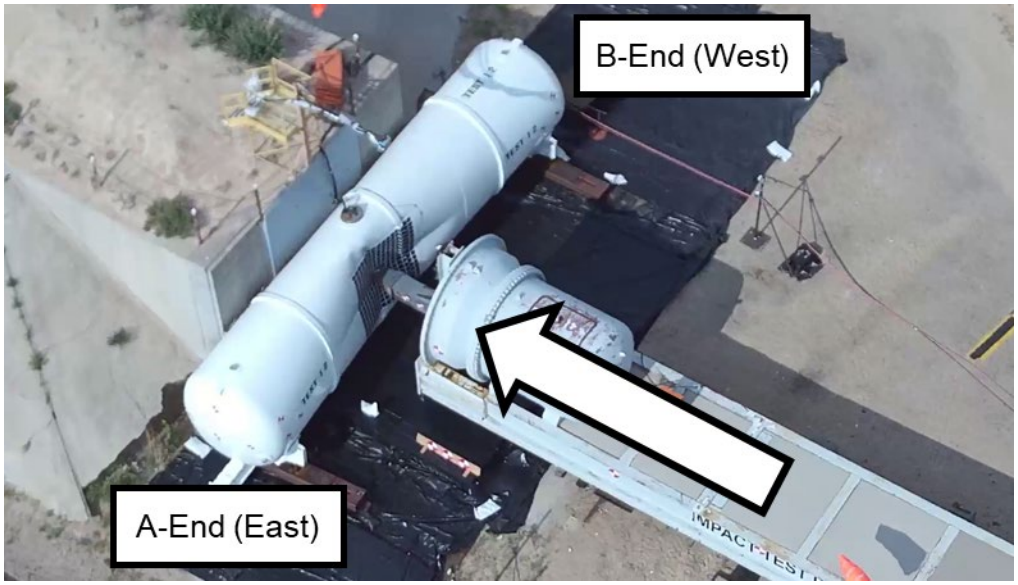


**Figure 2. Overhead View of Test Setup Extracted from Drone Video**

The DOT-113 surrogate tank car was offset by approximately 32 inches toward the west, resulting in an off-center impact. Figure 3 shows an annotated photo of the closure weld and a diagram of the nesting process where the outer tank (brown) is closed around the inner tank

(grey). The closure weld is a unique circumferential weld formed using a single welded butt joint with a backing strip on the inside of the joint instead of a fusion double welded butt joint per 49 CFR § 179.400–11. This weld is unique because it is not possible to weld from the inside of the outer tank after the inner tank is nested. This makes the closure weld the only circumferential weld in the inner and outer tank that is not a double-sided weld. Additionally, a PWHT of the entire tank car is not possible once the inner tank is nested. Thus, the double-sided welds on the two halves of the outer tank go through a global PWHT, but the closure weld is not required to undergo a PWHT by 49 CFR § 179.400–12.

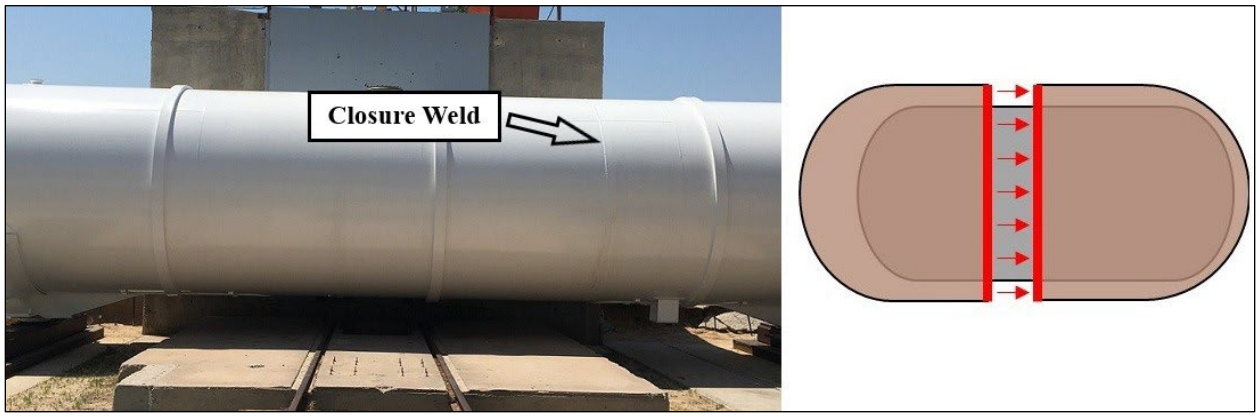


**Figure 3. Photo of Closure Weld (left) and Diagram of Nesting Process (right)**

Figure 4(a) shows one of the skids that the tank car was placed on oriented parallel to the track with one end near the impact barrier. Two sections of I-beams were welded to each skid and to the tank car for attachment, as Figure 4(b) shows. The tank car with skids attached was placed on 1-inch steel plates. These steel plates were placed on 4 3/4-inch-thick stacks of plywood to raise the tank car above the concrete slab in which the rails are embedded at the impact wall. This test configuration was designed to minimize the tank car rollback and allow the tank car on the skids to slide on the steel plates during the impact without contacting the concrete slab.


**Figure 4. Tank Support Skid System**

The desired level of LN2 in the tank car was calculated based on the nominal dimensions and capacity of the inner tank and the desired outage pressure and volume based on in-service

conditions for the transport of LNG (see Appendix G). Obtaining the desired lading level, outage pressure, and outage temperature was more challenging in this test due to the use of LN2 as the lading. The target lading and outage conditions are discussed in Section 2.2.2, and the actual lading and outage conditions are discussed in Section 4.5. A pipe (e.g., trycock line) that passed through both the inner and outer shells of the car was located such that once the desired 5 percent outage had been achieved, the LN2 would begin to flow out of the pipe. Once a stable liquid level, pressure, and temperature were established within the inner tank, the trycock valve was opened to allow the level of the LN2 to drain until reaching the bottom of the inlet pipe, thus achieving the desired filling volume of LN2. Additionally, a static head pressure gauge was installed on the tank car to measure the depth of the liquid in the tank car. During the filling process, the pipe was used to verify the liquid level indicated by the gauge. Figure 5 shows a static head pressure of approximately 66.5 inches of water, and Figure 6 shows the pipe used for setting the outage.


**Figure 5. Static Head Pressure Gauge**

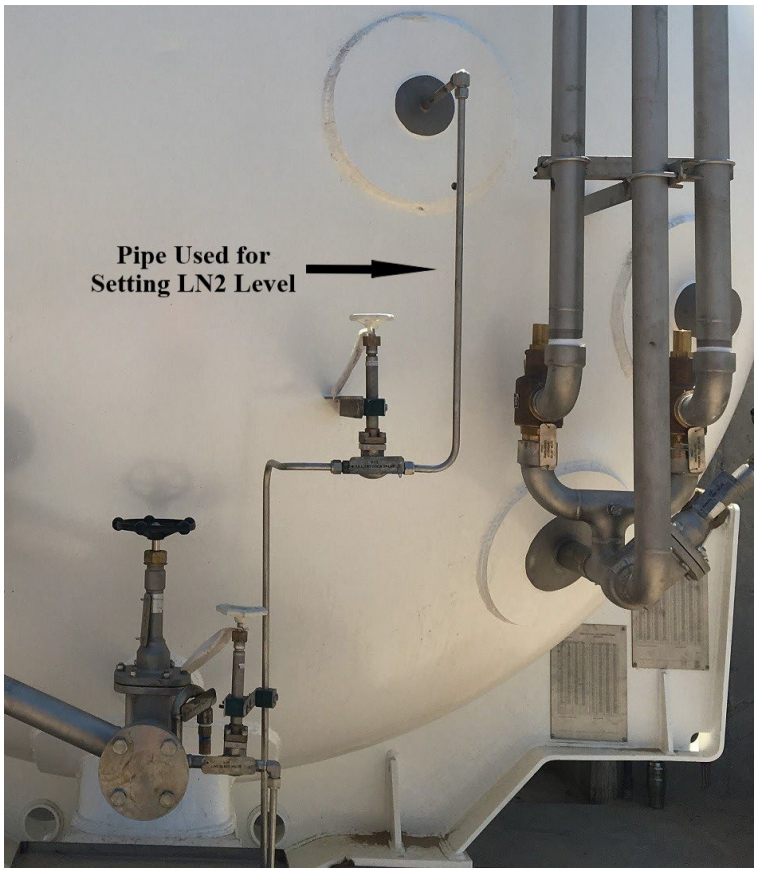


**Figure 6. Pipe Used for Setting the Lading Level**

The indenter was positioned to align with the mid height of the target tank car as closely as possible. The ram car was a modified flat car with an 8-foot ram installed on the leading end. This ram car was used in previous tank car tests and has a shortened tank attached to the ram end. Figure 7 shows the ram car, which is an image from a previous test. For this test, a 12-inch by 12-inch indenter with 1.0-inch radii on the edges and corners was used. The same indenter was used in the impact test of a DOT-111 tank car [9], a DOT-112 tank car [10], a DOT-117 tank car [12], a DOT-105 tank car [11], and a second DOT-111 tank car meeting voluntary industry standard CPC-1232 [14]. This same indenter was also used on the previous tests of a legacy DOT-113 [3] and DOT-113 surrogate [4] which were both filled with water.


**Figure 7. Ram Car and Head**

Figure 8 shows the 12-inch by 12-inch indenter attached to the ram car in an image taken from a prior test and Figure 9 shows the ram car aligned with the tank car. The ram car was weighed before the test to confirm the actual weight. The measured weight was 297,200 pounds.

**Figure 8. Ram Arm with 12-inch by 12-inch Indenter**


**Figure 9. Ram Arm with 12-inch by 12-inch Indenter Aligned with Impact Zone on the Tank Car**

The tank car used for this test had three large structural reinforcement rings, one near the center and one at each end of the car. These rings are shown in Figure 10.

**Figure 10. Tank Car Reinforcement Rings**

Prior to the November 2019 impact test of a legacy DOT-113 tank car, it was determined that one of the reinforcement rings would interfere with the typical interaction of the tank car with the

crash wall. The decision was made to add sections of 4-inch-thick plate steel to the wall to allow the entire outer tank to be initially in contact with the rigid wall, typical of the setup used in the previous tests. The layout of those sections is shown in Figure 11.

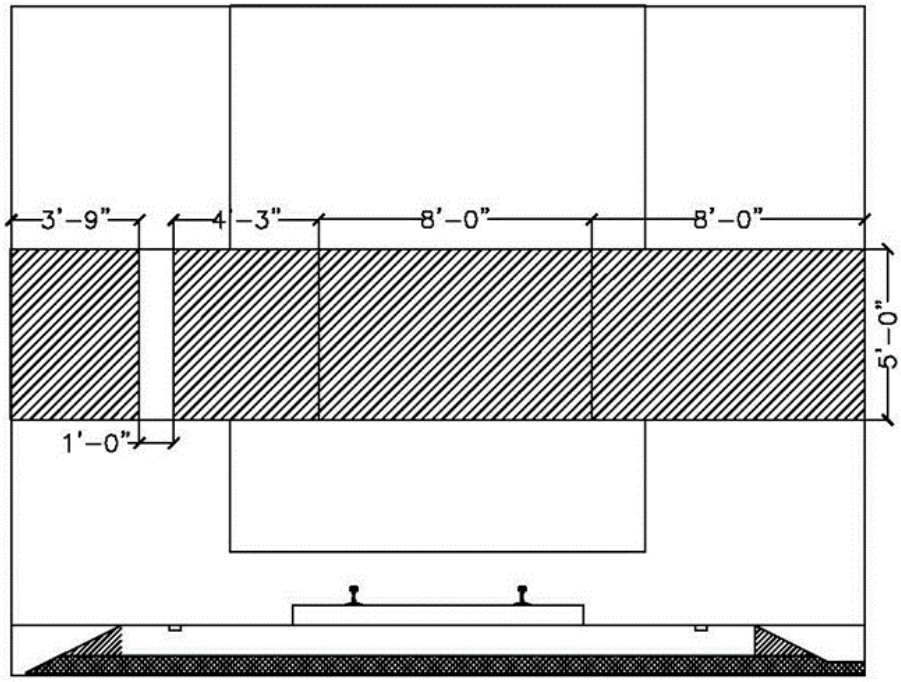


**Figure 11. Offset Plate Layout**

The surrogate DOT-113 tank car for this test had three structural rings, one of which was near the center of the car. The existing plate was modified to accommodate this configuration. The layout of the offset plate after the modifications is shown in Figure 12.

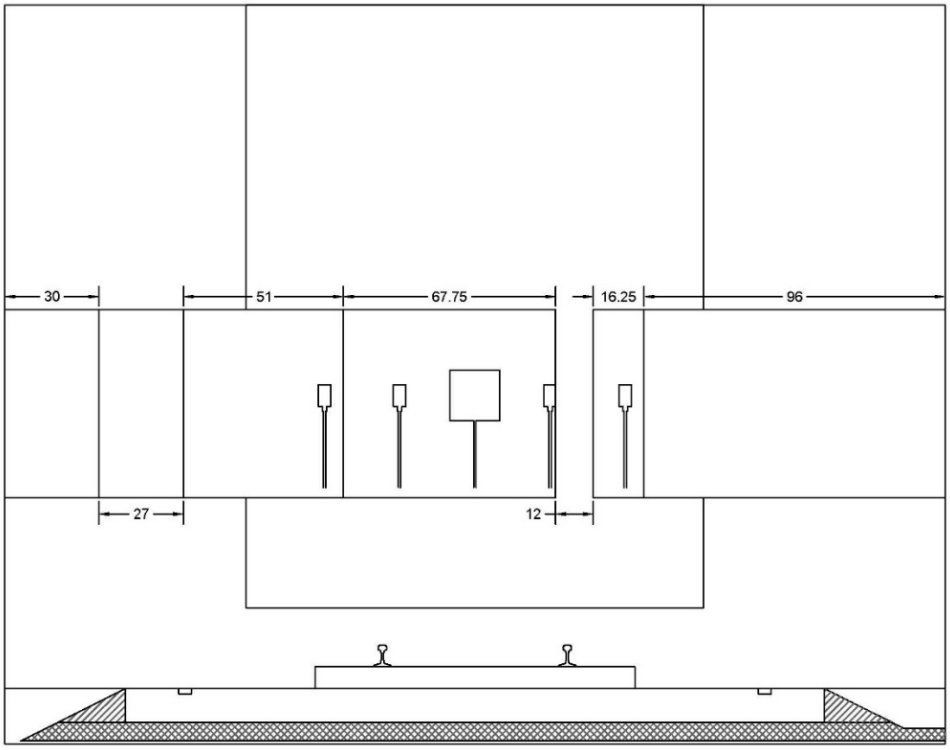


**Figure 12. Modified Offset Plate Layout**

### *2.2.2 Target Lading and Outage Conditions*

The next step in the progression toward a full-scale test of a modern DOT-113 tank car was to use a cryogenic liquid as lading in a DOT-113 surrogate. Using a cryogenic liquid presented new challenges compared to the previous DOT-113 tests that used water in the test setup. Additional challenges arose due to the need to use a stand-in cryogenic liquid (e.g., LN2) rather than the cryogenic liquid that the tank was designed to carry (e.g., LNG). As the test preparations progressed, the lading conditions ultimately chosen for the test also evolved. This section describes the initial lading conditions targeted for the test and, as appropriate, how those conditions changed in the actual test configuration.

Four lading conditions needed to be defined prior to the test. First, the lading to be used to had to be selected. Second, the volume of lading (and thus, the volume of vapor space or "outage") to be placed in the car had to be chosen. Third, the desired pressure for the outage had to be chosen. Fourth, the desired temperature for the outage had to be chosen. Several conditions affecting the lading were initially chosen to match the previously-conducted DOT-113 tests in this series, or to be consistent with the expected service conditions for LNG tank cars. The values for these established lading conditions that were chosen at the early stages of test preparation are summarized in Table 3.

**Table 3. Summary of Established Initial Lading Conditions**

| Condition | Value | Explanation | Citation |
|---|---|---|---|
| Outage Pressure | 50 psig | Consistent with values in previous DOT-113 tests | [3, 4] |
| Maximum Pressure When Offered for Transportation | 15 psig | Consistent with value in Final Rule | [18] |
| Filling Density (by mass) | 37.3% | Consistent with value in Final Rule | [18] |

### Lading

Careful consideration of the safety, environmental, logistical, and technical ramifications were given to the lading that was used in the tank car during this test. Testing using a cryogenic liquid in the tank car presented a more realistic test condition than the previous two tests that used water. While the DOT-113C120W9 tank car is specifically designed for use in LNG service, the intended outcome of this test was puncture of the inner tank. Thus, a stand-in cryogenic liquid was needed for LNG in the likelihood of a large-scale release during the test.

Ideally, the cryogenic liquid used for the test would have similar physical properties (e.g., density, viscosity, etc.) to LNG. The ideal cryogenic liquid would also be non-flammable and pose a minimum threat to the environment following a release. Further, the ideal cryogenic liquid would be able to be safely placed in the DOT-113 surrogate tank car without needing to modify the car to accommodate the stand-in cryogenic liquid, which was LN2 for this test.

### Initial Pressure

The initial pressure used in each of the previous two tests of DOT-113 tank cars and surrogates was 50 psig. For consistency, 50 psig was chosen as the initial target pressure for this test.

In the previous tests using water for the lading and air for the outage, the pressure at the start of the test could be readily controlled. If a higher pressure was desired, compressed air could be pumped into the vapor space through existing piping. As an incompressible liquid, the volume of the water within the tank would not be significantly affected by an increase in the vapor pressure. Similarly, a pressure reduction could be made by simply venting air from the tank. Again, the condition of the liquid water would be unaffected by the change in air pressure.

Using a cryogenic liquid introduced a new challenge into the test setup. The lading and vapor within the tank were a single substance, in this case nitrogen. A change in the thermodynamic condition of the GN2 in the vapor space could also affect the condition of the LN2 in the liquid space, and vice versa. There were several different techniques that could be used to adjust the pressure within the tank prior to the impact, but each technique offered varied levels of controllability, duration, and consequences to the other test conditions.

Once the tank was filled to its desired level with LN2, the valves could simply be closed and the tank allowed to settle. While the DOT-113 is a highly insulated container, no container is perfectly insulated from its environment. As heat leaked into the LN2, it would expand and occupy a larger volume of the tank. This increase in liquid volume would correspondingly

reduce the volume of the outage, increasing the outage pressure. If sufficient heat entered the liquid, evaporation would take place. Evaporation would decrease the volume of LN2 within the tank, as some of the LN2 was converted to GN2. The total volume of GN2 would increase, causing a pressure increase. This natural process would result in an increase to the pressure in the vapor space while maintaining a stable condition between the liquid and vapor. However, the expectation of the researchers was this process was time consuming because of the high level of insulation on the DOT-113 surrogate. Additionally, the liquid level would decrease below the desired initial filling level as LN2 was converted to GN2 if the LN2 was subject to heat leakage over a long duration of time.

A second approach to increasing pressure within the outage would be comparable to the procedures used in tests where water and air filled the tanks. Rather than using an air compressor, a tank of compressed GN2 at ambient temperature could be connected to a vapor line on the tank and used to add GN2 without reducing the amount of LN2 within the tank. The test team discussed this process, but there were several potential negative effects anticipated. The GN2 being added to the tank from the external tank would be much warmer than the GN2 already within the tank, resulting in an increase in the average temperature of the substances within the tank. The GN2 added from the exterior tank would mix with the GN2 already in the tank, resulting in some settling time for equilibrium to be reached. The added heat from the pumped in GN2 could cause additional LN2 to evaporate, further complicating the process of targeting a pressure and filling level. It was anticipated that the bottled GN2 would have to be added in several stages with settling time between filling processes to allow the tank to once again reach equilibrium.

If the initial pressure needed to be reduced prior to the test either LN2 or GN2 could be vented from the tank. If LN2 were vented from the tank, a larger quantity of material would need to be drained from the tank to cause the same pressure change that a small quantity of GN2 would produce. If GN2 were vented from the tank, the pressure within the tank would be reduced. However, this reduction in pressure could cause LN2 to undergo a phase change if the LN2 were at a temperature close to its saturation point. Venting GN2 could cause some of the LN2 to evaporate into a vapor, causing the remaining LN2 to auto-refrigerate (i.e., decrease its average temperature). While the outage pressure could be increased or decreased after the tank had been filled but before the test occurred, the process was likely to change the condition of the liquid at the same time. Due to its large thermal inertia, the condition of the liquid would be unlikely to change quickly in response to a change in the vapor conditions.

The initial pressure target changed during test preparations. The 50 psig initial pressure was chosen based on the initial pressures used in the previous two tests. As the test plans developed, concerns were raised about the potential for rapid phase change following a puncture outcome. As the pressure within the tank increases the saturation temperature of the nitrogen also increases. Consequently, the LN2 can exist in the liquid phase at higher temperatures when the internal pressure is higher than it could exist under lower pressure. In the event of a puncture outcome to the test, some portion of the LN2 would be immediately exposed to atmospheric pressure at the point of puncture. If this LN2 was at an elevated temperature (and, consequently, pressure) compared to its saturation temperature at atmospheric pressure, some of the liquid released would rapidly “flash” to form vapor. If all of the newly-created GN2 was able to escape to atmosphere, this behavior would not lead to a safety concern. However, if even a portion of the newly-created GN2 remained within the inner tank or escaped into the annular space between

the outer and inner tanks, pressure could rapidly build up within the DOT-113 surrogate. Depending on the amount of GN2 generated, its path to atmosphere, and the rate at which it was produced, a catastrophic failure to the surrogate tank car could not be completely eliminated.

The process of simulating phase change is very complex and could not be practically undertaken as a part of the preparations for this test. There were also no known situations in which the circumstances planned for the test occurred in an unplanned incident which resulted in catastrophic failure of the tank. However, this test sought to use several initial conditions that would be considered non-ideal in typical cryogenic liquid transportation. Typically, cryogenic liquids are transported at a low pressure, which corresponds to a lower temperature needed to maintain the liquid phase. The test was initially targeting a pressure of 50 psig, raising the potential for the liquid to exist at a higher initial temperature. The test also sought to deliberately cause damage to the tank, potentially up to the point of puncture.

### Volume of Lading

Another aspect of the lading and outage conditions to be determined prior to the test was the filling level for the tank car. For cryogenic materials authorized to be transported by DOT-113 tank cars, 49 CFR § 173.319(d)(2) contains a table of maximum permitted filling densities[9] for different commodities, initial pressures, tank car specifications, and STD pressures for the tank car's PRV. Because the tank would be filled with LN2 during the test, a target filling density had to be chosen based on the in-service condition expected to be encountered for a particular commodity.

At the time of conducting the two DOT-113 side impact tests in 2019 and 2020, LNG could only be transported on rail in DOT-113 tank cars under a Special Permit (DOT-SP 20534). PHMSA published a Notice of Proposed Rulemaking (NPRM) in the Federal Register [20] that proposed to allow the transportation of LNG by DOT-113C120W tank cars. This NPRM included a proposed updated version of the table contained in 49 CFR § 173.319(d)(2) that sets out the filling conditions for LNG. It is important to note that the test conditions used in 2019 and 2020 were based on the proposed requirements in the NPRM, which are different from the requirements in the final rule (85 FR 44994). The requirements from the NPRM and final rule are summarized in Table 4.

**Table 4 Summary of Pressure Control Valve Settings from NPRM and Final Rule for LNG**

| Property | NPRM | Final Rule |
|---|---|---|
| Tank Car Specification | 113C120W | 113C120W9 |
| Maximum STD | 75 psig | 75 psig |
| Maximum pressure when offered for transportation | 15 psig | 15 psig |
| Design service temperature | -260 °F | -260 °F |
| Maximum Permitted Filling Density (percent by weight) Methane | 32.5% | 37.3% |

[9] 49 CFR § 173.319(d)(1) states: *For purposes of this section, "filling density" is defined as the percent ratio of the weight of lading in the tank to the weight of water that the tank will hold at the design service temperature.*

Because the DOT-113 tests in 2019 and 2020 took place before the publication of the final rule, a filling density of 32.5 percent was used to determine the outage volume percentage and pressure for the tests. The 32.5 percent filling density from the NPRM resulted in an outage of 17.6 percent being used in both Test 10 and Test 11. The outage of 17.6 percent corresponded to the density of LNG at a saturation pressure of 45 psig. The calculations used to determine the outage volume and pressure in Tests 10 and 11 are appendices to the respective test reports [3, 4].

For this test, the updated filling density used in the final rule (e.g., 37.3 percent) was used to determine the filling level. Using a similar procedure to what was used in the previous two tests to calculate the outage with the updated filling density of 37.3 percent from the final rule, resulted in an updated outage of 5 percent. Calculations for the relationship between outage volume and outage pressure are contained in Appendix G.

At the target test pressure of 62.3 psia—50 psig plus 12.3 psi atmospheric pressure for Pueblo, CO—saturated LN2 has a weight density of approximately 6.7 pounds per gallon and a temperature of 92.1 K [21]. At the same pressure, saturated LNG has a weight density of approximately 3.3 pounds per gallon and a temperature of 132.7 K [21]. Consistent with the previously conducted DOT-113 tank car and surrogate tests, the filling volume in this test was targeted to match the volume of LNG that would be carried in typical service conditions. The DOT-113 surrogate filled with LN2 would be carrying roughly twice the weight of lading as a similar tank filled to the same volume with LNG. This extra load resulted in higher stresses in the inner tank, the inner tank's attachments to the outer tank, and the outer tank at the start of the test. Calculations of filling volume for the tested DOT-113 surrogate are included in Appendix G.

**Initial Temperature**

Filling the DOT-113 surrogate with any cryogenic liquid would cause thermal contraction of the inner tank. This thermal contraction causes stresses to develop anywhere the tank is constrained and causes the volume of the tank to decrease. These aspects were both investigated using pre-test FE models and determined to have relatively insignificant effects [5].

With LN2 as the lading the inner tank in the test had a lower temperature than an equivalent tank in LNG service. Following the first DOT-113 test in this series, mechanical tests were conducted on stainless steel samples excised from the inner tank at temperatures between room temperature and -321 °F (77 K) [3]. Post-test material coupons were excised from the inner tank of the surrogate DOT-113 tank car tested in June 2020, and these coupons were subjected to tensile testing at -320 °F (~77 K), -80 °F (~211 K), and 70 °F (~295 K). [4]. These material tests were also conducted over a range of strain rates. These material tests were performed so the model capabilities could be updated to include the use of a cryogenic liquid as lading.

The results of these mechanical tests demonstrated that the ductility, yield strength (YS), and ultimate tensile strength (UTS) of the T304 stainless steel in the inner tank exhibit sensitivity to the temperature at which the tensile tests were performed. Thus, substituting LN2 for LNG will result in a potentially different level of puncture resistance in the tested car than in actual service conditions. LN2 and LNG have different saturation temperatures at a pressure of 62.3 psia (50 psig). Above the saturation temperature either liquid will vaporize. At 62.3 psia, LNG has a higher saturation temperature (132.7 K) than LN2 (92.1K) [21]. However, compared to the difference in material properties at LNG temperature and room temperatures, the difference

between properties at LNG and LN2 temperatures are expected to be less significant. Further, since the LN2 temperature is colder than the LNG temperature, any detrimental effects on mechanical properties associated with decreasing temperature would be exacerbated by using LN2.

At an initial pressure of 14.7 psia (1 atmosphere at sea level), LN2 must be kept at or below 77 K to remain a liquid.[10] As discussed in the Initial Pressure section, after a puncture some amount of LN2 within the tank would suddenly be exposed to atmospheric pressure. Since LN2 cannot exist at atmospheric pressure and a temperature above 77 K, the LN2 within the tank would begin to vaporize. As LN2 evaporates to GN2 energy from the surroundings is absorbed, reducing the temperature of the remaining LN2 within the tank (e.g., auto-refrigeration). If the LN2 within the tank auto-refrigerated down to 77 K, it would exist at its saturation temperature under 1 atmosphere of pressure and the flash event would end. The LN2 would continue to evaporate as it warmed up, but at a much lower rate than if it were initially superheated.

The test team concluded that the ideal situation for the LN2 would be a temperature close to the saturation temperature at 1 atmosphere. If the temperature of the LN2 inside the tank was close to the saturation temperature corresponding to the atmospheric pressure at the test site (i.e., close to 1 atmosphere absolute pressure) there would not be a "flash" boiling of LN2 in the event of a puncture of the tank. To the extent possible, the temperature of the LN2 within the tank was to be kept as low as practical. The potential lading conditions considered prior to the test are further discussed in Appendix I2.

### Summary of Target Lading and Outage Conditions

The target lading and outage conditions chosen for the current test are summarized in Table 5. Pre-test models (Section 6.1) were used to help with the selection of the outage level and pressure for this test. Based on the modeling results, it was determined that a range of pressures, 15 to 35 psig, would be acceptable. The chosen outage volume target was 5 percent.

**Table 5. Summary of Lading and Outage Conditions Targeted for Test**

| Parameter | Target Value for Test |
|---|---|
| Commodity in Tank | LN2 |
| Outage Volume | 5% |
| Outage Pressure | 15–35 psig |

Note that the values shown in Table 5 were the values targeted for the test. The commodity in the tank (i.e., LN2) did not change as test preparations progressed but the actual outage volume and pressure at the time of the test varied from these target values. These differences are discussed in Section 4.5.

[10]At Pueblo, CO's, elevation LN2 has a saturation temperature of approximately 76 K under 1 atmosphere of pressure.

## 2.3 Comparison of DOT-113 Test Conditions

Table 6 summarizes the test conditions in the 2019 test of a DOT-113C120W, the 2020 test of a DOT-113 surrogate tank car filled with water, and the 2021 test of a DOT-113 surrogate tank car filled with LN2. The test conditions not detailed in Table 6 were kept the same between the tests where possible. After Test 10, the insulation was changed from perlite to MLI to be more representative of a modern DOT-113. In Test 11, the annular space was held at atmospheric pressure as this was not expected to have a significant effect on puncture to simplify the design and construction of the surrogate tank car. After Test 10, the inner tank volume and the length over the heads were reduced to simplify the design and construction of the DOT-113 surrogates, and this was not expected to have a significant effect on puncture [4]. After Test 10, the outer tank was intentionally changed from a 7/16-inch A516, Grade 70 (A516-70) carbon steel to a 9/16-inch TC-128 carbon steel to evaluate the crashworthiness improvement from using a higher strength, thicker steel in the outer tank. While it was preferrable to use a 9/16-inch-thick outer tank for Test 12 as well, a 0.608-inch TC-128 outer tank was used due to availability for manufacturing the surrogate. The target test speed was increased after each test (16.5 ± 0.5, 17.2 ± 0.5, and 17.7 ± 0.5 mph) to ensure that the kinetic energy of the impactor was equal to or greater than the previous test.

**Table 6. Summary of DOT-113 Side Impact Test Conditions**

| **Test Date** | **November 19, 2019** | **June 11, 2020** | **July 24, 2021** |
|---|---|---|---|
| **Test Number** | Test 10 | Test 11 | Test 12 |
| **Test Article** | DOT-113C120W | DOT-113 Surrogate | DOT-113 Surrogate |
| **Thickness (Outer Tank)** | 7/16-inch | 9/16-inch | 0.608-inch |
| **Material (Outer Tank)** | A516-70 Carbon Steel | TC-128 Carbon Steel | TC-128 Carbon Steel |
| **Diameter (Outer Tank)** | ~119 inches | ~120 inches | ~117 inches |
| **Length (Outer Tank)** | ~74 feet | ~45 feet | ~46 feet |
| **Thickness (Inner Tank)** | 1/4-inch | 1/4-inch | 1/4-inch |
| **Material (Inner Tank)** | T304 Stainless Steel | T304 Stainless Steel | T304 Stainless Steel |
| **Diameter (Inner Tank)** | ~106 inches | ~106 inches | ~103 inches |
| **Volume (Inner Tank)** | 32,900 gallons | 19,300 gallons | 17,900 gallons |
| **Tank Lading** | Water | Water | LN2 |
| **Outage (Actual)** | 17.6% | 17.6% | ~9% |
| **Pressure (Actual)** | 50 psig | 50 psig | 30 psig |
| **Insulation** | Perlite | Multilayer Insulation | Multilayer Insulation |
| **Annular Pressure** | Vacuum | Atmospheric | Vacuum |
| **Impact Speed (Actual)** | 16.7 mph | 17.3 mph | 18.3 mph |

It should be noted that the changes to the (1) insulation, (2) outer tank thickness and strength, (3) lading, and (4) outage volume were expected to have a large effect on the structural response of the DOT-113 surrogate tank car. Post-test FE analyses performed after the November 2019 test indicated that the presence of perlite in the annular space stiffened the force versus impactor travel response of the tank car and resulted in puncture at a lower impactor velocity than predicted in analyses without perlite. Typically, it would be desirable to only change one variable (i.e., insulation type or outer tank steel) between tests, multiple variables were changed between tests due to the high cost and time commitment associated with running a full-scale side impact test. However, once confidence is built in a validated FE model of a DOT-113 side impact test, the FE model can be used to carefully investigate the effect of each test variable on the structural response of the tank car to a side impact collision.

# 3. Test Instrumentation

## 3.1 Overview

Table 7 lists all instrumentation used for this test. Additional descriptions of the various types of instrumentation are provided in the following subsections.

**Table 7. Instrumentation Summary**

| Type of Instrumentation | Channel Count |
|---|---|
| Accelerometers | 11 |
| Speed Sensors | 2 |
| Pressure and Temperature Transducers | 6 |
| Thermocouples | 6 |
| String Potentiometers | 4 |
| Laser Displacement Transducers | 15 |
| **Total Data Channels** | **44** |
| Digital Video | 4 HS Cameras, 2 Go-Pros, and 1 Thermal Imaging Camera |

## 3.2 Ram Car Accelerometers and Speed Sensors

The local acceleration coordinate systems were defined relative to the ram car. Positive x, y, and z directions are forward, left, and up relative to the lead end of the ram.

Three triaxial accelerometers were mounted on the longitudinal centerline of the ram car at the front, rear, and near the middle of the car. Two uniaxial accelerometers were mounted on the left and right sides of the car to supplement recording of longitudinal acceleration. Figure 13 illustrates the positions of these accelerometers. Table 8 summarizes the ram car accelerometer ranges and positions.

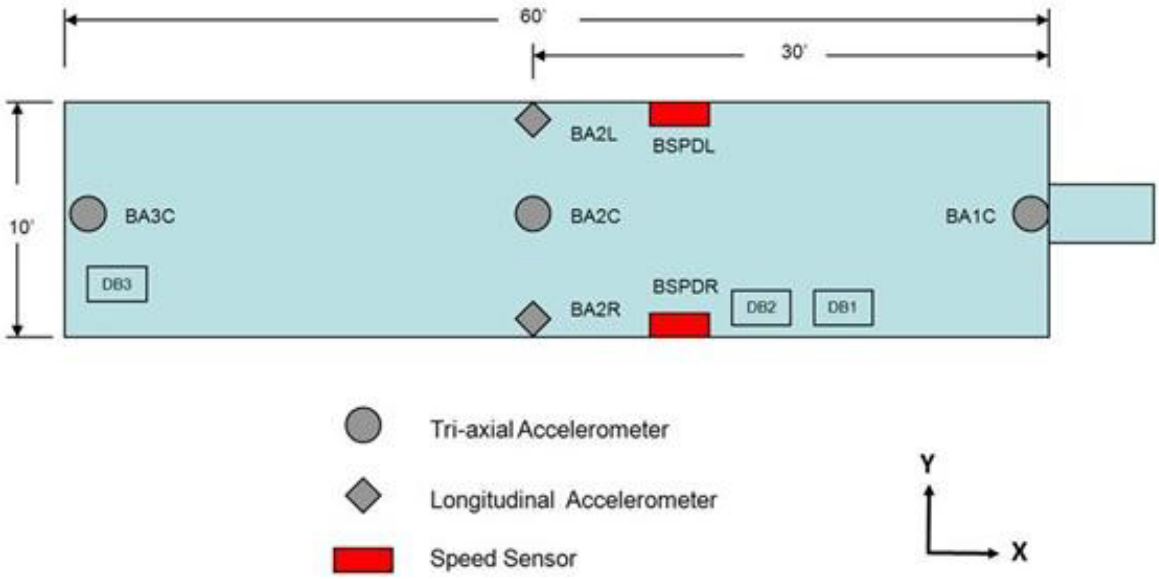


**Figure 13. Ram Car Instrumentation**

**Table 8. Ram Car Accelerometers**

| Channel Name | Sensor Description | Range |
|---|---|---|
| BA1CX | Leading End, Centerline, X Accel | 200 g |
| BA1CY | Leading End, Centerline, Y Accel | 100 g |
| BA1CZ | Leading, Centerline, Z Accel | 200 g |
| BA2LX | Middle, Left Side, X Accel | 100 g |
| BA2CX | Middle, Centerline, X Accel | 50 g |
| BA2CY | Middle, Centerline, Y Accel | 50 g |
| BA2CZ | Middle, Centerline, Z Accel | 50 g |
| BA2RX | Middle, Right Side, X Accel | 100 g |
| BA3CX | Trailing End, Centerline, X Accel | 200 g |
| BA3CY | Trailing End, Centerline, Y Accel | 100 g |
| BA3CZ | Trailing End, Centerline, Z Accel | 200 g |

Speed sensors were mounted on both sides of the ram car to provide an accurate measurement of the car's velocity within 20 inches of the impact point. The speed sensors were reflector based light sensors, which use reflectors on the ground separated by a known distance in conjunction with light sensors mounted on the car. The sensors were triggered as the car passed over the reflectors. The last reflector was positioned to align with the sensor when the ram head was within a few inches of the impact point. The time interval between passing the reflectors was recorded, and the speed was calculated from distance and time. A handheld radar gun was also used to take supplemental speed measurements.

## 3.3 Tank Car String Potentiometers and Thermocouples

The local displacement coordinate systems (except for the tank heads) were defined relative to the tank car. Positive x, y, and z directions are forward, right (away from the wall), and up relative to the A-end of the tank car. Tank head displacements were positive toward the impact wall.

Four string potentiometers were used to measure the tank motions at the ends of the tank car. Two potentiometers were attached to the skids that the tank car is mounted on, and the remaining two were attached to the center of the tank heads. The fixed anchor positions were established so that these measurements are for the longitudinal motions of the tank heads and skids. Figure 14 and Figure 15 show the string potentiometer locations. Table 9 lists the string potentiometers and their information.

**Table 9. Tank Car String Potentiometers**

| Area | Location | Axis | Channel Name | Range (inch) |
|---|---|---|---|---|
| Tank Head | A-End | Y | TDAend | 50 |
| Tank Head | B-End | Y | TDBend | 50 |
| Skid | A-End | Y | TDAskid | 50 |
| Skid | B-End | Y | TDBskid | 50 |

Six thermocouples were installed inside the tank. Three thermocouples were placed at the bottom of the tank—one at each end of the tank and one near the center of the tank—to measure the temperature of the liquid nitrogen. Two thermocouples were placed at the top of the tank—one at the A-end and one near the center of the tank—to measure the temperature in the vapor space. One thermocouple was mounted at the B-end of the tank car near the axial centerline to measure the temperature of the liquid nitrogen between the bottom of the tank and the vapor space. This thermocouple was mounted on an arm cantilevered off the B-end head. Figure 14 and Figure 15 show the thermocouple locations. Table 10 shown below lists the thermocouples and their information. It should be noted that the thermocouple located at A-end top (TT1000) was damaged and did not record any data.

**Table 10. Tank Car Thermocouples**

| Location | Sensor Description | Channel Name | Range |
|---|---|---|---|
| A Top | A-End Top | TT1000 | -326 °F to 122 °F |
| A Floor | A-End Floor | TT1180 | -326 °F to 122 °F |
| M Top | Mid Top | TT2000 | -326 °F to 122 °F |
| M Floor | Mid Floor | TT2180 | -326 °F to 122 °F |
| B Top | B-End Top | TT3000 | -326 °F to 122 °F |
| B Middle | B-End Middle | TT3C | -326 °F to 122 °F |

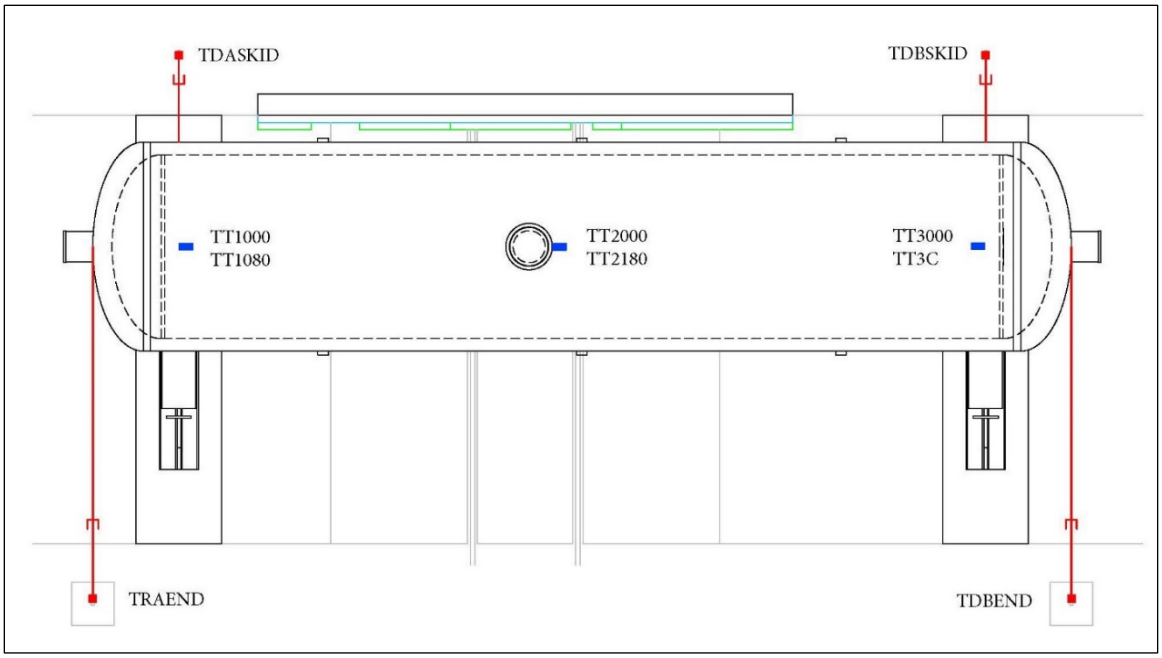


**Figure 14. Tank Car String Potentiometer and Thermocouple Locations (overhead)**

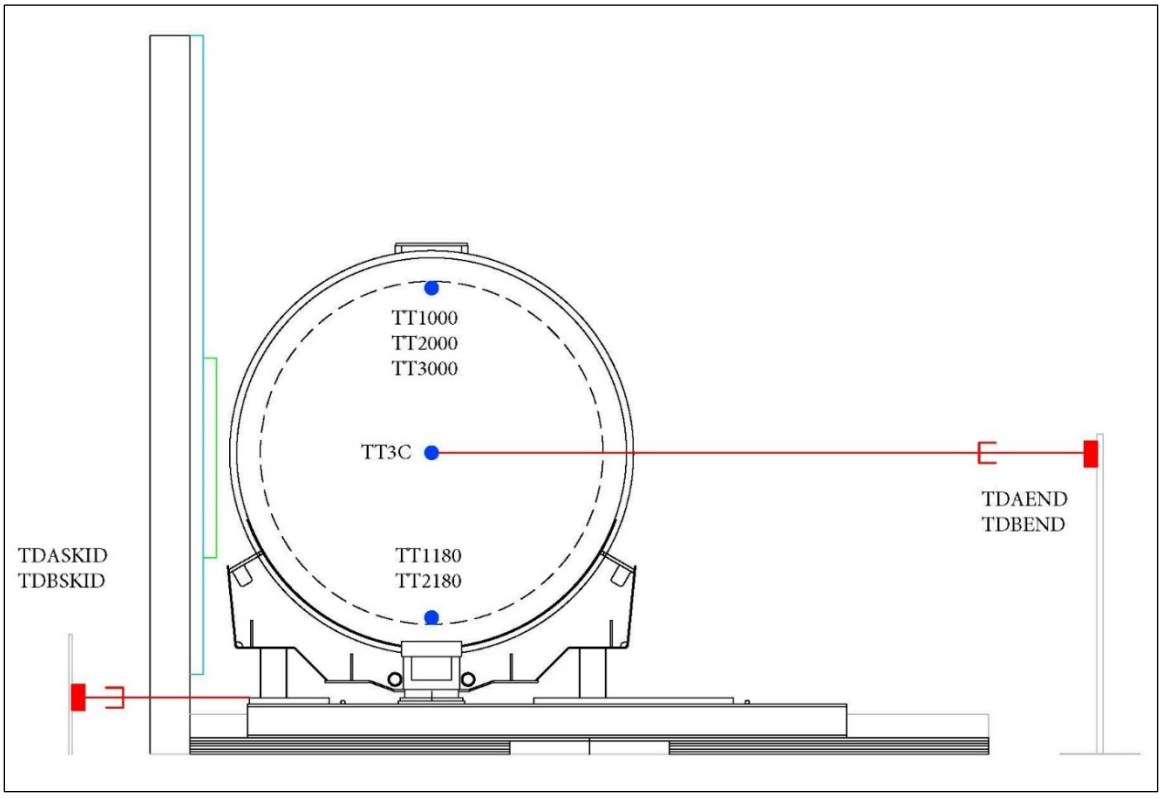


**Figure 15. Tank Car String Potentiometer and Thermocouple Locations (end view)**

## 3.4 Tank Car Combination Pressure and Temperature Sensors

Two combination pressure and temperature transducers were mounted in the inverted dome of the manway and were used to measure the pressure and temperature in the outage during the impact. Four additional pressure and temperature transducers were mounted at various locations in the piping of the tank car. The positions of the combination pressure and temperature transducers are shown in Figure 16 and Figure 17 and summarized in Table 11.

**Table 11. Tank Car Pressure and Temperature Transducers**

| Location | Channel Name | Range |
|---|---|---|
| Manway | TPM1 | 250 psig -320 °F to 70 °F |
| Manway | TPM2 | 250 psig -320 °F to 70 °F |
| Line to PRV | TPRV | 250 psig -320 °F to 70 °F |
| Top Fill Line | TP-V5 | 250 psig -320 °F to 70 °F |
| Low Pressure Isolation Valve | TP-V14 | 250 psig -320 °F to 70 °F |
| High Pressure Isolation Valve | TP-V15 | 250 psig -320 °F to 70 °F |

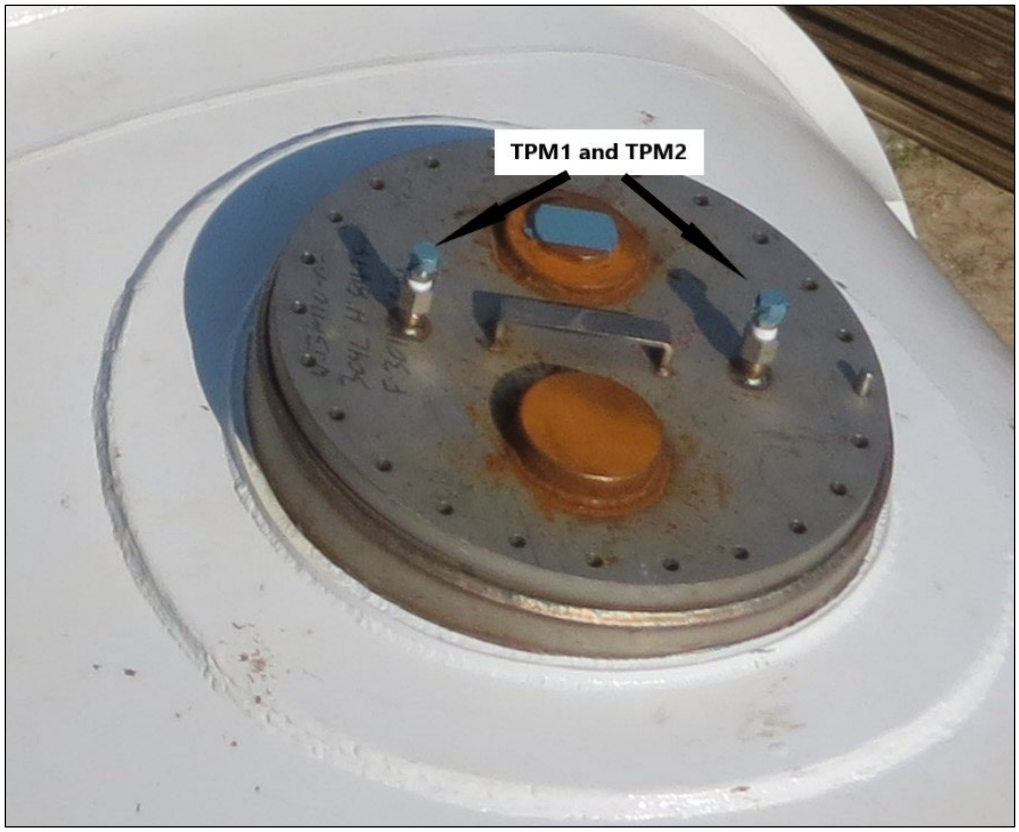


**Figure 16. Tank Car Pressure/Temperature Transducer Locations (manway)**


**Figure 17. Tank Car Pressure/Temperature Transducer Locations**

## 3.5 Laser Displacement Transducers

A series of laser displacement transducers mounted to the face of the ram car and in the recesses cut into the offset plate mounted to the crash wall were also used to record the tank car's response. Fifteen laser displacement transducers were set up to record the tank crush displacements around the immediate impact zone during the test. Four transducers were mounted to the ram car using brackets to measure the dent formation of the tank at locations of 24 inches and 48 inches to either side of the impact point. A fifth laser transducer was mounted on the ram car to measure the distance of the ram car from the crash wall. For this test, 10 lasers were mounted in pairs in pockets in the standoff plate attached to the crash wall. One laser of each pair measured distances that were extremely close to the wall, and the other laser of the pair measured longer distances. This pairing was necessary due to the designed measurement ranges and resolutions of the lasers. One of the laser pairs was mounted in line with the center of impact, and the other four pairs were mounted 24 inches and 48 inches on either side of the impact point. Table 12 provides a list of the laser displacement transducers used during the test. Figure 18 shows the positions of the lasers mounted to the ram car. Figure 19 shows the lasers mounted to the crash wall, and Figure 20 shows the relative positions of those lasers.

**Table 12. Laser Displacement Transducers**

| Location | Channel Name | Sensor Description | Range (mm) |
|---|---|---|---|
| Ram Car | BD1Y | Displacement EAST | 50–12,000 |
| Ram Car | BD2Y | Displacement 2nd from EAST | 50–12,000 |
| Ram Car | BD3Y | Displacement 3rd from EAST Aimed at Crash Wall Above Tank Car | 50–12,000 |
| Ram Car | BD4Y | Displacement 4th from EAST | 50–12,000 |
| Ram Car | BD5Y | Displacement 5th from EAST | 50–12,000 |
| Crash Wall | TD1YS | Displacement Short Range EAST | 35–110 |
| Crash Wall | TD1YL | Displacement Long Range EAST | 100–1,000 |
| Crash Wall | TD2YS | Displacement Short Range 2nd from EAST | 35–110 |
| Crash Wall | TD2YL | Displacement Long Range 2nd from EAST | 100–1,000 |
| Crash Wall | TD3YS | Displacement Short Range 3rd from EAST | 35–110 |
| Crash Wall | TD3YL | Displacement Long Range 3rd from EAST | 100–1,000 |
| Crash Wall | TD4YS | Displacement Short Range 4th from EAST | 35–110 |
| Crash Wall | TD4YL | Displacement Long Range 4th from EAST | 100–1,000 |
| Crash Wall | TD5YS | Displacement Short Range 5th from EAST | 35–110 |
| Crash Wall | TD5YL | Displacement Long Range 5th from EAST | 100–1,000 |

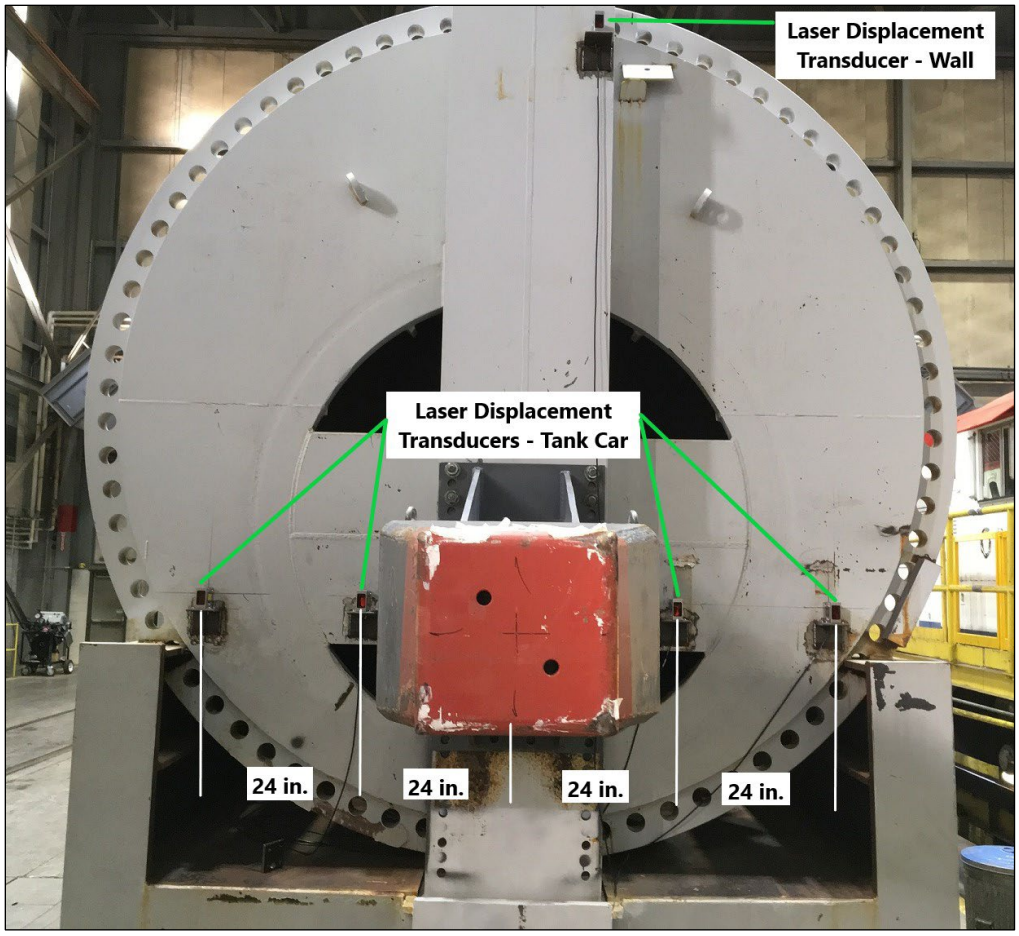


**Figure 18. Lasers Displacement Transducers on Ram Car**

**Figure 19. Lasers Displacement Transducers on Crash Wall**

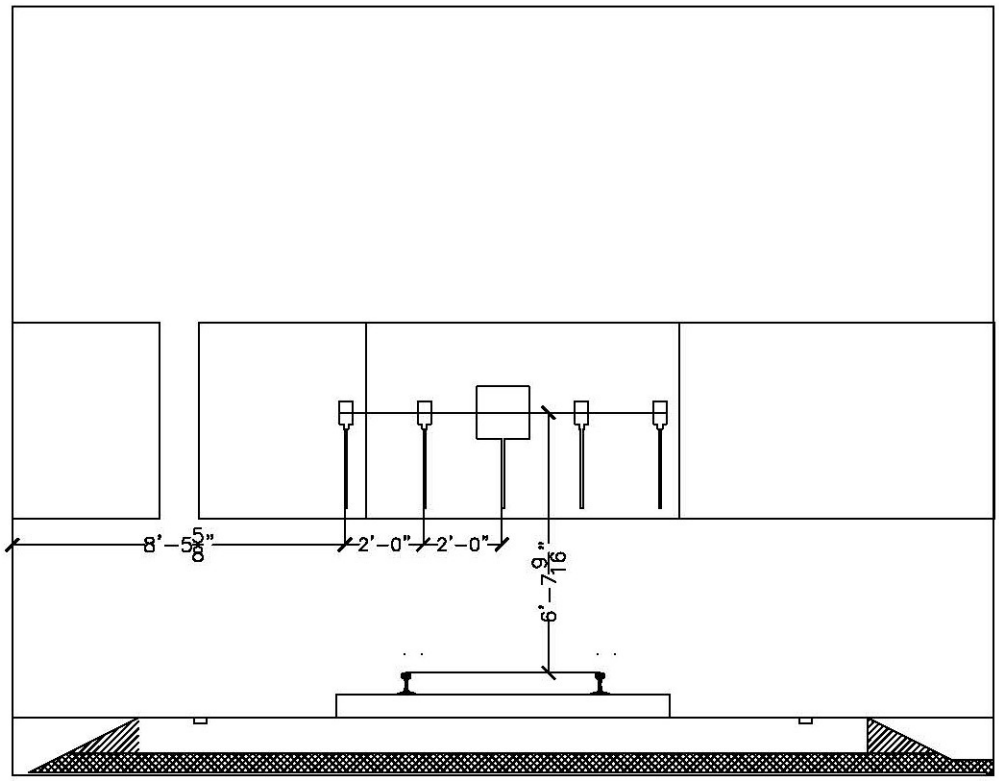


**Figure 20. Relative Positions of Crash Wall Laser Transducers**

## 3.6 Real Time and High-Speed Photography

Four high-speed (HS) and two real-time high-definition (HD) video cameras documented the impact event. Figure 21 shows a schematic of the camera position setup. Additionally, a thermal imaging camera was mounted to a drone to capture more details of the release of LN2 in the event of a tank puncture.

All the HS cameras were crashworthy and rated for peak accelerations of 100 gs. The final alignment and sighting in of the cameras were done when the ram car was positioned at the impact point prior to the start of test.

The ram car and the impact barrier were painted with flat light gray paint. The tip of the indenter was painted red. High contrast targets were applied to the ram car, the indenter, and at select ground reference points to aid in video analysis, should video analysis have been necessary.

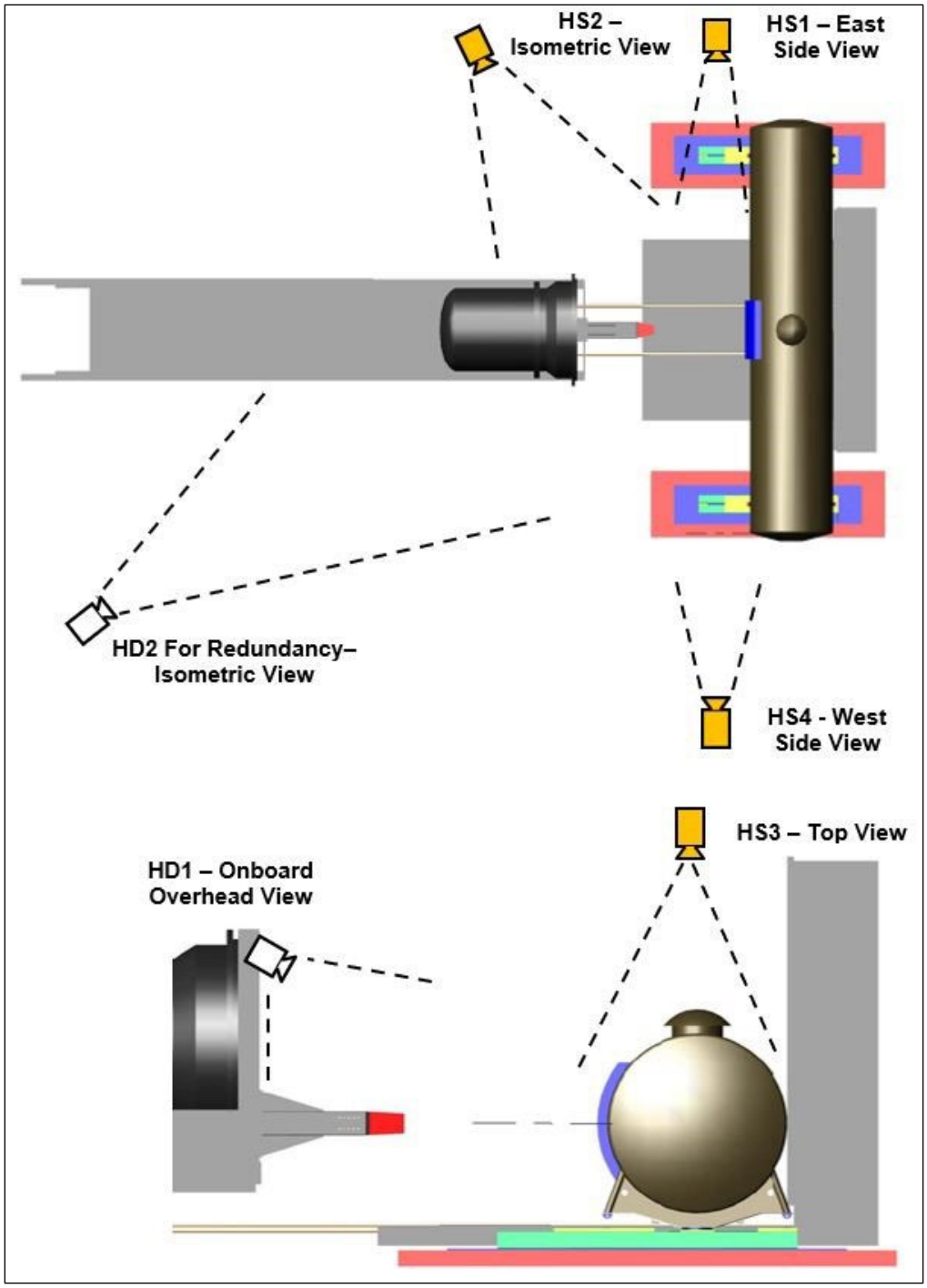


**Figure 21. Camera Views**

## 3.7 Data Acquisition

A set of 8-channel battery-powered onboard data acquisition systems was used to record the data from the instrumentation mounted on the ram car. These systems provided 1) excitation to the instrumentation, 2) analog anti-aliasing filtering of the signals, 3) analog-to-digital conversion,

and 4) a recording of each data stream. A similar set of ground-based data acquisition systems was used to record data from the pressure transducers and string potentiometers on the tank car.

The data acquisition systems were GMH Engineering Data BRICK Model III units. The data acquisition complied with the appropriate sections of Society of Automotive Engineers (SAE) J211 [23]. The data from each channel was anti-alias filtered at 1,735 Hz, then sampled and recorded at 12,800 Hz. The data recorded on the data bricks was synchronized to time zero when the tape switches were closed by the initial impact. The time reference came from the closure of the tape switches on the front of the test vehicle. Each data brick was ruggedized for shock loading up to at least 100 g's. Onboard battery power was provided by GMH Engineering 1.7 Amp-hour 14.4 Volt NiCad Packs. Tape Switches, Inc., model 1201-131-A tape switches provided event initial contact.

Software in the data bricks was used to determine zero levels and calibration factors rather than relying on set gains and expecting no zero drift. The data bricks were set to record 1 second of data before initial impact and 4 seconds of data after initial impact.

# 4. Results

This section describes the actual conditions of the test, some of which varied from the target conditions summarized in Section 2. This section also presents the test results in the form of photographs and a discussion of the damage to the tank car as well as graphs of test data. The results of post-test laser scans of the inner and outer tanks are also included in this section.

## 4.1 Test Conditions

As described in Sections 2 and 3, this test was a side impact of a surrogate DOT-113 tank car, performed on July 24, 2021. The test involved an 18.3 mph side impact by a structurally rigid 297,200-pound ram car with a 12-inch-square impactor head into the side of a tank car backed by a rigid impact barrier. The tank car was filled to approximately 95 percent capacity with LN2 to simulate the standard commodity lading volume of a DOT-113 tank car. The pressure in the inner tank was approximately 30 psig.

At the time of the test, the ambient conditions included a wind speed of 11 mph out of the north to northeast with gusts up to 20 mph and an air temperature of 84 °F.

## 4.2 Details of Test

Pre-test simulations estimated a puncture speed range of 16.7 to 19.5 mph based on the estimated material properties. The target test speed was 17.7 ±0.5 mph. This test speed was chosen because it was thought that it would provide sufficient energy to puncture both the outer and inner tanks without leaving a large amount of residual kinetic energy in the ram car after the puncture. Section 6 discusses the pre-test simulations used to help select the target test speed. The actual calculated impact speed from the speed sensors was 18.3 mph.

The ram car was brought to a stop during the test. Subsequently, both the ram car and the DOT-113 surrogate rebounded from the impact wall as the surrogate tanks recovered their elastic energy. The ram car separated from the DOT-113 surrogate and continued to roll back up the impact track until its brakes engaged, and the car came to a stop. Neither the inner nor outer tank punctured during this test.

Figure 22 shows the damage to the impacted side of the tank car. Figure 23 shows a detailed view of the impact zone on the outer tank. The impactor footprint is apparent in this figure. The upper left, lower left, and lower right corners of the impactor transferred paint onto the outer tank. Figure 24 shows the post-test position of the tank car relative to the supporting wall.


**Figure 22. Tank Car after the Impact (impact side)**

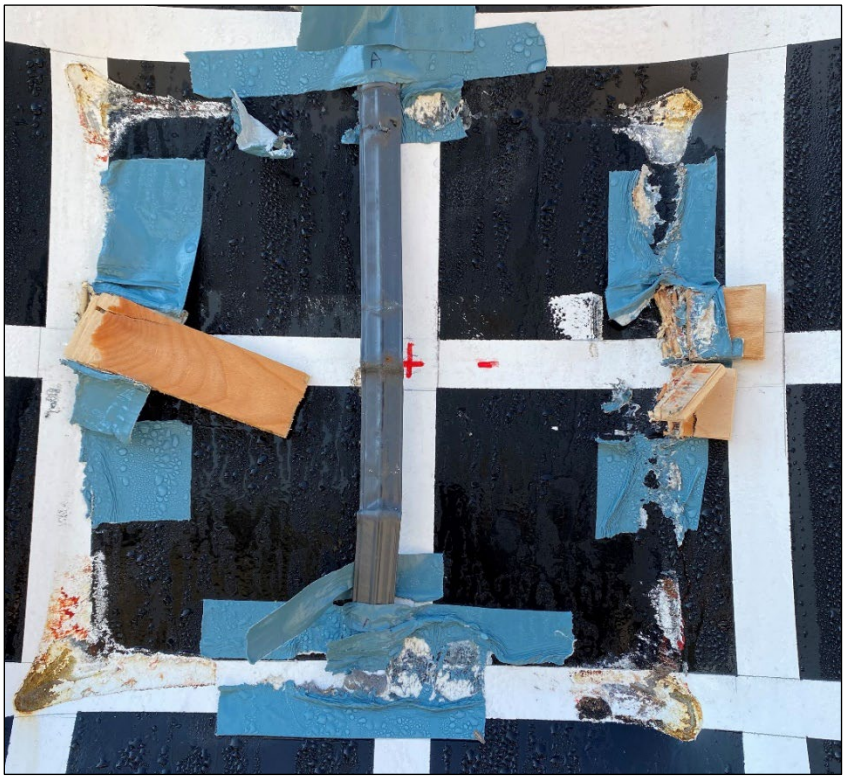

**Figure 23. Detail View of Impact Zone**

**Figure 24. Post-test Position of Tank Car (wall side)**

Figure 25 contains a still frame extracted from the isometric HS video of the test. This frame was extracted at 0.308 seconds. This is the approximate time at which the maximum forward motion of the ram car occurred. This figure shows the extent of the deformation that occurred during the test.


**Figure 25. Still Frame from HS Video Taken at Approximate Time of Maximum Indentation (0.308 seconds)**

## 4.3 Laser Scanning

After the test, complete light detection and ranging (LIDAR) scans of the outside and inside of the tested tank car were performed to document the deformation that occurred. Figure 26 shows the post-test scan of the DOT-113 surrogate tank car from the point of view of the ram car (front view). The area of impact is shown on the left side of the tank in this figure and the indentation has a diamond shape that is typical for side impact tests [15]. Square sections of the outer and inner tank were cut away near the B-end bolster (right) to access the inner tank for LIDAR scanning and to fabricate samples for material testing (refer to Section 4.5).

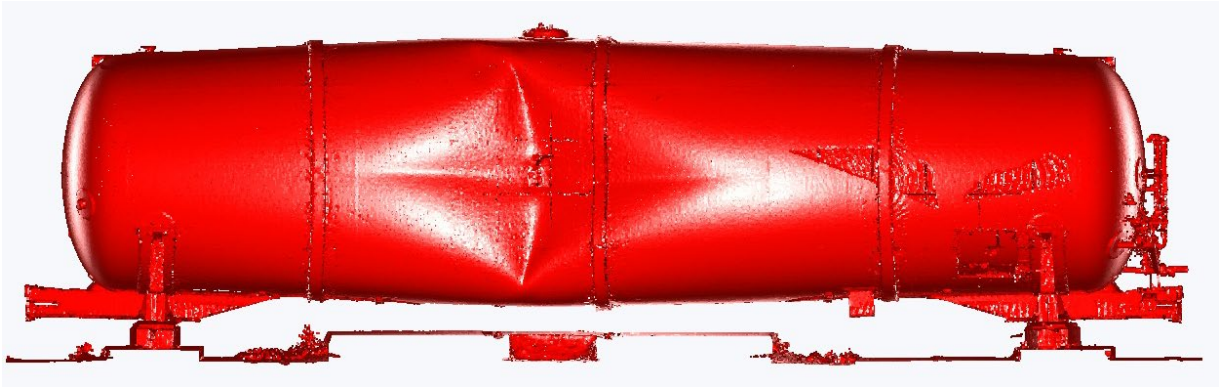

**Figure 26. LIDAR Scan Front View**

Figure 27 shows a post-test top view of the DOT-113 surrogate tank car. The indentation from the ram car is pictured on the bottom of the figure. The indentation from the wall is pictured on the top of the figure.

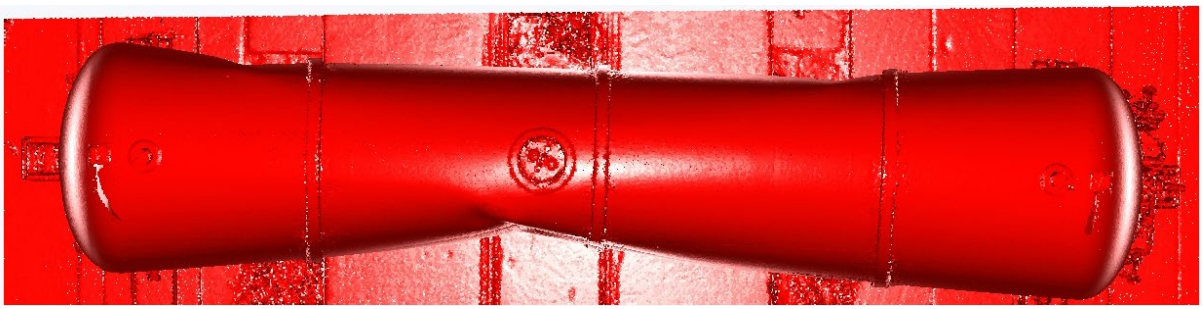

**Figure 27. LIDAR Scan Top View**

## 4.4 Measured Data – Impact Test

The data collected in the test were initially processed (i.e., offset corrections, filtering, etc.) by the research team and provided to Volpe for comparison with the FE analyses. The offset adjustment procedure ensured that the plotted and analyzed data included only impact-related accelerations and strains and excluded electronic offsets or steady biases in the data. The data collected before impact were averaged to determine the necessary offset correction. This offset was then subtracted from the entire data set for each channel. This post-test offset adjustment was independent of, and in addition to, the pre-test offset adjustment made by the data acquisition system.

The post-test filtering of the data was accomplished with a phaseless four-pole digital filter algorithm consistent with the requirements of SAE J211 [23]. A 60 Hz channel frequency class (CFC) filter was applied for the filtered acceleration data shown in this report. Appendix B contains the plots of the filtered data from all transducers.

The longitudinal acceleration of the ram car was one of the primary measurements in the test. Multiple accelerometers were installed on the ram car to capture this data. The data were then used to determine the impact energy, the deceleration of the ram car, and the contact forces between the ram and target tank car. The ram car's average longitudinal acceleration history, calculated from the onboard accelerometer data, is shown in Figure 28.

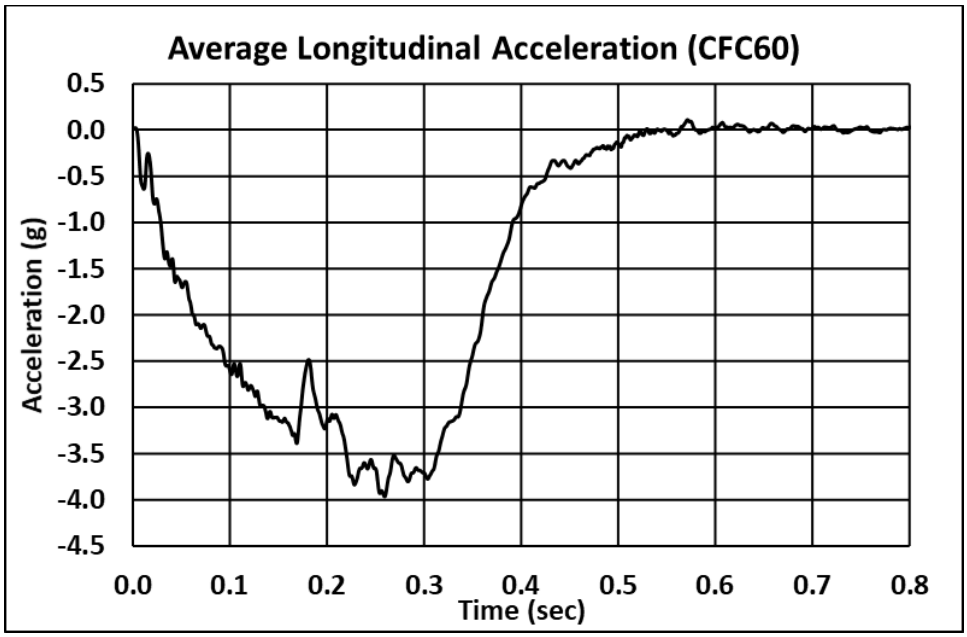


**Figure 28. Longitudinal Acceleration Data (averaged)**

The ram car velocity history for this test was calculated by integrating the average longitudinal acceleration of the ram car and using the measured impact speed as an initial condition. The contact forces between the ram and target tank car were calculated as the product of the average acceleration and the mass of the ram car. Figure 29 shows both the force-time and velocity-time histories for the ram car. The negative velocity shown indicates the speed of the rebounding ram car.

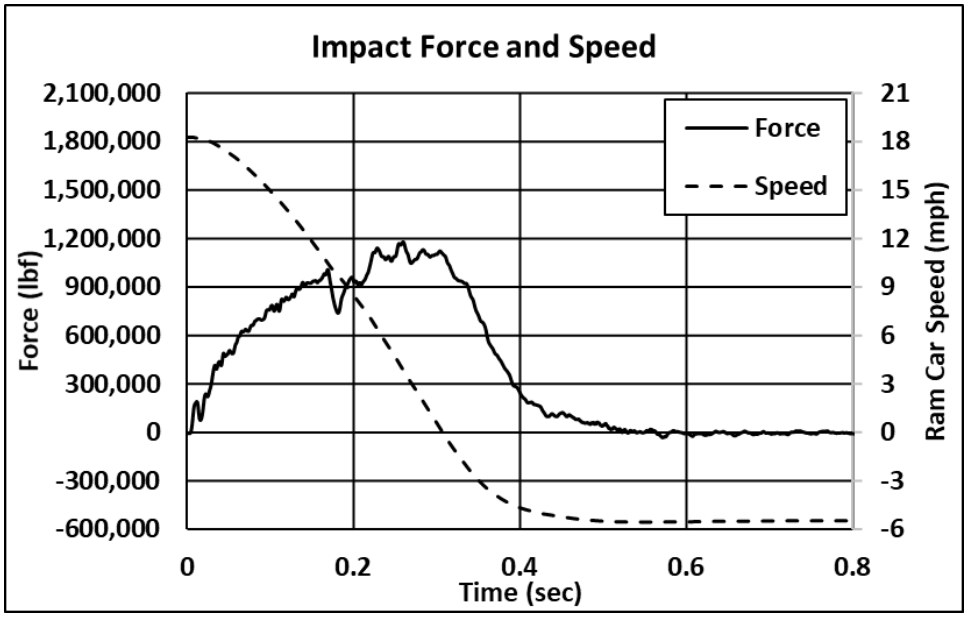


**Figure 29. Impact Force and Ram Car Speed**

Similarly, the kinetic energy was calculated based on the speed-time history and mass of the ram car. The energy absorbed by the tank car at any point in time was calculated as the difference between the ram car's current kinetic energy and its' kinetic energy at the time of impact. Figure

30 shows the kinetic energy time history of the ram car and the energy absorbed by the tank car. The energy absorbed by the tank car reached its' maximum when the forward motion of the ram car ended, approximately 0.308 seconds after impact.

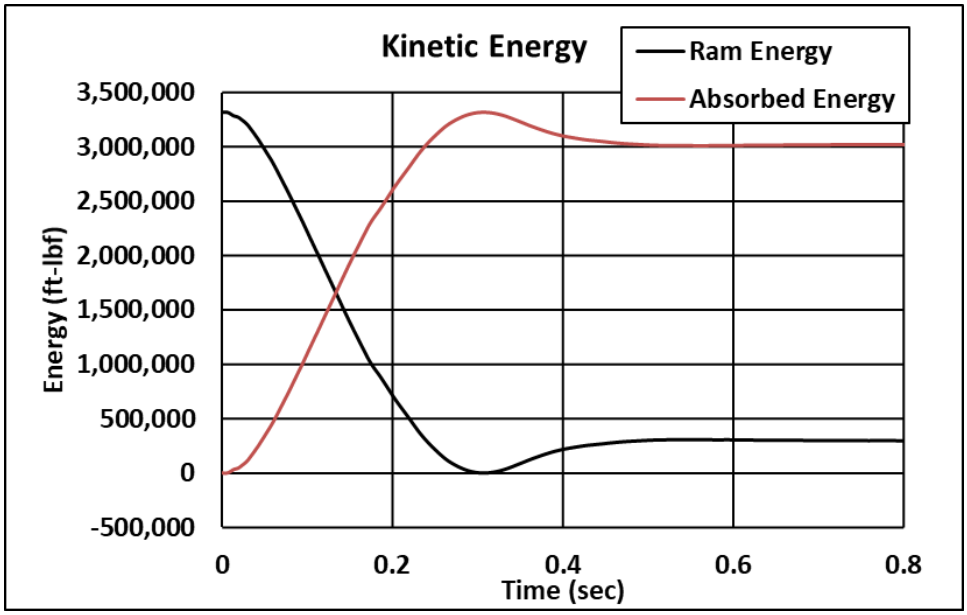


**Figure 30. Kinetic Energy Time-history of Ram Car**

The total kinetic energy of the ram car was just under 3.32 million ft-lbf, and the energy absorbed by the tank car just prior to rebound was also nearly 3.32 million ft-lbf. The difference between the initial kinetic energy and the energy absorbed by the tank before rebound was just under 800 ft-lbf, or about 0.00002 percent of the total kinetic energy. This insignificant difference is likely the result of round off during numerical integration, the averaging of multiple accelerometer channels, or the filtering the accelerometer signal.

Another significant impact response measured during the test was the effect of the internal pressure as the tank indentation formed and reduced the volume of the tank. The tank was initially filled to approximately a 5 percent outage volume with LN2, which was increased to approximately 9 percent by the time of the test (see Section 4.5). The pressure in the tank car was about 30 psig prior to impact. As described in Section 3.3, four combination temperature and pressure transducers were mounted at different locations in the piping outside the tank car, and two were mounted in the inverted dome at the bottom of the manway to measure pressure and temperature in the outage.

Figure 31 shows the pressure data from the vapor space below the manway. The two sensors have very similar readings up to about 0.1 second after the impact. At this point, the readings diverged significantly, with the transducer P-MH1 indicating a maximum pressure of around 10 psig less than P-MH2. The readings did come back into alignment at around 0.35 seconds after the impact, and the pressure in the outage post-impact dropped to around 26 psig. The reason for this discrepancy is unclear. However, the maximum pressure recorded by P-MH2 is believed to be correct.

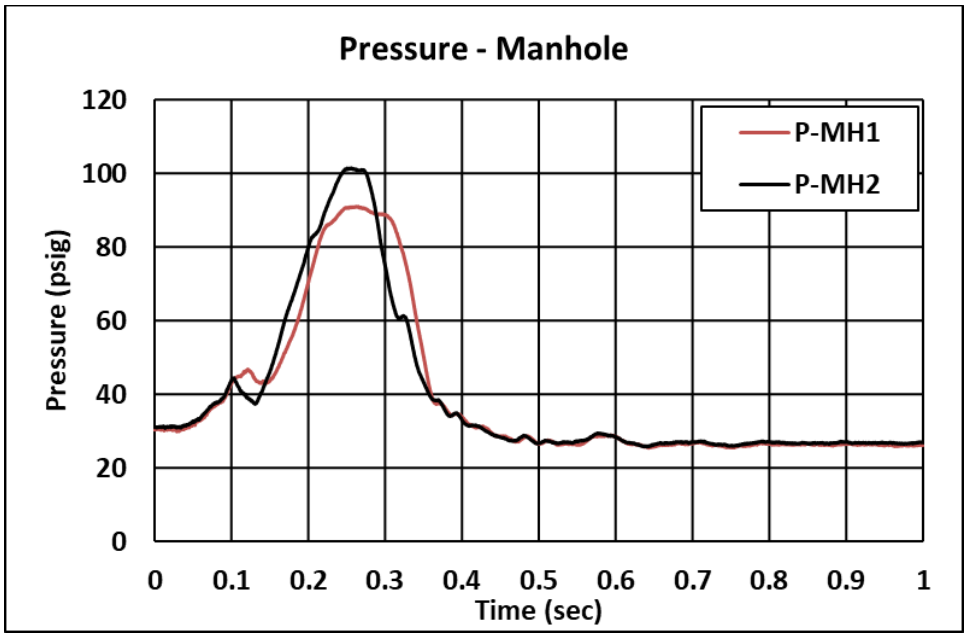


**Figure 31. Pressure Data from the Outage at the Manway**

Figure 32 shows the pressure data from the piping on the outside of the car. The maximum pressures recorded at locations P-V14 and P-V15 were around 100 psig and just over 80 psig at location P-V5. The post-impact pressure at both P-V5 and P-V14 dropped to around 26 psig while the pressure at P-V15 remained slightly higher at around 29 psig.

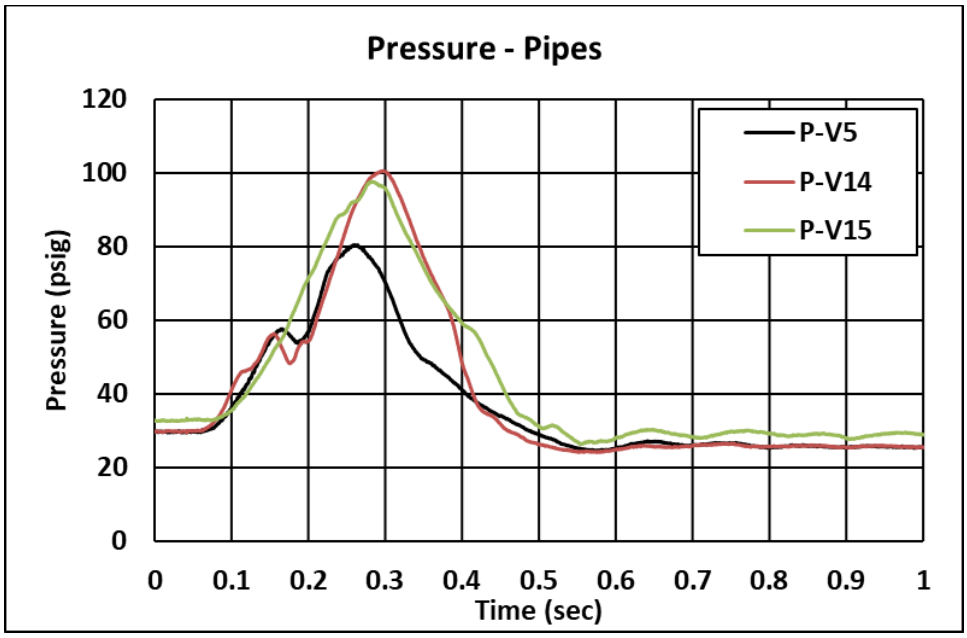


**Figure 32. Pressure Data from the Pipes**

Figure 33 shows the pressure response at the PRV. The surrogate tank car used in this test had two PRVs, one set to discharge at 75 psig and the other set for 90 psig, both of which were above the maximum pressure of around 70 psig seen upstream of the PRVs. The post-impact pressure at the PRV dropped to around 23 psig.

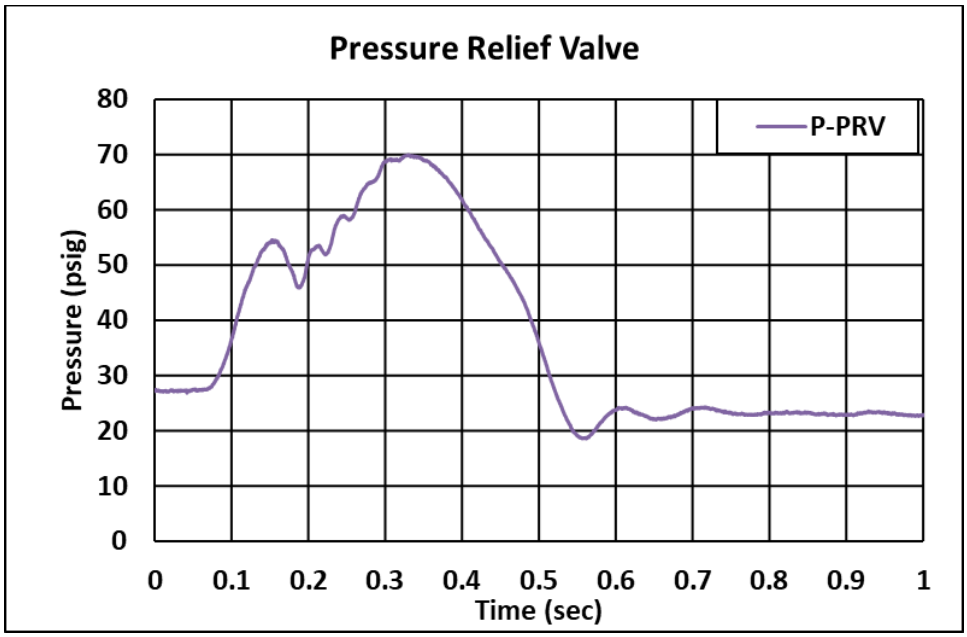


**Figure 33. Pressure Data at the Pressure Relief Valve**

The transient pressure measurements varied across the different sensor locations. Recall that none of the pressure transducers were in the outage itself. The transducers were installed in external piping, or on the manway with a flexible hose in the outage space. The presence of piping or hose between the outage volume and the transducer, the potential for entrapped liquid within the piping, or the higher temperature of the piping outside of the tank may lead to the pressure measurements differing from not only one another but also from the bulk pressure within the outage. The researchers believe that the pressures measured within the piping are correct (i.e., the transducers did not malfunction), but reflect a higher pressure than the bulk GN2 in the outage.

The remaining quantitative measurements taken for the tank car impact behavior were displacement histories recorded with string potentiometers and laser displacement transducers. These measurements included the external tank deformations (measured with lasers) and the external tank movements at both ends of the tank (measured with string potentiometers). The layout of the string potentiometers was described in Section 3.3. Section 3.4 described the layout of the lasers.

The deformation of the tank in the impact area was calculated using the lasers on the front of the ram car. Figure 34 shows the deformation of the tank at positions 24 inches (BD4Y) and 48 inches (BD5Y) to the right of the impact centerline. These locations had a maximum deformation of just over 51 and 45 inches, respectively. Normally, these calculations would also be made for the locations 24 inches (BD2Y) and 48 inches (BD1Y) to the left of the impact centerline, unfortunately the laser transducers at these two locations failed prior to capturing any data from the impact. The maximum deformation at the impact centerline was just over 58 inches.

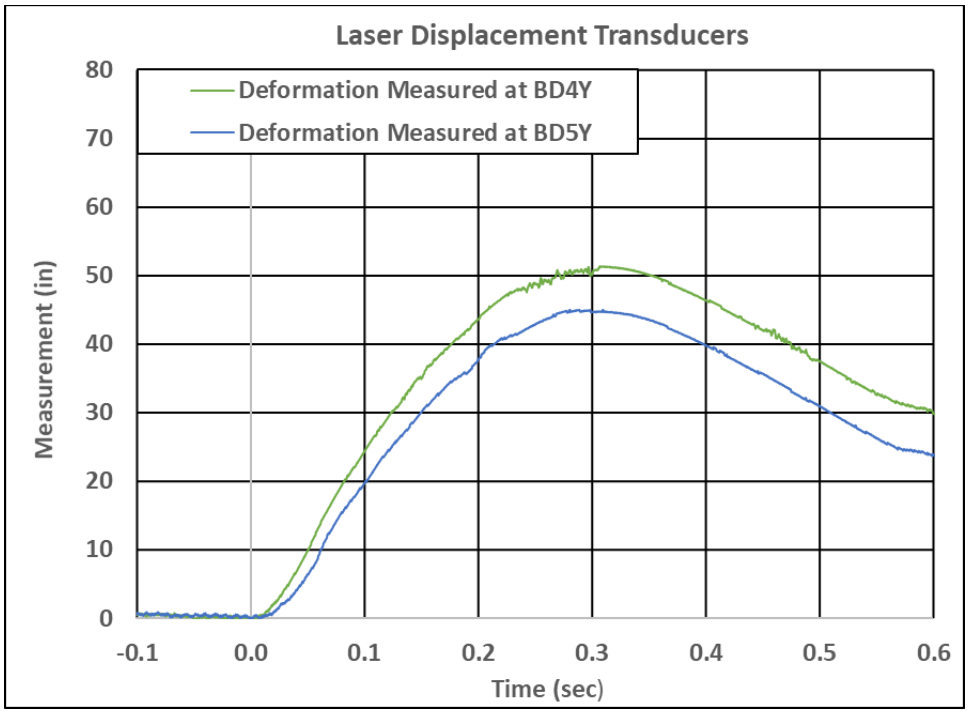


**Figure 34. Tank Car Deformation Measured with Laser Displacement Transducers**

The measured displacements for the tank car external string potentiometers are shown in Figure 35 and Figure 36. The displacements of the ends of the car were significantly delayed compared to the motions in the impact zone and little displacement is seen for the first 0.1 second of the response. The responses at the two ends are noticeably different with the A-end showing less displacement toward the crash wall and rebounding away from the crash wall sooner than the B-end. The B-end also comes to a stop further away from the crash wall after the rebound.

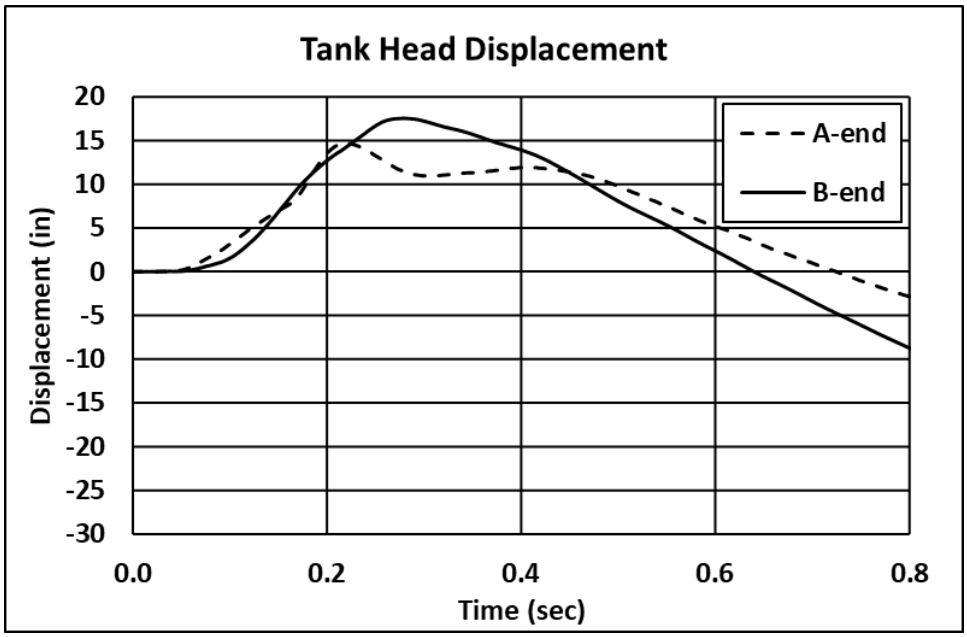


**Figure 35. External Longitudinal Displacements – Tank Car Heads**

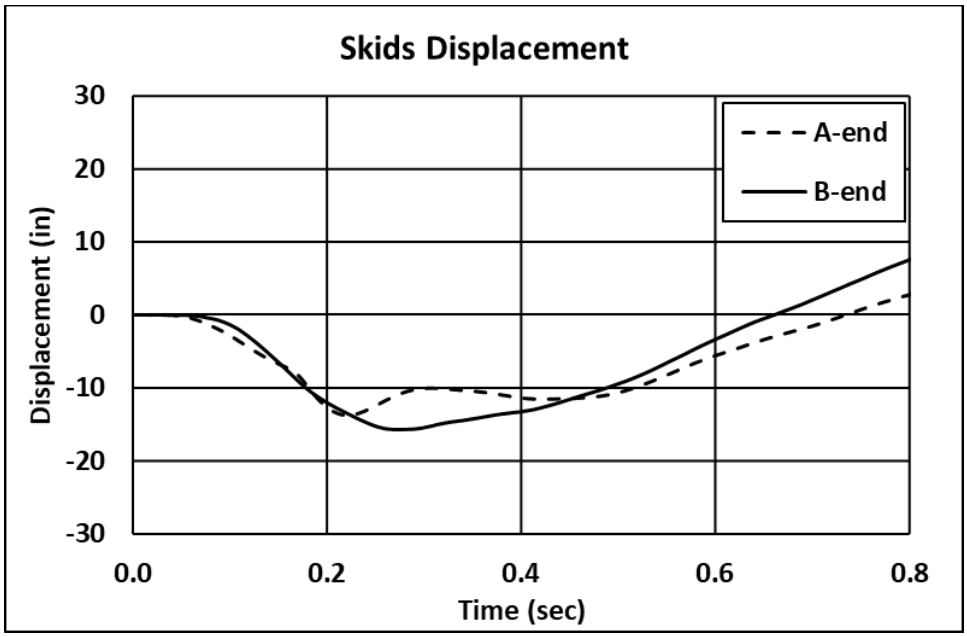


**Figure 36. External Longitudinal Displacements – Skids**

The temperature during the impact was recorded by the thermocouples inside the inner tank (see Figure 37 through Figure 39). The temperature readings remain fairly constant until about 0.1 seconds after the initial contact. After this point, the temperature in both the lading and the vapor space oscillates. While the liquid temperature begins to settle back to the original levels, the vapor space temperature shows a noticeable drop, with the B-end temperature dropping by over 40 °F.

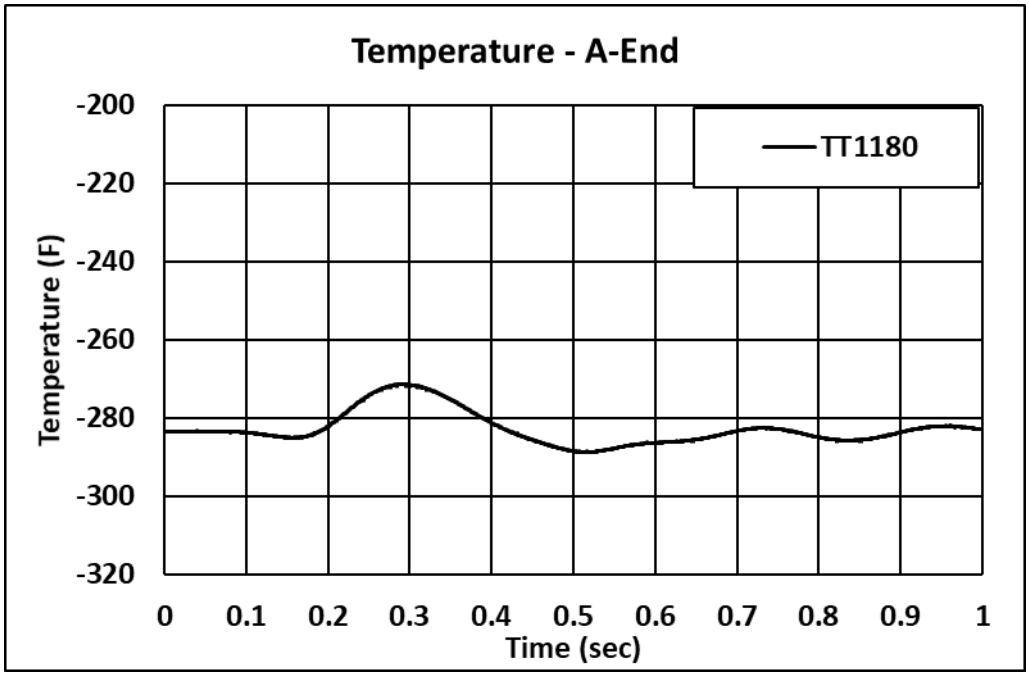


**Figure 37. Temperature Recorded in Liquid Nitrogen, A-End of Car Bottom of Tank**

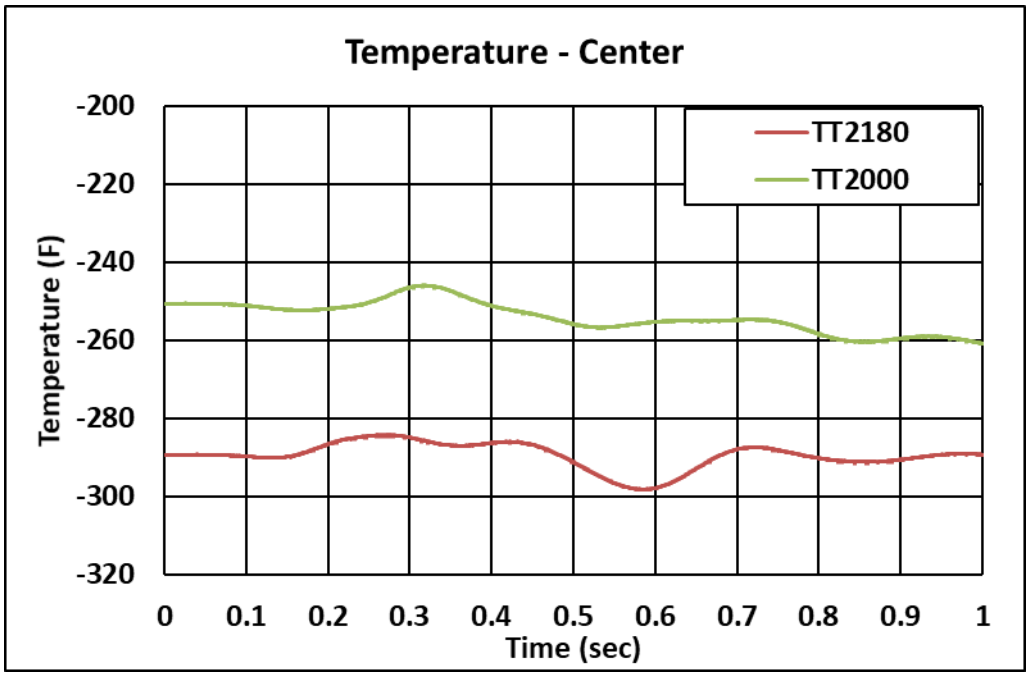


**Figure 38. Temperature Recorded in Liquid Nitrogen and Vapor Space, Center of Car Bottom of Tank and Next to Manway Respectively**

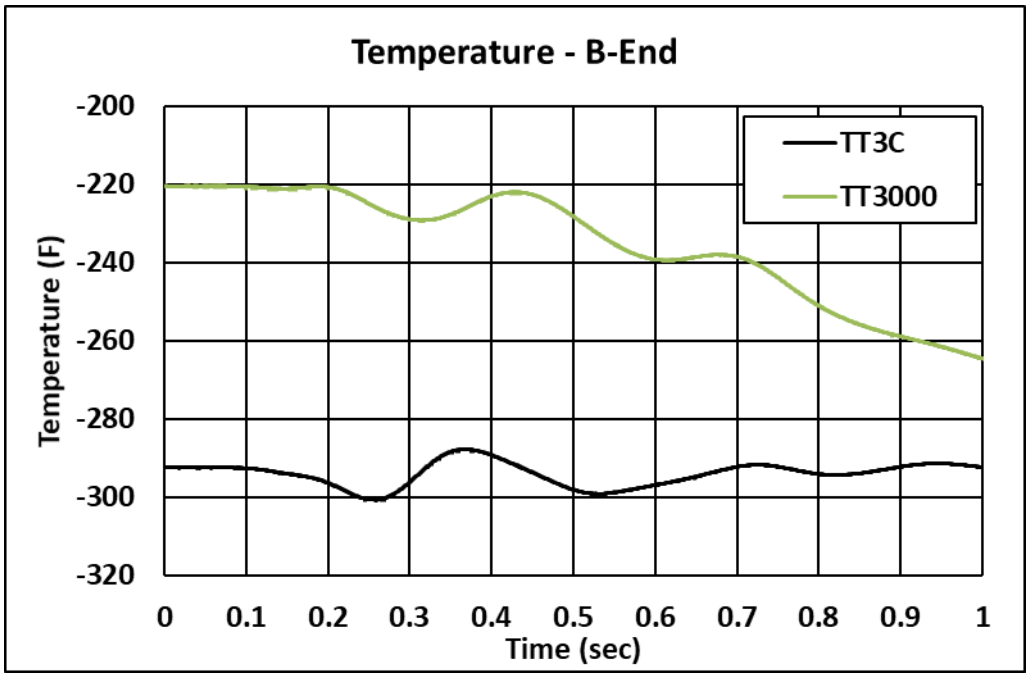


**Figure 39. Temperature Recorded in Liquid Nitrogen and Vapor Space, B-End of Car Mid Height and Top of Tank Respectively**

## 4.5 Summary of Actual Lading and Outage Conditions

Section 2.2.2 described the target values for pressure, temperature, and filling volume of LN2 and GN2. The actual lading and outage conditions at the time of the test differed somewhat from

the target lading and outage conditions. Some of the differences were known to exist prior to the test, while other variations were identified upon examination of the test measurements.

### Initial Pressure

Data were measured from 1 second prior to impact until 30 seconds after the impact. The pressure-time histories measured during the impact event were previously shown in Figure 31 through Figure 33. Appendix G shows additional plots of the pressure measurements recorded 1 second prior to impact and at the end of the 30 second window.

Table 13 shows the pressures measured by each transducer at the time of impact and at 30 seconds after impact. Each transducer was recording a near constant value at each time period, indicating the pressure within the tank was stable before and 30 seconds after impact. The difference between the initial and final pressures are also shown in this table. Overall, the change in pressure from beginning of impact to 30 seconds after is consistent for each transducer. The average pressure measured at the time of impact was 30.2 psig and the average pressure that the outage settled to after the impact was 25.1 psig. Regardless of its initial pressure, each pressure transducer measured a consistent pressure reduction of between 5.0 and 5.2 psi.

**Table 13. Summary of Pressure Changes Measured Before and After Impact**

| Channel | Units | Value at Impact | Value at +30 Seconds | Final - Initial |
|---|---|---|---|---|
| P-MH1 | psig | 30.5 | 25.3 | -5.2 |
| P-MH2 | psig | 31.1 | 26.0 | -5.1 |
| P-V5 | psig | 29.6 | 24.7 | -5.0 |
| P-V14 | psig | 29.8 | 24.6 | -5.2 |
| P-V15 | psig | 32.9 | 27.7 | -5.2 |
| P-PRV | psig | 27.2 | 22.2 | -5.1 |
| **Average** | **psig** | **30.2** | **25.1** | **-5.1** |

Additionally, a mechanical pressure gauge measured a pressure of 30 psig just prior to the release of the ram car (see Figure 40). This value is in agreement with the average pre-test pressures measured by the pressure transducers.


**Figure 40. Mechanical Pressure Gauge Prior to Test**

The researchers have a high level of confidence that the initial pressure was approximately 30 psig based on the consistent readings from the electronic and mechanical gauges. The researchers are also confident that by 30 seconds after the test the average pressure within the tank had stabilized at a lower pressure than prior to the test, in spite of the loss of tank volume resulting from permanent deformation.

### Initial Temperature

Researchers encountered several challenges while interpreting the temperature data from the 12 temperature sensors. Six thermocouples were installed at various positions inside the inner tank to determine the average bulk temperature of the LN2. However, the thermocouple installed at the top of the tank on the A-end did not function in the test. The locations of these thermocouples are shown on Figure 14 and Figure 15. Additionally, two combination pressure/temperature sensors were installed in flexible piping installed in the manway of the inner tank and four combination pressure/temperature sensors were installed within the piping external to the tank as shown in Figure 16 and Figure 17. The temperature measurements made via thermocouples and combination temperature/pressure sensors were not in agreement with each other. Appendix G provides additional discussion on the challenges researchers encountered with interpreting temperature data, and the temperature measurements made using the combination pressure/temperature sensors were not suitable for estimating the initial temperature

of the lading. The remainder of the temperature discussion in this section is focused on the thermocouple measurements.

Test data were recorded for 30 seconds following the impact. This duration captured the impact event itself (approximately 0.5 seconds) and 29.5 seconds of the LN2 and GN2's response after impact. The post-impact behavior inside the tank was of particular interest to the researchers seeking to understand the behaviors of LN2 and GN2 under impact conditions. The thermocouple measurements during and after the test are plotted in Figure 41. The saturation temperature of LN2 (87.6 K/ -302 °F) at the initial pressure (30 psig)[11] [21]. At 30 psig, LN2 can only exist at a temperature at or below the saturation temperature. All of the recorded temperatures measured via thermocouple remained above this level throughout the test, in spite of several thermocouples being installed below the liquid level of the inner tank. The two thermocouples initially above the liquid line (i.e., TT3000 and TT2000) exhibited sudden drops in temperature followed by a gradual increase. The researchers believe this behavior is associated with cold LN2 sloshing during the impact and contacting these thermocouples, decreasing the measured temperatures. Following the impact, the LN2 settled below these two thermocouples, which began to warm up once again. The three thermocouples initially submerged within the liquid (i.e., TT1180, TT 2180, and TT3C) measured a change in temperature during the impact, but quickly returned to near their pre-impact temperatures.

[11] Because the pressure inside the tank changed during the test, the instantaneous saturation temperature would also vary based on the instantaneous pressure. For simplicity, only the saturation temperature at the initial pressure of 30 psig is shown.

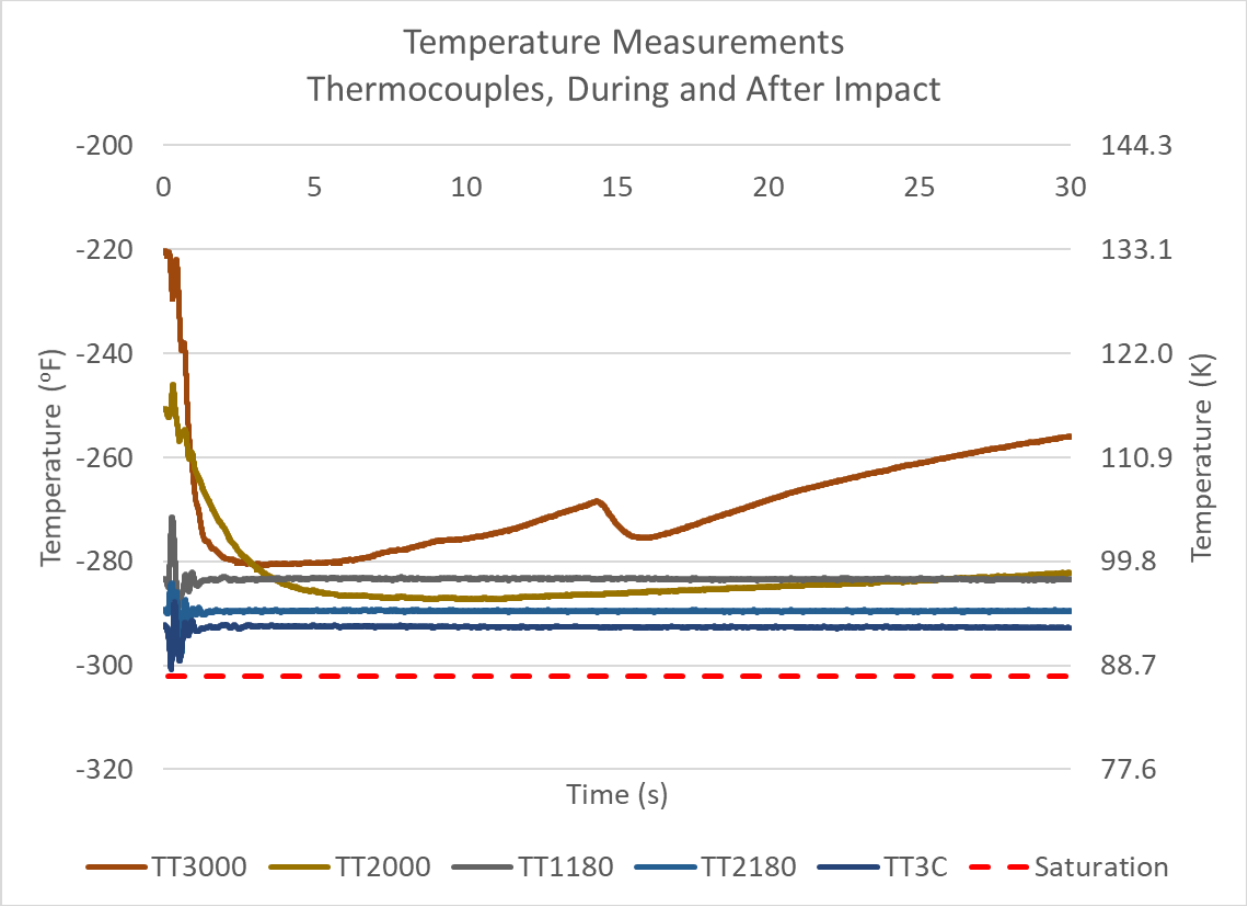


**Figure 41. Temperature Measurements from Thermocouples Measured in the 30 Seconds After Impact**

The temperatures measured by each thermocouple at the time of impact and 30 seconds after impact are shown in Table 14. This table also shows the difference between the initial and final temperatures measured by each thermocouple. Channels TT3000 and TT2000 experienced the largest decrease in temperature during the test, and the value measured at 30 seconds had not yet stabilized (see Figure 41). The remaining three thermocouples showed a near-constant temperature by 30 seconds after the impact that was within 1 °F of the temperature measured at the time of impact.

**Table 14. Summary of Temperature Changes Measured by Thermocouples Before and After Impact**

| Channel | Units | Value at Impact | Value at +30 Seconds | Final - Initial |
|---|---|---|---|---|
| TT3000 | °F | -220.4 | -256.0 | -35.6 |
| TT2000 | °F | -250.7 | -282.2 | -31.5 |
| TT1180 | °F | -283.4 | -283.5 | -0.2 |
| TT2180 | °F | -289.3 | -289.5 | -0.2 |
| TT3C | °F | -292.4 | -292.9 | -0.5 |

The researchers determined that the temperatures recorded by the thermocouples could not be relied upon to describe the temperature of the LN2 since prior to and after impact the thermocouples reported temperatures at which LN2 could not exist, yet LN2 was known to exist within the tank. One possible explanation for this apparent discrepancy was that heat was being transferred from the warm inner tank to which most of the thermocouples were attached. Another possibility considered was that the surfaces of the thermocouples were not in contact with liquid, but rather with a thin film of vapor that had formed between the tank and the LN2. While the thermocouples do not appear to have malfunctioned, the temperatures measured prior to and during the test do not directly describe the conditions in the LN2.

After careful consideration, the researchers determined that the post-test saturation temperature was the best estimate of the bulk average LN2 temperature. The researchers assumed that the LN2 was close to a saturated state after the impact because it was violently sloshed during the impact and the temperature of the LN2 did not change during the impact (see Table 14) due to the large heat capacity of the large volume of liquid. Therefore, the researchers used the post-test measured pressure of approximately 26 psig (38.3 psia) from the manhole pressure transducers (see Table 13) to calculate the saturation temperature of LN2 as -305 °F (86 K)[12] [21]. This temperature is physically reasonable to describe the pre-test state since at the known initial pressure of 30 psig LN2 must be kept at or below -302 °F (87.6 K).

**Volume of Lading**

A liquid level valve (trycock) was installed approximately 92 inches above the bottom of the inner tank, corresponding to a 95 percent full liquid level. The mechanical pressure gauge on the tank reported a pressure corresponding to 71 inches of water at a time when the trycock was submerged in liquid (see Figure 42). The density of LN2 must be used to convert from inches of water to inches of LN2. The density of LN2 depends on its pressure and temperature. By assuming that the LN2 was at an average temperature of 86 K and at the known pressure of 30 psig (42.3 psia) prior to the impact, the researchers estimated that the density of the LN2 was approximately 0.765 g/ml [21]. Thus, a column height of 71 inches of water corresponded to 93 inches of LN2 at 86 K, placing the liquid level approximately 1-inch above the trycock position. This height of LN2 was reasonable, as any heat transferred through the inner tank to the LN2 after filling would have resulted in thermal expansion (i.e., an increase in LN2 volume). When the trycock valve was opened after filling, liquid sputtered out confirming that the trycock was indeed submerged.

[12] Using the average post-test pressure of 25.1 psig gives a similar LN2 saturation temperature of -304.4 °F (86.3 K).


**Figure 42. Static Head Pressure Gauge, Day Before Test**

After filling the tank but prior to the test, GN2 was vented to auto-refrigerate the lading and mitigate the risk of flash boiling LN2 (refer to Appendix I). After venting, the static head pressure gauge measured approximately 66.5 inches of water (see Figure 5), which corresponds to approximately 86 inches of LN2 at 86 K and an outage volume of approximately 9 percent (see Appendix G). Thus, the liquid level was approximately 5–6 inches below the trycock at the time of the test. When the trycock valve was opened immediately prior to the impact test, liquid was not vented from the tank, confirming that the liquid level was below the trycock height.

### Summary of Actual Lading and Outage Conditions

The estimated actual lading and outage conditions from Test 12 are summarized in Table 15.

**Table 15. Summary of Actual Initial Lading and Outage Conditions in Test**

| Parameter | Actual Value from Test |
|---|---|
| Commodity in Tank | LN2 |
| Commodity Temperature | ~ -305 °F (~86 K) |
| Outage Volume | ~9% |
| Outage Pressure | 30 psig |

## 4.6 Steel Tensile Testing

In most of the prior side impact tests, the tensile properties of the steels composing the tanks were not measured prior to the tests due to the risk of structurally compromising the tank [15]. Tensile coupons were cut after the test, and the pre-test FE model was updated with the actual material properties when creating the post-test FE model. Tests 11, 12, and the planned 13 are unique side impact tests in the overall program where a tank car or tank car surrogate is constructed for the purpose of the side impact test.

### *4.6.1 AAR TC-128, Grade B Carbon Steel*

For the TC-128 outer tank, the pre- and post-test FE models for Test 12 used the results from the pre-test material characterizations performed on the Test 11 DOT-113 surrogate tank car because the TC128 properties from Test 11 were determined to be typical. Before assembly of the Test 11 surrogate tank car, the manufacturer of the outer tank excised a representative section of the 9/16-inch TC-128 outer shell in the post-weld heat treated (PWHT) condition and machined ASTM E8 smooth round bar (SRB) coupons with a 2-inch gage length (GL) and 0.5-inch diameter. The pre-Test 11 SRB coupons were tested at quasi-static strain rate and room temperature, and the measured tensile properties were used to define the material behavior in the pre- and post-test FE models for Test 11 [4].

Following Test 12, samples of TC-128 carbon steel were excised from the outer tank and subjected to tensile testing. The results of those tests are provided in Appendix B5.1. The results of these tests confirmed that the mechanical properties of the Test 12 TC-128 were similar to the properties of the Test 11 TC-128 so the post-test FE model was not updated using the new material test data. The average YS, UTS, and elongation at break in a 2-inch gage length (EB-2in) measured in various coupons taken from the Test 11 car and average corresponding properties for samples taken from shell plates in the Test 12 outer tank are shown in Table 16.

**Table 16. Comparison of Test 11 and Test 12 TC-128 Mechanical Properties**

| Steel | YS | UTS | EB-2in |
|---|---|---|---|
| - | ksi | ksi | % |
| Test 11 TC-128 (pre-test, average) | 64.9 | 88.8 | 31.4 |
| Test 11 TC-128 (post-test, average) | 64.5 | 86.5 | 37.1 |
| Test 12 TC-128 (post-test, average) | 60.2 | 86.2 | 37.5 |

### *4.6.2 ASTM A240, Type 304 Stainless Steel*

For the T304 inner tank, the pre- and post-test FE models for Test 12 used the results from the post-test material characterization performed on the Test 11 DOT-113 surrogate tank car because the T304 properties from Test 11 were determined to be typical. After Test 11, the inner tank had ASTM E8 subsize rectangular or dogbone (DB) coupons cut from an undamaged portion. The T304 coupons had a 1-inch GL, 0.25-inch width, and 0.067-inch thickness, and they were subjected to tensile testing at various combinations of strain rates and temperatures. The T304 coupons were tested from room temperature down to -320 °F (77 K) and from quasi-static

(0.0005 in/in/s) to 15 in/in/s strain rates. While it was preferred to test full thickness (1/4-inch) T304 specimens with a 2-inch gage length, the cryogenic test lab had difficulties with gripping the desired specimens with T304 stainless steel's high strength at cryogenic temperature.

Following Test 12, the manufacturer of the DOT-113 surrogate provided the test team with the material test reports from the steel vendor that supplied the plates used to construct the tank's shell. These test reports included reported values for YS, UTS, and elongation. These results confirmed that the strength properties of the Test 12 T304 were similar to the properties of the Test 11 T304 at room temperature and a quasi-static strain rate. The average elongation reported on the Test 12 MTRs was lower than the typical elongations reported for the Test 11 T304. The average YS, UTS, and EB measured in various coupons taken from the Test 11 car and average corresponding properties from the several MTRs for T304 shell plates in the Test 12 inner tank are shown in Table 17.

**Table 17. Comparison of Test 11 and Test 12 T304 Mechanical Properties**

| Steel | Temp. | Strain Rate | YS | UTS | EB |
|---|---|---|---|---|---|
| | *Kelvin* | *$s^{-1}$* | *ksi* | *ksi* | *%* |
| Test 11 T304 Stainless Steel (pre-test, average) | 295 | QS | 56.7 | 96.3 | 64.1 (2-in) |
| Test 11 T304 Stainless Steel (post-test, full-size, average) | 295 | QS | - | 96.5 | 62.6 (2-in) |
| Test 11 T304 Stainless Steel (post-test, sub-size, average) | 295 | 5e-04 | 47.3 | 95.0 | 63.8 (1-in) |
| Test 12 T304 Stainless Steel (MTR, average) | 295 | QS | 45.9 | 96.8 | 52.7 (2-in) |

### *4.6.3 Summary*

The results of the tensile characterization revealed that the TC-128 outer tank and T304 inner tank met their respective requirements in AAR Specifications for Tank Cars Appendix M-1002 [16] and ASTM A240 [6] respectively for YS, UTS, and elongation at break with a 2-inch GL (EB-2in). Table 18 summarizes the average mechanical properties from eight TC-128 samples and three T304 samples, which were used in the calibration of material definitions in the Test 12 DOT-113 FE model. The T304 stainless steel material properties shown in this table were obtained from samples tested at a temperature of 77 K, which is the saturation temperature of LN2 at 1 atmosphere. The T304 had a higher strength and greater ductility at QS rates than at any of the tested elevated strain rates (i.e., 0.05 to 15 $s^{-1}$). The T304 stainless steel material properties were similar for all the tested elevated strain rates so the authors chose the strain rate at 0.05 $s^{-1}$ to calibrate the behavior of the Test 12 FE model as a conservative estimate of puncture onset.

**Table 18. Summary of Average YS, UTS, and EB from Tensile Tests in Test 11 [4]**

| Steel | Temp. | Strain Rate | YS | UTS | EB |
|---|---|---|---|---|---|
| | *Kelvin* | *$s^{-1}$* | *ksi* | *ksi* | *%* |
| T304 Stainless Steel | 77 | 0.05 | 77.0 | 179.3 | 29.4 in 1-inch |
| TC-128 Carbon Steel | 294 | QS | 64.9 | 88.8 | 31.4 in 2-inch |

# 5. FE Model Development

Researchers at Volpe developed FE models of the DOT-113 surrogate tank car prior to the test to help determine the targeted impact speed. The purpose of these pre-test FE models was to provide estimates of the speed range where puncture could be expected to occur while considering uncertainties in the exact puncture speed, lading conditions, etc. Volpe developed the FE models that incorporated and expanded upon several modeling techniques that had been used during simulations of previous tank car impact tests [7, 8, 9, 10, 11, 12, 13, 14, 15]. The DOT-113 models required definition of the tank car geometry, geometry of the impact setup (e.g., impact wall, impactor, etc.), definition of boundary conditions, constraints, initial conditions, and development of several material models. Additionally, modeling features such as element types, mesh sizes, and fluid/structure interactions were selected.

The models were developed using the Abaqus/CAE preprocessor and executed in Abaqus/Explicit [24]. Abaqus/Explicit is a commercially-available, general purpose nonlinear FE solver capable of simulating dynamic impacts involving complex material behaviors such as plasticity and puncture. The solid mechanics simulation features used in the DOT-113 models included defining material models to describe the elastic-plastic behavior and fracture behavior of the inner and outer steel tanks. To model damage initiation for fracture, the Bao-Wierzbicki (B-W) triaxiality-based damage initiation model was used [25].

The Abaqus software also includes several modeling techniques to represent the gas and liquid phases of the lading, permitting these two parts to be modeled explicitly. The LN2 and GN2 of the tank were modeled using Lagrangian Equation-of-State (EOS) and pneumatic cavity approaches respectively. Between Tests 11 and 12, simulation studies were conducted to examine several different modeling techniques to account for the change from water and air (Test 11) to LN2 and GN2 (Test 12) in the tanks. The results of this simulation study were published in a standalone report [5].

## 5.1 Overview of Models

A DOT-113 tank car filled with LN2 presents several unique FE modeling challenges compared to modeling single-walled tank cars filled with water:

1. The modeling techniques needed to be able to simulate puncture of two tanks because a DOT-113 tank car features outer and inner tanks.
2. The inner tank was at a cryogenic temperature and its steel needed to be modeled with material definitions capturing the temperature and strain rate dependence of its plasticity and fracture behavior.
3. The GN2 in the outage could not be modeled directly as an ideal gas because, during the impact, the model needed to capture the effect of intermolecular forces affecting GN2's compressibility and a phase change from gas to liquid (condensation).

The pre-test FE model for this test used material property definitions for the inner and outer tank steels developed based on tensile characterizations of specimens excised from the previous DOT-113 surrogate tank car [4]. The development of the FE model material inputs for the TC-128 outer tank material responses is described in detail in the Test 11 report [4]. The

development of the FE model material inputs for the T304 inner tank material is described in detail in Appendix F3.

Puncture-capable FE models feature more complex material definitions and meshes than non-puncture models. Puncture-capable models include inner and outer tanks with refined meshes in the impactor contact areas, and material modeling behaviors to simulate element degradation and removal. For the DOT-113 surrogate, the refined area was meshed using solid elements on both the inner tank and the outer tank. While the desired outcome of the DOT-113 test was to puncture of both tanks, the solid patch of elements on the outer tank needed to be large enough to not only capture the initial tearing of the tank (i.e., typically occurs beneath a corner of the impactor), but also to allow the tear to propagate until such a time as the inner tank punctured. This required a much larger solid patch of elements on the outer tank than for single-walled tanks. It was important to include a sufficiently large patch of solid elements in the outer tank to allow the tear to propagate fully without being artificially arrested by reaching the limits of the solid patch, as that could result in the modeled DOT-113 placing less demand on the inner tank than would be experienced during an impact test.

The previously-tested DOT-113 surrogate filled with water used MLI in the annular space over an 8-foot length centered on the impact without a vacuum because it was intended to investigate a possible structural contribution and not insulate the inner tank. Based on the results of the previous two DOT-113 tests, it was determined that perlite insulation does contribute to the structural response of a shell impact test, but MLI does not. While MLI was determined to not contribute to the structural response of a DOT-113, it was included in the current DOT-113 surrogate with LN2 test to insulate the inner tank, and a vacuum was pulled on the annular space. The FE model included a pressure load to represent the vacuum on the annular space but did not include a representation of the MLI.

The point of impact on the tested DOT-113 tank car surrogate was planned to be slightly offset (approximately 32 inches) from the centerline of the car. Both the pre- and post-test models included the full-length of the tank car without a symmetry condition. The tank car's geometry was simplified, and small structures expected to have an insignificant effect on the puncture speed were omitted. These simplifications have a relatively minor effect on the impact response of the tank under the test conditions. The FE model is shown in Figure 43.

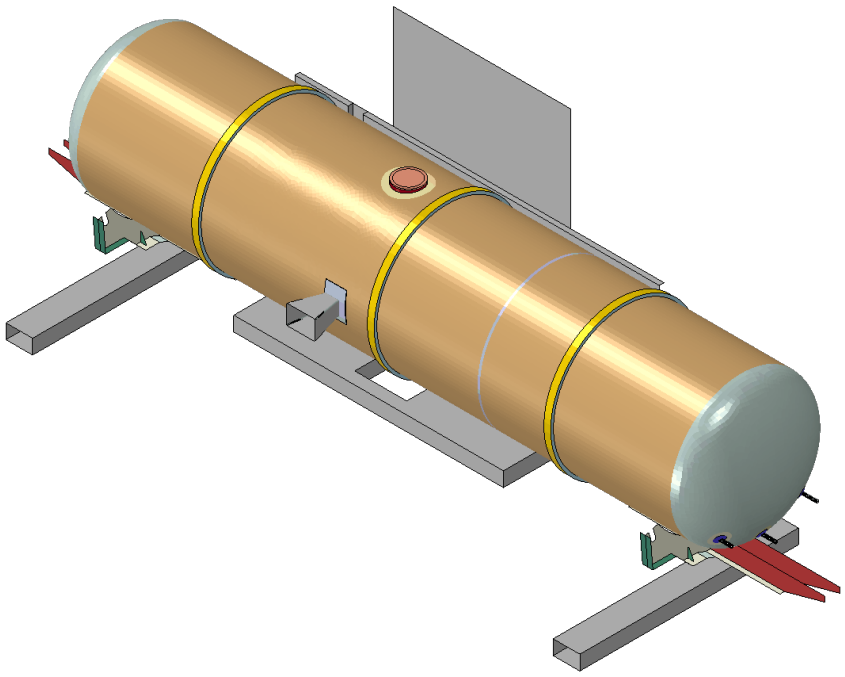

**Figure 43. DOT-113 Surrogate with LN2 FE Model**

The lading in the DOT-113 surrogate FE model was represented using a Lagrangian EOS for the LN2. The use of a Lagrangian EOS is different than the hydraulic cavity approach that was used for the FE models of the two previous DOT-113 shell impact tests because the current test used a lower outage to mirror changes made in PHMSA's Final Rule on LNG (85 FR 44994). Volpe's previous modeling experience with different tank car specifications informed the modeling team that the hydraulic cavity approach was less computationally intensive and gave accurate results with outages greater than approximately 10 percent, but a Lagrangian EOS approach was better able to represent the sloshing behavior of tank cars with outages less than approximately 10 percent. A Lagrangian EOS approach was previously used to model the water in a test of a DOT-117 tank car [12] and a DOT-111 tank car meeting voluntary industry standard CPC-1232 [14].

The outage in recent shell impact FE models (Tests 6–12) has been represented with a pneumatic cavity. The pneumatic cavity approach is a simplified modeling technique that represents a gas using uniform pressure over its entire volume. This uniform pressure will change over the course of the impact simulation by solving the ideal gas equation as the volume enclosing the pneumatic cavity is reduced through tank deformation. The cavity approach is commonly referred to as the uniform pressure method (UPM) in FE models of air bags in automotive crash simulations. The pneumatic cavity approach can be applied using either an adiabatic or an isothermal assumption.

The parts included in the model can generally be divided into three categories: rigid bodies, deformable bodies made of steel, and deformable bodies made of other materials (i.e., membrane and lading). A section view, with the cutting plane passing through the center of the impactor, is shown in Figure 44. This image includes annotations denoting the various parts making up the assembly of the DOT-113 tank car FE model.

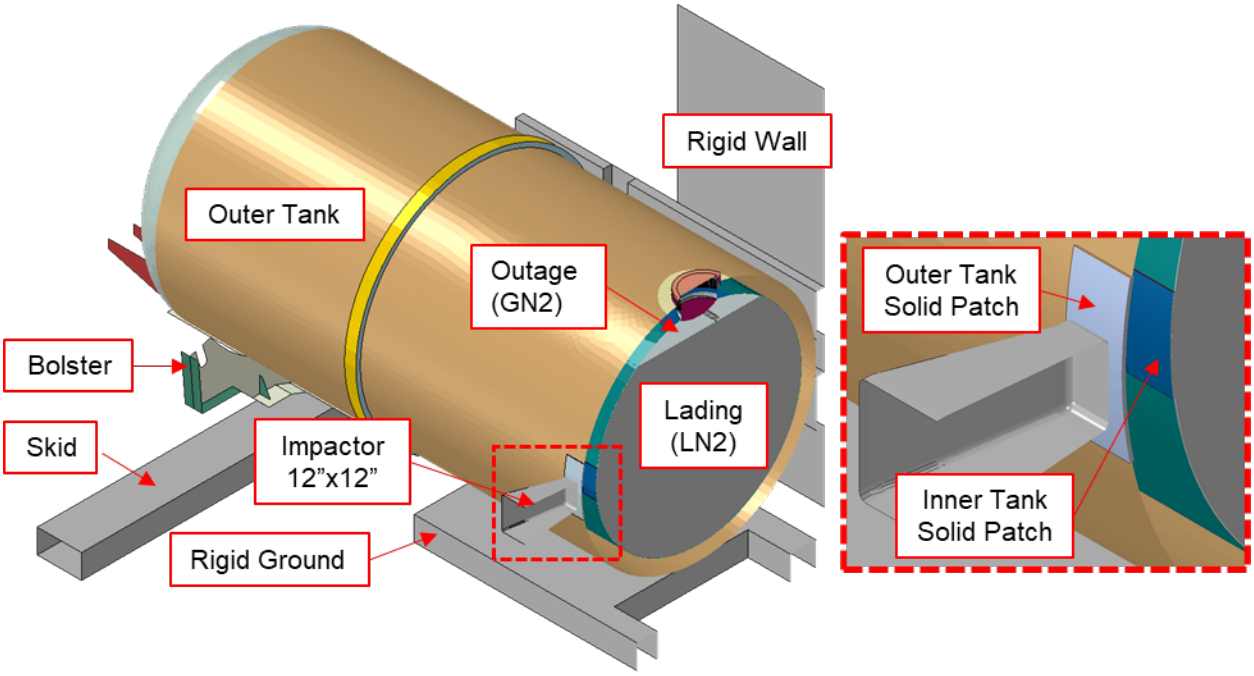


**Figure 44. Section View Through Impact Plane with Annotated Parts**

Table 19 summarizes the parts making up the FE model used in the pre-test puncture simulations. This table contains the weight of the part in the FE model and the number of elements in that part's mesh. Due to adjustments made between the pre-test models and the post-test models, the meshes and part weights were slightly different between the pre-test and post-test models. A full description of each part in the pre-test and post-test models can be found in Appendix D.

**Table 19. Summary of Parts in Post-Test FE Models (9% Outage)**

| Part Name | Type of Body | Material | Number of Elements | Part Weight |
|---|---|---|---|---|
| - | - | | # | *lbf* |
| Impactor | Rigid | - | 78,913 | 297,200 |
| Wall | Rigid | - | 3,130 | - |
| Skid | Rigid | - | 370 | 3,500 |
| Ground | Rigid | - | 1,673 | - |
| Outer Tank (Shell) | Deformable | TC-128 | 50,403 | 40,000 |
| Outer Tank (Solid) | Deformable | TC-128 | 384,160 | 71 |
| Inner Tank (Shell) | Deformable | T304 | 28,991 | 12,500 |
| Inner Tank (Solid) | Deformable | T304 | 392,000 | 14 |
| Bolster and Stub Sill | Deformable | TC-128 | 4,956 | 3,000 |

| Part Name | Type of Body | Material | Number of Elements | Part Weight |
|---|---|---|---|---|
| - | - | | # | *lbf* |
| Piping | Deformable | T304 | 30,164 | 211 |
| Lading | Deformable | LN2 | 134,448 | 104,000 |
| Internal Membrane | Deformable | Other | 21,104 | 372 |

In this table, the total weight of the parts in the FE model corresponding to the entire DOT-113 surrogate (e.g., inner and outer tanks, LN2, etc.) was approximately 170,000 lbf. As previously discussed in Section 2.2.2, LN2 was used in the test to:

1. Account for the fluid mass
2. Consider the dynamic effects of a fluid-filled tank at a cryogenic temperature
3. Chill the stainless steel inner tank and alter its material properties

As this surrogate tank car was designed to be representative of a DOT-113 carrying cryogenic material (LNG) having a lower density than that of LN2, the surrogate tank car was intentionally overloaded (by weight) for the test to maintain a filling volume that was similar to what would be expected in actual service.

## 5.2 Material Behaviors in FE Models

Several material definitions were used in both the pre-test and post-test FE models: ASTM A240 Type 304 stainless steel, AAR TC-128, Grade B carbon steel, a membrane material, GN2, and LN2. The material properties input to the FE models are summarized in this section. Complete descriptions of the development of the stainless steel and carbon steel material models are given in Appendix F.

### *5.2.1 ASTM A240 Type 304 Stainless Steel*

After Test 11, a section of that tank car's T304 inner tank was cut into flat ASTM E8 subsize tensile coupons, as discussed in Section 4.5. Tensile tests were performed on three DB coupons having typical dimensions of 1-inch GL, 0.25-inch gage width, and 0.1-inch thickness. Tensile tests were conducted at a range of strain rates and temperatures, down to LN2's temperature (77 K). A more complete description of the material tests performed on the Test 11 tank car's steel can be found in Test 11 [4].

An FE model of the T304 coupons was created in Abaqus/Explicit using similar modeling techniques, i.e., mesh size, step time, mass scaling, etc., to the tank car puncture model to calibrate a material input to the puncture model. A more detailed description of the calibration procedure of the T304 material input is contained in Appendix F3. Figure 45 shows that the calibrated T304 material input was able to match the repeated tensile tests at 77 K and 0.05 in/in/s.

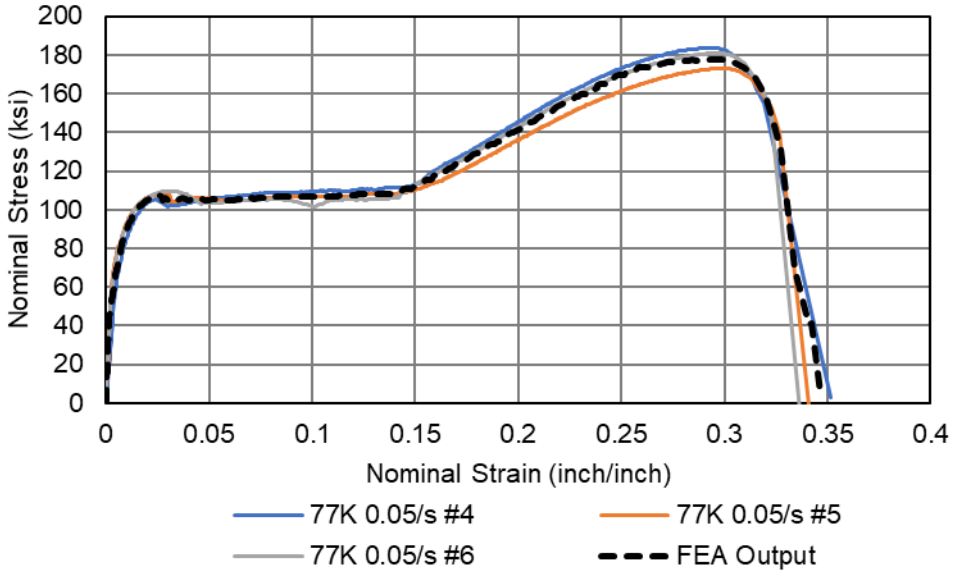


**Figure 45. Nominal Stress-Strain Response from the T304 Stainless Steel Coupon FE Model (dashed black) with Tensile Test Data (solid color) for Comparison at 77 K and 0.05/s**

Table 20 summarizes the material properties used for the T304 stainless steel inner tank in the FE models of the DOT-113 surrogate tank car. Damage progression was only specified for the solid patch.

**Table 20. Summary of Material Properties for T304 Stainless Steel**

| Parameter | Value |
|---|---|
| Mass Density | 7.35 x $10^{-4}$ lbf-$s^2$/$in^4$ |
| Modulus of Elasticity | 3 x $10^7$ psi |
| Poisson's Ratio | 0.25 |
| Plasticity | Isotropic Hardening (see Appendix F3) |
| Damage Initiation | Ductile Damage (see Appendix F3) |
| Damage Progression | Displacement = 0.005 in/$in^2$, exponent = -2 |
| Mesh Implementation | 0.05-inch Reduced Integration Brick (C3D8R) Elements |

### *5.2.2 AAR TC-128 Carbon Steel*

The same material input from Test 11 [4] was used in the Test 12 pre- and post-test models. As discussed in Section 4.5, a spare section of the TC-128 outer tank from Test 11 was cut into smooth round bar ASTM E8 tensile coupons during manufacturing. Tensile tests were performed on eight coupons having typical dimensions of 2-inch GL and 0.5-inch diameter. An FE model

of the TC-128 coupon geometry was used to calibrate a material model to match the average YS, UTS, and EB-2in as depicted in Figure 46.

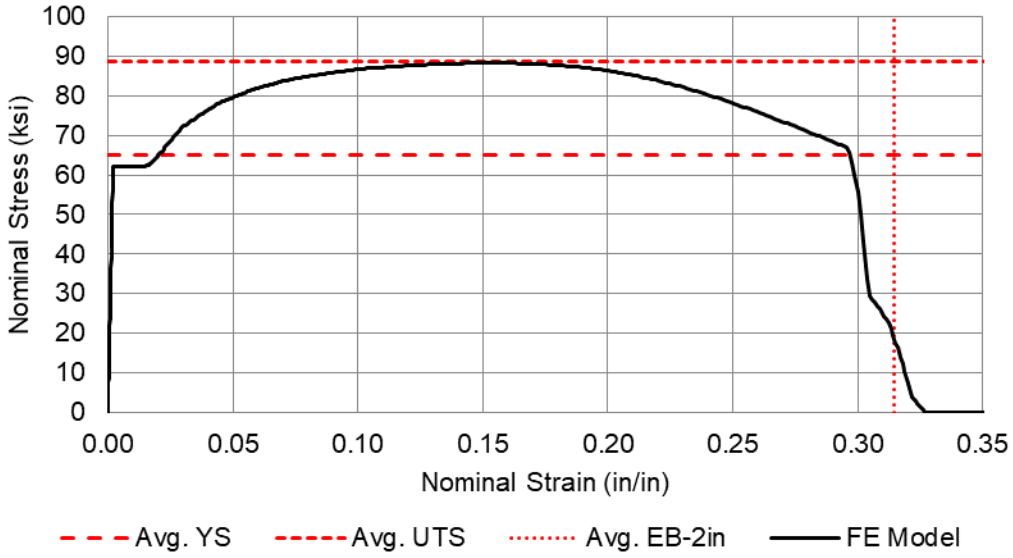


**Figure 46. Nominal Stress-Strain Response from the TC-128 Carbon Steel Coupon FE Model (solid black) with Average Tensile Properties (dashed red)**

The material properties of TC-128 steel used in the outer tank of the FE models is summarized in Table 21. Damage progression was only specified for the solid patch.

**Table 21. Summary of Material Properties for TC-128 Carbon Steel**

| Parameter | Value |
|---|---|
| Mass Density | $7.35 \times 10^{-4}$ lbf-s$^2$/in$^4$ |
| Modulus of Elasticity | $3 \times 10^7$ psi |
| Poisson's Ratio | 0.3 |
| Plasticity | Isotropic Hardening<br>(see Test 11 report [4]) |
| Damage Initiation | Ductile Damage<br>(see Test 11 report [4]) |
| Damage Progression | Displacement = 0.005 in/in$^2$, exponent = -1 |
| Mesh Implementation | 0.081-inch Reduced Integration Brick (C3D8R) Elements |

The DOT-113 surrogate FE model for this test (Test 12) used the same TC-128 material properties as the last DOT-113 surrogate FE model (Test 11) because material characterization was not conducted on the Test 12 outer tank before the impact test. The authors determined that the mechanical properties of TC-128 from Test 11 were typical, and it was expected that the TC-128 fracture toughness would be close between the two DOT-113 surrogates.

### 5.2.3 Membrane

As described in Appendix D11, an artificial surface was modeled within the tank to define the limits of the hydraulic and pneumatic cavities. Because this surface does not correspond to any physical structure within the tank, modeling techniques were chosen to minimize the increase in either artificial mass or stiffness introduced to the model by the membrane while not negatively impacting the FE model's stability or runtime. The material properties of the membrane are summarized in Table 22.

**Table 22. Material Properties Defined for Membrane Material**

| Parameter | Value |
|---|---|
| Density | $7.35 \times 10^{-6}$ lbf·s$^2$/in$^4$ |
| Modulus of Elasticity | $1 \times 10^4$ psi |

### 5.2.4 Gaseous Nitrogen (GN2)

The gas phase of the lading was modeled as GN2 within Abaqus using different approaches in the pre- and post-test models. The initial pressure in the pre-test model was parameterized to 0, 25, and 50 psig because it was uncertain how well the test team could control the initial test pressure after filling the tank with LN2. The post-test model used an initial pressure of 30 psig which was averaged from the DOT-113 surrogate tank car's outage pressure transducers immediately prior to impact.

The GN2 modeling approaches are listed below:

**Pre-test**

1. Adiabatic
2. Isothermal (constant temperature)
3. Isobaric (constant pressure)

**Post-test**

1. Isothermal
2. Isobaric
3. Isothermal with Phase Change (fluid exchange)
4. Pressure Load Time History

The pneumatic cavity approach models the entire cavity with a single uniform pressure and uniform temperature value. If the pneumatic cavity was *isothermal*, then the temperature was held constant at 92 K. An isothermal condition means that heat generated due to pneumatic compression was able to quickly exit the outage, resulting in no change to the GN2's temperature. If the pneumatic cavity was *adiabatic*, then the temperature was allowed to increase during compression, i.e., no heat was able to exit the outage. The *isobaric* approach represented a situation where the outage was initially at its saturation point and any decrease in volume resulted in condensation, so the pressure was held constant throughout the simulation. The

isothermal with phase change approach represented a situation where the outage was initially below its saturation pressure but reached its saturation pressure after building pressure during the impact. The pressure load time history approach did not explicitly solve for the outage pressure during the simulation. Rather, the test measurements were used as an input.

The membrane enclosing the outage was included in every FE model to maintain consistency regardless of whether it was necessary or not based on the outage modeling approach. The isobaric approach used a constant pressure load applied to the interior surface of the membrane enclosing the outage. The adiabatic, isothermal, and isothermal with phase change approaches used an ideal gas pneumatic cavity. The initial pressure and temperature are discussed further in Appendix E9. The modeling inputs defined for the GN2 phase of the model are summarized in Table 23, using the unit system used in the FE models.

**Table 23. Properties for GN2 (pneumatic cavity)**

| Property | Pre-test Value | Post-test Value | Reference |
|---|---|---|---|
| Universal Gas Constant ($R$) | 73.583 in-lbf/(mol·K) | 73.583 in-lbf/(mol·K) | [26] |
| Molecular Weight ($MW$) | 1.60 x $10^{-4}$ lbf·s$^2$/(in·mol) | 1.60 x $10^{-4}$ lbf·s$^2$/(in·mol) | [21] |
| Initial Temperature | 92 K | 92 K | |
| Initial Pressure | 0, 25, 50 psig | 30 psig | |
| Molar Specific Heat at Constant Pressure ($c_{p,m}$) | 257.59 in-lbf/(mol-K) | 257.59 in-lbf/(mol-K) | [21] |

The molar specific heat capacity at constant pressure ($c_{p,m}$) for GN2 was calculated according to Equation 1.

**Equation 1. Calculation of Molar Specific Heat**

$$c_{P.m} = c_P \cdot MW$$

Values for the specific heat capacity of GN2 at constant pressure ($c_p$) were obtained from published values [21].

### 5.2.5 Liquid Nitrogen (LN2)

The pre-test target initial conditions for the side impact test of the surrogate DOT-113 tank car were set to an outage volume of 5 percent and internal pressure of 50 psig. Within Abaqus, a Lagrangian Mie-Grüneisen EOS with the linear Us − Up Hugoniot form was used to describe the behavior of the LN2. The key material properties that must be input to this material model are the material's density, speed of sound, and viscosity. The necessary material properties were obtained from the NIST Chemistry WebBook, SRD 69 [21]. Initial conditions are discussed further in Appendix E9.

The fluid's bulk modulus ($K$) can be determined from the speed of sound ($c$) and density ($\rho$) according to the Newton-Laplace equation given in Equation 2 [27]. Abaqus calculates the bulk modulus internally using this equation to determine the compressibility of the fluid.

**Equation 2. Calculation of Bulk Modulus**

$$K = c^2\rho$$

The material properties of LN2 were determined at 77 K (-320 °F) and 62.3 psia (50 psig) in the pre-test models based on the planned test conditions at the time of the modeling. After the test, the post-test properties of LN2 models were determined at 86 K (-305 °F) and 42.3 psia (30 psig) based on the measured pressures and temperatures before and after the impact test. Table 24 summarizes the material properties of LN2 used in the pre- and post-test models. This table includes the specific units used in the unit system of the FE model.

**Table 24. Properties of LN2 Used in FE Models**

| Property | Pre-test Value | Post-test Value | Reference |
|---|---|---|---|
| Mass Density ($\rho$) | 7.57 x $10^{-5}$ lbf·s$^2$/in$^4$ | 7.16 x $10^{-5}$ lbf·s$^2$/in$^4$ | [21] |
| Speed of Sound ($c$) | 3.38 x $10^4$ in/s | 3.00 x $10^4$ in/s | [21] |
| Bulk Modulus ($K$) | 8.65 x $10^4$ psi | 6.44 x $10^4$ psi | Equation 2 |
| Viscosity ($\mu$) | 2.37659 x $10^{-8}$ psi·s | 1.6987 x $10^{-8}$ psi·s | [21] |

An initial hydrostatic compression stress corresponding to the outage pressure was applied to the LN2 in the pre-test (0–50 psig) and post-test (30 psig) models to maintain equilibrium with the pressure from GN2. The material property definition of LN2 was not updated in the pre-test parametric study based on the initial outage pressure because the LN2 was relatively incompressible when compared with GN2. The slight pressure dependence of LN2's density, bulk modulus, and viscosity were not expected to have a significant effect on the puncture outcomes over the range of pressures included in the parametric study.

## 5.3 Modeling Techniques Adjusted Between Pre-test and Post-test Models

A few modeling parameters were adjusted from the pre-test to post-test models. The adjustments were made based on the actual test conditions and based on considerations of model runtime. These modeling techniques and their adjustments are summarized in Table 25.

**Table 25. Summary of Adjustments Made Between Pre- and Post-test Models**

| Modeling Feature | Condition in Pre-test Model | Condition in Post-test Model | Explanation |
|---|---|---|---|
| Impact Speed | Varied | 18.3 mph | Adjusted to match test speed |
| Impactor Offset | 1 in | 2.2 in | Adjusted to match delayed rise in impactor acceleration test data due to tape switch support |
| Lading Temperature | 77 K (-320 °F) | 86 K (-305 °F) | Adjusted to match saturation temperature at measured post-impact pressure |
| Fluid Pressure | 0, 25, 50 psig | 30 psig | Initial pre-test outage pressure was uncertain before filling and was updated to reflect average measured pressure |
| Outage Volume | 5% | 9% | Adjusted to match outage volume calculated from LN2 static head pressure at 86 K |
| GN2 Modeling Techniques | Isothermal, isobaric, or adiabatic | Isothermal, isobaric, or simulated phase change | Adjusted to investigate whether the pressure increase during the test was limited by vapor-to-liquid condensation |

### *5.3.1 Impact Speed*

Pre-test FE models were used to simulate impacts over a range of speeds from 16 to 20 mph. The purpose of the pre-test models was to aid in test planning by estimating the outcomes (e.g., impact forces, puncture of one or both tanks, etc.) over a range of speeds so that a target impact speed could be chosen. Post-test FE models were run using 18.3 mph, the measured impact speed from the test. The post-test FE models were run at the same speed as the test to facilitate the comparison of test and model results as part of a model validation program.

### *5.3.2 Impactor Offset and Time Zero*

It was observed that the initial rise in impact force occurred approximately 4 milliseconds later in the test results than the FE results. This delay was attributed to the thickness of the wooden supports for the tape switches on the impactor and outer tank. The tape switches determine time zero in the test and are visible in Figure 8 on the end of the impactor. The pre-test simulations started with the impactor 1-inch away from making contact with the outer tank. The post-test simulations adjusted the impactor initial position to 2.2 inches away from the outer tank to account for the early triggering of the tape switches in the test.

### *5.3.3 Lading Temperature*

The pre-test models used a lading temperature of 77 K (-320 °F), which is the saturation temperature of LN2 at atmospheric pressure. The actual temperature of the LN2 in the tank was unknown at the time the pre-test models were developed and executed. It was determined that the

LN2 inside the tank would not be colder than the saturation temperature at atmospheric pressure (77 K) because the LN2 which would be used to fill the tank car would be transported at a slightly elevated temperature. A cold-biased estimate of lading temperature was used because it resulted in an overall slightly stiffer response from the filled tank car since the bulk modulus of LN2 is higher at colder temperatures. The authors preferred to err on the side of overestimating the tank car's stiffness so that the puncture model was slightly conservative.

The lading temperature in the post-test models was set at 86 K (-305 °F). The redundant temperature readings from inside the tank car were in disagreement with each other, and the measurements taken from the lading were above the saturation temperature at the measured fluid pressure (refer to Section 4.4). This indicated that the temperature measurements were higher than the true average temperature of the LN2 inside the tank. Because the authors did not consider the thermocouples to be a reliable measurement of the average liquid temperature, the average liquid temperature was estimated to be approximately 86 K as discussed in Section 2.2.2.

### 5.3.4 Fluid Pressure

The fluid pressure assigned to GN2 and LN2 in the pre-test model was parametrically set at 0, 25, and 50 psig because the test team was uncertain of what level of control they would have on the pressure inside the DOT-113 surrogate once it was filled with LN2. The post-test model used 30 psig, the average measured pressure just prior to impact.

### 5.3.5 Outage Volume

The target outage volume for the test was 5 percent as explained in Section 2.2.2 and Appendix G, and the pre-test FE models used an outage volume of 5 percent corresponding to a liquid level height approximately 10 inches from the top of the inner tank. After the test, the authors determined that the actual outage was approximately 9 percent (refer to Section 4.5), and the post-test FE model was updated to an outage volume of 9 percent. This volume corresponded to a liquid level height approximately 15 inches from the top of the inner tank.

# 6. Comparison of Test Responses to Finite Element Analyses

This section compares the result from the pre- and post-test FE models with the test measurements. While the post-test model was run at the measured test speed of 18.3 mph, measured initial pressure of 30 psig, and calculated outage volume of 9 percent, the pre-test models were not run with these parameters as they were unknown prior to the test. The force-displacement results and pressure-time history results from the analyses using the pre-test model are presented for comparison with the test measurements in Section 6.1. The post-test model was updated from the pre-test version as discussed in Section 5.3, and the results from the post-test model are compared with test measurements in Section 6.2.

## 6.1 Pre-test FE Model Comparison

One of the intended uses of the pre-test models was to assist in test planning by estimating the range of impact speeds over which puncture of both the inner and outer tanks would be likely to occur. Due to uncertainties in the behavior of cryogenic GN2 in the outage, the pre-test models were run using three different approaches to bound the potential pressure-volume responses. Section 5.2.4 discusses the three approaches: adiabatic, isothermal, and isobaric.

Table 26 summarizes the puncture outcomes of the pre-test parametric FEA study on the behavior of GN2. In addition to varying the approaches used to represent GN2, the pre-test parametric study varied the initial pressure of the GN2. All these simulations were run at an impact speed of 17.3 mph. The speed of 17.3 mph was chosen because it was in a speed range that may or may not result in puncture and because it was the same speed from the previous test (Test 11). Using the same impact speed in the Test 12 pre-test models allowed the modeling team to easily compare model results with the previous test's results. The residual impactor speed, i.e., the speed of the impactor at the time of puncturing the inner tank, is given for the cases that resulted in puncture to give an indication of how close the model was to resisting puncture.

**Table 26. Summary of Pre-test FE Model Parametric GN2 Study at 17.3 mph**

| **Pressure** *psig* | **Adiabatic** | **Isothermal** | **Isobaric** |
|---|---|---|---|
| 0 | Puncture<br>3.0 mph | Puncture<br>2.7 mph | Puncture<br>5.9 mph |
| 15 | Puncture<br>2.5 mph | Puncture<br>1.9 mph | Puncture<br>3.7 mph |
| 25 | Puncture<br>2.5 mph | Puncture<br>1.8 mph | Puncture<br>2.3 mph |
| 35 | Puncture<br>2.6 mph | Puncture<br>1.0 mph | Non-Puncture<br>N/A |
| 50 | Puncture<br>2.1 mph | Puncture<br>0.1 mph | Non-Puncture<br>N/A |

A large solid patch was used on the outer tank to allow the tear to propagate without artificially arresting its growth (see Appendix D8). The inner tank had a smaller solid patch because a non-puncture versus puncture outcome could be determined once the inner tank just started to tear under a corner of the impactor (see Appendix D6).

Two of the cases run at 17.3 mph resulted in a non-puncture outcome. These cases were each run using an isobaric assumption for the GN2. These two cases featured an initial pressure of 35 and 50 psig, respectively.

The target speed for the test was chosen to be 17.7 ± 0.5 mph (actual impact speed 18.3 mph) on the basis of these pre-test FE results because a puncture outcome was desired for this test. The highest pre-test estimate of the speed necessary to cause puncture was 19.5 mph, corresponding to an isobaric assumption with an initial pressure of 50 psig. However, this speed was not targeted for the test because it could have resulted in a large amount of residual speed and excessive damage to the DOT-113 surrogate if the puncture resistance of the tank car were overestimated. With a target speed of 17.7 ± 0.5 mph, puncture was a possibility but not a certainty, and the researchers believed that it would not result in an overspeed puncture where an excessive amount of impact energy was applied to the DOT-113 surrogate. Because this was the first test of a tank car filled with cryogenic lading, there were additional uncertainties in the cryogenic fluid behavior, outage, temperature, pressure, and exact material behavior of stainless steel at cryogenic temperatures which warranted caution in the execution of the test.

Figure 47 compares the impact force versus impactor travel for the pre-test FE models using each of the three assumed gas behaviors at the closest pre-test initial pressure (25 psig) to the actual test result (30 psig). While the initial pressures were close, the pre-test model used an initial impactor speed of 17.3 mph versus the test at 18.3 mph. Also, the pre-test model used an outage of 5 percent while the test outage was calculated to be approximately 9 percent. While the FE model used a rigid impactor with a single acceleration-time history, the ram car in the test featured five longitudinal accelerometers. The test force reported is the average of three of the five longitudinal accelerometer channels because two channels experienced instrumentation failure. Both the test and FE forces reported in this section were filtered using a CFC-60 filter [23].

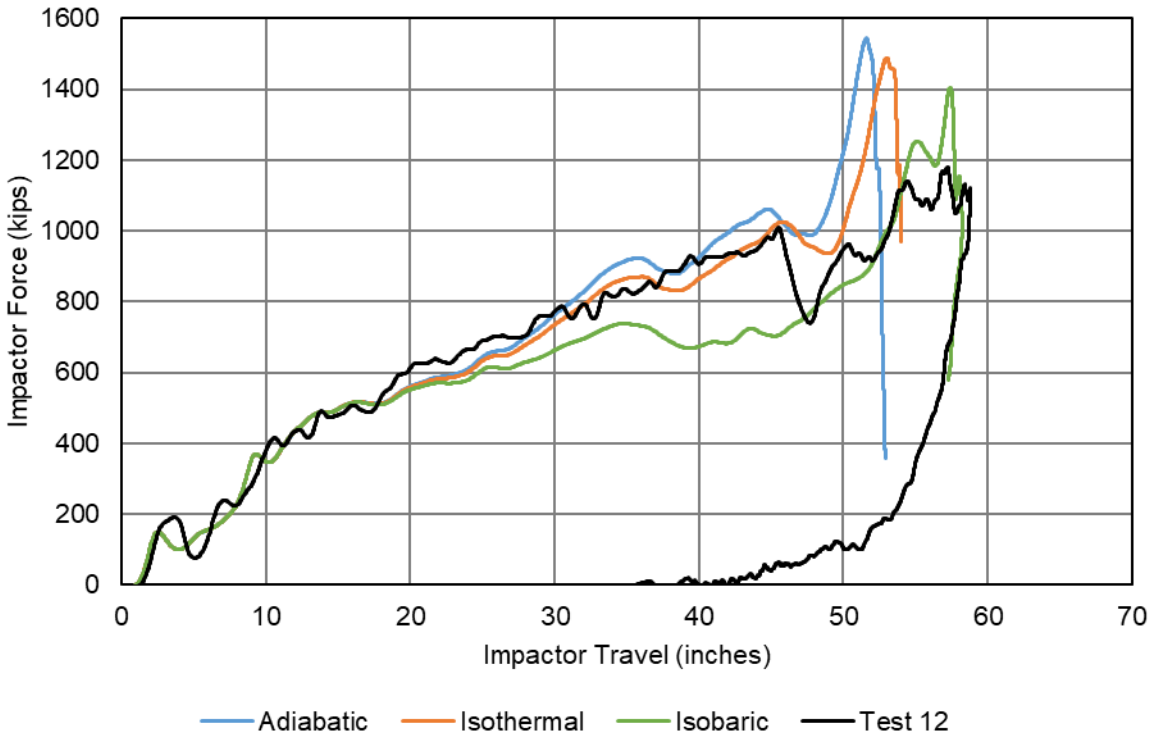


**Figure 47. Force-displacement Responses from Pre-test FEA at 17.3 mph, 25 psig, and 5% Outage Compared to Test Results at 18.3 mph, 30 psig, and 9% Outage**

While the pre-test models were intended to bound the test response, the pre-test models overestimated the peak force measured in the test. This overestimate is due to the pre-test models using a much lower outage than the test, i.e., 5 percent outage versus 9 percent outage.[13] The pre-test simulations were set to terminate after 0.35 seconds of impact time to save on computation time since a large parametric study was conducted with the pre-test model. Both the adiabatic and isothermal models terminated early once the outer and inner tanks were punctured because the models were only designed to be numerically stable to the point of puncture.

Figure 48 compares the GN2 pressure-time histories from the pre-test FE models shown in Figure 47 with the average outage test pressure. The test measurements were made using seven GN2 pressure transducers placed inside piping and flexible hosing leading to the inner tank's outage. It should be noted that the researchers believe that the average outage test pressure based on these remote measurements is an overestimate of the actual outage test pressure as discussed in Section 4.4. Similarly, to how the pre-test models overestimated the peak force in Figure 47, the peak outage pressure was also overestimated by the isothermal and adiabatic models, principally because the targeted outage of 5 percent was not achieved in the test.

[13] A lower outage means that the tank has a higher liquid level.

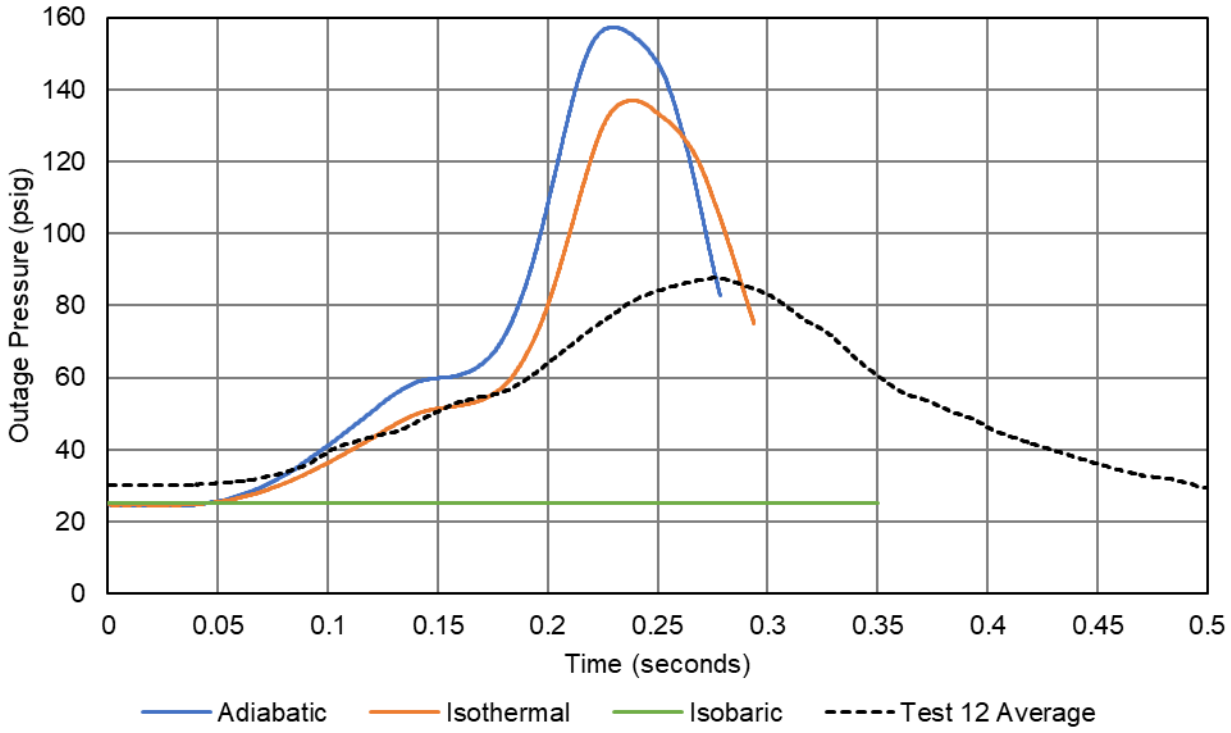


**Figure 48. GN2 Pressure-time Responses from Pre-test FEA at 17.3 mph, 25 psig, and 5% Outage Compared to Test Results at 18.3 mph, 30 psig, and 9% Outage**

Pre-test FE simulation results at 17.3 mph are contained within Appendix C1.

## 6.2 Post-test FE Model Comparison

The isothermal and isobaric pre-test FE models were updated as discussed in Section 5.3 to reflect the actual test conditions; however, the adiabatic model was not carried over to a post-test state because the authors reviewed the pressure and temperature measurements from the outage during the test and determined that the GN2 did not exhibit an adiabatic behavior. In this section, comparisons are made between the post-test FE model and the test measurements, and it was found that the post-test FE model was able to bound the test measurements. The post-test model only punctured in the isothermal case, which did not allow the GN2 in the outage to undergo a phase change. The isobaric model did not result in a puncture to either tank because the GN2's pressure rise was neglected. The lower outage pressures in the isobaric model allowed the outage volume to compress down further during the impact than the isothermal model, resulting in a softer global impact response and less localized plastic strain on the outer and inner tanks under the impactor. The isothermal and isobaric post-test model results are discussed in Section 6.2.1.

Based on the results of the post-test models run using the isothermal and isobaric assumptions, the modeling team used an iterative approach to combine these two behaviors in a third post-test model. The combined approach represents GN2 that could initially isothermally build up pressure to a pre-determined saturation pressure (70 psia). Once this saturation pressure was reached, the GN2 was able to exit the outage through a fluid exchange. This modeling approach is discussed in Section 6.2.2. Table 27 summarizes the post-test modeling outcomes, and for cases resulting in puncture, the impactor speed at the time of puncture is denoted.

**Table 27. Summary of Post-test FE Model Outcomes at 18.3 mph, 30 psig, and 9 Percent Outage**

| Isothermal | Isobaric | Saturation 70 psia |
|---|---|---|
| Puncture<br>0.5 mph | Non-puncture<br>N/A | Non-puncture<br>N/A |

### *6.2.1 Pre-test Modeling Techniques Updated with Test Conditions*

Figure 49 compares the impact force versus impactor travel responses from the post-test FE models with the average test measurements. The isothermal and isobaric post-test models used modeling techniques directly from the pre-test models. If reasonable test-model agreement had been reached with either of these models using the updated test conditions (e.g., impact speed, initial pressure, and estimated outage), then one might argue that the pre-test FE model was validated and that the GN2 behavior in the test was adequately represented by the chosen assumption. However, the authors do not consider the level of agreement exhibited by these post-test models to be sufficient for model validation. The lack of agreement with the test measurements is not surprising given that the goal of the isothermal and isobaric models was to bound the test behavior. In that respect, these modeling approaches were successful. The models were set to terminate after simulating 0.4 seconds of the impact; however, it should also be noted that the isothermal model terminated at 0.32 seconds after puncture of both tanks. While the isothermal model did result in puncture, the impactor was close to rebounding at the time of puncture (0.5 mph).

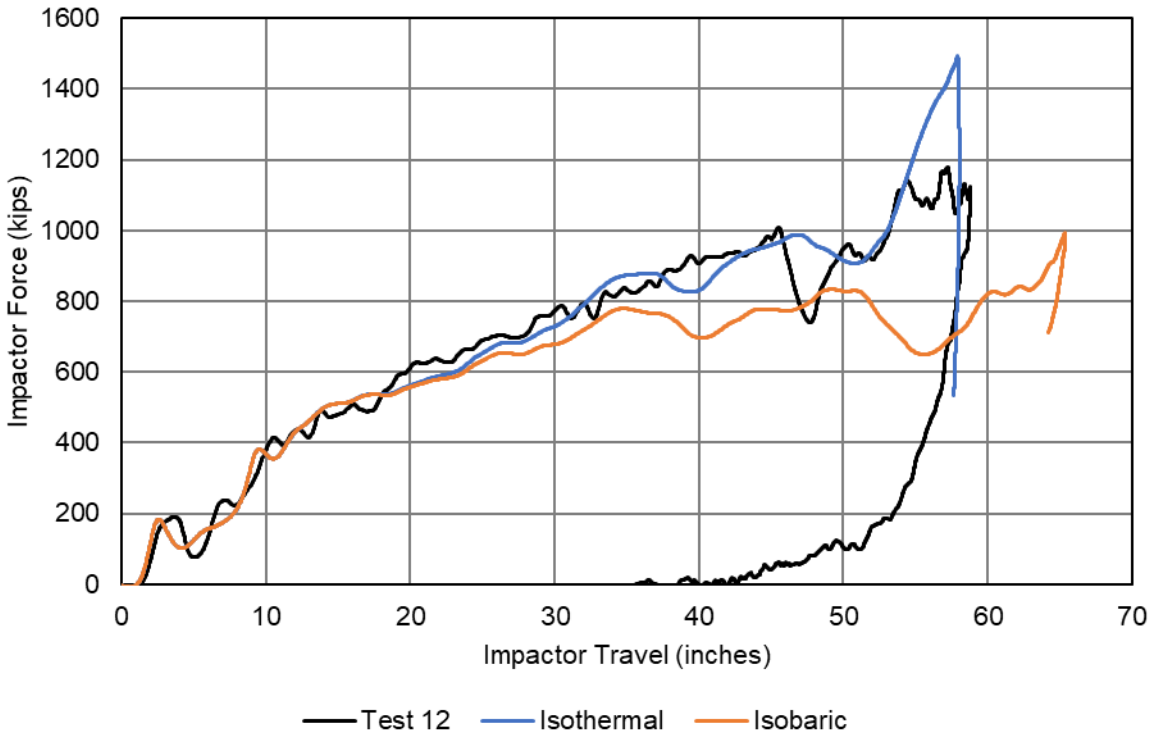


**Figure 49. Force-displacement Responses from the Isothermal and Isobaric Post-test Models Compared to Test Result**

The isothermal model was in excellent agreement with the test's force-displacement behavior up to approximately 54 inches of impactor travel. The authors attribute the overly stiff response of the isothermal model beyond this distance to the model's inability to allow the GN2 to undergo a phase change to LN2 after reaching the saturation pressure. Compared to the isothermal model, the isobaric model was in worse agreement with the test's force-displacement behavior and diverged from the test result after approximately 35 inches of travel. The authors attribute the overly soft response of the isobaric model to the intentional oversimplification in the model that the GN2 in the outage was uniformly at a saturation pressure of 42.3 psia for the duration of the impact.

Figure 50 compares the GN2 pressure time histories from the post-test FE models with the average of the test measurements. The test measurements were made using six GN2 pressure transducers (MH1, MH2, V5, V14, V15, and PRV) placed in piping or hosing leading to the outage. All six pressure transducers had different pressure-time histories, but the qualitative shapes of the pressure curves were generally in agreement across all sensors except for the sensor leading to the PRV (see Appendix H). The isothermal and isobaric post-test models used the same modeling approaches for the outage that were used in the pre-test models.

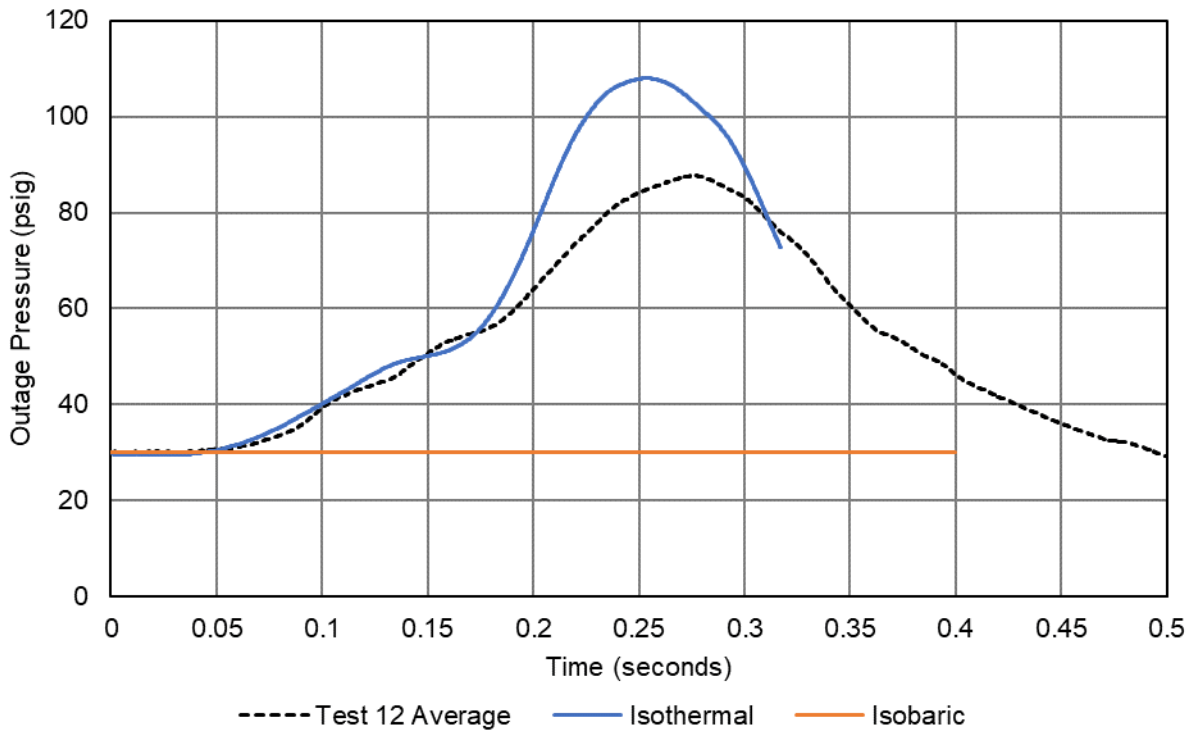


**Figure 50. GN2 Pressure Time History from the Isothermal and Isobaric Post-test FE Models Compared to Average GN2 Pressure from the Test**

It should be noted that the authors believe that the average test pressure measurement was higher than the true average pressure inside the outage during the test due to the sensors being remotely located in piping rather than in direct communication with the bulk outage. Additionally, the combination pressure-temperature transducers measured temperatures near 100 °F which was far above the cryogenic temperatures inside the inner tank (see Appendix G2).

As a further investigation of the outage modeling techniques, the authors used the pressure-time history data measured by each sensor as a pressure load input to the model instead of using a pneumatic cavity. Using each sensor's measured data as a model input resulted in an overestimation of the tank car's global stiffness. The model results are presented in Appendix H.

### 6.2.2 Post-test FE Model Incorporating Saturation Pressure

The post-test model results presented in Figure 49 for the isothermal and isobaric approaches to modeling the outage effectively bounded the test results. The isothermal model was in excellent agreement with the early stages of the impact response but overestimated the forces at higher displacements. The isobaric response was softer than the test measurements at an early stage of the impact response and subsequently did not experience as large a spike in force at the end of the impact. These results support the authors' belief that the actual behavior of the outage during the test was a more complicated behavior than could be accurately modeled with either the isothermal or isobaric assumptions.

An iterative approach was taken to combine pre-test isothermal and isobaric modeling approaches so that the GN2 could initially build up pressure according to the isothermal response. The pressure would need to be limited once a threshold value was reached if the model results were to be in better agreement with the test measurements. One physical explanation for a pressure limit would be activation of a PRV during the test. However, reviewing the HS video and pressure measurements from piping upstream of the PRV showed that the pressure never built up high enough to reach the STDP.

Another physical justification for using a pressure limit in the outage model is phase change taking place in which the vapor condenses to a liquid. The isobaric assumption made in both the pre- and post-test FE models was based on the vapor's initial temperature and pressure corresponding to the saturation conditions. A reduction in outage volume with a saturated vapor would cause the vapor to condense into a liquid, rather than to build pressure. However, if the vapor was initially at a pressure below the saturation pressure, a reduction in outage volume would result in pressure building, until the saturation pressure was reached. Once the saturation pressure was reached, the model would be assumed to behave in an isobaric manner as vapor to liquid condensation commenced.

Because the pressure measurements from the test were not taken directly in the outage, the authors believe the dynamic pressure increases measured during the test are overestimates. The authors examined the test and model results and estimated that the isothermal pressure-time behavior started to diverge from the average test pressure at approximately 70 psia (57.7 psig). This value was used as an estimation of the actual saturation pressure.

To simulate condensation in the outage, the authors specified a fluid exchange from the GN2 pneumatic cavity starting at 70 psia (57.7 psig) with the volumetric flow rate versus pressure behavior shown in Figure 51. After triggering the fluid exchange at 70 psia, the fluid exchange follows a steep linear slope of 75,000 $in^3$/s-psia. This value was chosen on a trial-and-error basis as a means of assessing whether vapor condensing to liquid was a probable explanation for disagreement between the post-test FE model and the test measurements. The exchange was defined to expel the excess GN2 to atmosphere when in reality the mass would be transferred to LN2. However, defining a fluid exchange between a pneumatic cavity (GN2) and a Lagrangian

EOS (LN2) was not possible in Abaqus, and the authors determined that the small increase in volume of LN2 would have a negligible effect on the global response of the DOT-113 surrogate.

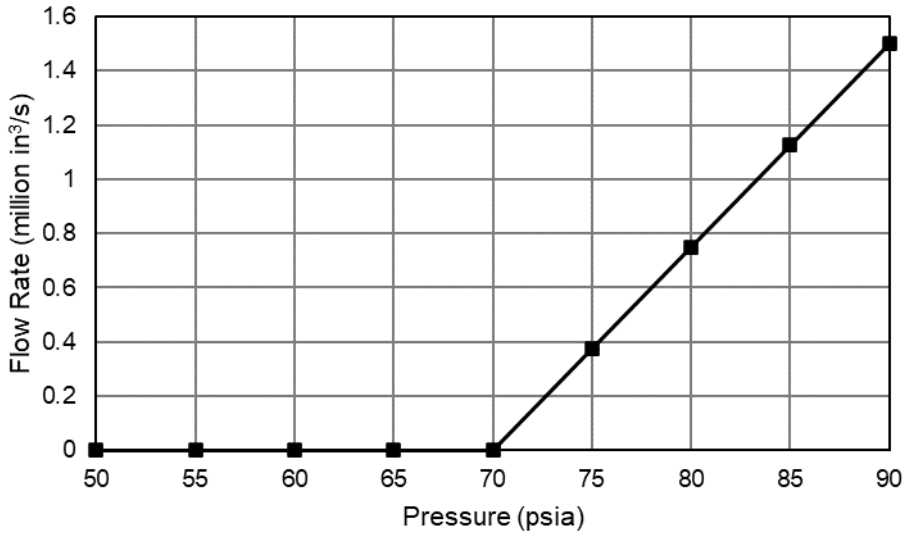


**Figure 51. Volumetric Flow Rate vs. Pressure Fluid Exchange Behavior for Phase Change at 70 psia**

This approach to modeling, where the saturation pressure is chosen based upon the pressure where the test and isothermal model results diverge, cannot be considered model validation as input conditions to the model are being chosen based on test measurements. While it would have been preferrable to specify the saturation pressure in the model based on accurate temperature or pressure measurements representing the average GN2 condition during the test, no such data exist for this test. The authors wanted to investigate whether simulating vapor condensation during the test would provide a more accurate comparison of the test measurements with the results of the post-test simulations.

Figure 52 compares the force-displacement response from the test with the post-test model, which initiates a phase change at 70 psia (57.7 psig). While the dynamic sloshing effects visible in the test response between 45 and 50 inches are not well captured by the model, the overall stiffness, peak force, and peak displacement were captured. The simulation was run for 0.4 seconds and did not result in puncture.

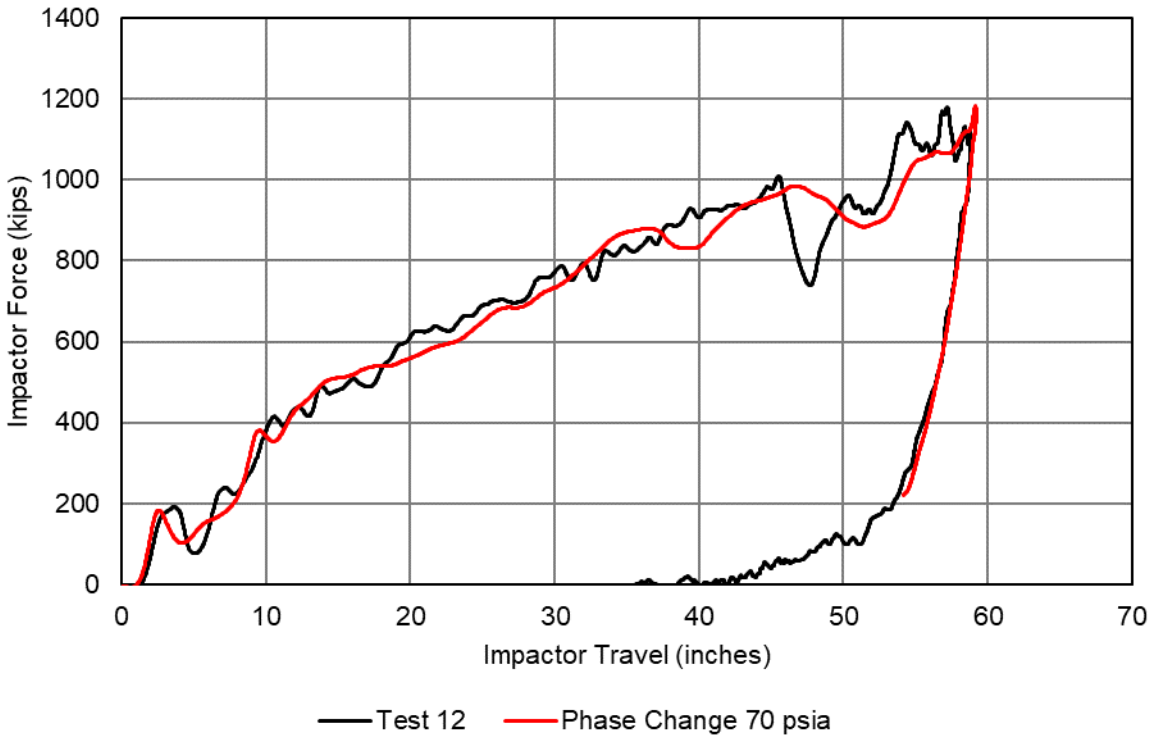


**Figure 52. Force-displacement Response from Post-test Model Saturated at 70 psia (57.7 psig) Compared to Test Result**

Figure 53 compares the GN2 pressure time history from the post-test FE model which initiates a phase change at 70 psia (57.7 psig) with the average of the test measurements. The peak pressure from the post-test FE model using this saturation pressure underestimates the average peak pressure from the test; as previously stated, the authors believe that the test measurements were an overestimate of the actual peak pressure in the outage. The post-test phase change model behaved identically to the post-test isothermal model up to approximately 0.19 seconds when the fluid exchange triggered after the outage reached 70 psia (57.7 psig). After GN2 was able to leave the outage, the rate of pressure climb was reduced compared to the isothermal model. The phase change model reached a peak pressure of 76.4 psig (i.e., 18.7 psi above the 57.7 psig starting pressure of the fluid exchange) while the isothermal model reached a peak pressure of 108 psig before puncturing (see Figure 50).

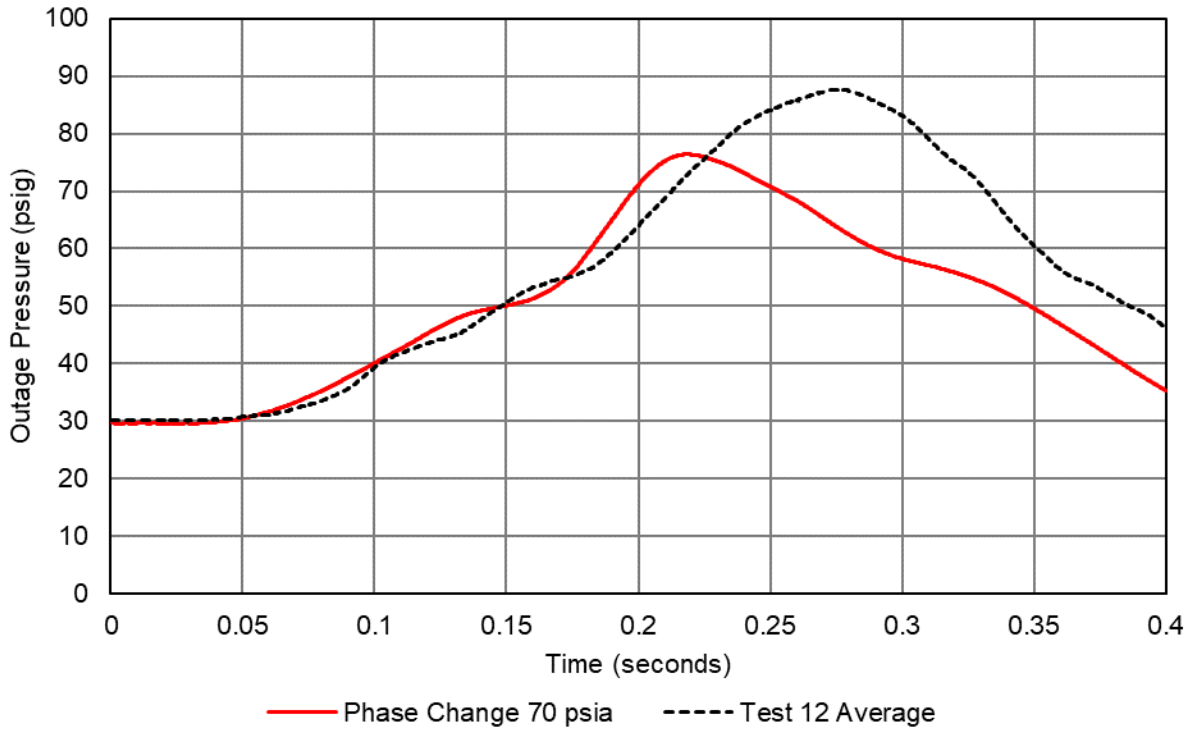


**Figure 53. GN2 Pressure Time History from the Post-test FE Model Saturated at 70 psia (57.7 psig) Compared to Average GN2 Pressure Transducers from the Test**

Figure 54 shows the state of the inner tank solid patch, i.e., the region on the inner tank under the impactor where the tank can tear, at the end of the post-test simulations. The *isothermal* model resulted in element deletion up to the edges of the puncture capable region, and the authors consider this to be a case of complete puncture of the inner tank. In some cases, if elements are not deleted through the thickness of the tank wall or if a tear does not run to the extents of the puncture-capable region, then it is unclear if the tank was fully punctured. Both the *isobaric* model and the post-test model using a saturation pressure of 70 psia (57.7 psig) did not result in any elements lost. The corresponding outer tank solid patches for each model (not shown) had similar outcomes to the respective inner tank solid patches.

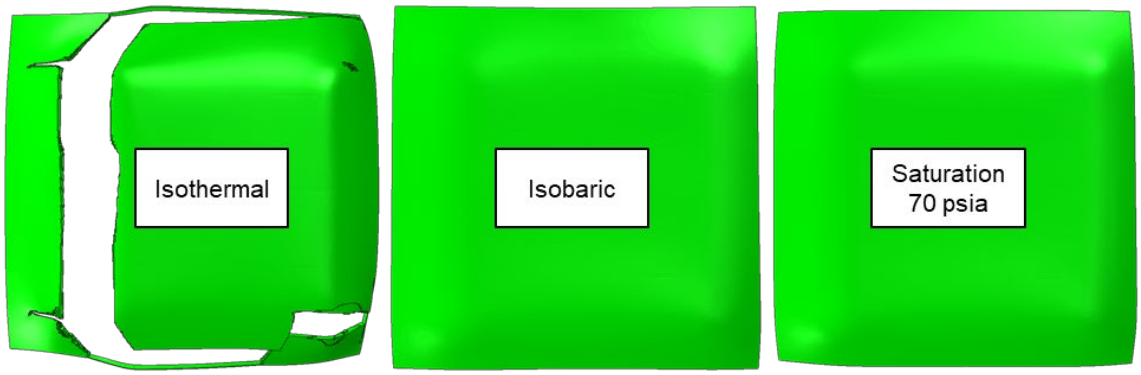


**Figure 54. Inner Tank Solid Patch State from Post-test FE Models After Termination**

A complete set of post-test FE simulation are presented in Appendix C2. Table 28 summarizes the peak results from the post-test FE models and compares them with the test results. Table 29 summarizes the percent difference between the test and each FEA model result.

**Table 28. Comparison of Peak Results from Post-test FEA and Test Measurements**

| Peak Measurement | Test | FEA | | |
|---|---|---|---|---|
| | | Isothermal | Isobaric | Saturation 70 psia |
| Longitudinal Acceleration (g) | 3.97 | 5.02 | 3.34 | 3.99 |
| Impactor Force (kip) | 1,180 | 1,492 | 992 | 1,184 |
| Impactor Travel (inch) | 58.8 | 58.0 | 65.4 | 59.2 |
| East Skid Displacement (inch) | -13.7 | -15.7 | -16.8 | -15.8 |
| West Skid Displacement (inch) | -15.7 | -14.4 | -15.8 | -14.5 |
| East Head Displacement (inch) | 14.7 | 15.4 | 17.1 | 15.6 |
| West Head Displacement (inch) | 17.6 | 17.2 | 18.7 | 17.3 |
| Avg. GN2 Pressure (psig) | 87.7 | 108.0 | 30.0 | 76.4 |

**Table 29. Comparison of Percent Differences Between Post-test FEA and Test Measurements**

| Peak Measurement | Isothermal | Isobaric | Saturation 70 psia |
|---|---|---|---|
| Impactor Force | 26.5% | -15.9% | 0.4% |
| Impactor Travel | -1.3% | 11.2% | 0.7% |
| East Skid Displacement | 14.6% | 22.5% | 14.8% |
| West Skid Displacement | -8.6% | 0.5% | -7.8% |
| East Head Displacement | 4.5% | 15.7% | 5.9% |
| West Head Displacement | -2.0% | 6.2% | -1.9% |
| Avg. GN2 Pressure | 23.1% | -65.8% | -12.9% |

# 7. Comparison of Results with Previous DOT-113 Tests

This test was the third test in a planned series of four tests to be conducted on DOT-113 tank cars and tank car surrogates. The objective of this test series is to examine the potential improvement in shell puncture resistance for a DOT-113 tank car with an outer shell made of 9/16-inch-thick TC-128 steel compared to a baseline DOT-113 tank car using 7/16-inch-thick A516-70 steel under LNG service conditions. Four tests are planned, with each test increasing in both complexity and realism compared to the previous test. Companion FE modeling is planned for each test, with the FE model expected to increase in complexity as results and observations from each test are studied and synthesized. Details of the planned testing sequence are summarized in Table 30.

**Table 30. Summary of DOT-113 Side Impact Test Conditions**

| **Test Number** | Test 10 | Test 11 | Test 12 (this report) | Test 13 |
|---|---|---|---|---|
| **Test Date** | November 2019 | July 2020 | July 2021 | Summer 2022 |
| **Test Article** | DOT-113C120W | DOT-113 surrogate | DOT-113 surrogate | DOT-113C120W9 |
| **Thickness (Outer Tank)** | 7/16 inch | 9/16 inch | 0.608 inch | 9/16 inch |
| **Material (Outer Tank)** | A516-70 | TC-128 | TC-128 | TC-128 |
| **Diameter (Outer Tank)** | ~119 inches | ~120 inches | ~120 inches | ~120 inches |
| **Length (Outer Tank)** | ~74 feet | ~45 feet | ~46 feet | ~76 feet |
| **Thickness (Inner Tank)** | 1/4 inch | 1/4 inch | 1/4 inch | 0.296 inch |
| **Material (Inner Tank)** | T304 stainless steel | T304 stainless steel | T304 stainless steel | T304 stainless steel |
| **Diameter (Inner Tank)** | ~106 inches | ~106 inches | ~106 inches | ~106 inches |
| **Volume (Inner Tank)** | 32,900 gal | 19,300 gal | 17,900 gal | 34,500 gal |
| **Tank Lading** | Water | Water | LN2 | LN2 |
| **Outage** | 17.6% | 17.6% | 9% (estimated) | 5% (target) |
| **Pressure** | 50 psig | 50 psig | 30 psig | 30 psig (target) |
| **Insulation** | Perlite | MLI | MLI | MLI |
| **Annular Pressure** | Vacuum | Atmospheric | Vacuum | Vacuum |
| **Impact Speed** | 16.7 mph (actual) | 17.3 mph (actual) | 18.3 mph (actual) | TBD, sufficient to puncture |

Figure 55 shows force-displacement responses from all of the DOT-113 tank cars and surrogates tested in the series to-date. Out of the three, the legacy DOT-113 tank car from Test 10 was the only tank car that punctured. The legacy DOT-113 tank car punctured at a lower force (800 kips) and impactor displacement than the Test 11 and Test 12 DOT-113 surrogate tank cars. The legacy DOT-113 tank car was unable to resist a 16.7 mph impact. However, the Test 11 DOT-113 surrogate tank car resisted an impact of 17.3 mph and the Test 12 DOT-113 surrogate tank car resisted and impact of 18.3 mph. This difference may be partially attributed to the different insulation schemes used in each tank car. The legacy DOT-113 tank car featured an annular space between tanks that was filled with granular perlite, while both DOT-113 surrogate tank cars featured an annular space with MLI[14]. Other key differences between the tests were the outer tank's steel type and thickness, outage volume, and outage pressure as described in Table 30.

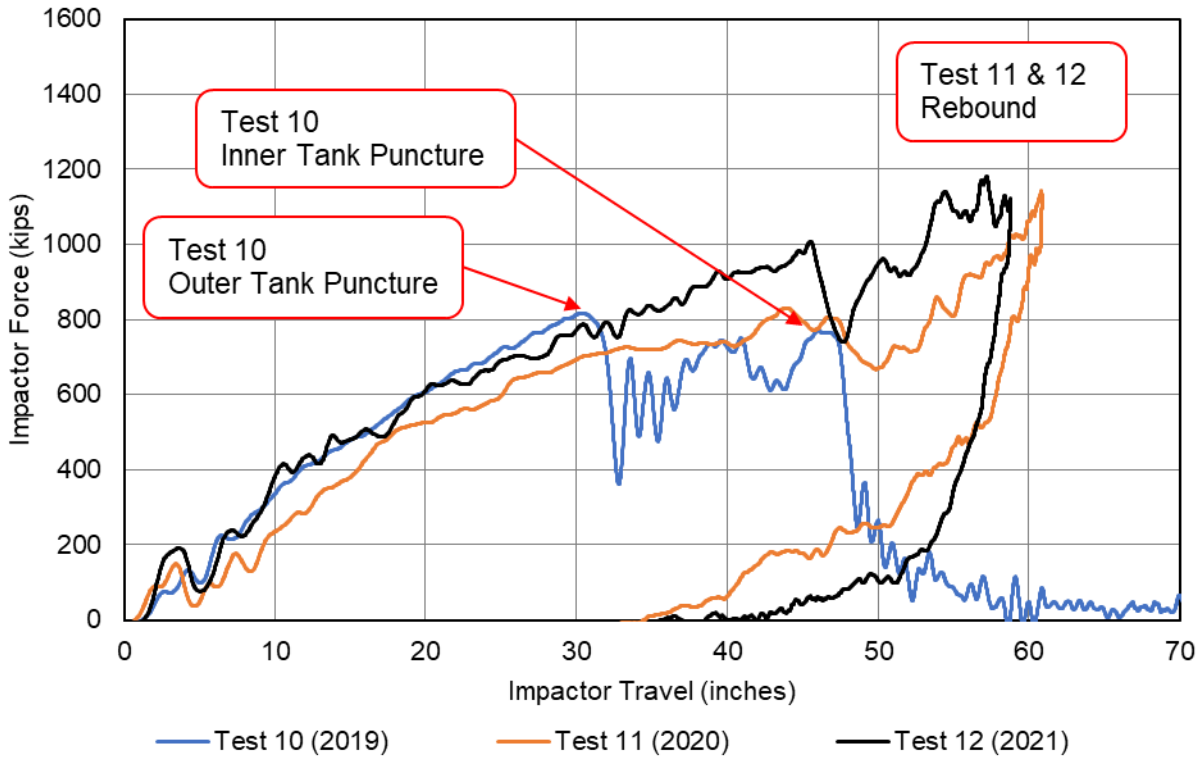


**Figure 55. Comparison of Force-Displacement Responses from Test 10, 11, and 12**

The next test in this planned series (Test 13) will use a newly constructed DOT-113C120W9 tank car having a 9/16-inch outer tank made of TC-128 steel, where the Test 10

[14] Note that the DOT-113 surrogate tank car from Test 11 only had MLI wrapped around a section of the inner tank that was within approximately 4 feet of the impact zone.

DOT-113C120W had a 7/16-inch outer tank made of A516-70 steel. Test 13 will also use a cryogenic liquid, LN2. The outage volume and pressure will be based on the expected in-service conditions for LNG. This final test is expected to be the closest approximation to LNG in-service conditions to be examined through testing in this program. Following Test 13, additional FEA using LNG in the model and inner tank at LNG temperature are planned to confirm the performance of the DOT-113C120W9 under LNG service conditions.

# 8. Conclusion

This report documents the testing and analyzing the side impact puncture performance of a surrogate DOT-113 tank car using a cryogenic lading. The inner tank was intended to be filled to 95 percent of its volume with LN2 but was actually filled to approximately 91 percent due to technical challenges with cooling the LN2 prior to the impact. At the time of the test, the pressure inside the inner vessel was approximately 30 psig. The test was intended to cause a strike to the tank car at a speed high enough to puncture both tanks. The tank car was impacted by a 297,200 lbf ram car equipped with a 12-inch by 12-inch indenter at a speed of 18.3 mph on July 24, 2021, at the TTC. The impact resulted in approximately 58 inches of compression of the outer tank, a peak pressure rise of approximately 70 psig, and a peak force of approximately 1.2 million pounds. The test resulted in both the inner and outer tanks withstanding the impact without puncturing.

Pre-test analyses predicted that puncture of the tank car was a possibility but not a certainty under the range of initial conditions and fluid behaviors investigated. Due to uncertainties in the initial conditions and fluid behavior, the goal of the pre-test modeling was to bound the observed behavior in the test, not to predict the exact threshold puncture speed. The FE modeling performed in this effort used a Lagrangian EOS and a pneumatic cavity to simulate the LN2's and the GN2's physical responses, respectively. The test measurements confirmed that these modeling techniques provided a good representation of the two-phase fluid behavior within the tank car. The test resulted in both tanks withstanding the impact. The test behavior was successfully bounded after the pre-test models were updated to reflect the measured test speed, initial pressure, and outage volume. The agreement was improved in the post-test model after calibrating a fluid behavior that simulated a phase change (GN2 condensing to LN2) occurring once the outage reached an elevated pressure during the impact.

In the reports accompanying the previously performed impact tests in this program, the authors acknowledged that there would be a large jump in complexity between testing a DOT-113 surrogate with water and LN2. While numerous technical challenges arose during pre-test planning, modeling, and execution phases of this first full-scale side impact test of a tank car filled with LN2, the test was successful in providing meaningful scientific data to understand the complexities of cryogenic steel and fluid behavior. The initial pressure within the tank was measured with certainty by a variety of sensors and mechanical gauges. The initial temperature and filling level were not measured directly prior to the test, resulting in the authors using post-test calculations to set the corresponding values in the post-test model. Pressure-time histories were measured during the test within piping connected to the inner tank. This approach to measuring pressure led to uncertainty in interpreting the pressure measurements, which the authors believe did not accurately reflect the actual pressure changes from the impact within the outage. The LN2 filling level within the tank was known to be below the height of the trycock valve at the time of the test, but the exact height had to be interpolated based on the measurement of a mechanical level gauge that measured in inches of water.

The next test in the DOT-113 test series (Test 13) will build upon that knowledge with the goals of improving the reliability of temperature and pressure measurements, the control of the outage volume, and the validation of the FE model. Several of the lessons that were learned in this first test using LN2 will be used to improve the test setup and procedures in the planned final test in this series. Pressure transducers will be installed near the vertical center of the outage so that the

bulk pressure of the GN2 will be directly measured. The mechanical level gauge will be supplemented with measurements of the mass and temperature of LN2 used to fill the tank, which can be used to calculate the volume of LN2. The pre-test FE model for Test 13 will incorporate fluid modeling improvements based on the outcome of this test, including consideration of the effects of condensation of GN2 into LN2 during the impact.

This testing and analysis supports FRA's tank car research program to provide the technical basis for rulemaking on enhanced and alternative performance standards for tank cars. One additional test is planned in this testing series where a full-size DOT-113 tank car, constructed to the latest specification, will be tested when filled with LN2. Future reports will further discuss the results of this test compared to the other tests in the DOT-113 test series.

# 9. References


[1] Pipeline and Hazardous Materials Safety Administration, DOT, "Title 49 § 179.16, Tank-head puncture-resistance systems," 2015. [Online]. Available: https://www.govinfo.gov/content/pkg/CFR-2015-title49-vol3/pdf/CFR-2015-title49-vol3-sec179-16.pdf.

[2] Pipeline and Hazardous Materials Safety Administration, DOT, "Title 49 § 179.202–12, Performance standard requirements (DOT-117P)," 2015. [Online]. Available: https://www.govinfo.gov/content/pkg/CFR-2019-title49-vol3/pdf/CFR-2019-title49-vol3-sec179-202-12.pdf.

[3] S. Trevithick, M. Carolan, S. Eshraghi and N. Wilson, "Side Impact Test and Analyses of a Legacy DOT-113 Tank Car," U.S. Department of Transportation, Federal Railroad Administration, Technical Report No. DOT/FRA/ORD-21/28, Washington, DC, September 2021.

[4] N. Wilson, M. Carolan, S. Trevithick and S. Eshraghi, "Side Impact Test and Analyses of a DOT-113 Surrogate Tank Car with Water," U.S. Department of Transportation, Federal Railroad Administration, Technical Report No. DOT/FRA/ORD-21/35, Washington, DC, 2021.

[5] S. Eshraghi, A. Krishnamurthy and M. Carolan, "Finite Element Analyses of Side Impacts to DOT-113 Surrogate Tank Cars with Water and Liquid Nitrogen," U.S. Department of Transportation, Federal Railroad Administration, Technical Report No. DOT/FRA/ORD-22/22, Washington, DC, June 2022.

[6] ASTM International, *ASTM A240/A240M: Standard Specification for Chromium and Chromium-Nickel Stainless Steel Plate, Sheet, and Strip for Pressure Vessels and for General Applications.,* Conshocken, PA, 2019.

[7] S. W. Kirkpatrick, "Detailed Puncture Analyses of Various Tank Car Designs - Final Report - Revision 1," U.S. Department of Transportation, Federal Railroad Administration, Washington, DC, 2010.

[8] M. Carolan, D. Jeong, B. Perlman, M. Yellapu, S. Namboodri, B. Kurtz, R. Elzey, S. Anankitpaiboon, L. Tunna and R. Fries, "Application of Welded Steel Sandwich Panels for Tank Car Shell Impact Protection," U.S. Department of Transportation, Federal Railroad Administration, Technical Report No. DOT/FRA/ORD-13/19, Washington, DC, April 2013.

[9] S. W. Kirkpatrick, P. Rakoczy, R. A. MacNeill and A. Anderson, "Side Impact Test and Analyses of a DOT-111 Tank Car," U.S. Department of Transportation, Federal Railroad Administration, Technical Report No. DOT/FRA/ORD/15-30, Washington, DC, October 2015.

[10] P. Rakoczy and M. Carolan, "Side Impact Test and Analysis of a DOT-112 Tank Car," U.S. Department of Transportation, Federal Railroad Administration, Technical Report No. DOT/FRA/ORD-16/38, Washington, DC, December 2016.

[11] M. Carolan and P. Rakoczy, "Side Impact Test and Analyses of a DOT-105 Tank Car," U.S. Department of Transportation, Federal Railroad Administration, Technical Report No. DOT/FRA/ORD-19/12, Washington, DC, May 2019.

[12] P. Rakoczy, M. Carolan, T. Gorhum and S. Eshraghi, "Side Impact Test and Analyses of a DOT-117 Tank Car," U.S. Department of Transportation, Federal Railroad Administration, Technical Report No. DOT/FRA/ORD-19/13, Washington, DC, May 2019.

[13] N. Wilson, S. Eshraghi, S. Trevithick, M. Carolan and P. Rakoczy, "Side Impact Test and Analyses of a DOT-105 Tank Car- 6 x 6 Inch Indenter," U.S. Department of Transportation, Federal Railroad Administration, Technical Report No. DOT/FRA/ORD-20/38, Washington, DC, September 2020.

[14] S. Eshraghi, S. Trevithick, M. Carolan, P. Rakoczy and N. Wilson, "Side Impact Test and Analyses of a DOT 111 (CPC-1232) Tank Car," U.S. Department of Transportation, Federal Railroad Adminstration, Technical Report No. DOT/FRA/ORD-20/43, Washington, DC, 2020.

[15] A. Krishnamurthy, S. Trevithick, M. Carolan, U. Spangenberg, N. Wilson, S. Eshraghi and S. Kirkpatrick, "Review of Tank Car Side Impact Test Research and Analyses of 2007–2019," U.S. Department of Transportation, Federal Railroad Administration, Technical Report No. DOT/FRA/ORD-22/14, Washington, DC, 2022.

[16] Association of American Railroads, "Manual of Standards of Recommended Practices, Section C Part III - Specifications for Tank Cars Standard M-1002, Appendix M," 2014. [Online]. Available: https://aarpublications.com/section-c-part-iii-specifications-for-tank-cars-m-1002-2014g.html.

[17] Pipeline and Hazardous Materials Safety Administration, DOT, "Title 49 § 179.302 Subpart F – Specification for Cryogenic Liquid Tank Car Tanks and Seamless Steel Tanks (Classes DOT-113 and 107A)," 1983. [Online]. Available: https://www.govinfo.gov/content/pkg/CFR-2018-title49-vol3/pdf/CFR-2018-title49-vol3-part179-subpartF.pdf.

[18] Federal Register, "Federal Register/Vol 85, No. 143/Friday, July 24, 2020/Rules and Regulations," 2020. [Online]. Available: https://www.govinfo.gov/content/pkg/FR-2020-07-24/pdf/2020-13604.pdf.

[19] ASTM International, "ASTM A240/A240M-19, Standard Specification for Chromium and Chromium-Nickel Stainless Steel Plate, Sheet, and Strip for Pressure Vessels and for General Applications," 2020. [Online]. Available: https://www.astm.org/a0240_a0240m-19.html.

[20] Federal Register, "Federal Register/Vol. 84, No. 206/Thursday, October 24, 2019/Notices," 2019. [Online]. Available: https://www.govinfo.gov/content/pkg/FR-2019-10-24/pdf/2019-21515.pdf.

[21] E. W. Lemmon, I. H. Bell, M. L. Huber and M. O. McLinden, "Thermophysical Properties of Fluid Systems," in *NIST Chemistry WebBook, NIST Standard Reference Database Number 69*, P. J. Linstrom and W. G. Mallard, Eds., 2022, p. National Institute of Standards and Technology.

[22] SAE International, *Instrumentation for Impact Test - Part 1: Electronic Instrumentation,* Warrendale, PA, PA: SAE International, 2007.

[23] Dassault Systèmes Simulia Corp., *Abaqus 2017,* Providence, RI, RI, 2017.

[24] Y. Bao and T. Wierzbicki, "On fracture locus in the equivalent strain and stress triaxiality space," *International Journal of Mechanical Sciences,* vol. 46, no. 2004, p. 81–98, 2004.

[25] The Engineering Toolbox, "Universal and Individual Gas Constants," The Engineering Toolbox, 2004. [Online]. Available: https://www.engineeringtoolbox.com/individual-universal-gas-constant-d_588.html.

[26] A. J. Smits, A Physical Introduction to Fluid Mechanics, New York: John Wiley and Sons, 2000.

[27] ASTM International, *ASTM E8/E8M: Standard Test Methods for Tension Testing of Metallic Materials,* West Conshocken, PA: American Society for Testing and Materials, 2013.

[28] The Engineering Toolbox, "Air - Altitude, Density and Specific Volume vs. Altitude," The Engineering Toolbox, 2003. [Online]. Available: https://www.engineeringtoolbox.com/air-altitude-density-volume-d_195.html.

[29] United States Geological Survey (USGS), "Geographic Names Information System (GNIS) Detail - City of Pueblo, CO," 2002. [Online]. Available: https://edits.nationalmap.gov/apps/gaz-domestic/public/summary/2411501.

[30] M. Paredes, D. Sarzosa, R. Savioli, T. Wierzbicki, D. Jeong and D. Tyrell, "Ductile Tearing Analysis of TC128 Tank Car Steel Under Mode I Loading," *Theoretical and Applied Fracture Mechanics,* vol. 96, p. 658–675, 2018.

[31] H. W. Swift, "Plastic instability under plane stress," *Journal of the Mechanics and Physics of Solids,* vol. 1, no. 1, p. 1–18, 1952.

[32] E. Voce, "The relationship between stress and strain for homogenous deformations," *Journal of the Institute of Metals,* vol. 74, p. 537–562, 1948.

[33] Y.-W. Lee and T. Wierzbicki, "Quick Fracture Calibration for Industrial Use," Massachusetts Institute of Technology Impact & Crashworthiness Laboratory, Cambridge, MA, 2004.

[34] Y.-W. Lee, "Fracture Prediction in Metal Sheets," Massachusetts Institute of Technology, Cambridge, MA, 2005.

[35] M. Paredes, V. Grolleau and T. Wierzbicki, "On Ductile Fracture of 316L Stainless Steels at Room and Cryogenic Temperature Level: An Engineering Approach to Determine Material Parameters," *Materialia,* vol. 15, p. 101009, 2020.

[36] American Society of Heating, Refrigerating and Air-Conditioning Engineers, ASHRAE Thermodynamic Properties of Refrigerants, New York: ASHRAE, 1969.

[37] Engineers Edge, "Specific Heat Capacity of Metals Table Chart," 2022. [Online]. Available: https://www.engineersedge.com/materials/specific_heat_capacity_of_metals_13259.htm.

[38] Pipeline and Hazardous Materials Safety Administration, DOT, "Title 49 CFR Part 179 Subpart F, Specification for Cryogenic Liquid Tank Car Tanks and Seamless Steel Tanks (Classes DOT-113 and 107A)," eCFR, 2022. [Online]. Available: https://www.ecfr.gov/current/title-49/subtitle-B/chapter-I/subchapter-C/part-179/subpart-F.

[39] T. R. Strobridge, "Technical Note 129 - The Thermodynamic Properties of Nitrogen from 64 to 300° K Between 0.1 and 200 Atmospheres," United States Department of Commerce Natural Bureau of Standards, Office of Technical Services, Report No. PB 16130, Washington, DC, 1962.

[40] J. E. Jensen, W. A. Tuttle, R. B. Stewart, H. Brechna and A. G. Prodell, "Brookhaven National Laboratory Selected Cryogenic Data Notebook," Brookhaven National Laboratory Associated Universities, Inc., 1980.

[41] R. C. Reid, J. M. Prausnitz, B. E. Poling and T. K. Sherwood, Properties of Gases & Liquids, 4th Edition, New York: McGraw Hill, 1987.

[42] Transportation Technology Center, Inc., "Test Implementation Plan for FRA Tank Car Side Impact, Revision 2," Pueblo, CO, 2019.

# Appendix A.
# Camera and Target Positions

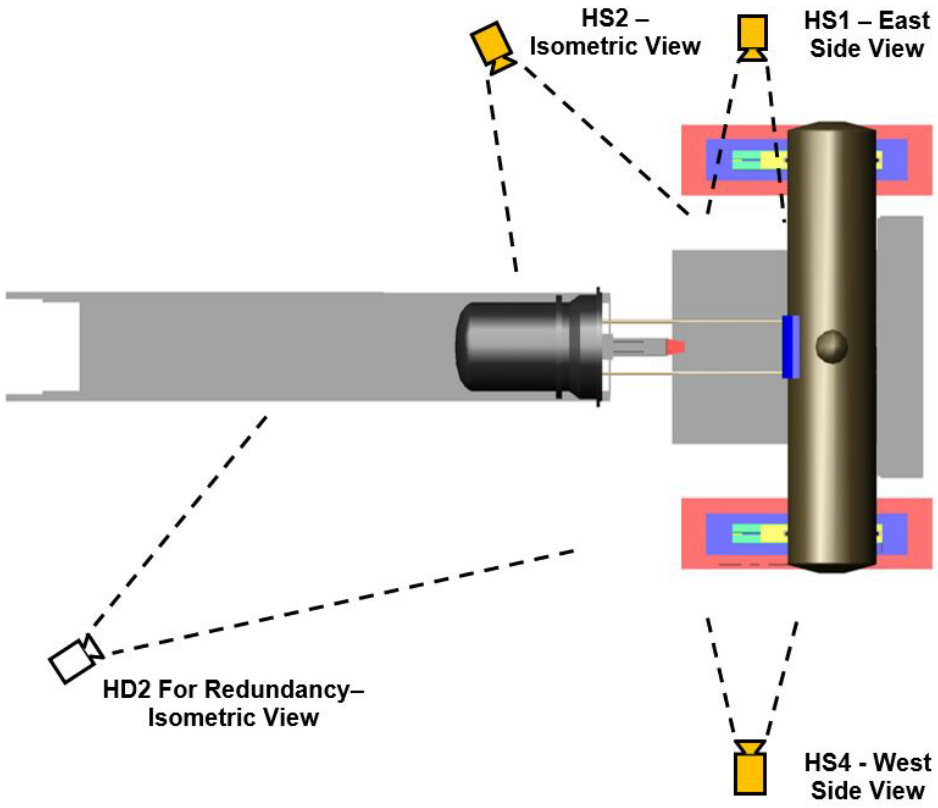


**Figure A1. Camera Positions (top) — High Speed (HS), High Definition (HD)**

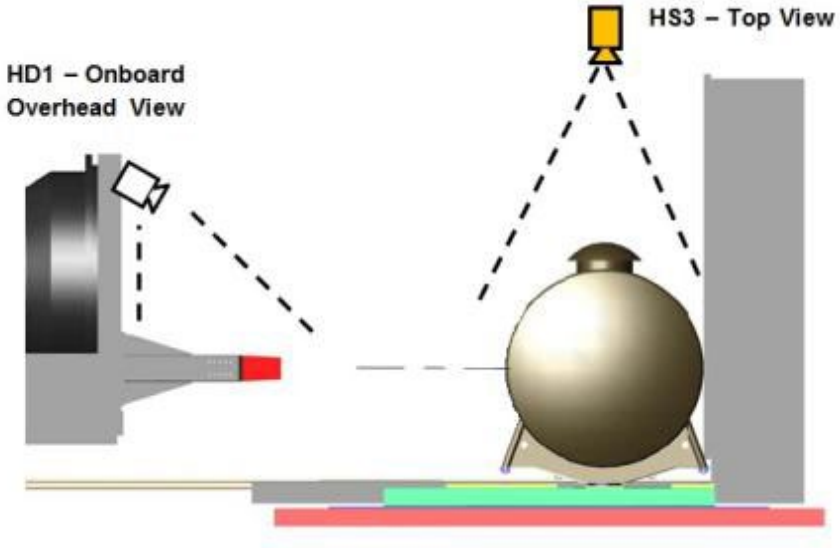


**Figure A2. Camera Positions (side) — HS, HD**

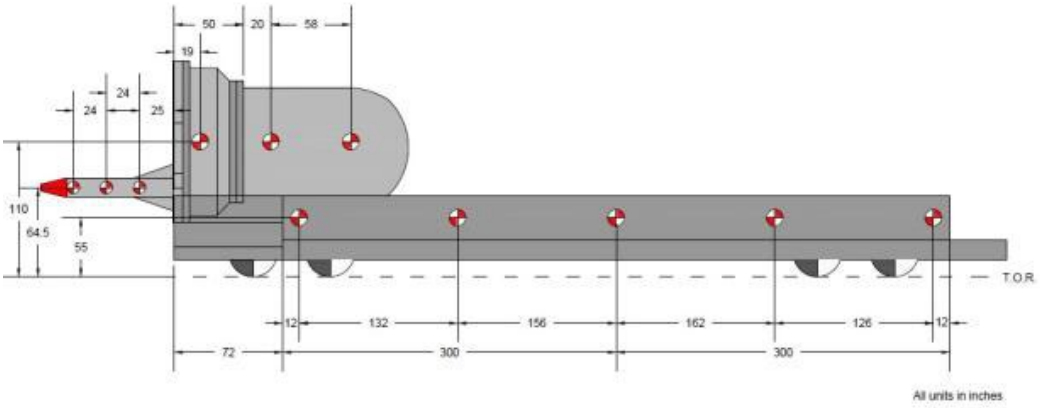


**Figure A3. Ram Car Target Positions**

# Appendix B.
# Test Data

This appendix contains raw and filtered test data. The raw accelerations and internal pressures measured on different locations on the impact cart were processed as follows. The test data from -1 to -0.1 seconds on each channel were averaged, and this value was subtracted from the test measurements in order to remove any initial offsets in the data. Each channel was then filtered to channel frequency class (CFC) 60, using the procedures given in SAE J211 [23]. Displacement data did not require any filtration.

## B1. Accelerations

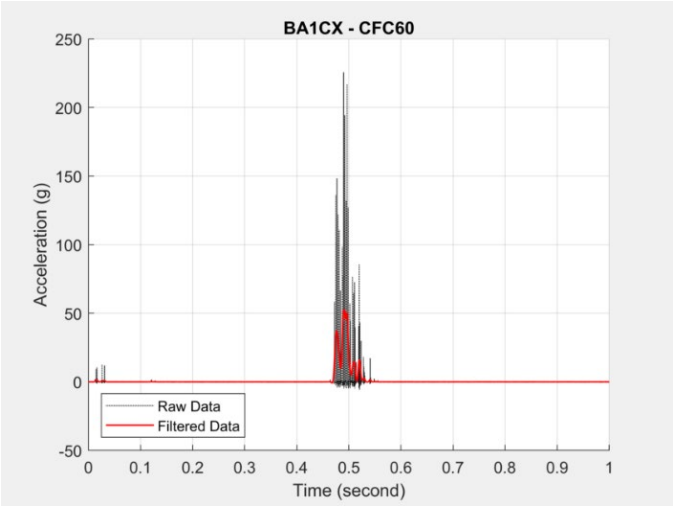


**Figure B1. Raw and CFC60 Filtered Acceleration-Time Data from BA1CX**

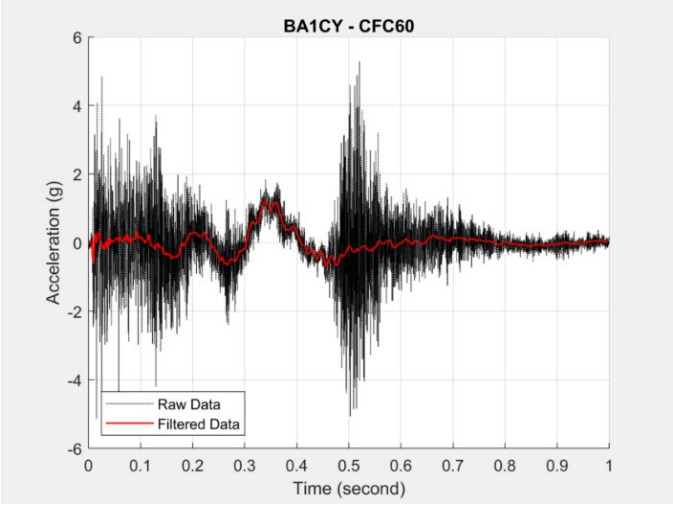


**Figure B2. Raw and CFC60 Filtered Acceleration-Time Data from BA1CY**

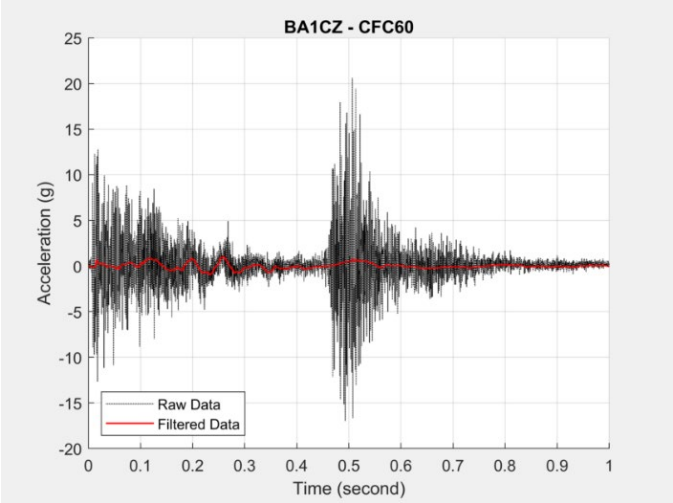


**Figure B3. Raw and CFC60 Filtered Acceleration-Time Data from BA1CZ**

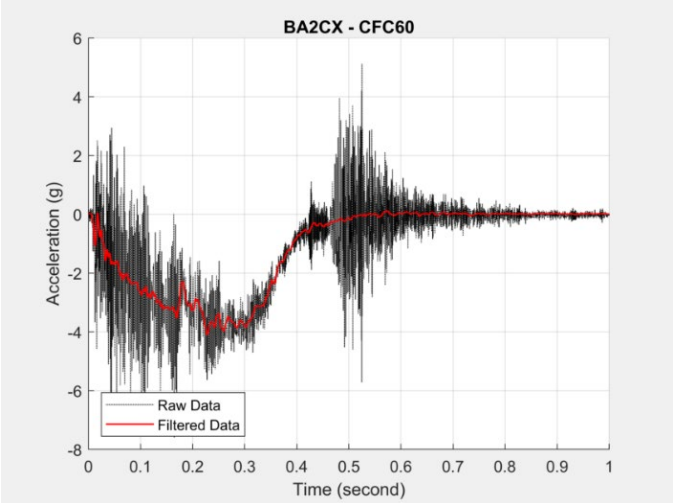


**Figure B4. Raw and CFC60 Filtered Acceleration-Time Data from BA2CX**

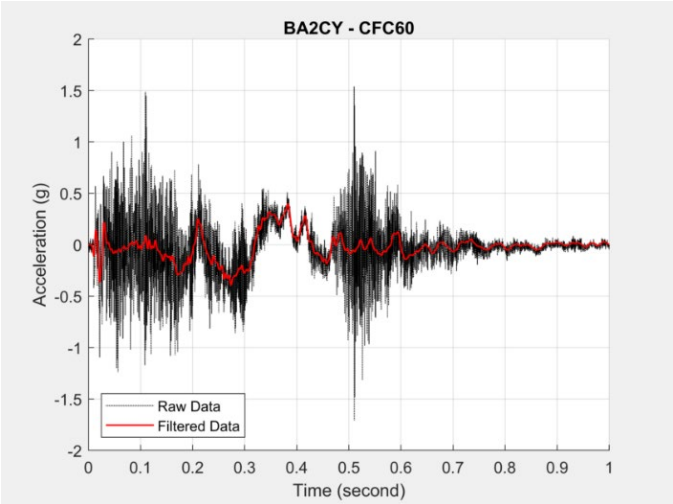


**Figure B5. Raw and CFC60 Filtered Acceleration-Time Data from BA2CY**

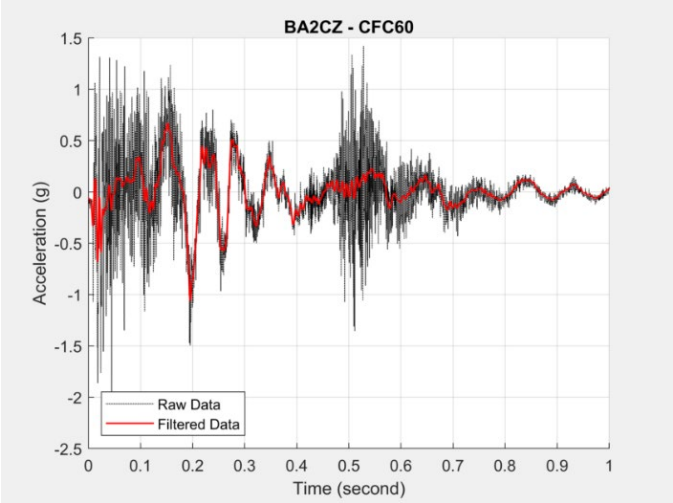


**Figure B6. Raw and CFC60 Filtered Acceleration-Time Data from BA2CZ**

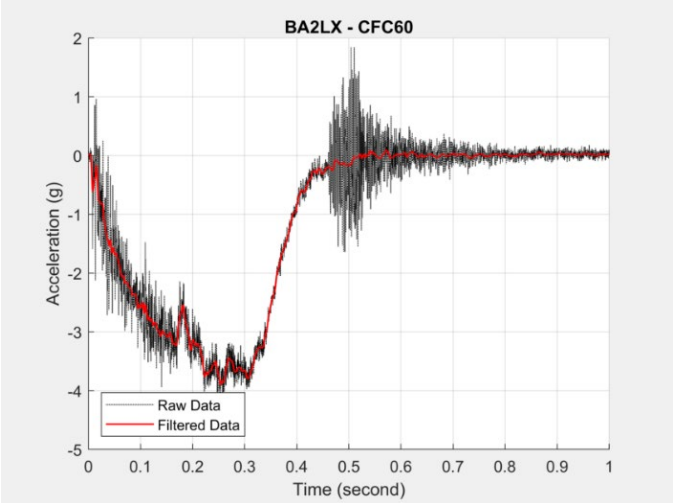


**Figure B7. Raw and CFC60 Filtered Acceleration-Time Data from BA2LX**

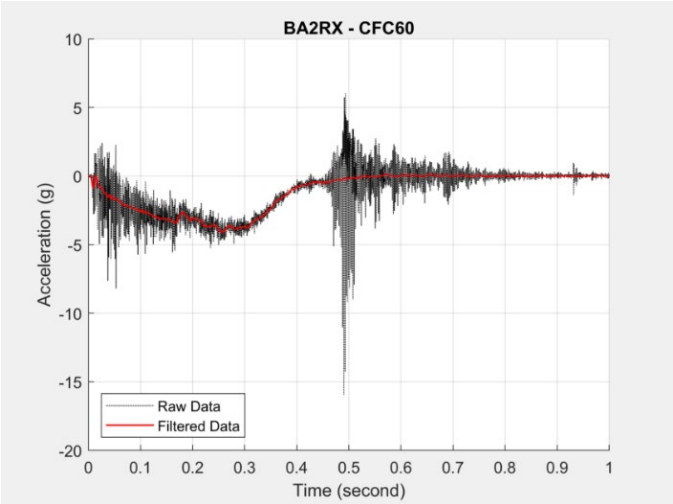


**Figure B8. Raw and CFC60 Filtered Acceleration-Time Data from BA2RX**

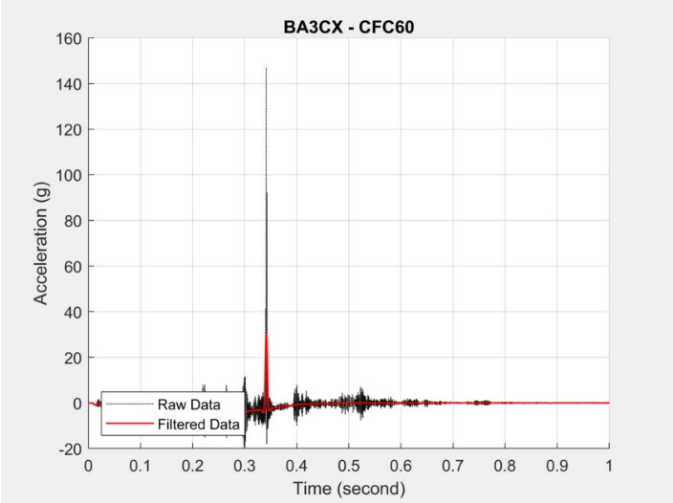


**Figure B9. Raw and CFC60 Filtered Acceleration-Time Data from BA3CX**

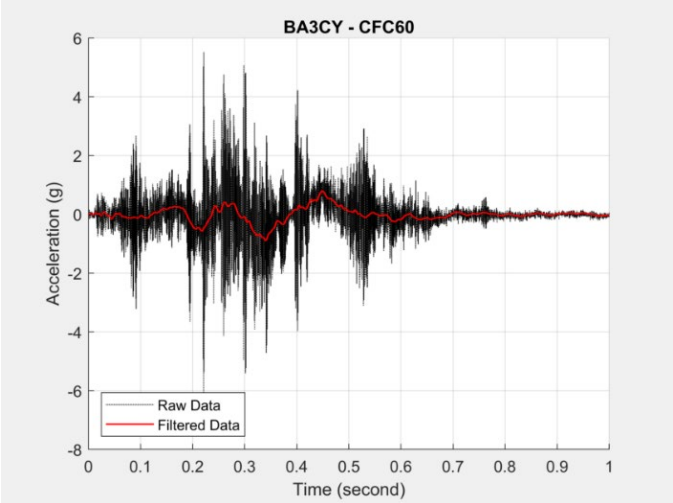


**Figure B10. Raw and CFC60 Filtered Acceleration-Time Data from BA3CY**

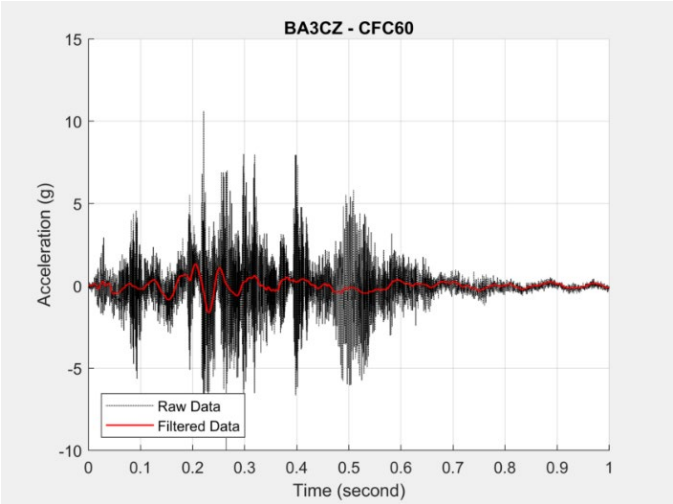


**Figure B11. Raw and CFC60 Filtered Acceleration-Time Data from BA3CZ**

## B2. Pressures

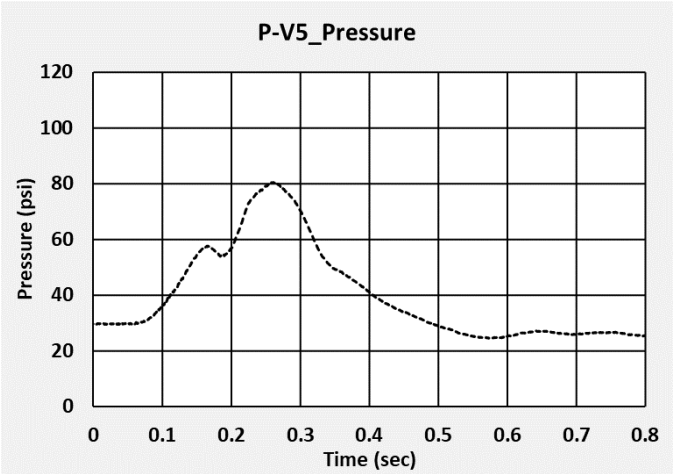


**Figure B12. Raw Pressure-Time Data from P-V5**

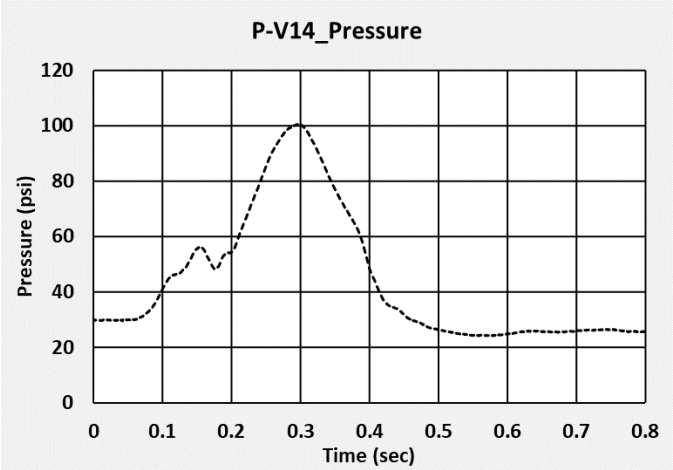


**Figure B13. Raw Pressure-Time Data from P-V14**

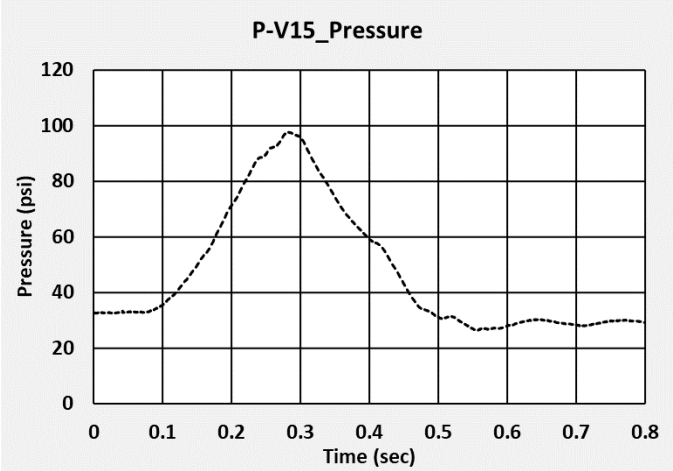


**Figure B14. Raw Pressure-Time Data from P-V15**

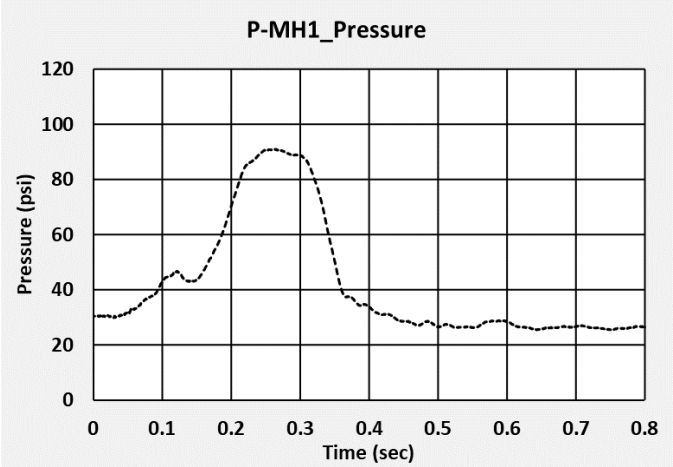


**Figure B15. Raw Pressure-Time Data from P-MH1**

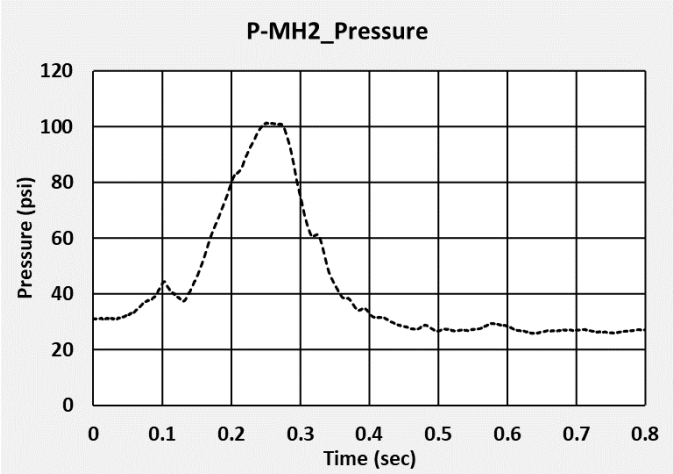


**Figure B16. Raw Pressure-Time Data from P-MH2**

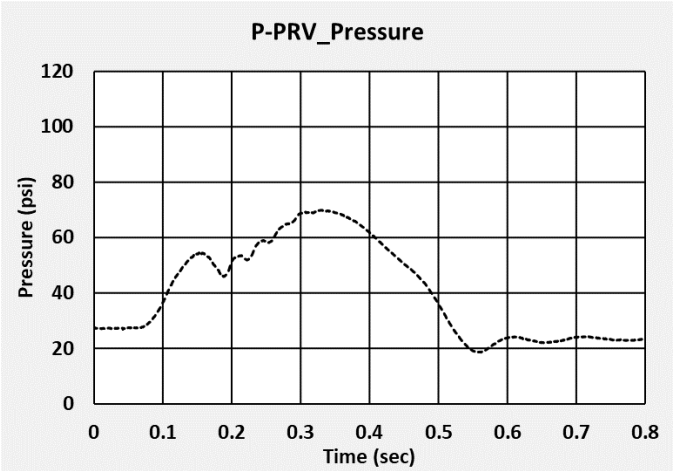


**Figure B17. Raw Pressure-Time Data from P-PRV**

## B3. Displacements

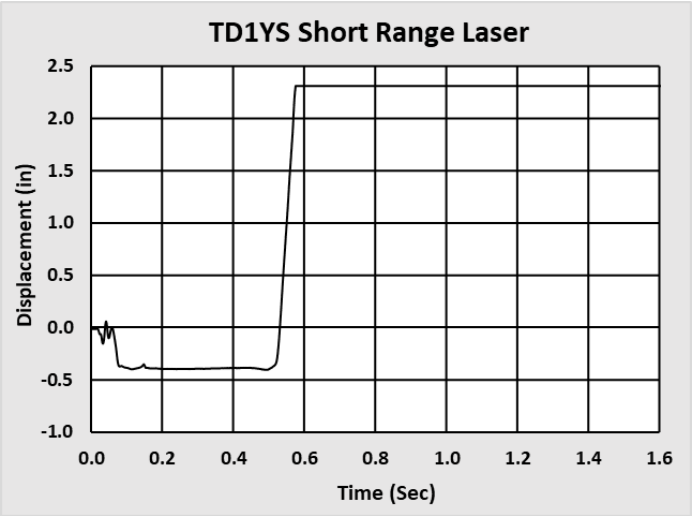


**Figure B18. Raw Displacement-Time Data from Short Range Wall Mounted Laser Displacement Transducer (Range: 1.4 in to 4.3 in)**

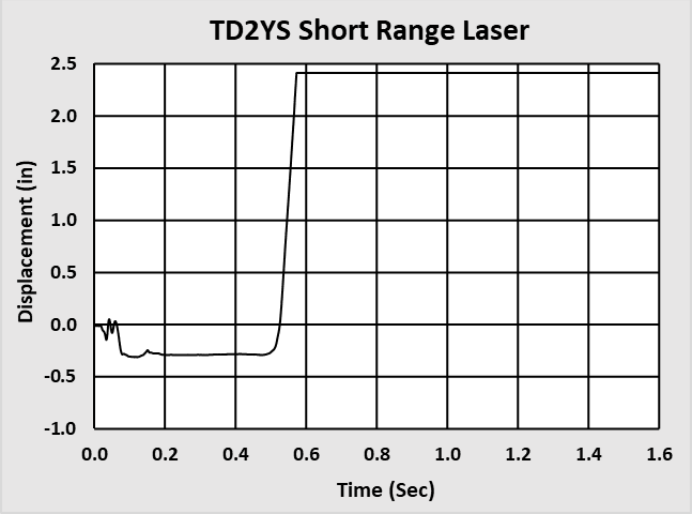


**Figure B19. Raw Displacement-Time Data from Short Range Wall Mounted Laser Displacement Transducer (Range: 1.4 in to 4.3 in)**

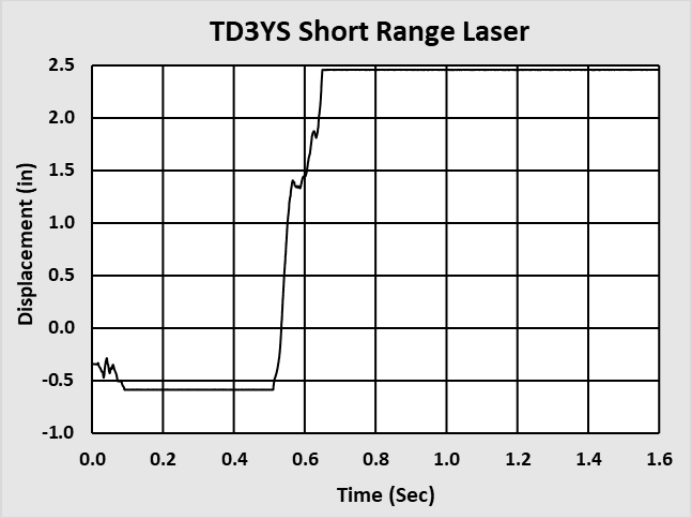


**Figure B20. Raw Displacement-Time Data from Short Range Wall Mounted Laser Displacement Transducer (Range: 1.4 in to 4.3 in)**

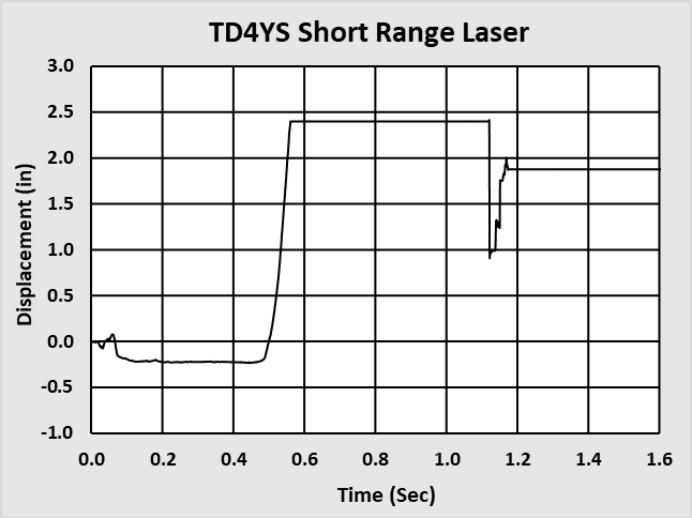


**Figure B21. Raw Displacement-Time Data from Short Range Wall Mounted Laser Displacement Transducer (Range: 1.4 in to 4.3 in)**

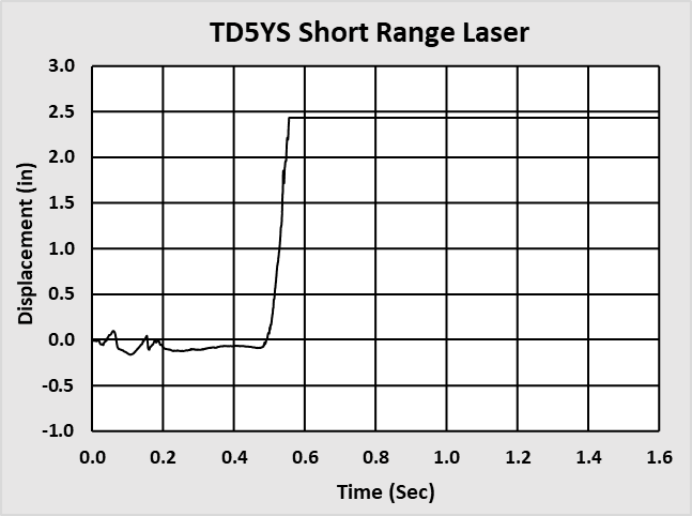


**Figure B22. Raw Displacement-Time Data from Short Range Wall Mounted Laser Displacement Transducer (Range: 1.4 in to 4.3 in)**

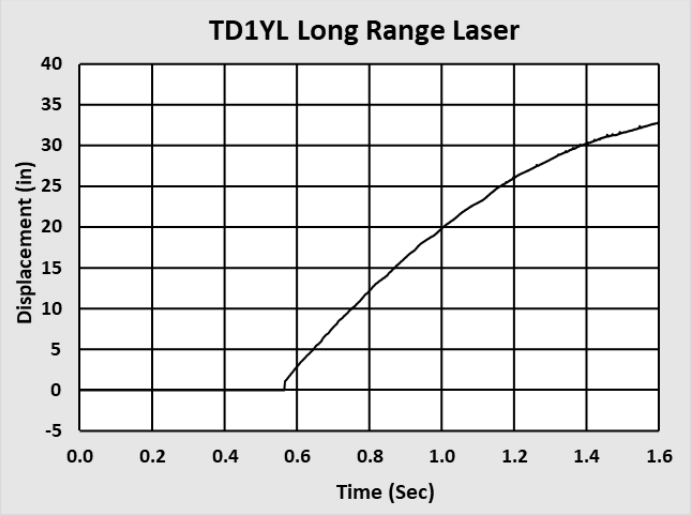


**Figure B23. Raw Displacement-Time Data from Long Range Wall Mounted Laser Displacement Transducer (Range: 4 in to 39 in)**

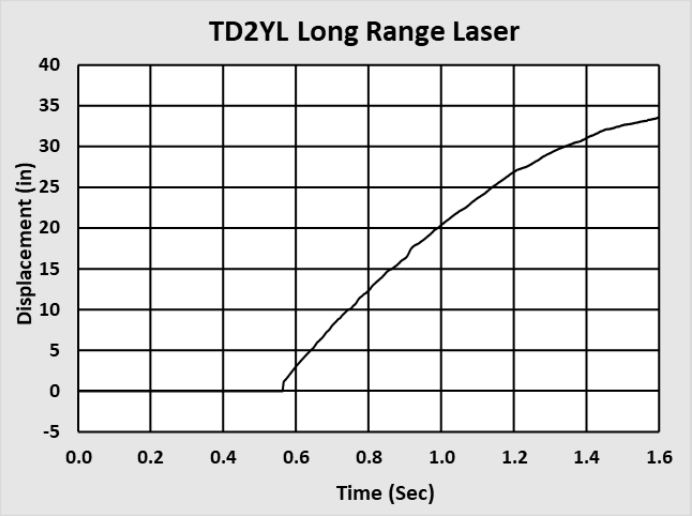


**Figure B24. Raw Displacement-Time Data from Long Range Wall Mounted Laser Displacement Transducer (Range: 4 in to 39 in)**

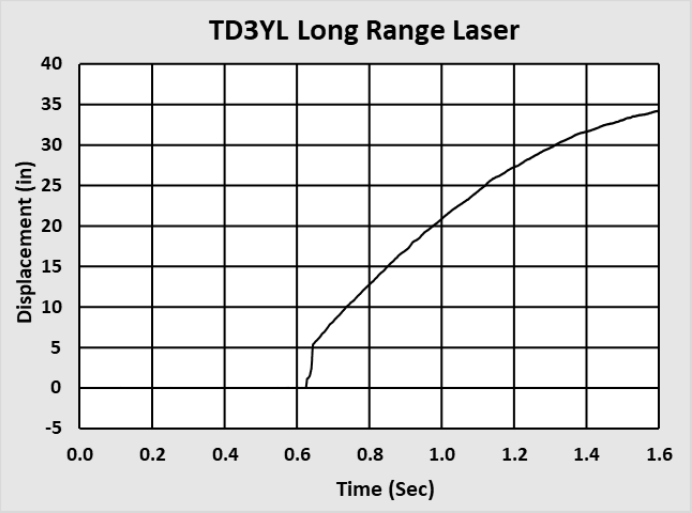


**Figure B25. Raw Displacement-Time Data from Long Range Wall Mounted Laser Displacement Transducer (Range: 4 in to 39 in)**

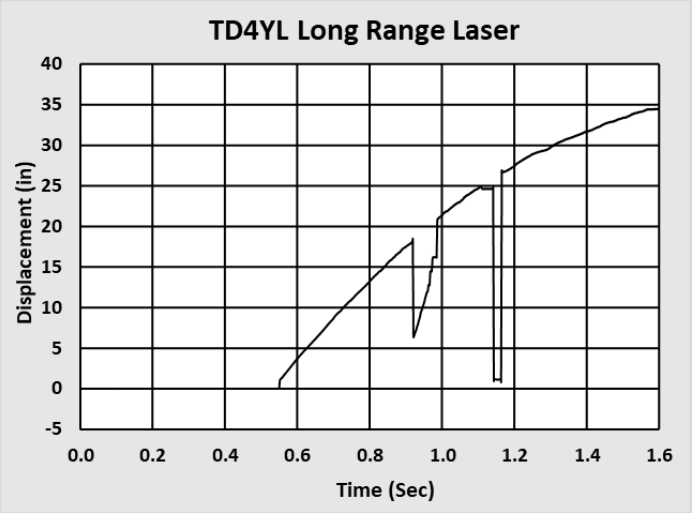


**Figure B26. Raw Displacement-Time Data from Long Range Wall Mounted Laser Displacement Transducer (Range: 4 in to 39 in)**

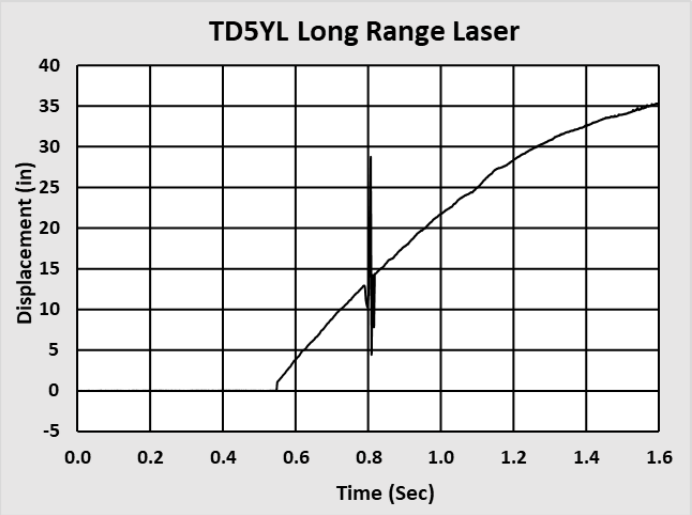


**Figure B27. Raw Displacement-Time Data from Long Range Wall Mounted Laser Displacement Transducer (Range: 4 in to 39 in)**

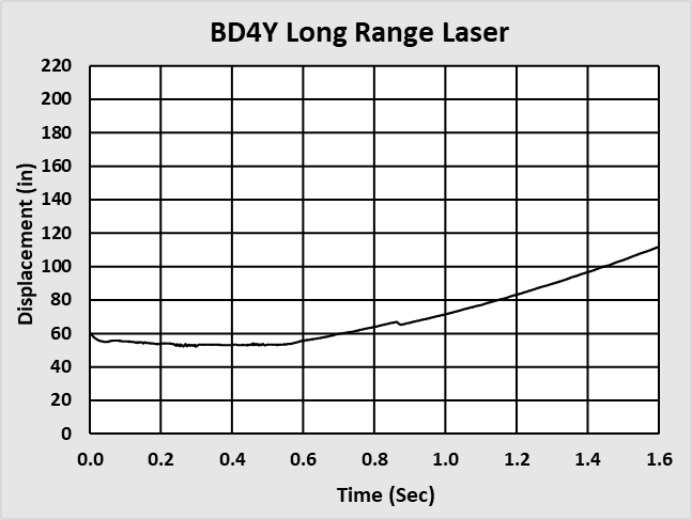


**Figure B28. Raw Displacement-Time Data from Long Range Ram Car Mounted Laser Displacement Transducer (Range: 2 in to 39 ft)**

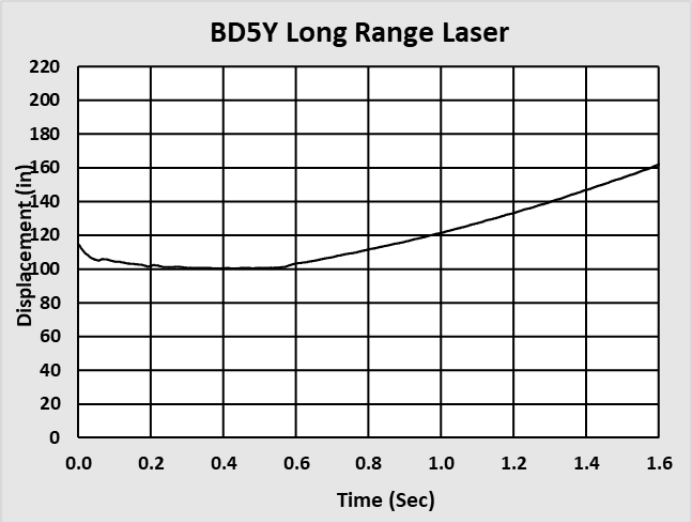


**Figure B29. Raw Displacement-Time Data from Long Range Ram Car Mounted Laser Displacement Transducer (Range: 2 in to 39 ft)**

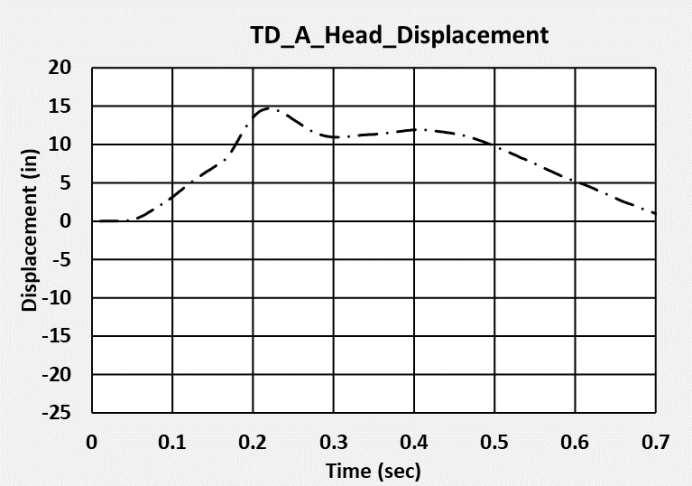


**Figure B30. Raw Displacement-Time Data from Displacement Transducer on A-End Head**

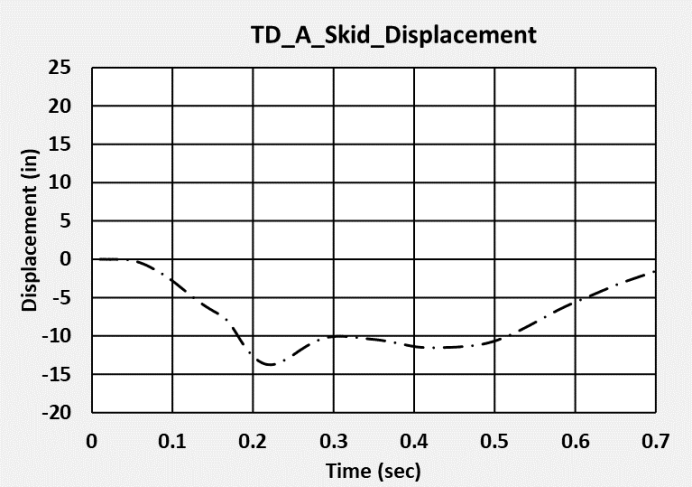


**Figure B31. Raw Displacement-Time Data from Displacement Transducer on A-End Skid**

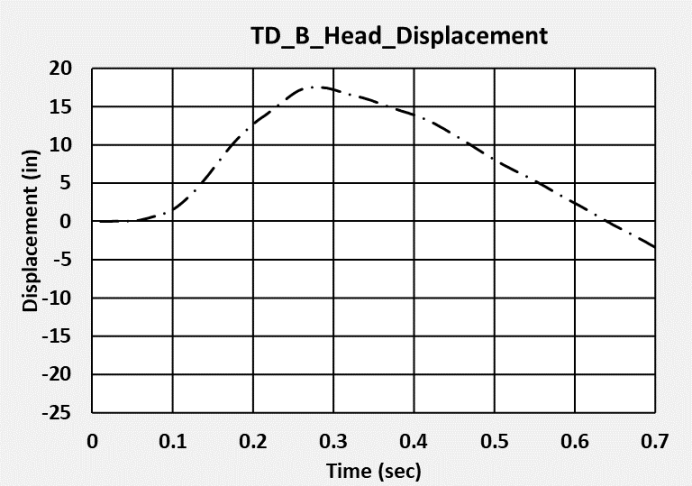


**Figure B32. Raw Displacement-Time Data from Displacement Transducer on B-End Head**

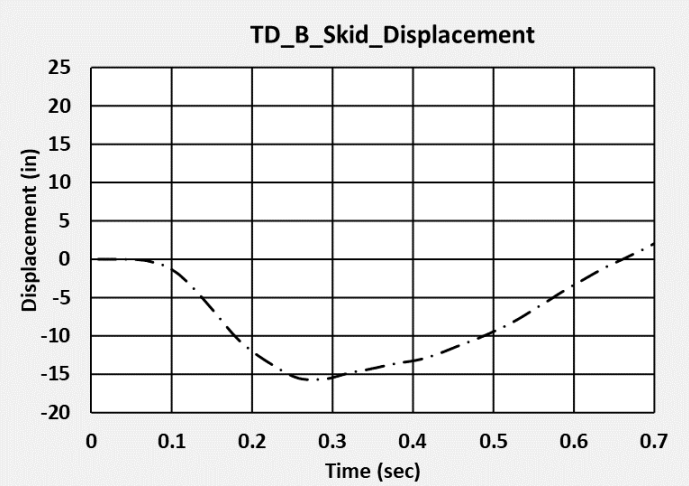


**Figure B33. Raw Displacement-Time Data from Displacement Transducer on B-End Skid**

## B4. Thermocouples

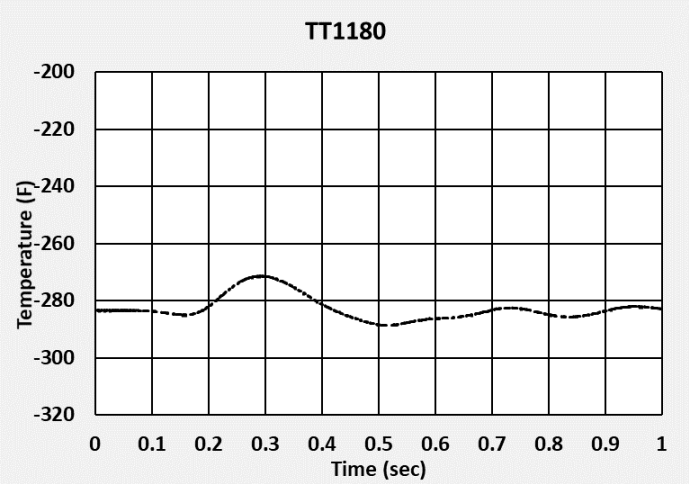


**Figure B34. Raw Temperature-Time Data from Thermocouple at A-End Bottom of Tank**

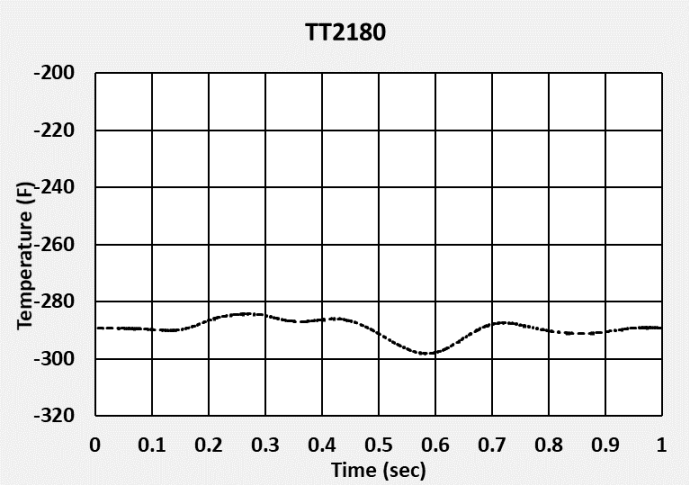


**Figure B35. Raw Temperature-Time Data from Thermocouple Near Center at Bottom of Tank**

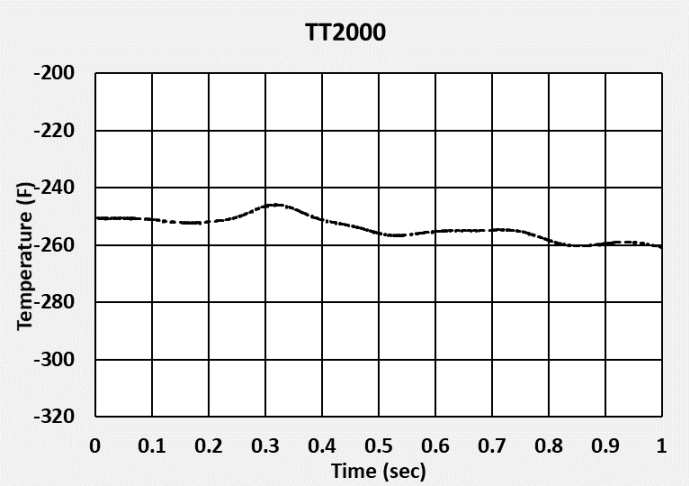


**Figure B36. Raw Temperature-Time Data from Thermocouple at Top of Tank Near the Manhole**

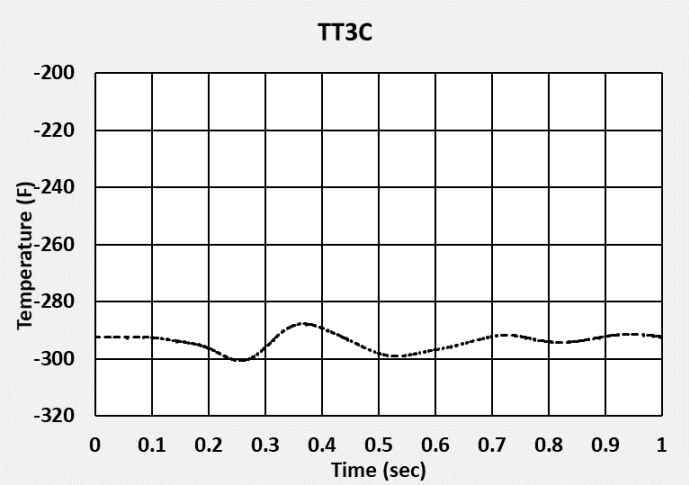


**Figure B37. Raw Temperature-Time Data from Thermocouple at B-End of Tank, Mid-Height**

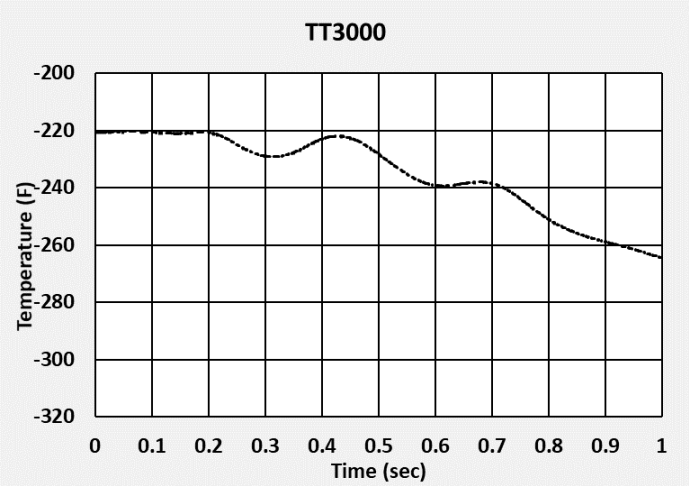


**Figure B38. Raw Temperature-Time Data from Thermocouple at B-End Top of Tank**

## B5. Material Characterization Results

Material characterization tests were not performed on either the TC-128 carbon steel used in the outer tank or the T304 stainless steel used in the inner tank prior to the test. After the DOT-113 surrogate was tested, material characterization tests were performed on the TC-128 carbon steel to confirm its properties. Post-impact material testing was not performed on the T304 inner tank steel for this test.

### *B5.1 AAR TC-128 Carbon Steel (Pre-test)*

The outer tank of the DOT-113 surrogate tank car used in this test (Test 12) was not characterized by tensile testing prior to the side impact test. The authors used tensile test results from the previously tested DOT-113 surrogate tank car (Test 11) as an estimate for the TC-128 properties. This approach was taken because the TC-128 mechanical properties from Test 11 appeared to be typical based on the experience of the authors, and there was not expected to be a large amount of variation between the TC-128 steels in the DOT-113 surrogate outer tanks.

Thus, the same FE material input parameters which were used in the pre- and post-test FE models for Test 11 [4] were applied to the pre-test FE models for Test 12.

### *B5.2 AAR TC-128 Carbon Steel (Post-test)*

TTCI contracted with an independent test lab to conduct tensile testing on the TC-128 carbon steel used to fabricate the outer tank. A section of the Test 12 outer tank that did not show visible permanent deformation was excised from the surrogate after the test. Two-inch gage length coupons were machined from this plate. The nominal thickness of the tank was 0.608 inches. However, the combination of coupon thickness and material strength led to difficulty maintaining a grip on the coupon within the test fixture. The laboratory reduced the thickness of the specimens to approximately 0.36 inches.

The research team provided the lab with four specimens for tensile testing according to ASTM E-8 [28]. One of the specimens (Specimen 2) was rejected by the lab during post-processing of the results owing to a problem gripping this sample which may have led to an initial yielding of the material. The results of the remaining three specimens taken from the Test 12 car are summarized in Table B1, alongside the average properties measured during pre- and post-impact material testing of the Test 11 tank car [4]. The average properties measured for the three Test 12 specimens are similar to the average properties for the TC-128 taken from the Test 11 car. Based on these similarities, the TC-128 material response developed using Test 11 properties was unchanged in the Test 12 post-test FE model.

**Table B1. Summary of AAR TC-128 Steel Tensile Test Results**

| Specimen | YS | UTS | EB-2in |
|---|---|---|---|
| - | ksi | ksi | % |
| Test 12 – 1 | 58.2 | 83.7 | 42.7 |
| Test 12 – 3 | 58.5 | 87.8 | 36.3 |
| Test 12 – S | 63.8 | 87.3 | 33.4 |
| *Test 12 - Average* | *60.2* | *86.2* | *37.5* |
| *Test 11 – Average (pre-test)* | *64.9* | *88.8* | *31.4* |
| *Test 11 – Average (post-test)* | *64.5* | *86.5* | *37.1* |

### *B5.3 ASTM A240, Type 304 Stainless Steel (Pre-test)*

Tensile coupons were extracted from the inner tank of the DOT-113 surrogate, which was tested with water on June 11, 2021, i.e., Test 11. Researchers contracted with an independent test lab to conduct tensile testing at cryogenic temperature and elevated strain rates. The material characterization from the DOT-113 surrogate test with water was used as a pre-test estimate of the material properties in the DOT-113 surrogate test with LN2.

Table B2 shows the material characterization test matrix of T304 stainless steel using temperatures from room temperature (295 K) to the saturation temperature of nitrogen at sea level (77 K) and strain rates from 0.0005 in/in/s to 15 in/in/s for uniaxial tensile coupons. Charpy V-notch (CVN) tests were also included to measure the fracture energy of the specimens under

three point bending at a very high strain rate. Each of the 19 test conditions presented in Table B2 was tested 3 times.

**Table B2. Temperature and Strain Rate Test Matrix of T304 Stainless Steel**

| Strain Rate | 295 K | 210 K | 111 K | 77 K |
|---|---|---|---|---|
| **$5.0 \cdot 10^{-4}$ $s^{-1}$** | 1 | 2 | N/A | 3 |
| **$5.0 \cdot 10^{-2}$ $s^{-1}$** | 4 | 5 | N/A | 6 |
| **$5.0 \cdot 10^{-1}$ $s^{-1}$** | 7 | 8 | N/A | 9 |
| **$5.0 \cdot 10^{+0}$ $s^{-1}$** | 10 | 11 | N/A | 12 |
| **$1.5 \cdot 10^{+1}$ $s^{-1}$** | 13 | 14 | N/A | 15 |
| **Charpy** | 16 | 17 | 18 | 19 |

Figure B39 shows the nominal stress-strain curves for the T304 tensile coupons at 77 K; however, the results at 5 in/in/s and 15 in/in/s were omitted due to disagreement between the extensometer readings and post-failure EB measurements. The T304 tensile coupons had a flat, rectangular ASTM-E8 sub-size geometry with a 1-inch GL, 0.25-inch width, and 0.067-inch thickness. While a thicker coupon close to 0.25 inches was preferred, the cryogenic test equipment could not accommodate the material's high strength at cold temperatures. When comparing the quasi-static (QS) specimens with the higher rate specimens, reductions in UTS of 24 percent, EB of 20 percent, and fracture toughness of 30 percent were observed. While the 5 in/in/s and 15 in/in/s results are not shown in Figure B39, they had similar measured values for YS, UTS, EB, and fracture toughness to the specimens at 0.05 in/in/s and 0.5 in/in/s.

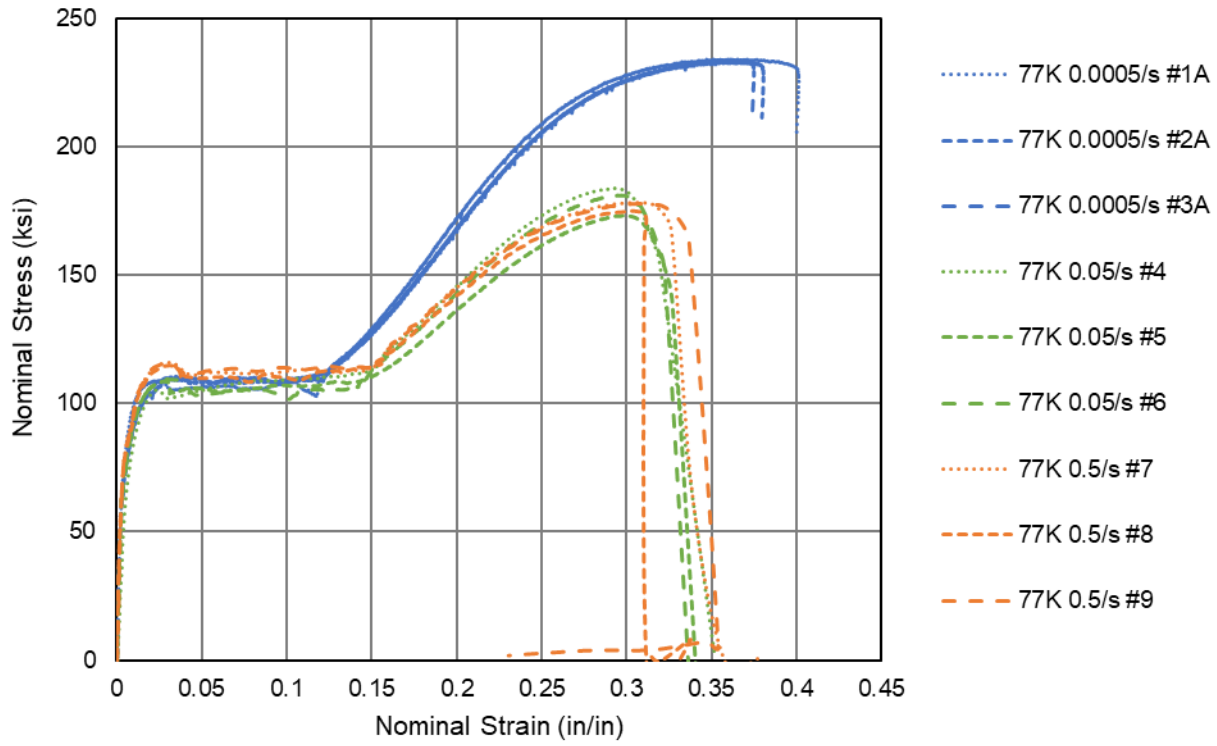


**Figure B39. Nominal Stress-Strain Responses of ASTM A240, Type 304 Steel Using ASTM-E8 1-inch Gage Length Flat Dogbone Specimens at 77 K**

Table B3 provides the tensile properties (YS, UTS, and EB-2in) for the pre-test T304 tensile specimens.

**Table B3. Summary of ASTM A240, Type 304 Steel Tensile Pre-test Results at 77 K**

| Specimen | Rate | YS | UTS | EB-1.5 in | Fracture Toughness |
|---|---|---|---|---|---|
| # | *in/in/s* | *ksi* | *ksi* | *%* | *in-kip/in$^3$* |
| 1 | 5.00E-04 | 82.53 | 234.2 | 39.1 | 67.6 |
| 2 | 5.00E-04 | 71.38 | 232.9 | 39.2 | 62.3 |
| 3 | 5.00E-04 | 72.96 | 233.5 | 38 | 60.9 |
| 4 | 5.00E-02 | 78.38 | 183.7 | 29.5 | 44.9 |
| 5 | 5.00E-02 | 76.61 | 173.1 | 29.4 | 44.2 |
| 6 | 5.00E-02 | 76.14 | 181.0 | 29.4 | 44.1 |
| 7 | 5.00E-01 | 84.6 | 178.1 | 30.5 | 46.2 |
| 8 | 5.00E-01 | 85.49 | 174.9 | 32 | 40.9 |
| 9 | 5.00E-01 | 87.75 | 177.7 | 31.2 | 47.5 |
| 10 | 5.00E+00 | 93.97 | 177.1 | 34.3 | - |
| 11 | 5.00E+00 | 117.79 | 178.9 | 37.7 | - |
| 12 | 5.00E+00 | 110.74 | 175.5 | 35.1 | - |
| 13 | 1.50E+01 | 116.88 | 181.6 | 35.9 | - |
| 14 | 1.50E+01 | 108.52 | 181.0 | 35.3 | - |
| 15 | 1.50E+01 | 116.78 | 179.4 | 34.2 | - |

A full set of results from the characterization tests shown in Table B2 as presented in the report on the June 11, 2020, DOT-113 surrogate test with water [4].

# Appendix C.
# FEA and Test Results

For all results presented in this appendix, the acceleration data from the test and output from the FE model have been filtered using a CFC60 filter. Pre-test FEA was run at an initial speed of 17.3 mph and the initial pressure was parameterized at 0, 15, 25, 35, and 50 psig. Following the test, post-test FEA was run using the measured initial test conditions of 18.3 mph and 30 psig.

## C1. Pre-test FEA and Test Results

The appendix presents a limited set of pre-test FEA results. The GN2 behavior was described using three different modeling approaches, adiabatic, isothermal, and isobaric, as discussed in Section 6.1. The pre-test model used an outage volume of 5 percent; however, it should be noted that the outage was calculated as 9 percent immediately prior to the test using the static head pressure. The pre-test model tended to overpredict puncture because the model's outage was lower than the test's outage. Additional conservative modeling approaches (adiabatic and isothermal) were used in describing the GN2 behavior that also tended to overpredict puncture. Table 26 summarizes the pre-test FE model outcomes.

### *C1.1 Initial Pressure at 0 psig*

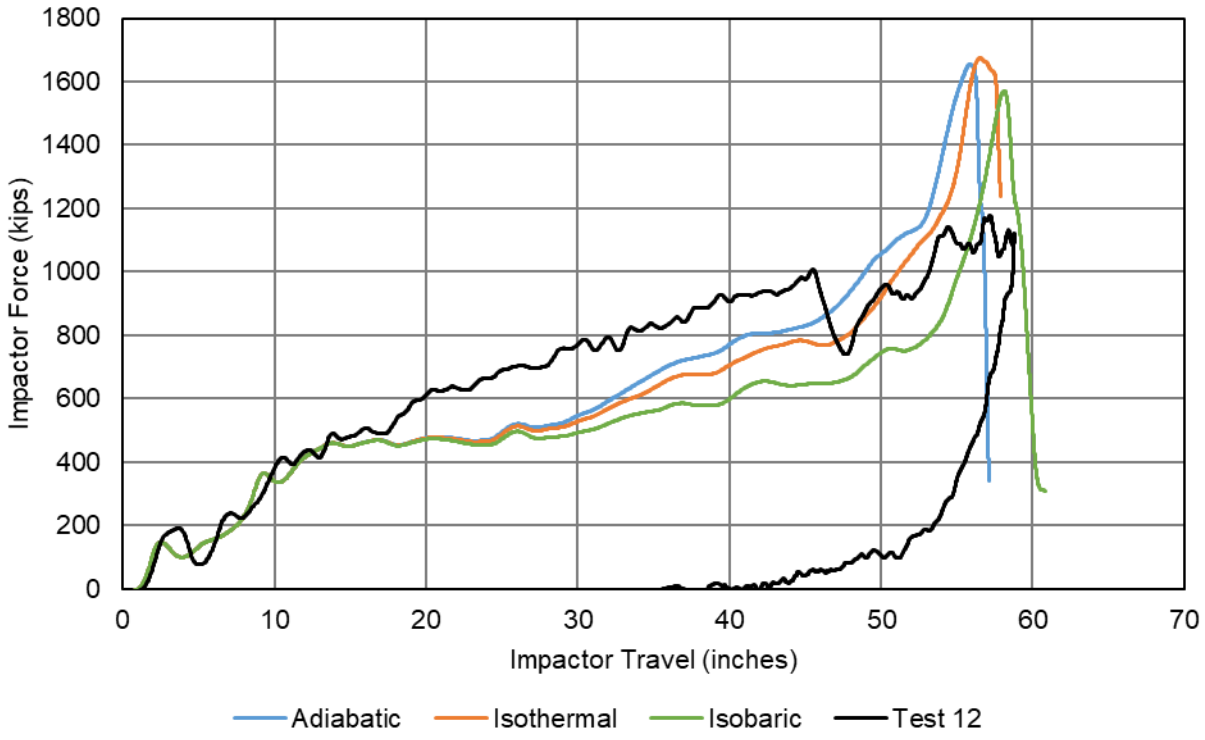


**Figure C1. Impactor Force vs. Displacement, Pre-test Model at 0 psig and 17.3 mph**

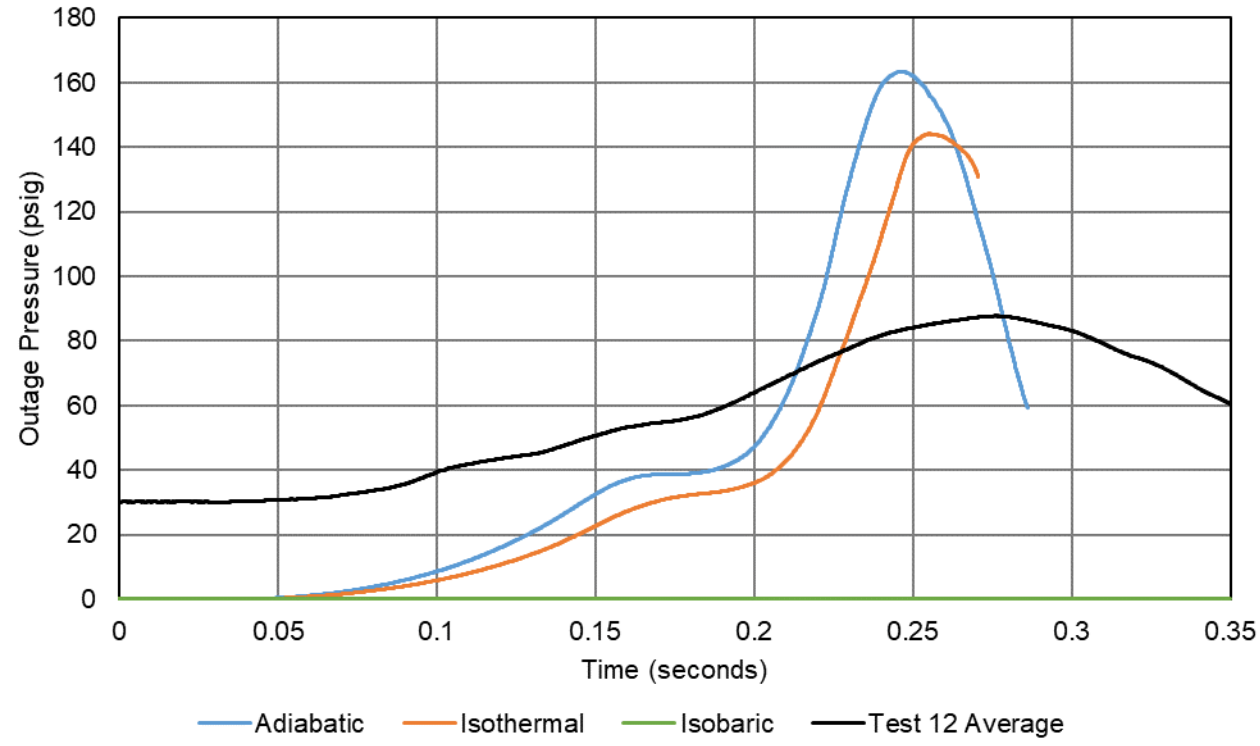


**Figure C2. Outage Pressure vs. Time, Pre-test Model at 0 psig and 17.3 mph**

### *C1.2 Initial Pressure at 15 psig*

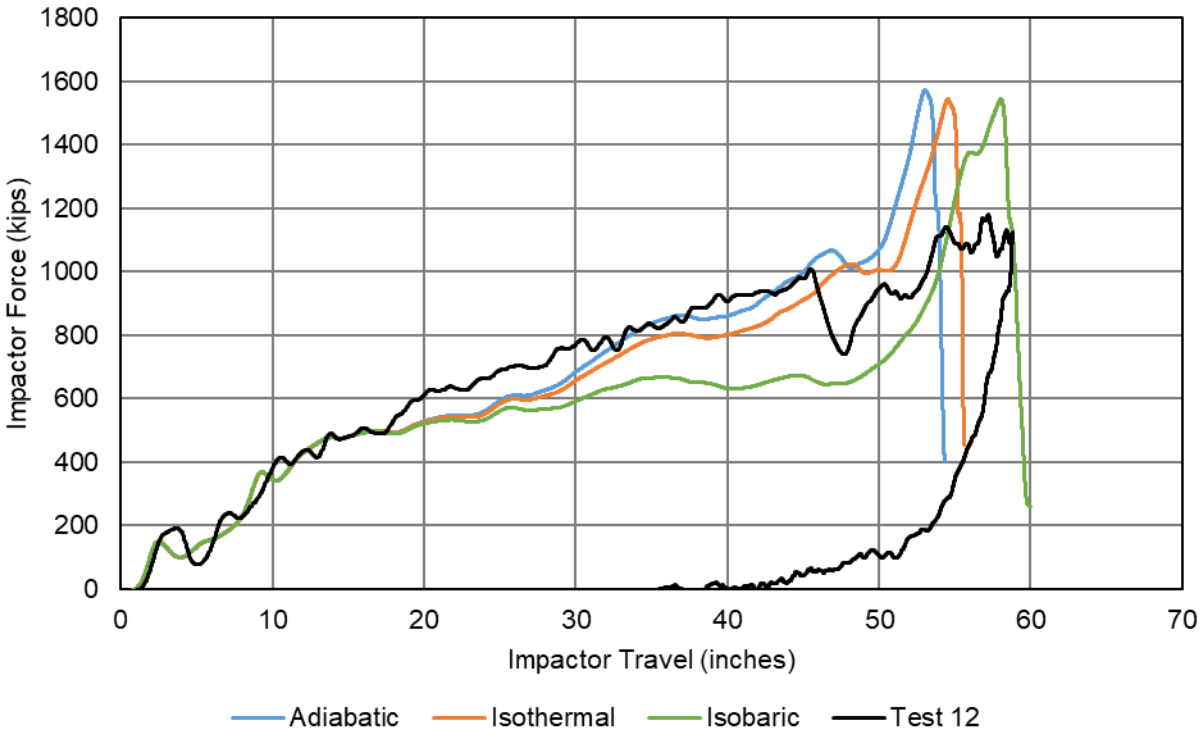


**Figure C3. Impactor Force vs. Displacement, Pre-test Model at 15 psig and 17.3 mph**

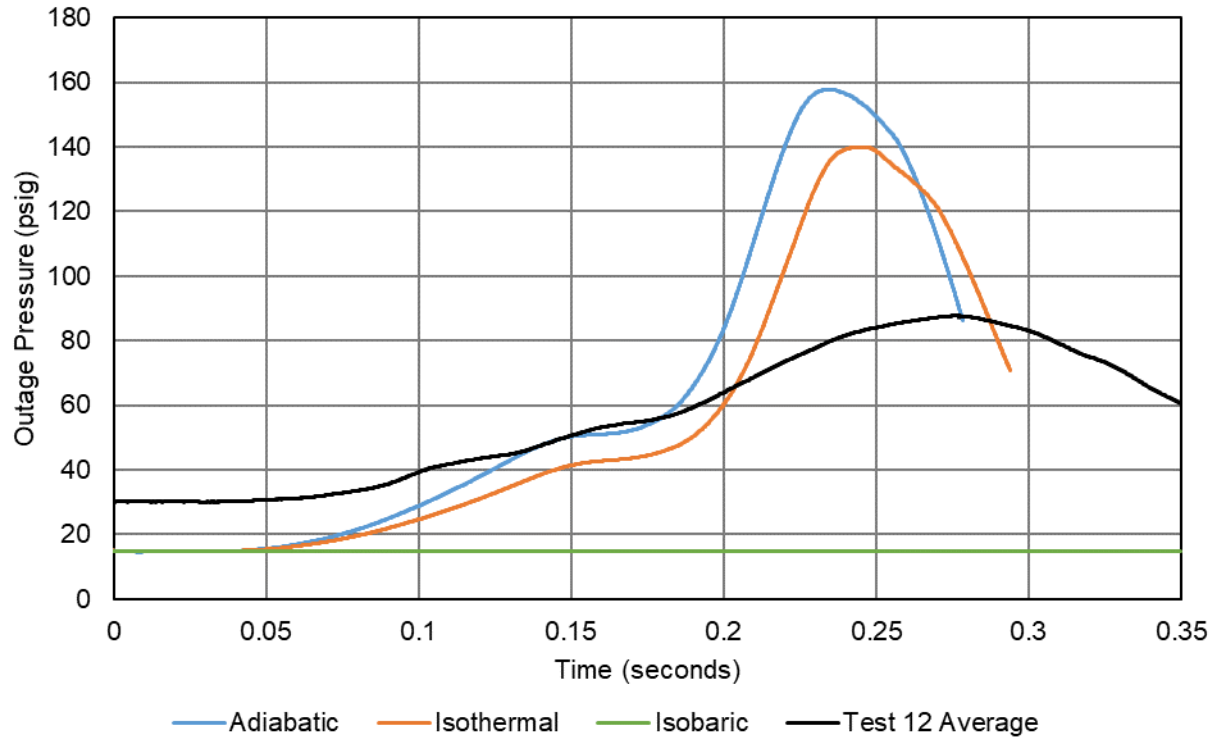


**Figure C4. Outage Pressure vs. Time, Pre-test Model at 15 psig and 17.3 mph**

### *C1.3 Initial Pressure at 25 psig*

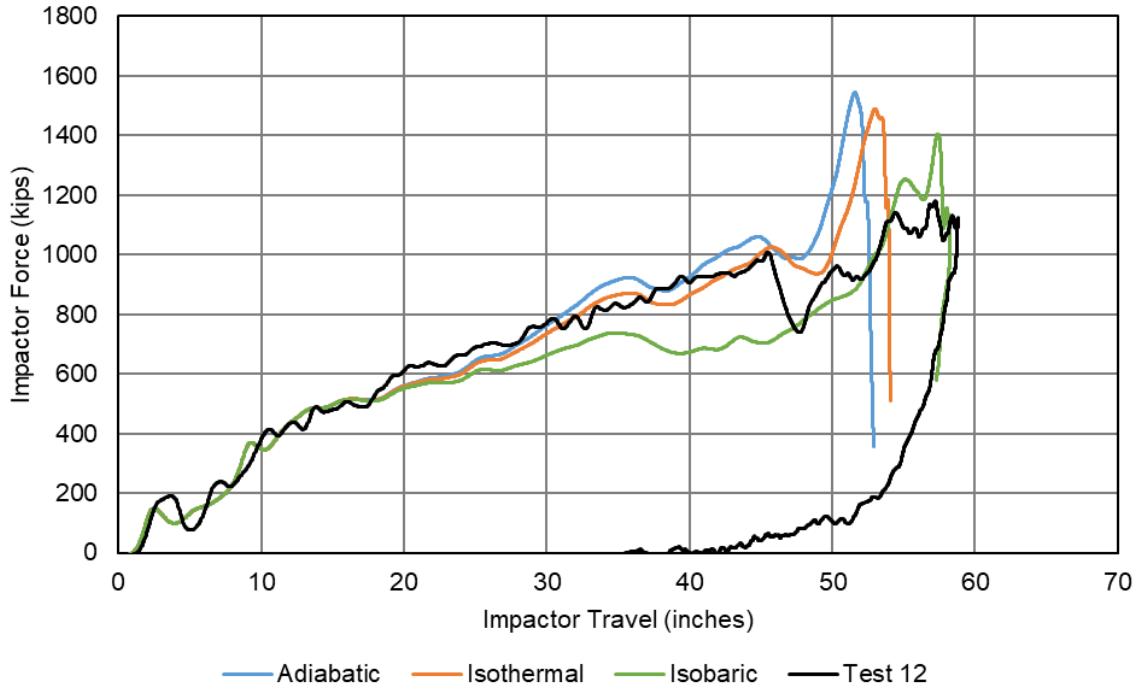


**Figure C5. Impactor Force vs. Displacement, Pre-test Model at 25 psig and 17.3 mph**

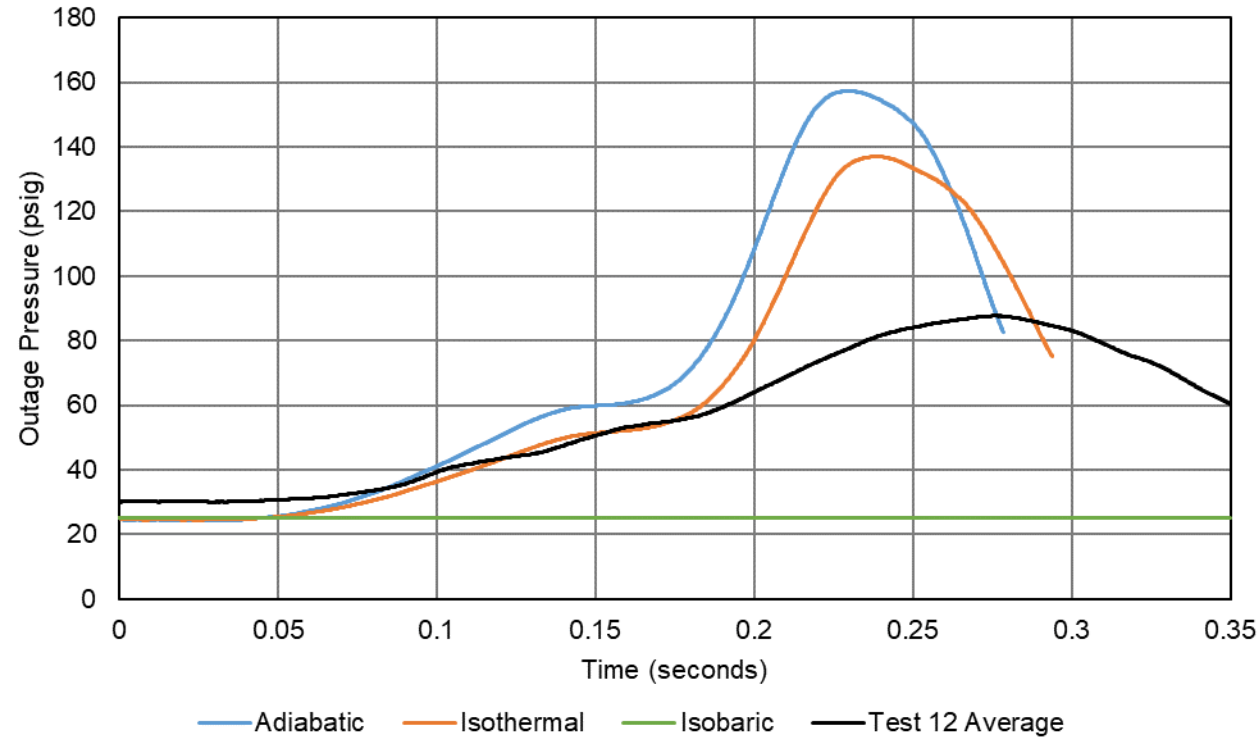


**Figure C6. Outage Pressure vs. Time, Pre-test Model at 25 psig and 17.3 mph**

### *C1.4 Initial Pressure at 35 psig*

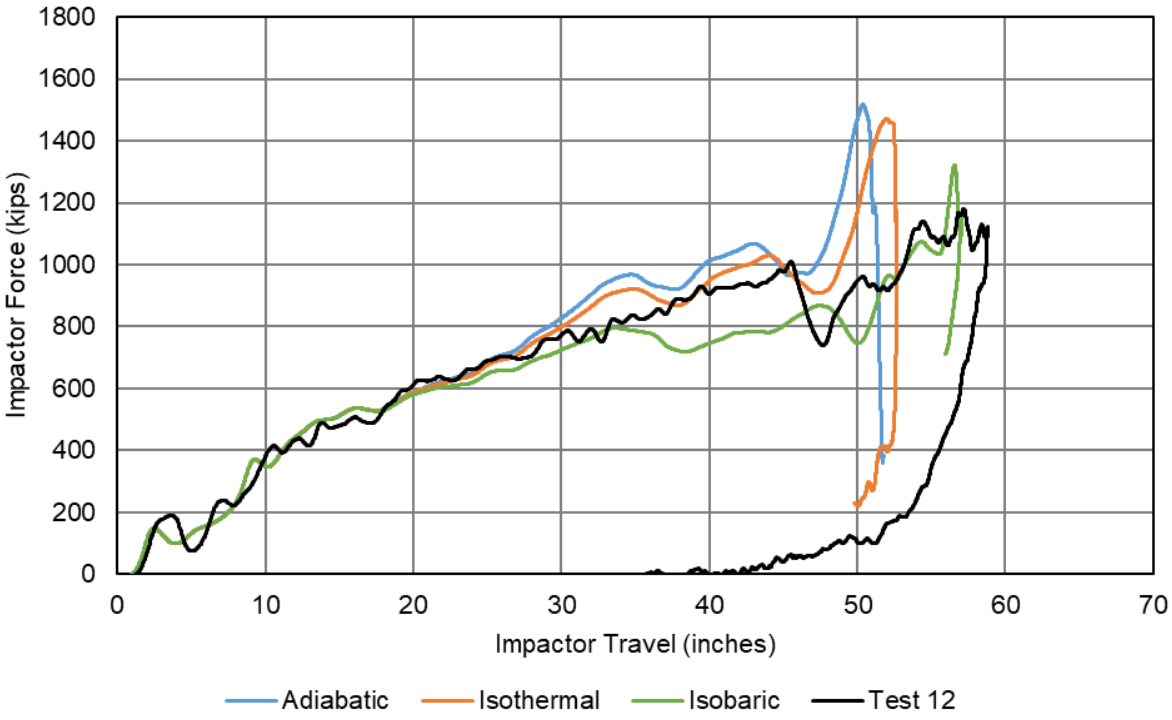


**Figure C7. Impactor Force vs. Displacement, Pre-test Model at 35 psig and 17.3 mph**

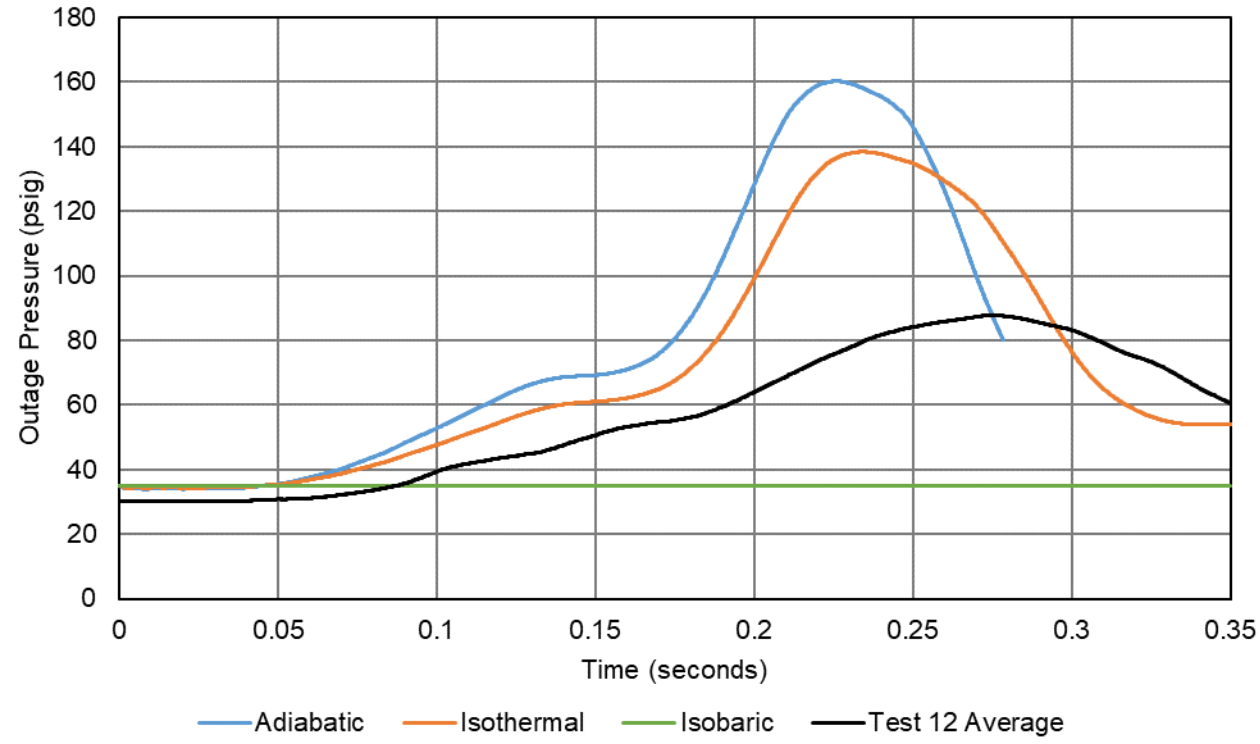


**Figure C8. Outage Pressure vs. Time, Pre-test Model at 35 psig and 17.3 mph**

### *C1.5 Initial Pressure at 50 psig*

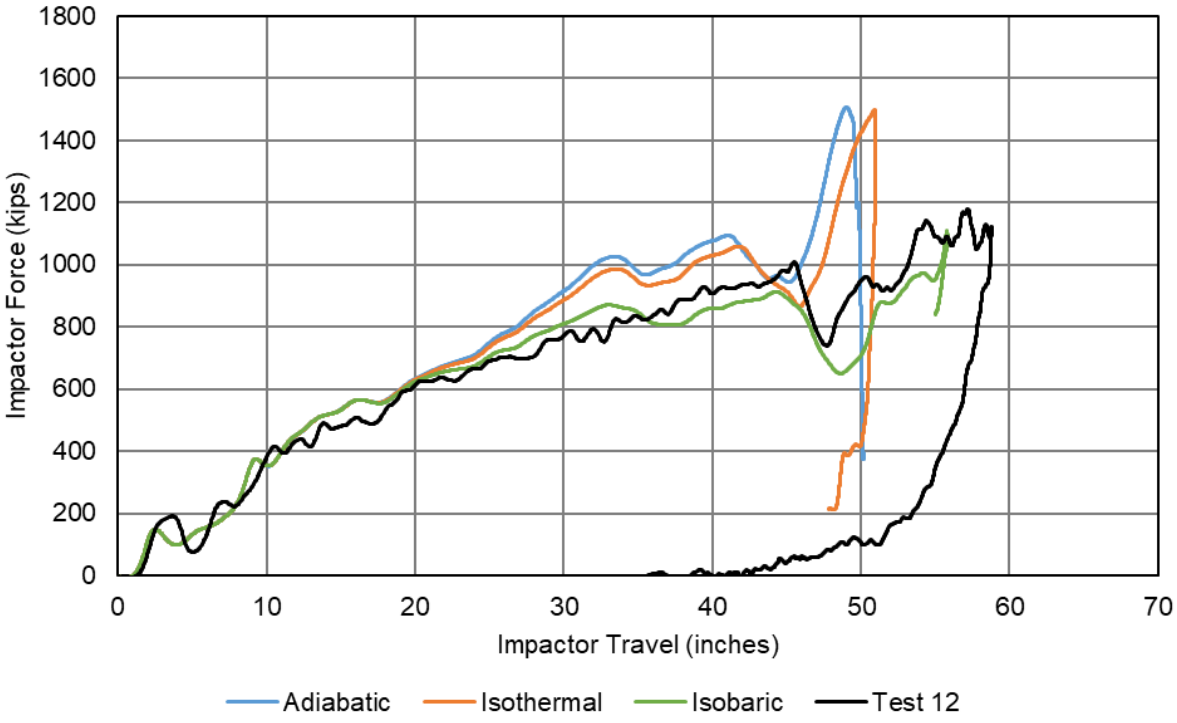


**Figure C9. Impactor Force vs. Displacement, Pre-test Model at 50 psig and 17.3 mph**

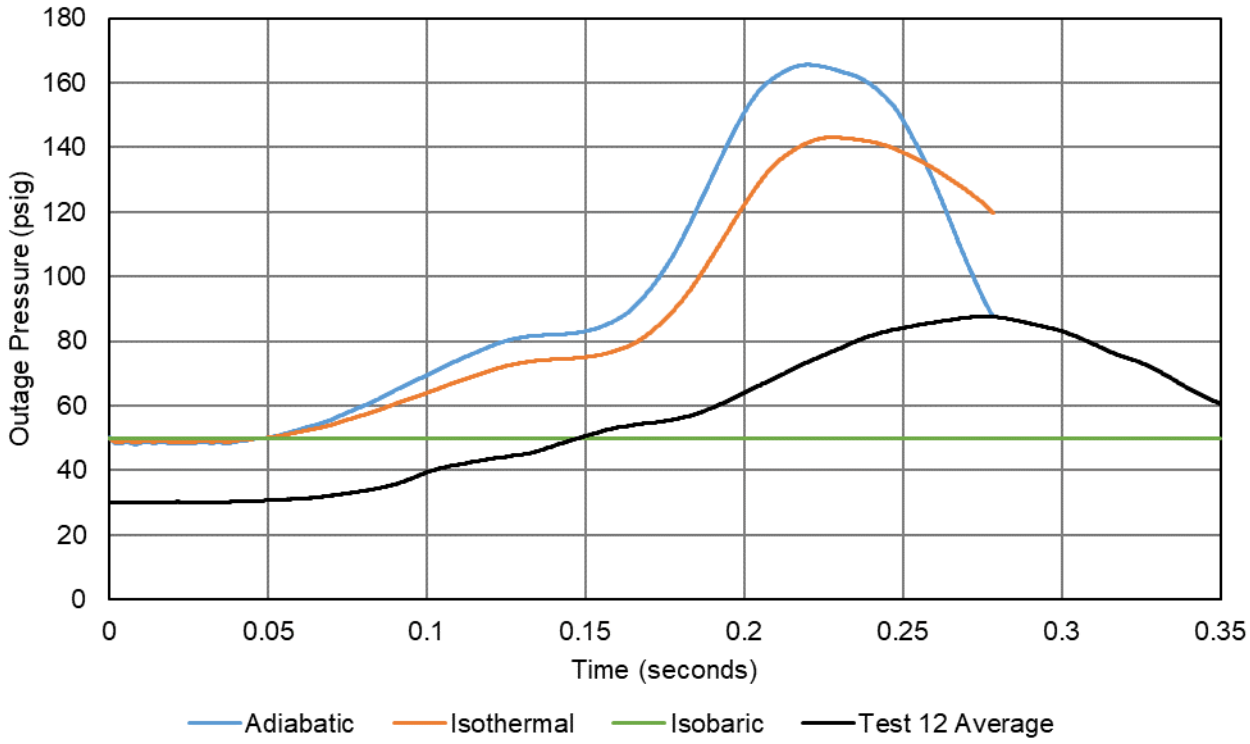


**Figure C10. Outage Pressure vs. Time, Pre-test Model at 50 psig and 17.3 mph**

## C2. Post-test FEA and Test Results

This appendix describes the post-test FE results presented in Section 6.2. The *isothermal* and *isobaric* models used the same approaches to represent the GN2 from the pre-test models. The *phase change 70 psia* model was calibrated after the test by modifying the *isothermal* model with a fluid exchange to represent the condensation of GN2 after reaching a pressure of 70 psia (57.7 psig). Some initial conditions were adjusted from the pre-test to post-test models as described in Section 5.3. Note that the *isothermal* model terminated at approximately 0.32 seconds after both tanks punctured, and the *isobaric* and *phase change 70 psia* models terminated normally after 0.4 seconds of simulation without puncturing. The post-test FE results are summarized in Table 27.

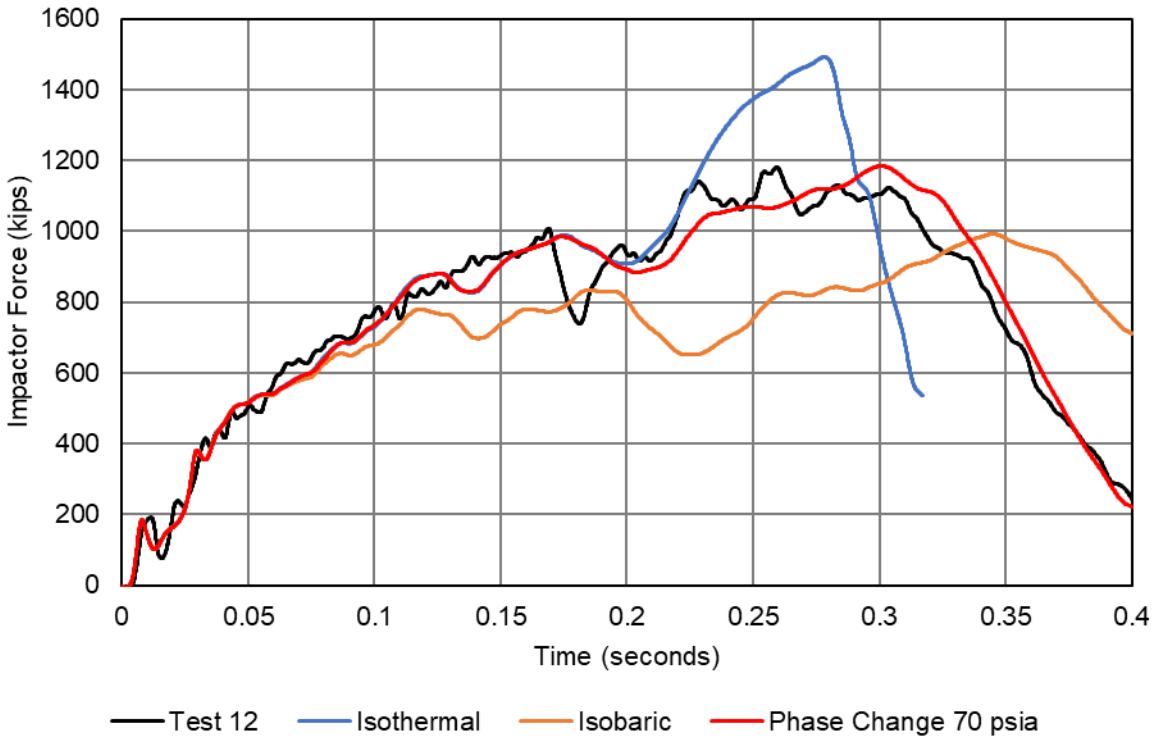


**Figure C11. Impactor Force vs. Time**

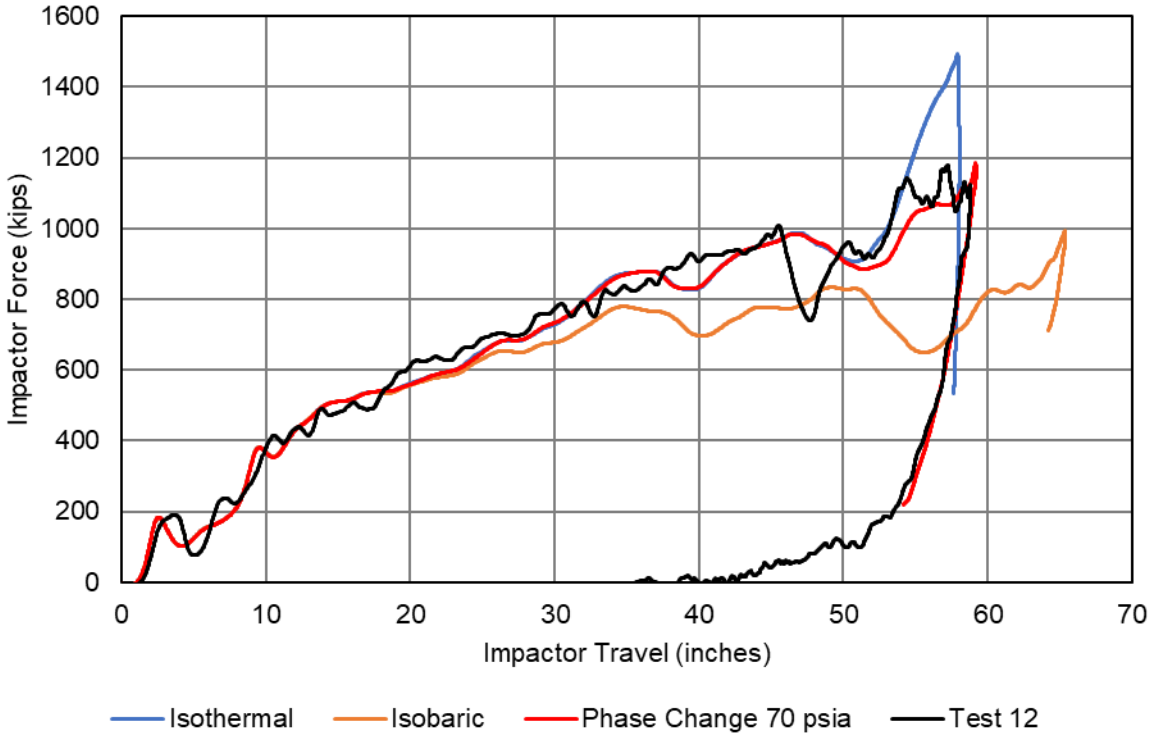


**Figure C12. Impactor Force vs. Travel**

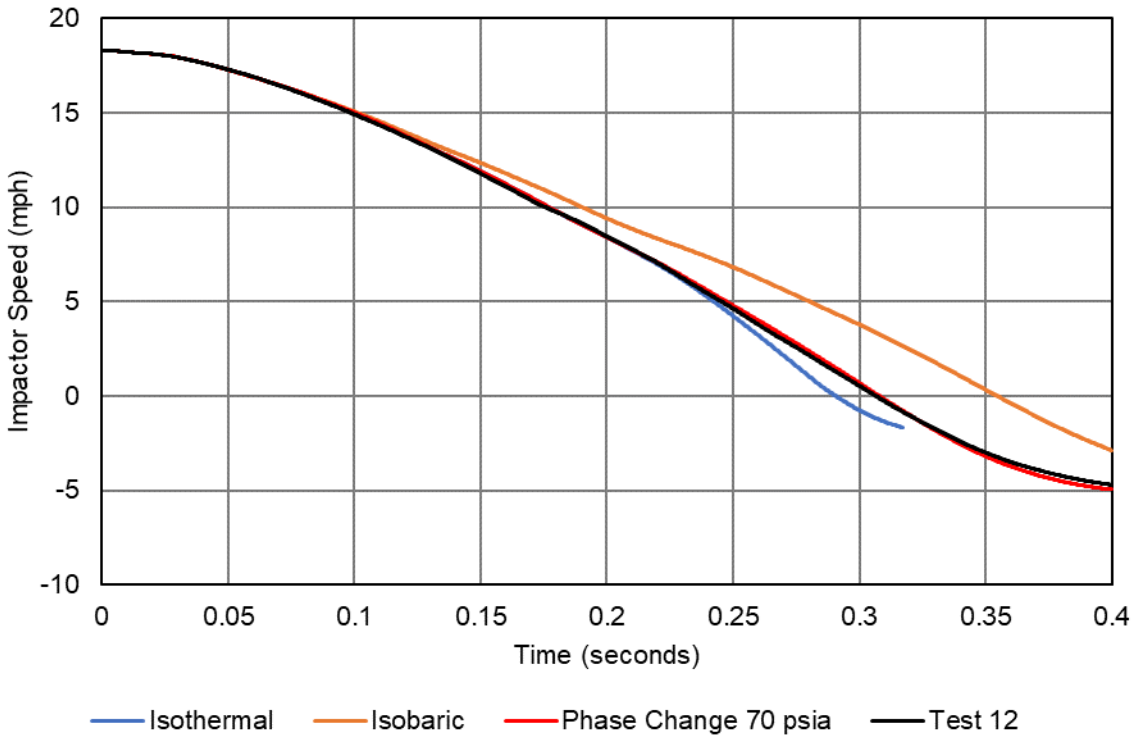


**Figure C13. Impactor Velocity vs. Time**

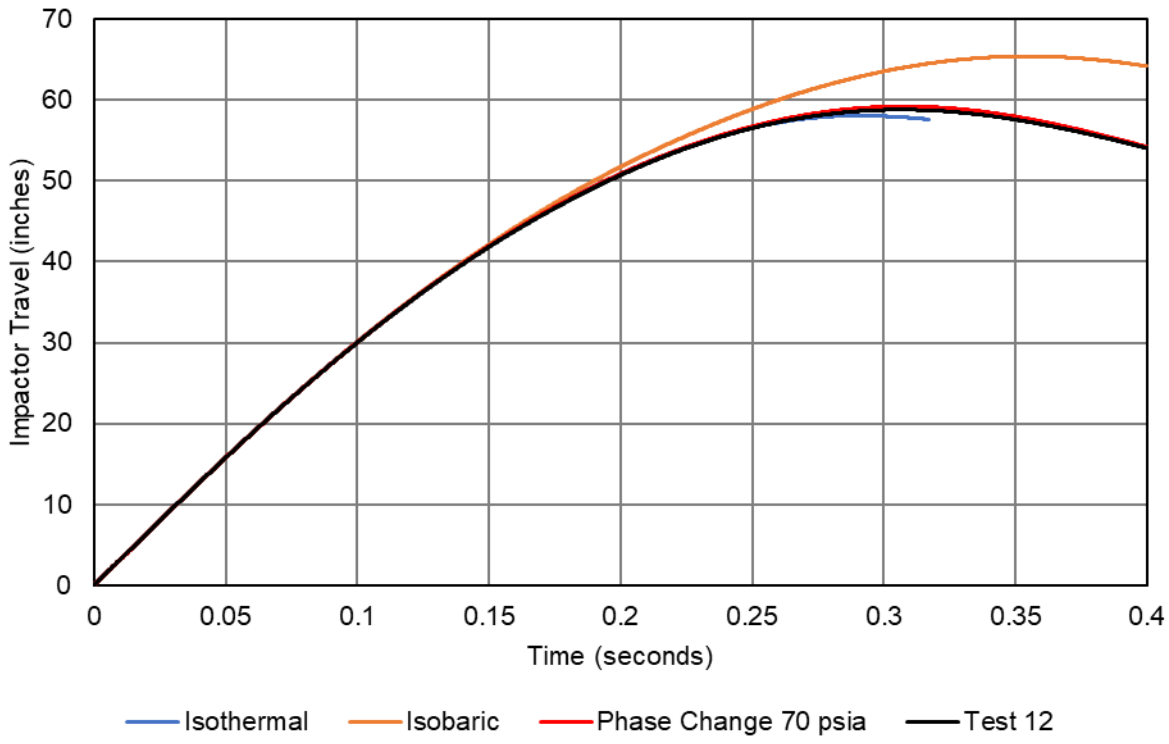


**Figure C14. Impactor Travel vs. Time**

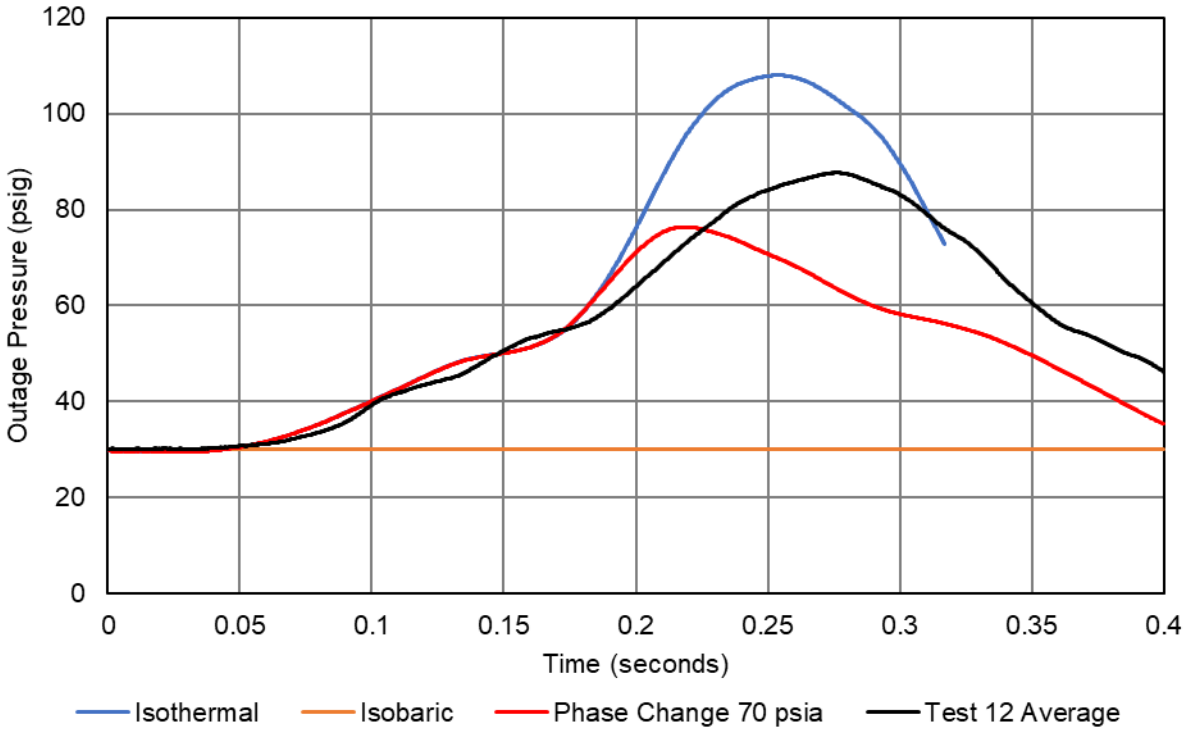


**Figure C15. Outage Pressure vs. Time**

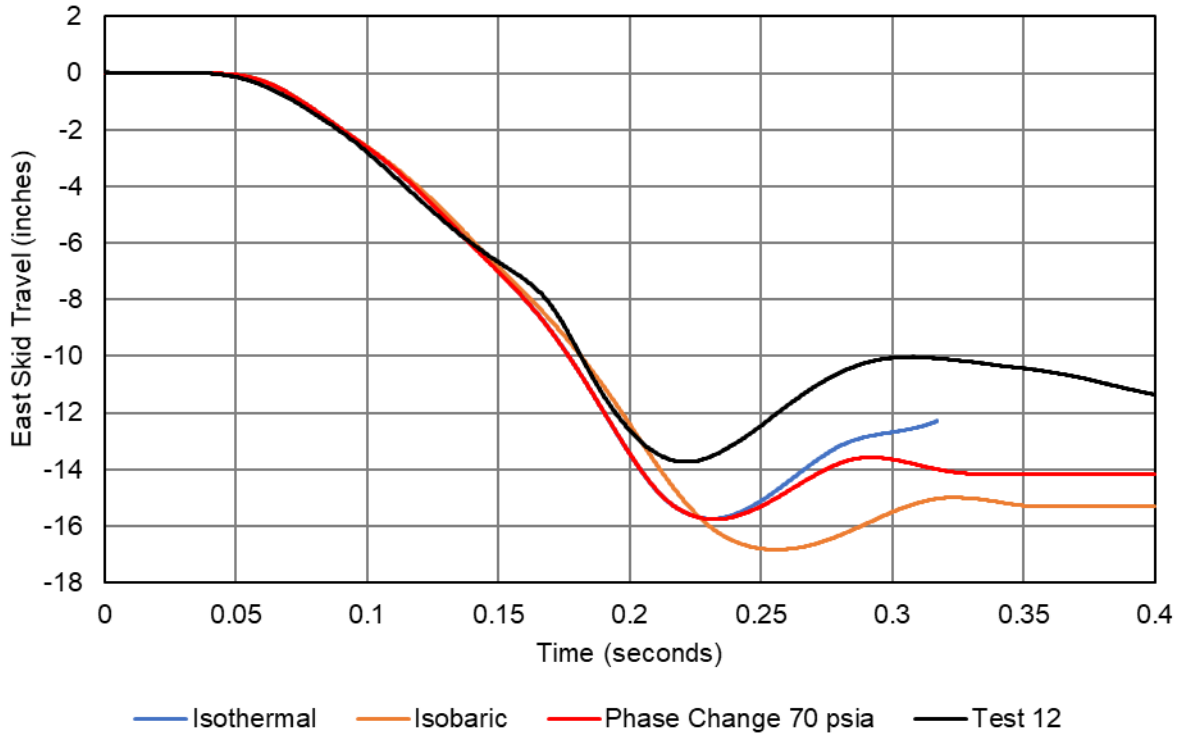


**Figure C16. East Skid Travel vs. Time**

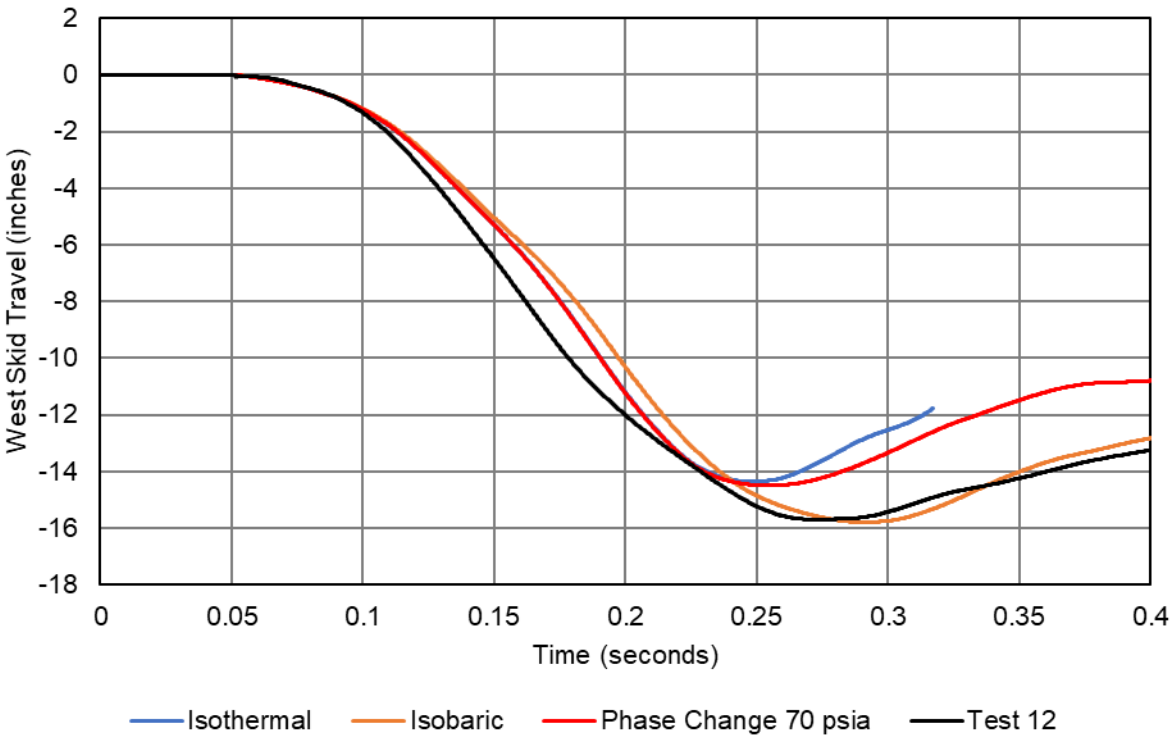


**Figure C17. West Skid Travel vs. Time**

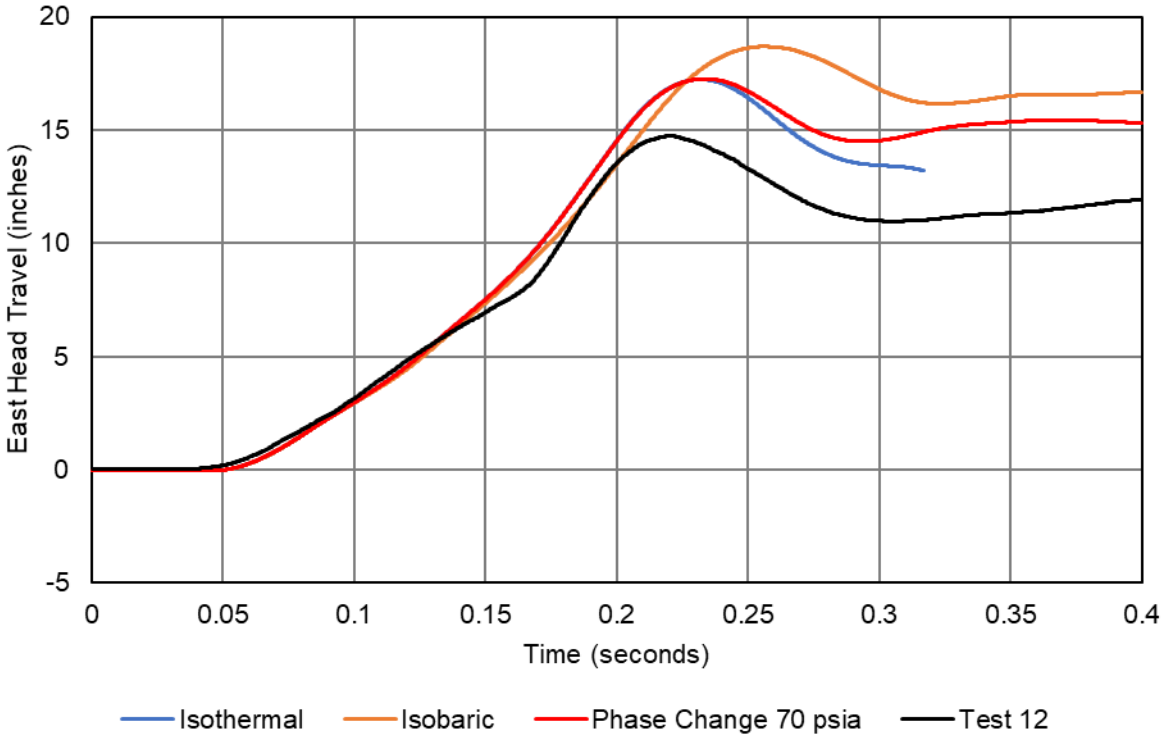


**Figure C18. East Head Travel vs. Time**

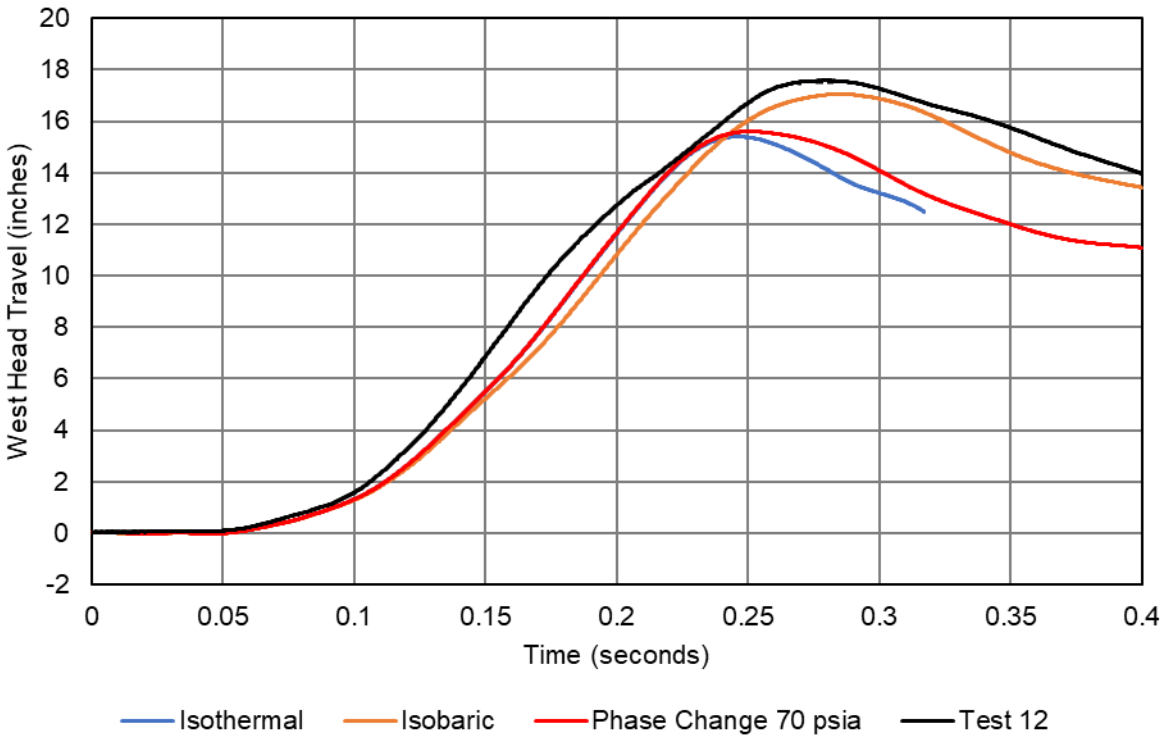


**Figure C19. West Head Travel vs. Time**

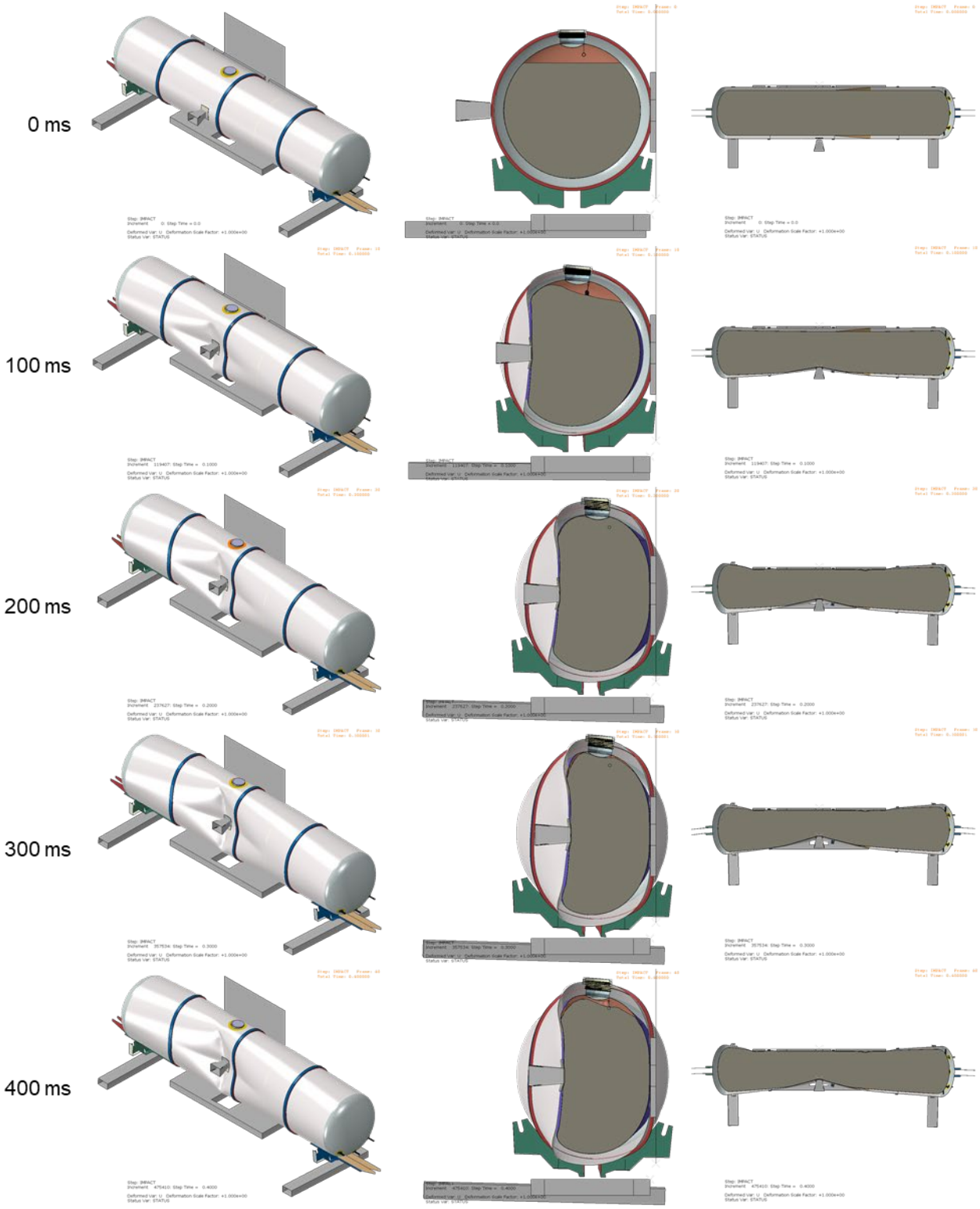


**Figure C20. Isometric (left), Side Section (middle), and Top Section (right) Views of Post-test FE Model (Phase Change 70 psia) Impact Sequence**

# Appendix D.
# Geometry in Pre-test and Post-test FE Models

This appendix contains a discussion of each of the parts that made up the assemblies for the pre- and post-test FE models. Rigid parts were used when it was important to include a part for its inertia or for its interaction through contact, but where the deformation of the part could be neglected in the calculations. Four parts were modeled as rigid bodies. The remaining bodies were modeled as deformable bodies. A summary of the element types used to mesh the model assembly is provided in Table D1.

**Table D1. Summary of Element Types [24]**

| Element Designation | Description |
|---|---|
| C3D8 | 8-node linear brick element, fully integrated |
| C3D8R | 8-node linear brick element, reduced integration |
| CONN3D2 | Connector element between two nodes or ground and a node |
| DCOUP3D | Three-dimensional distributing coupling element |
| M3D3 | 3-node triangular membrane element |
| M3D4R | 4-node quadrilateral membrane element (reduced integration) |
| MASS | Point mass |
| R3D3 | 3-dimensional, 3-node triangular facet rigid element |
| R3D4 | 3-dimensional, 4-node bilinear quadrilateral rigid element |
| RNODE3D | 3-dimensional reference node |
| S3R | 3-node triangular general-purpose shell, finite membrane strains (identical to element S3) |
| S4R | 4-node general-purpose shell, reduced integration with hourglass control, finite membrane strains |
| SPRINGA | Axial spring between two nodes, whose line of action is the line joining the two nodes. This line of action may rotate in large-displacement analysis. |

## D1. Rigid Impactor

The impactor was modeled as a rigid body in the DOT-113 FE models. The geometry was a 12-inch by 12-inch square impactor with 1-inch radii edges around the impact face. The geometry included the impact face, the tapered cone back to the portion of the impactor where the impactor attached to the ram car, and a representation of the ram arm and width of the ram car's body. The impactor is shown in Figure D1 for the pre- and post-test model, and the mesh is summarized in Table D2.

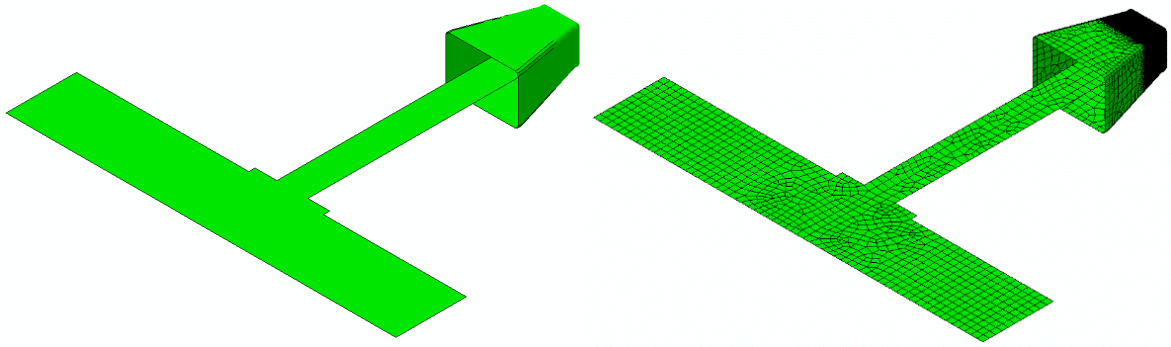

**Figure D1. Impactor Geometry (left) and Mesh (right)**

**Table D2. Properties of Impactor Mesh**

| Property | Pre-test and Post-test Models |
|---|---|
| Type of Part | Rigid |
| Number of Elements | R3D4: 78,468<br>R3D3: 438<br>RNODE3D: 6<br>MASS: 1 |
| Approximate Mesh Size | 0.081–2 inches |
| Approximate Part Weight | 297,200 lbf |

## D2. Rigid Wall

The impact wall was modeled as a rigid body. Because the wall was constrained against motion in any direction, no mass needed to be defined for this part. The wall's geometry and mesh are shown in Figure D2 for the pre- and post-test model, and the properties are summarized in Table D3. Note that the pre-test model used the Test 11 post-test rigid wall geometry [4], which did not have cutouts positioned for the Test 12 DOT-113 surrogate's stiffener channels, so contact exclusions were assigned to those stiffeners.

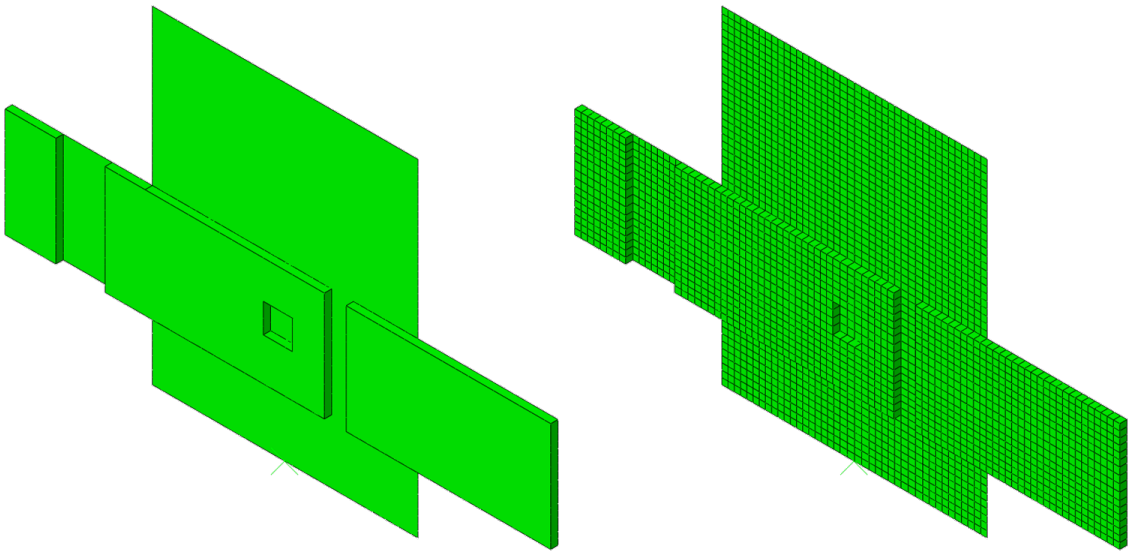

**Figure D2. Rigid Wall Geometry (left) and Mesh (right)**

**Table D3. Properties of Rigid Wall Mesh**

| Property | Pre-test Model | Post-test Model |
|---|---|---|
| Type of Part | Rigid | Rigid |
| Number of Elements | R3D4: 1,658<br>RNODE3D: 9 | R3D4: 3,122<br>RNODE3D: 8 |
| Approximate Mesh Size | 5 inches | 3.5 inches |

## D3. Rigid Skid

The bolster of the car rested directly upon a set of skids, which themselves rested upon steel plates (see Figure 4). The skids were designed to inhibit roll of the tank car following rebound from the rigid wall during a test and were introduced early in the shell impact test series. The skid geometry and mesh are shown in Figure D3, and the mesh properties are summarized in Table D4.

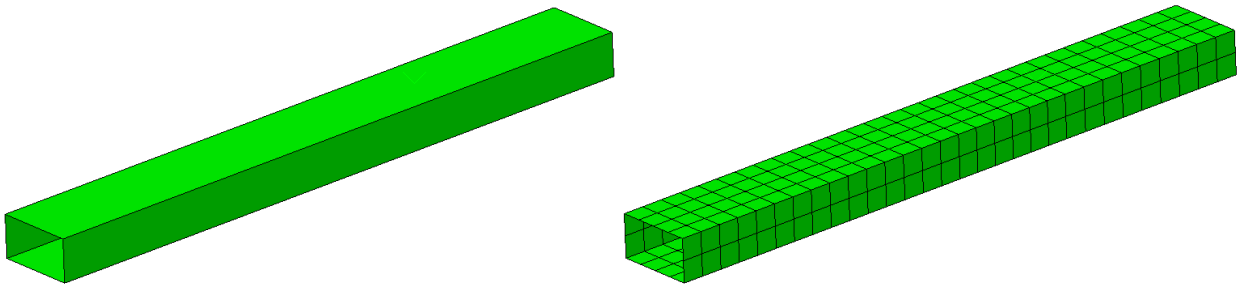

**Figure D3. Skid Geometry (left) and Mesh (right)**

**Table D4. Properties of Skid Mesh**

| Property | Pre-test and Post-test Models |
|---|---|
| Type of Part | Rigid |
| Number of Elements | R3D4: 368<br>MASS: 1<br>RNODE3D: 1 |
| Approximate Mesh Size | 6 inches |

The rigid skids used in the test weighed approximately 3,500 pounds each. This mass was included in the model using a point mass at the rigid body reference node of each skid. In previous models the mass of each bolster and stub sill was lumped into the corresponding skid; however, the skids in this model did not account for the masses of the bolsters and stub sills because they were modeled with deformable shell elements (see Appendix D9). The masses on each skid are summarized in Table D5.

**Table D5. Point Masses Added to Skid Reference Point in Models**

| Component | Approximate Weight |
|---|---|
| Skid | 3,500 lbf |

## D4. Rigid Ground

For both the pre-test and post-test models, the rigid ground was modeled with all six degrees-of-freedom (DOF) fixed. Figure D4 shows the rigid ground, and Table D6 summarizes the mesh properties.

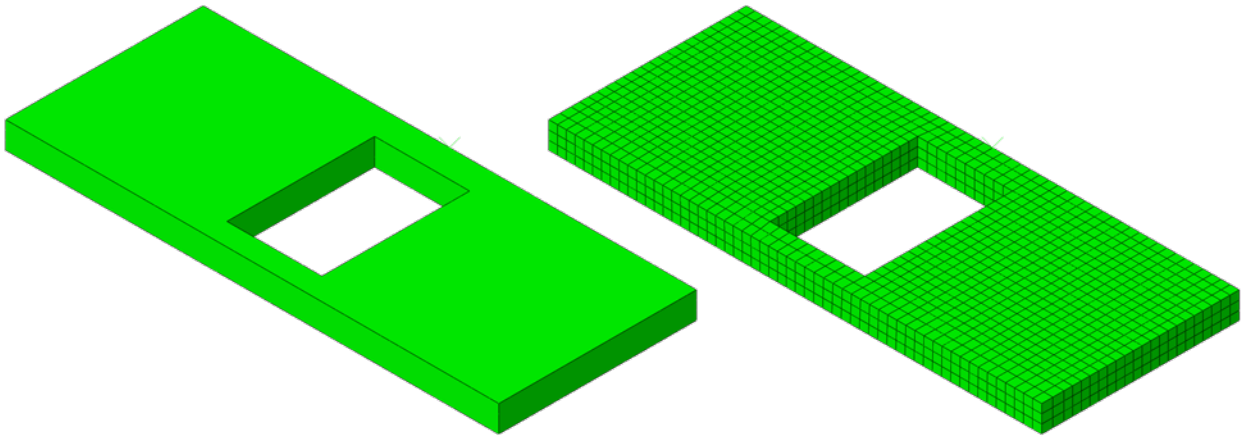

**Figure D1. Rigid Ground Geometry (left) and Mesh (right)**

**Table D6. Properties of Rigid Ground Mesh**

| Property | Pre-test and Post-test Models |
|---|---|
| Type of Part | Rigid Body |
| Number of Elements | R3D4: 1,664<br>RNODE3D: 9 |
| Approximate Mesh Size | 4 inches |

## D5. Inner Tank – Shell Elements

The inner tank was modeled using two different techniques. In the impact zone, the inner tank was modeled using solid "brick" elements. This part is described in Appendix D6. Away from the impact zone, the inner tank was modeled using shell elements. The shell portion of the tank is described in this section.

Figure D5 shows the shell portion of the inner tank, and Table D7 summarizes the mesh properties. This part was globally meshed using quadrilateral reduced integration (S4R) elements and a small number of triangular shell elements (S3R). At the edges of the impact zone, the mesh was refined (0.1 inches) to provide a transition between the fine solid mesh of the impact zone and the coarse shell mesh of the distant tank. A technique referred to as shell-to-solid coupling (SSC) was used to attach the solid patch to the edges of the shell mesh on the tank. The shell part of the tank represents the midplane surface of the tank.

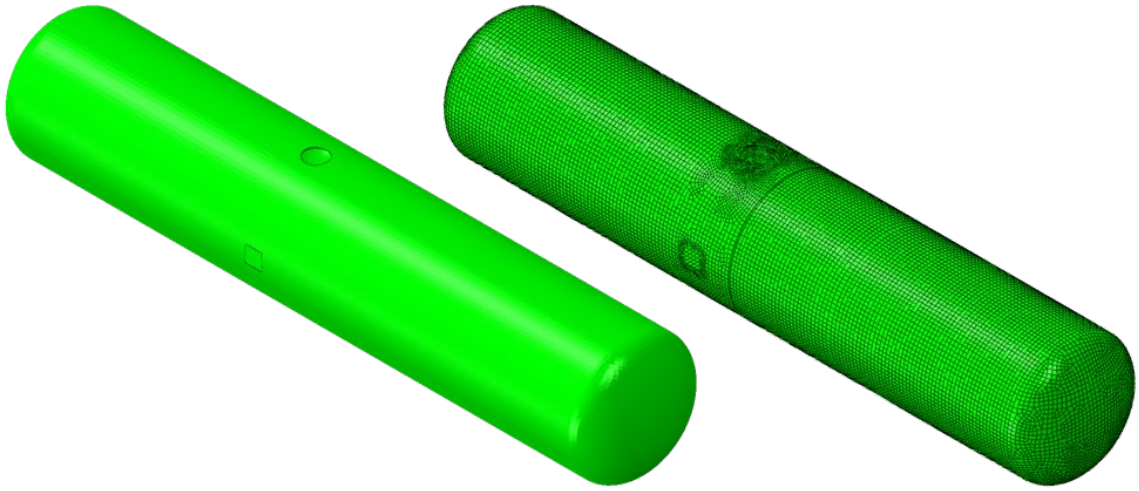

**Figure D5. Inner Tank Shell Geometry (left) and Mesh (right)**

**Table D7. Properties of Inner Tank Shell Mesh**

| Property | Pre-test and Post-test Models |
|---|---|
| Type of Part | Deformable, Shell |
| Number of Elements | S4R: 28,537<br>S3R: 354 |
| Approximate Mesh Size | 0.1–3 inches |
| Material | T304 Stainless Steel |
| Shell Thickness | 0.25 inches |
| Head Thickness | 0.25 inches |
| Approximate Part Weight | 12,500 lbf |

## D6. Inner Tank – Solid Elements

The inner tank was modeled using two different techniques. Away from the impact zone, the inner tank was modeled using shell elements. This part is described in Appendix D5. In the impact zone, the inner tank was modeled using solid "brick" elements. This part is described in this section.

Figure D6 shows the solid portion of the tank, and Table D8 summarizes the mesh properties. Note that because of the fine mesh, the right-hand image appears to show the mesh as a solid-colored part. The part was meshed using 5 elements through the thickness of the part. This corresponded to a global mesh seed of 0.05 inches. The mesh consisted of 8-noded reduced integration hexahedral "brick" (C3D8R) elements. The solid tank mesh was attached to the shell tank mesh along the outer and inner edges using SSC. The elements along the inner and outer edges of the solid tank that were involved in the SSC were given the same elastic and plastic material responses as the rest of the solid patch, but did not have failure behaviors defined. This was done to prevent elements involved in the SSC coupling from being removed from the model, as that could cause the coupling itself to fail and the simulation to terminate.

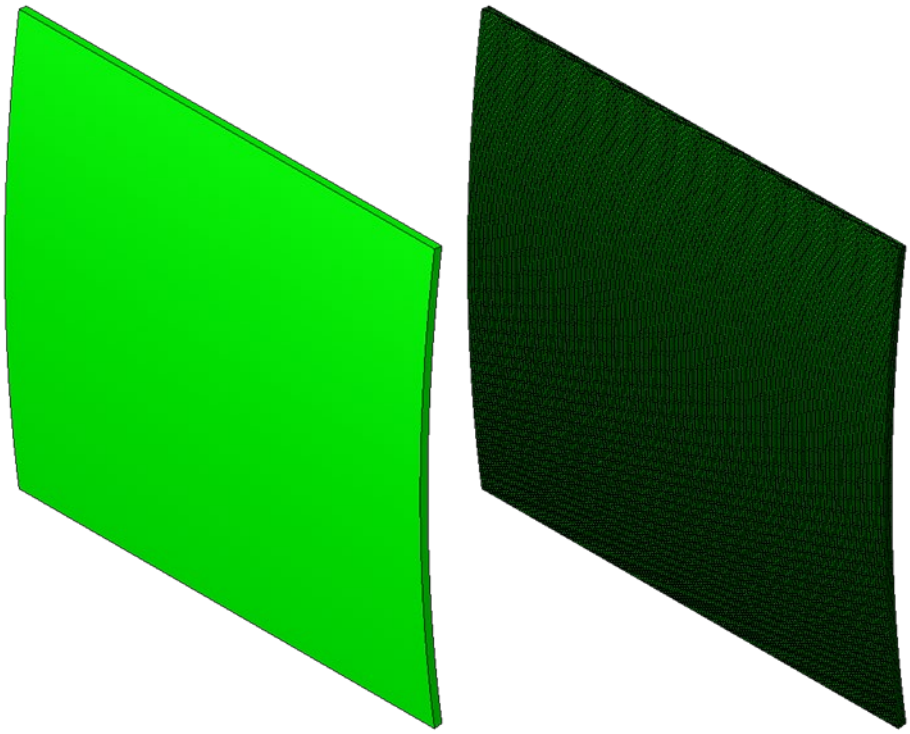

**Figure D6. Inner Tank Solid Geometry (left) and Mesh (right)**

**Table D8. Properties of Inner Tank Solid Mesh in FE Models**

| Property | Pre-test and Post-test Models |
|---|---|
| Type of Part | Deformable, Solid |
| Number of Elements | C3D8R: 392,000 |
| Approximate Mesh Size | 0.05 inches |
| Material | T304 Stainless Steel |
| Thickness | 0.25 inches |
| Approximate Part Weight | 14 lbf |

## D7. Outer Tank – Shell Elements

The outer tank was modeled using two different techniques. In the impact zone, the outer tank was modeled using solid "brick" elements. This part is described in Appendix D8. Away from the impact zone, the outer tank was modeled using shell elements. The shell portion of the tank is described in this section.

Figure D7 shows the shell portion of the outer tank from the pre- and post-test model, and Table D9 summarizes the mesh properties. The part includes the stiffener channels, support structure for the inner tank, manway, and connections for piping on the head (right side). This part was globally meshed using 3-inch quadrilateral reduced integration (S4R) elements and a small

number of triangular shell elements (S3R). At the edges of the impact zone, the mesh was refined to 0.17 inches to provide a transition between the fine solid mesh of the impact zone and the coarse shell mesh of the distant tank. The mesh was also refined near the manway and piping connections to 0.5 inches. While most of the outer tank was 0.608-inch thick TC-128 carbon steel, the support structure, manway, and piping connections were composed of various thicknesses of T304 stainless steel. The shell part of the tank represents the midplane surface of the tank.

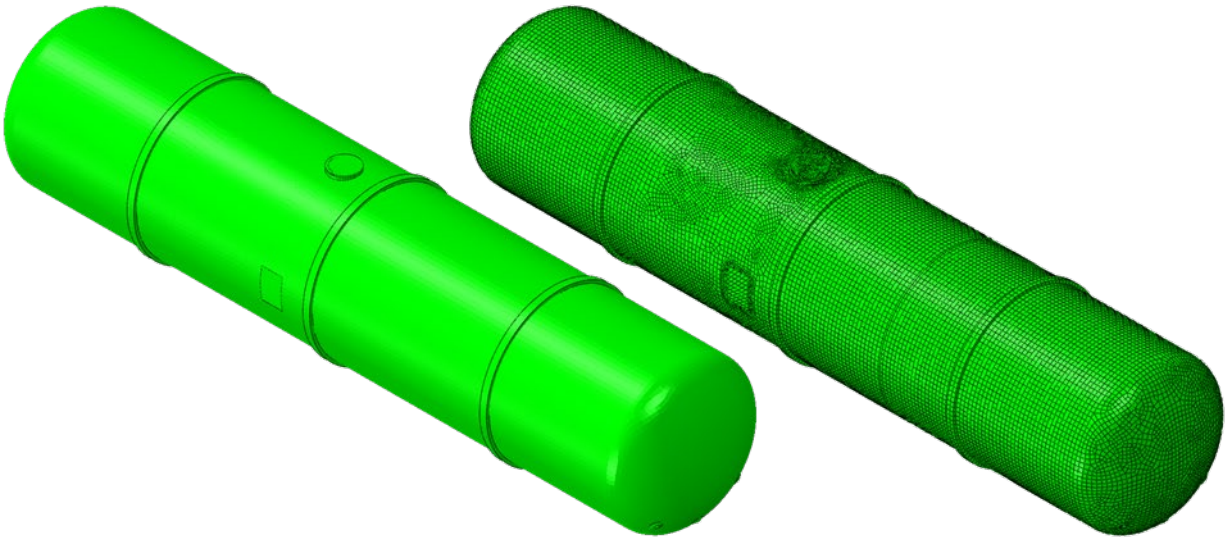

**Figure D7. Outer Tank Shell Geometry (left) and Mesh (right)**

**Table D9. Properties of Outer Tank Shell Mesh in FE Models**

| Property | Pre-test and Post-test Models |
|---|---|
| Type of Part | Deformable, Shell |
| Number of Elements | S4R: 49,946<br>S3R: 457 |
| Approximate Mesh Size | 0.17–3 inches |
| Materials | TC-128 Carbon Steel<br>T304 Stainless Steel |
| Shell Thickness | 0.608 inches |
| Head Thickness | 0.608 inches |
| Approximate Part Weight | 40,000 lbf |

## D8. Outer Tank – Solid Elements

The outer tank was modeled using two different techniques. Away from the impact zone, the outer tank was modeled using shell elements. This part is described in Appendix D7. In the impact zone, the outer tank was modeled using solid "brick" elements. This part is described in this section.

Figure D8 shows the solid portion of the outer tank, and Table D10 summarizes the mesh properties. Note that because of the fine mesh, the right-hand image appears to show the mesh as a solid-colored part. The outer tank solid patch was meshed using 7 elements through the thickness. This corresponded to a global mesh seed of 0.081 inches. The solid portion of the tank was meshed using C3D8R elements. The solid tank mesh was attached to the shell tank mesh along the outer and inner edges using SSC. The elements along the inner and outer edges of the solid tank that were involved in the SSC were given the same elastic and plastic material responses as the rest of the solid patch, but did not have failure behaviors defined. This was done to prevent elements involved in the SSC from being removed from the model, as that could cause the coupling itself to fail and the simulation to terminate.

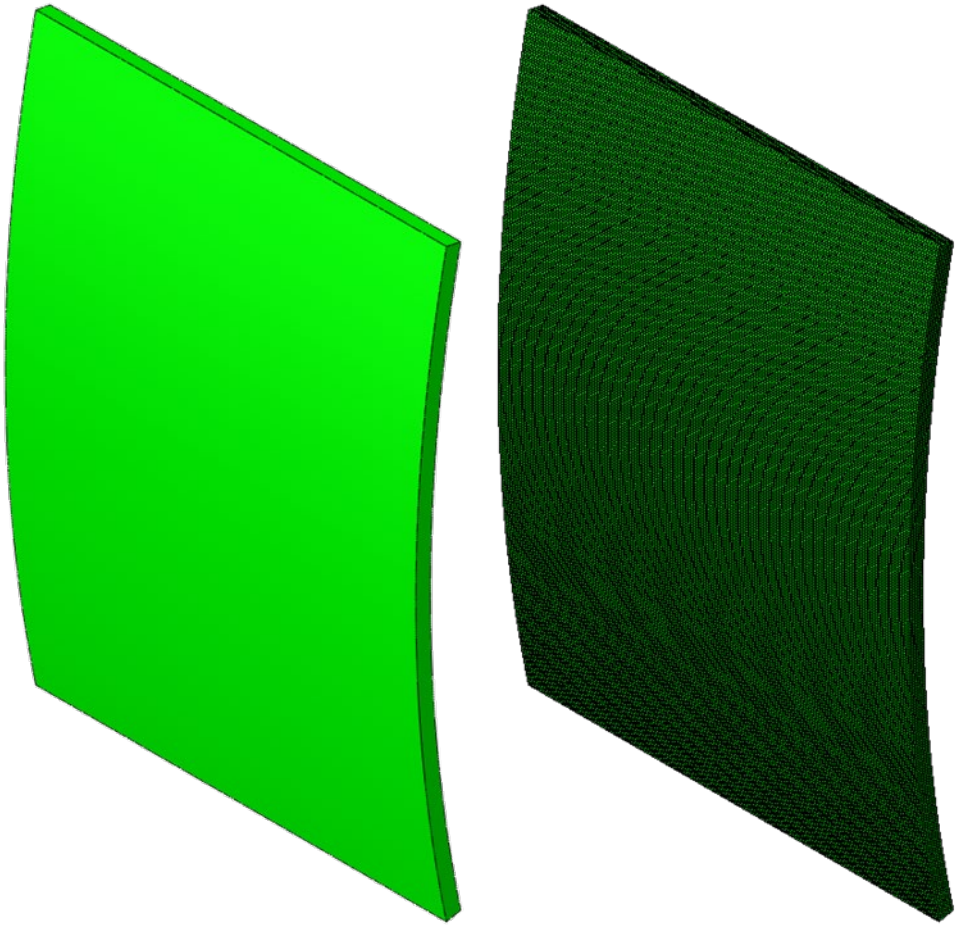

**Figure D8. Outer Tank Solid Geometry (left) and Mesh (right)**

**Table D10. Properties of Outer Tank Solid Mesh in FE Models**

| Property | Pre-test and Post-test Models |
|---|---|
| Type of Part | Deformable, Solid |
| Number of Elements | C3D8R: 384,160 |
| Approximate Mesh Size | 0.087 inches |
| Material | TC-128 Carbon Steel |
| Thickness | 0.608 inches |
| Approximate Part Weight | 71 lbf |

## D9. Bolster and Stub Sill

The A-end and B-end bolster and stub sill of the DOT-113 surrogate were represented with the same part mirrored across the center of the tank car. Figure D9 shows the bolster and stub sill part, and Table D11 summarizes the mesh properties. The bolster and stub sill were tied to the outer tank shell through tied constraints along the approximate weld locations.

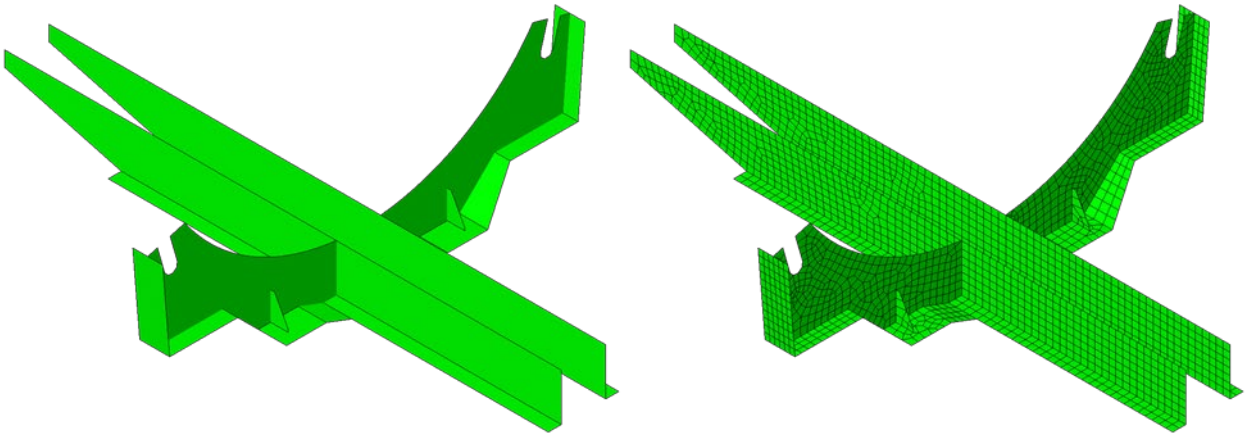

**Figure D9. Bolster and Stub Sill Geometry (left) and Mesh (right)**

**Table D11. Properties of Bolster and Stub Sill Mesh**

| Property | Pre-test and Post-test Models |
|---|---|
| Type of Part | Deformable, Shell |
| Number of Elements | S4R: 2,448<br>S3R: 30 |
| Approximate Mesh Size | 3 inches |
| Material | TC-128 Carbon Steel |
| Approximate Part Weight | 1,500 lbf |

## D10. Lading

The LN2 lading inside the inner tank was modeled as a Lagrangian EOS solid with fully integrated 3-inch "brick" elements. Figure D10 shows the lading part with a 9 percent outage from the post-test model, and Table D12 summarizes the mesh properties. A deformable solid representation of the lading was used in the FE model of the DOT-113 surrogate with LN2 while a less computationally-intensive hydraulic cavity representation was used in the previous DOT-113 FE models because the lower outage of LN2 was expected to result in more dynamic sloshing forces [3, 4].

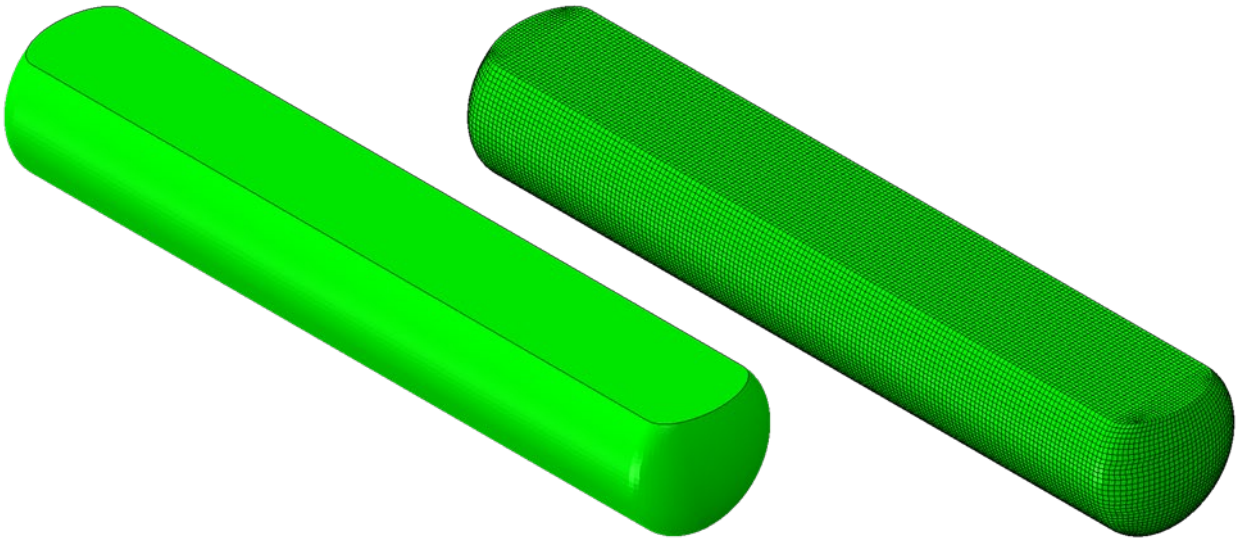

**Figure D10. Lading Geometry (left) and Mesh (right) Post-test**

**Table D12. Properties of Lading Mesh**

| Property | Pre-test Model | Post-test Model |
|---|---|---|
| Type of Part | Deformable, Solid | Deformable, Solid |
| Number of Elements | C3D8: 148,232 | C3D8: 134,448 |
| Approximate Mesh Size | 3 inches | 3 inches |
| Material | Liquid Nitrogen @ 77 K & 62.3 psia | Liquid Nitrogen @ 86 K & 42.3 psia |
| Approximate Part Weight | 115,000 lbf | 104,000 lbf |

## D11. Membrane

The FE model of the DOT-113 tank car included a deformable membrane part which was non-physical that represented the extents of the outage. The gas phase (GN2) contents of the tank were modeled within the tank using a pneumatic cavity which used the membrane as an external surface to apply contact forces to the surrounding inner tank and lading.

The pneumatic cavity approach was a simplified method of capturing the pressure effects of changing the outage volume while compressing the inner tank during the impact. The solver calculated the uniform pressure and temperature in each time increment during the impact. As the tank deformed from the impact, the GN2 and LN2 changed shape. Because the LN2 was relatively incompressible compared to the GN2, the indentation of the tank mostly reduced the volume of the GN2 in the outage. The pneumatic cavity modeled the GN2 as an ideal gas with user-defined initial pressure and temperature, and a universal gas constant. Thus, as the volume of the tank was reduced, the volume of the pneumatic cavity decreased and the pressure within the pneumatic cavity increased.

Because a pneumatic cavity only calculates the uniform pressures and temperatures within the cavity and not the fluid pressure or temperature at discretized points throughout the volume of the lading, this approach reduced the simulation runtime compared to techniques that represented the fluid explicitly as a Lagrangian or Eulerian mesh or collection of particles, i.e., smooth particle hydrodynamics (SPH). However, the uniform behavior simplification may not be well suited to all conditions, such as an impact that features an extremely small outage, or an outage that is divided into smaller volumes by a sloshing liquid.

A pneumatic cavity requires a geometric surface to be defined within the model that represents its boundary, and a reference point defined within the volume of the cavity. This reference point is used to define the interior of the cavity, and it is also the point to which initial temperatures and pressures are defined.

The membrane part was meshed using membrane-type elements for both the portion of the part that is in contact with the interior of the tank and the portion of the part that defined the interface between the LN2 and the GN2 within the tank. Frictionless hard contact was specified between the membrane and surrounding parts. The membrane mesh was refined in the region around the manway to match its mesh size and facilitate contact. The post-test geometry and mesh of the membrane part with a 9 percent outage are shown in Figure D11, and the mesh is summarized in Table D13.

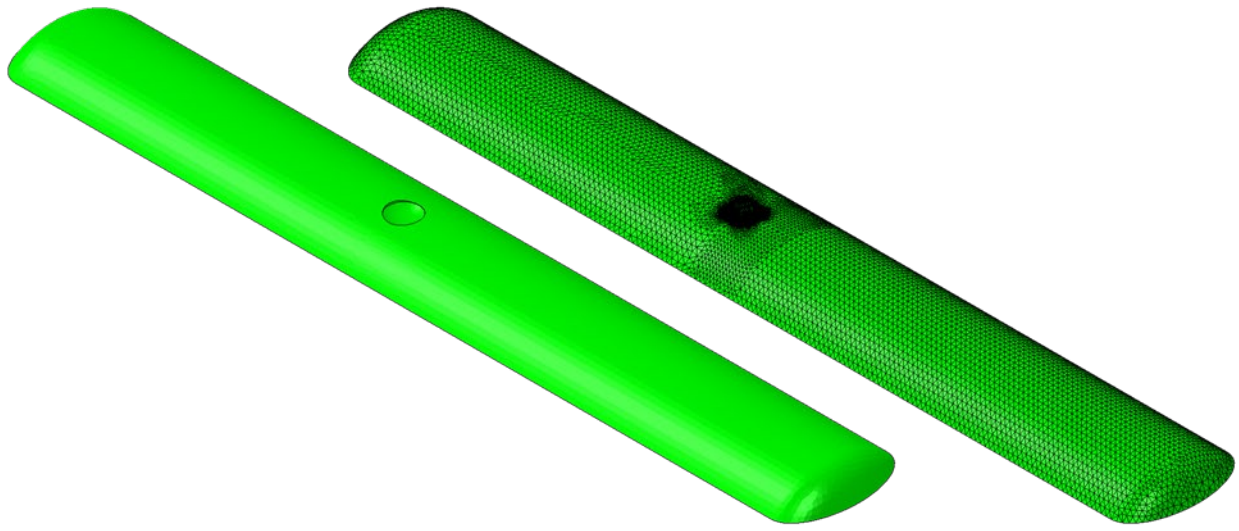

**Figure D11. Membrane Geometry (left) and Mesh (right) Post-test**

**Table D13. Properties of Membrane Mesh in FE Model**

| Property | Pre-test Model | Post-test Model |
|---|---|---|
| Type of Part | Deformable, Membrane | Deformable, Membrane |
| Outage | 5% | 9% |
| Number of Elements | M3D3: 17,980 | M3D3: 21,104 |
| Membrane Thickness | 0.05 inches | 0.05 inches |
| Material | Membrane | Membrane |
| Approximate Mesh Size | 0.5–3 inches | 0.5–3 inches |
| Approximate Part Weight | 304 lbf | 372 lbf |

Because the membrane represents geometry that is not physically present within the tank, a membrane element representation was chosen to be as thin and flexible as practical within the model without causing the model to terminate due to excessively distorted membrane elements. With these constraints, a thickness of 0.05 inch was chosen for the membrane.

The height of the horizontal plane (measured from the top of the lading to the top of the inner tank) was adjusted to yield the desired outage. The outage height was set to approximately 15 inches to yield a 9 percent outage in the post-test model, and the pre-test model used an outage height of approximately 10 inches to yield a 5 percent outage. Figure D12 shows the outage height reference measurement in the post-test model.

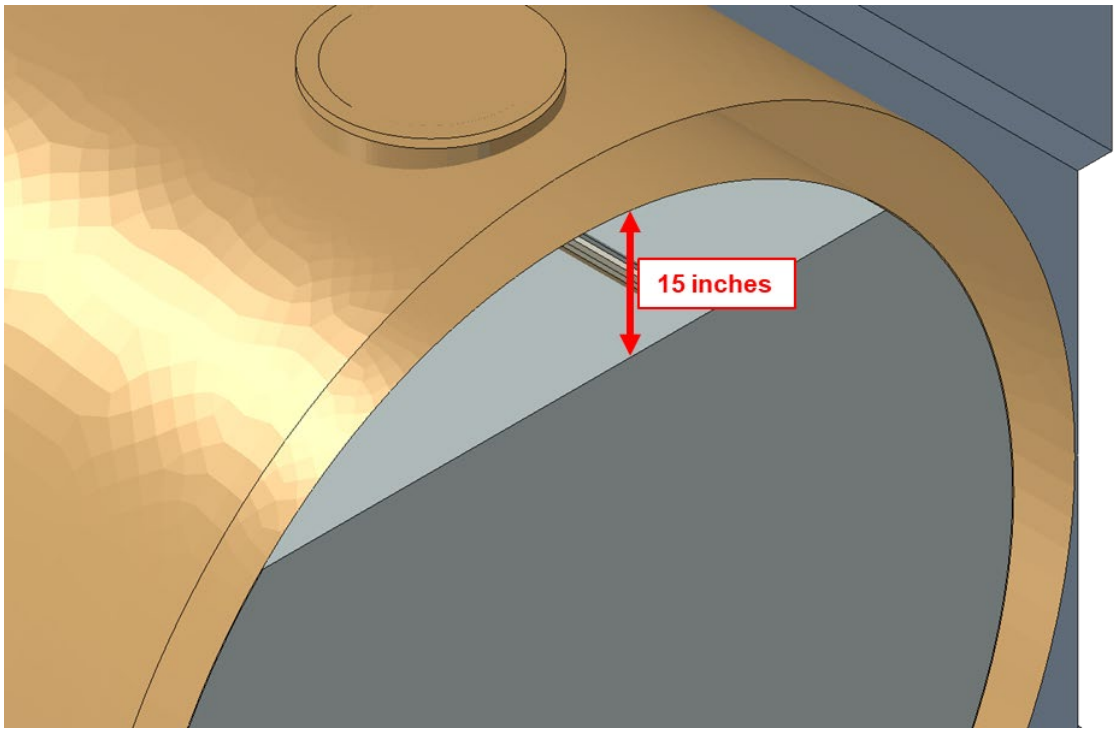


**Figure D12. Reference Measurement for Post-test Outage Height**

# Appendix E.
# Modeling Techniques

This appendix describes the FE modeling techniques that were used in both the pre-test and post-test models.

## E1. Rigid Impactor Boundary Conditions

The rigid impactor was constrained against all motion except for longitudinal displacement. The pre-test models were run at various speeds, and the post-test model was run at the measured test speed of 18.3 mph.

## E2. Rigid Wall Boundary Conditions

The rigid wall was constrained against motion in all six degrees-of-freedom (DOF).

## E3. Rigid Ground Boundary Conditions

The ground was constrained in all six DOF.

## E4. Bolster and Stub Sill Coupling

The bolster and stub sill were tied to the outer tank as shown in Figure E1 with the tied connections displayed in red. The tied locations approximately aligned with the weld locations in the actual DOT-113 surrogate. A position tolerance of 4 inches was used to connect nearby nodes between the parts.

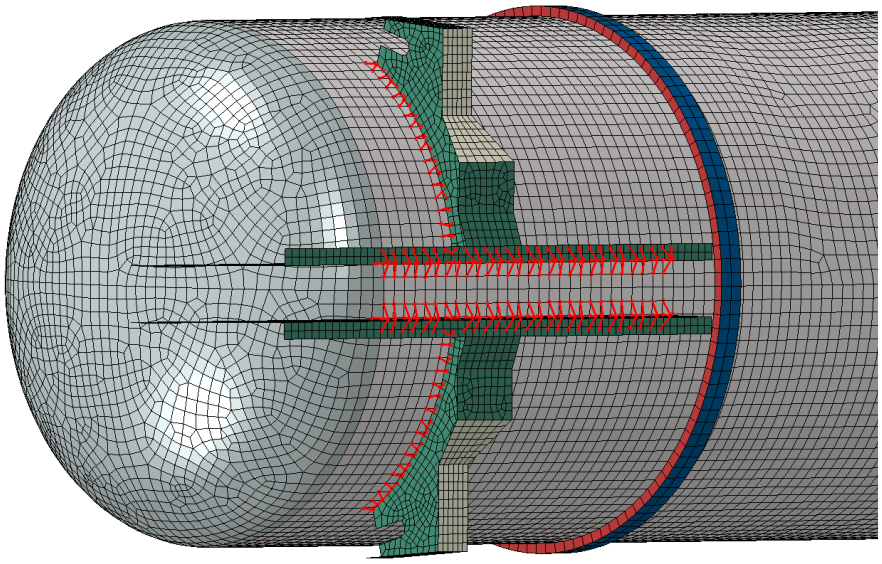

**Figure E1. Tied Constraint Between East End Bolster-Stub Sill and Outer Tank (bottom view only showing tied parts)**

## E7. Skid Coupling

A beam-type multi-point constraint (MPC) was used to attach the bolster at each end of the tank car to the corresponding skid. The rigid body reference node on each skid was used as the control point of the MPC. The bolster nodes subject to the constraint included nodes on the bottom where the bolster was rigidly attached to the skids during the test. The B-End MPC constraint is shown in Figure E2 with the beam connectors displayed in red.

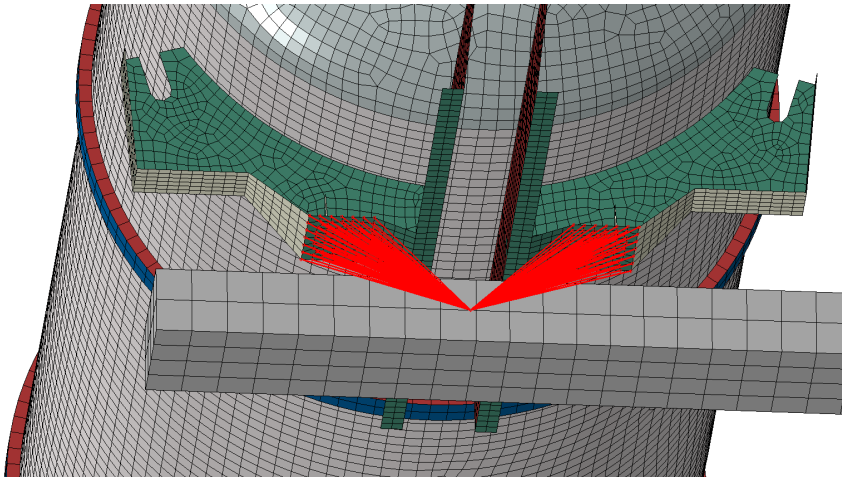

**Figure E2. MPC Between East End Bolster and Skids (bottom view)**

Additionally, a "Cartesian" type of connector was used to constrain the motion of the skid in both the vertical and the longitudinal (i.e., direction of impactor travel) directions. A nonlinear damper was defined between the skid and ground to constrain longitudinal motion. This damper defined the longitudinal resistance force as a function of skid speed, such that the skid had to overcome an initially high force when it was moving slowly. Once this initial peak was overcome, the resistance offered to skid motion diminished as the skid moved more quickly. This simplified model was intended to approximate the effect of static friction being overcome as the skid initially begins its motion, followed by a reduced resistance from kinetic friction. The longitudinal relationship used in the Cartesian connector is shown in Table E1 and plotted in Figure E3.

**Table E1. Longitudinal Skid Behavior**

| **Reaction Force** ***lbf*** | **Skid Velocity** ***in/s*** |
|---|---|
| -100 | -10 |
| -38,000 | -1 |
| 0 | 0 |
| 38,000 | 1 |
| 100 | 10 |

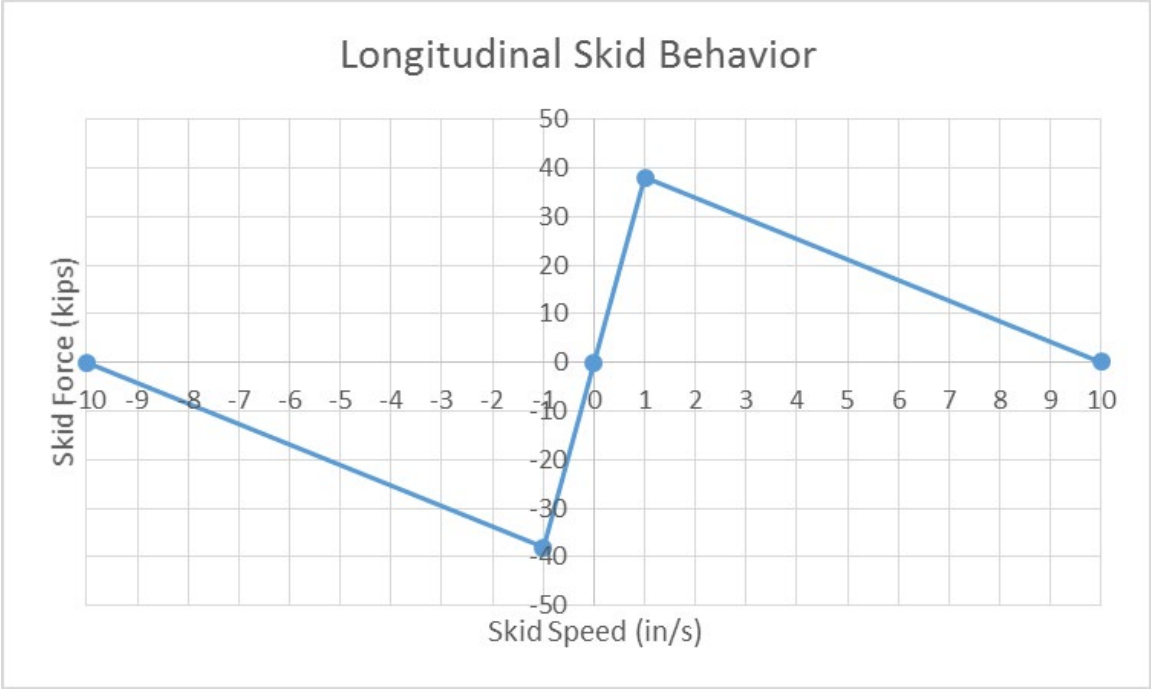


**Figure E3. Longitudinal Skid Behavior**

In the vertical direction, the skid used a "Stop" behavior assigned to a connector element between skid and ground to limit its range of motion. In the vertical downward direction, the reference point of the skid was prevented from having any displacement. In the upward direction, a limit of 100 inches was used. This number is arbitrary, but it was chosen to be larger than any anticipated vertical motion of the skid. These two vertical stops approximated the behavior of the skid on the ground during the physical test, where the skid was prevented from moving downward through contact with the ground but was free to lift upward if sufficient lifting forces overcame the weight resting on it.

## E8. Inner and Outer Tanks SSC

SSC constraints were used on the inner tank and the outer tank to attach each patch of solid elements in the vicinity of the impact zone to the rest of the shell-meshed tank. This type of constraint is necessary to ensure a smooth transition from solid elements that possess only translational DOF to shell elements that possess translational and rotational DOF. The shell part of each tank featured a refined mesh in the vicinity of the SSC constraint. Since the shell part corresponded to the mid-plane thickness of the tank, the shell part was aligned with the mid-plane of the solid patch. The interface between the solid elements and shell elements is shown in Figure E4 for the outer tank and Figure E5 for the inner tank.

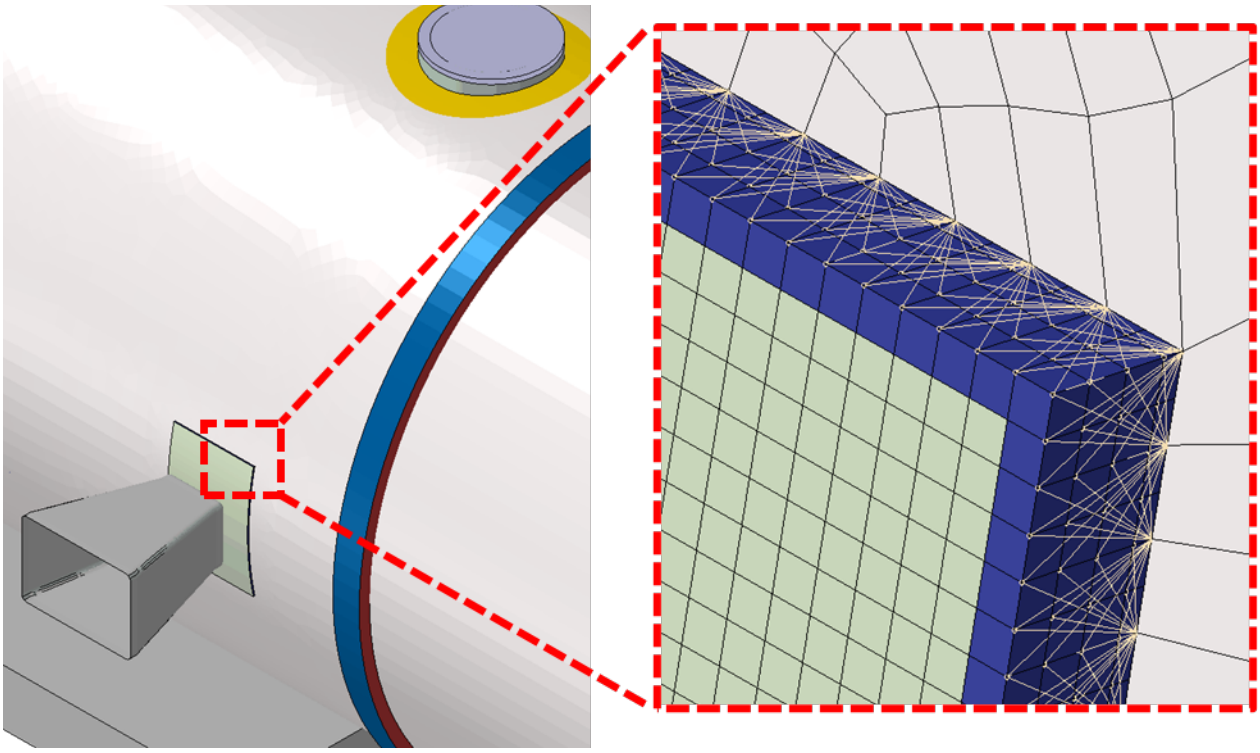

**Figure E4. Shell-to-Solid Coupling Region on Outer Tank Geometry (left) and Detailed Mesh View of Corner (right)**

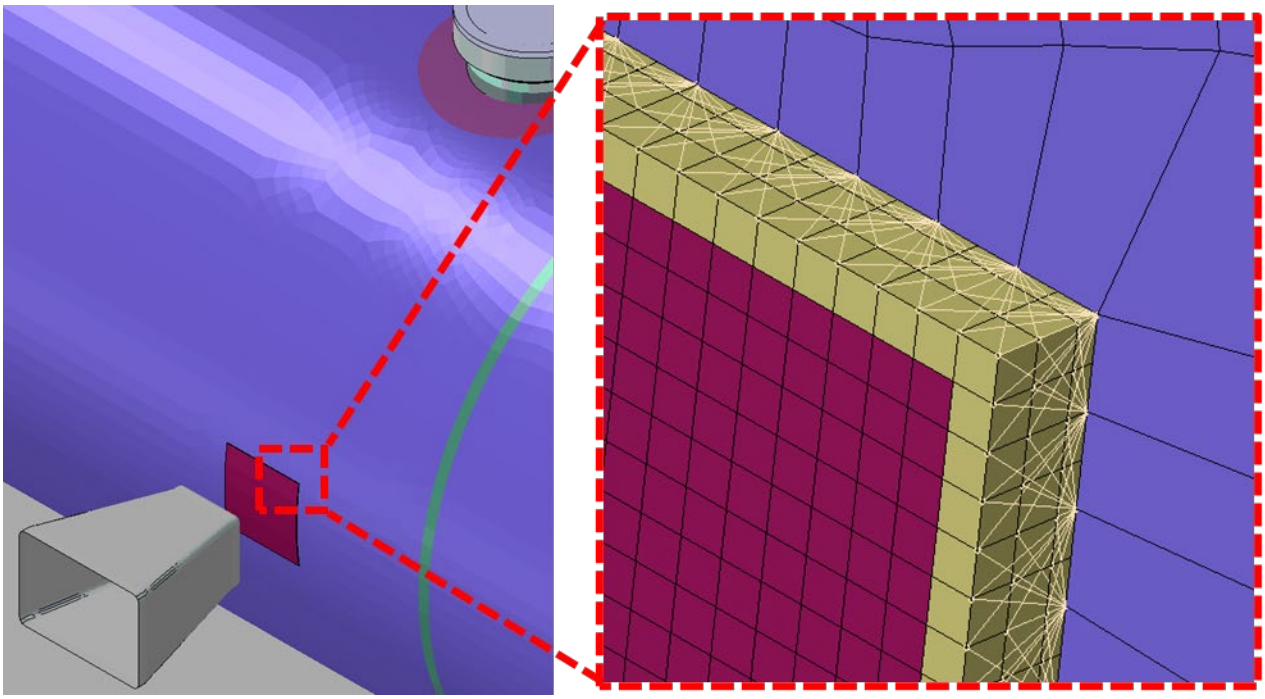

**Figure E5. Shell-to-Solid Coupling Region on Inner Tank Geometry (left) and Detailed Mesh View of Corner (right) with Outer Tank Hidden**

## E9. Pressures and Temperatures

The tested DOT-113 surrogate tank car had an initial pressure above atmospheric pressure within the inner tank and the annular space between the tanks was held under vacuum. The pre-test and post-test FE models attempted to replicate these pressure conditions as initial conditions on the model. Initial values for lading temperature were defined in the models.

The LN2 lading and GN2 outage within the inner tank were each given an initial pressure of 0, 15, 25, 35, or 50 psig in the pre-test models and 30 psig for the post-test model. As the surfaces describing the boundaries of the liquid and gas phases deformed, the pressure was free to change in response except for the isobaric models and the models using pressure-time data as an input (described in Appendix H). The models also require the definition of the ambient pressure on the outer tank. A value of 12.3 psi, corresponding to atmospheric pressure at Pueblo, CO's [29], altitude of approximately 4,700 feet [30], was used for ambient pressure. Initial temperatures were defined for both the LN2 and GN2. These initial temperatures were used to determine the appropriate material properties for each fluid type. The pre-test models used temperatures of 77 K for the LN2 and 92 K for the GN2. The post-test models used temperatures of 86 K for the LN2 and 92 K for GN2.

## E10. Mass Scaling

Variable mass scaling was used in the puncture-capable models. Because of the need for a refined mesh of solid elements in the impact zone on both the inner and outer tanks, the puncture-capable models feature a large number of very small elements. Variable mass scaling was employed in the FE models to decrease the runtime without decreasing either the span or the resolution of the refined meshes. Variable mass scaling is a technique in which the user sets a target time increment for a set of elements within the model (up to and including all elements within the model) and the Abaqus solver increases the mass of any element required to bring the minimum time step up to the user-defined minimum. "Variable" refers to the software's ability to increase the mass of each element by a different amount, based on the material and geometry of each element. While mass scaling is an efficient way of reducing runtime without re-meshing a model, care must be exercised when using this technique with highly dynamic simulations. If an overly aggressive mass scaling is applied, the amount of artificial mass added to the model in the refined mesh area can significantly affect both the overall dynamic response as well as the puncture behavior of the model.

The tensile coupon models of TC-128 and T304 steels used a variable mass scaling with a target time increment of $1 \times 10^{-6}$ seconds. The puncture-capable FE models used a variable mass scaling to achieve a target time increment of $9 \times 10^{-7}$ seconds over the entire model. The mass scaling factors were re-calculated for the full-scale puncture models every 2,000 increments, i.e., approximately every 1.8 milliseconds.

## E11. Contact

A general contact definition was used in all models. The global contact used frictionless contact, except for metal-on-metal contact. A coefficient of friction of 0.3 was defined for regions of metal-on-metal contact. Contact exclusions were defined between the shell tank and the solid tank patch for both the inner and outer tanks. A contact thickness reduction was used on the membrane mesh in the vicinity of the impact zone.

# Appendix F.
# Material Behaviors in FE Models

## F1. Introduction

Pre- and post-test FE models used TC-128 carbon steel and T304 stainless steel material inputs which were calibrated from ASTM-E8 tensile test results. The ASTM-E8 tensile tests were conducted on samples that were excised from the previous DOT-113 surrogate tank car tested with water in June 2020 (Test 11). The TC-128 material inputs were identical between the Test 11 and Test 12 FE models because the outer tank was at room temperature in both tests. The T304 material input was updated because the inner tank of Test 11 was at room temperature while the inner tank of Test 12 was at cryogenic temperature (LN2). Information regarding the TC-128 material inputs is available in the Test 11 report [4]. This appendix focuses on the process used to create the cryogenic T304 material inputs for the FE model.

## F2. Material Calibration Coupon Models

FE simulations of the T304 stainless steel ASTM-E8 subsize rectangular, i.e., dogbone (DB), uniaxial tensile tests were used to calibrate the material definitions in Abaqus/Explicit for the full-scale models of the DOT-113 surrogate side impact test with LN2. First, the plastic true stress-plastic equivalent strain (PEEQ) characteristic was specified. Then, the damage initiation envelope was calculated. Finally, a reasonable damage progression was empirically determined.

As the material responses developed using coupon models were planned for implementation in the full-scale DOT-113 surrogate model with LN2, modeling techniques for performing the coupon simulations were deliberately chosen to be similar to the modeling techniques planned for side impact analyses of the DOT-113 tank car. Where possible, the same solver (Abaqus/Explicit), element types (C3D8R), and mesh sizes were chosen for the coupon models and the DOT-113 side impact models. This was done to attempt to minimize the uncertainty associated with calibrating a material behavior using one set of modeling techniques but applying that behavior to model puncture in the full-scale tank car impact simulation with a different set of techniques. If the tank car model was run using a different solver or different mesh density for example, it is expected that the material behaviors would need to be recalibrated using coupon simulations that used similar solvers and mesh density.

For all tensile coupon simulations, a soft ($1 \times 10^{-6}$ lbf/in) discrete spring was attached to the ends of the gage. This spring was a representation of an extensometer in the model and simplified the process of requesting the change-in-length of the gage section from the model.

The subsize DB tensile coupon FE model used for the T304 stainless steel calibration is shown in Figure F1. The T304 DB coupon had a 1-inch gage length, 0.25-inch width, and approximate 0.067-inch thickness (refer to Appendix B5.3 ). The FE model used planes of symmetry across the width and thickness, which are not shown in Figure F1, and it had a mesh size of approximately 0.0084 inches corresponding to 4 elements across the half thickness. It should be noted that the authors preferred to test with a full 0.25-inch-thick specimen so that a larger mesh size could be used in the T304 coupon model to match the mesh of the inner tank solid patch in the full-scale DOT-113 surrogate puncture model; however, the test lab had mechanical difficulties with tensile testing a full 0.25-inch-thick specimen at cryogenic temperature due to the high strength of the material.

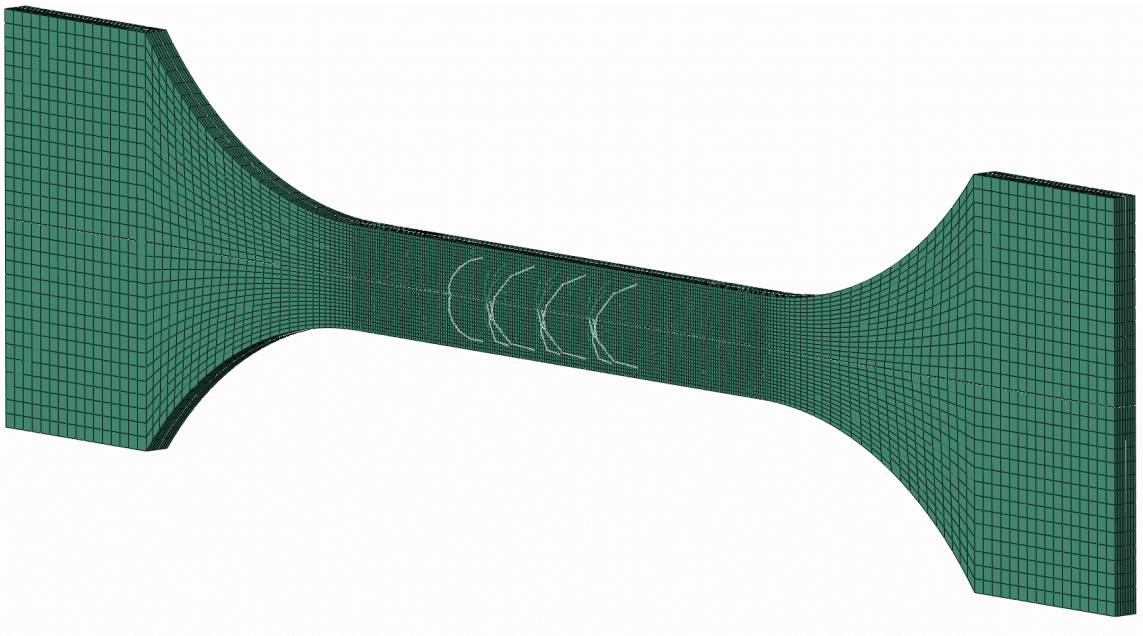

**Figure F1. FE Model of T304 Stainless Steel DB ASTM E8 Sub-size Coupon with 1-inch Gage Length**

In the full-scale puncture model of the DOT-113 tank car, the 0.608-inch thick TC-128 carbon steel outer tank shell was meshed with 7 elements across the thickness corresponding to a mesh size of approximately 0.087 inches (refer to Appendix D8). The 1/4-inch-thick T304 stainless steel inner tank shell was meshed with 5 elements across the thickness corresponding to a mesh size of 0.05 inches (refer to Appendix D6).

Because of the difference in mesh size between the T304 solid elements in the ATSM E8 subsize coupon (0.0084-inch) and full-scale tank car (0.05-inch), a study was conducted to investigate the effect on damage progression (refer to Section F3.1).

### *F2.1 Plastic Hardening*

Abaqus requires metal plasticity to be defined in terms of true stress and PEEQ. The plastic behavior of each steel was input to the Abaqus model as isotropic hardening using a discrete number of data points. True stress and PEEQ can be calculated from nominal stress-strain tensile coupon data according to Equation F1.

**Equation F1. True Stress-strain Transformation**

$$\sigma_{true} = \sigma_{nom} \cdot (1 + \varepsilon_{nom})$$

$$\varepsilon^{pl} = \ln(1 + \varepsilon_{nom}) - \frac{\sigma_t}{E}$$

$\sigma_{nom}$ nominal (engineering) stress
$\sigma_{nom}$ nominal (engineering) strain
$\sigma_{true}$ true stress
$\varepsilon^{pl}$ plastic equivalent strain

Because necking dominates the nominal stress-strain response of the tensile coupon characteristic after the maximum force is achieved, the true stress-PEEQ relationship was extrapolated for strains beyond the strain at maximum force using the inverse method. The inverse method involves iteratively adjusting the true stress-PEEQ relationship until agreement is achieved between the tensile coupon simulation and test results. Two methods were used to describe the true stress-PEEQ relationships for TC-128 and T304 respectively in this study.

Paredes et al. [31] applied a Mixed Swift-Voce Law hardening expression to extrapolate true stress at high strains for TC-128. The Mixed Swift-Voce Law is a conjunction of the Swift (power) Law [32] and the Voce (exponential/saturation) Law [33] which describe plastic hardening. The Mixed Swift-Voce Law is a function of PEEQ ($\varepsilon^{pl}$) and is formed by combining the Swift term ($\sigma_t^{Swift}$) with the Voce term ($\sigma_t^{Voce}$) using a weighting factor ($\alpha$) as shown in Equation F2.

**Equation F2. Swift (Power), Voce (Exponential/Saturation), and Mixed Swift-Voce Laws for Plastic Hardening**

$$\sigma_t^{Swift}(\varepsilon^{pl}) = A \cdot (\varepsilon_0 + \varepsilon^{pl})^n$$

$$\sigma_t^{Voce}(\varepsilon^{pl}) = K_0 + Q \cdot \left(1 - e^{-\beta \varepsilon^{pl}}\right)$$

$$\sigma_t^{Mixed} = \alpha \cdot \sigma_t^{Swift} + (1 - \alpha)\sigma_t^{Voce}$$

The Swift-Voce constants are calibrated using the calculated true stress-PEEQ (see Equation F1) from a tensile test and performing a least squares regression fit on the Swift and Voce equations. The Swift and Voce expressions are independently fit on the test data from a PEEQ close to zero to the PEEQ at max force because the plastic behavior of the coupon is not dominated by necking for that range of strains. After the constants for the Swift and Voce expressions are independently determined by least-squares regression, a FE model of the uniaxial tensile test is iteratively executed while varying $\alpha$ until the nominal stress-strain output from the model is in agreement with the test results up to the point of crack initiation.

In the previous test of a DOT-113 surrogate filled with water (Test 11), the authors calibrated Swift Law Plastic Hardening constants for TC-128 and Swift-Voce Law Plastic Hardening constants for T304 at room temperature [4]. The authors determined that these extrapolation methods captured the post-necking behavior of the tensile coupons better than linear extrapolation. They applied the same TC-128 material definition from Test 11 to the current DOT-113 surrogate filled with LN2 [4]. However, they calibrated new Voce Law Plastic Hardening constants for T304 (see Section F3) because T304 has a much higher strength at cryogenic temperature than the previously calibrated room temperature material model.

Ductile damage initiation and progression can be used in Abaqus to simulate the crack initiation and propagation experienced in the actual coupon test through element stiffness degradation and deletion. The process of calibrating a damage initiation envelope and then empirically determining a suitable damage progression value is explained in the following section.

### *F2.2 Bao-Wierzbicki (B-W) Damage Initiation*

Figure F2 shows a schematic of the B-W triaxiality ($\eta$)-based damage initiation envelope that was used in the TC-128 material failure models [25]. Triaxiality is defined as the ratio of the

hydrostatic stress (mean stress) divided by the von Mises stress (equivalent stress) and describes the general stress state of an element. The B-W envelope consists of three regions: I – Ductile Fracture, II – Mixed Fracture, and III – Shear Fracture.

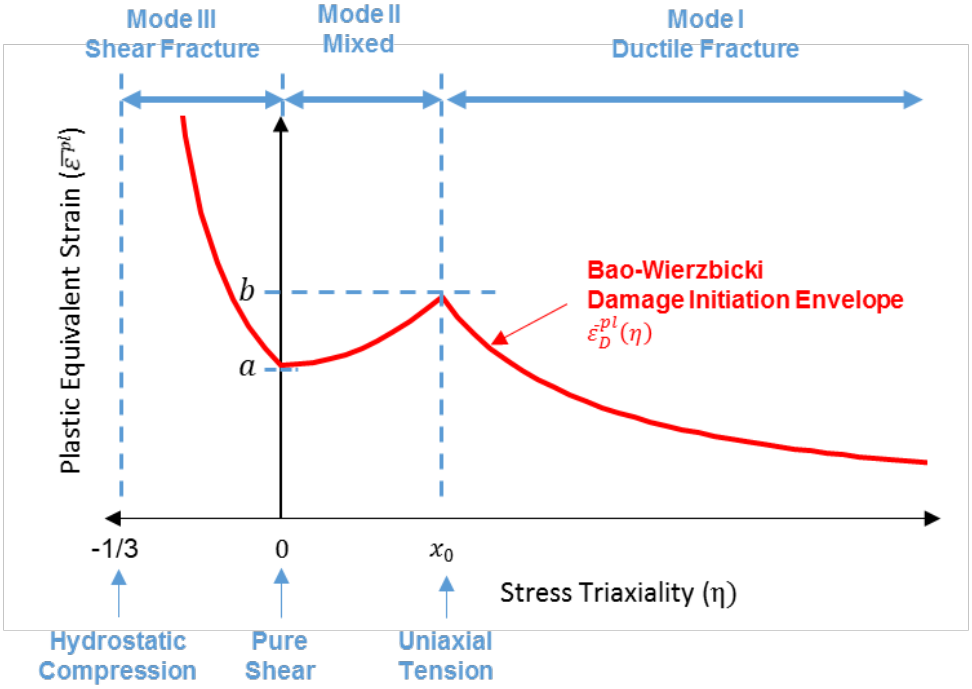


**Figure F2. Schematic of B-W Damage Initiation Envelope**

When $\eta$<0 the element is in a state of compression, and when $\eta$>0 the element is in a state of tension. A triaxiality of $\eta$=-1/3 corresponds to a stress state of hydrostatic compression and $\eta$=0 corresponds to pure shear. The cusp of the B-W envelope is intended to be located at the average triaxiality on the fracture surface of a smooth round bar specimen under uniaxial tension at $\eta=x_0$ and is typically close to a value of 0.4.

Three constants ($a$, $b$, $x_0$) govern the shape of the B-W damage initiation envelope (Equation F3) and are calibrated based on coupon test results. The critical strain to fracture in pure shear ($a$) corresponds to the PEEQ on the B-W envelope ($\varepsilon^{pl}$) when $\eta$=0 (pure shear). The critical strain to fracture in uniaxial tension ($b$) corresponds to ($\varepsilon_D{}^{pl}$) at the cusp of the B-W envelope when $\eta=x_0$.

**Equation F3. B-W Damage Initiation Envelope**

$$\varepsilon_D^{pl}(\eta) = \begin{cases} \dfrac{a}{1+3\cdot\eta} & -\dfrac{1}{3} \le \eta \le 0 \\ (b-a)\cdot\left(\dfrac{\eta}{x_0}\right)^2 + a & 0 \le \eta \le x_0 \\ \dfrac{b\cdot x_0}{\eta} & x_0 \le \eta \end{cases}$$

The complete damage initiation envelope can be developed through a series of mechanical tests on 11 unique specimen geometries intended to cover a wide range of stress triaxialities, but a

simplified “quick calibration” approach that requires only one uniaxial tensile geometry to estimate the entire failure envelope was developed for industrial use by Lee and Wierzbicki [34], [35]. According to Lee, the quick calibration approach is intended to be within 10 percent agreement with a failure envelope that was developed using the complete set of 11 specimens.

The quick calibration procedure for smooth round bar tensile tests allows the calculation of the B-W envelope constants (*a, b, $x_0$*) by measuring the initial radius ($a_0$), final radius ($a_f$), displacement at max force ($\delta_d$), and initial gage length ($L_0$). For flat (dogbone) coupons the calculation is performed by measuring initial thickness ($t_0$) and final thickness ($t_f$) instead of initial and final radius. As seen in Equation F4, the quick calibration procedure also uses the hardening exponent ($n$) which is used to describe the plastic hardening behavior of metals by the power law. The hardening exponent is estimated as a function of engineering strain at maximum force.

**Equation F4. Quick Calibration Procedure for Smooth Round Bar (left) and Flat DB (right) Uniaxial Tensile Coupons**

**Smooth Round Bar**

$$n = \ln\left(1 + \frac{\delta_d}{L_0}\right)$$

$$b = 2 \cdot \ln\frac{a_o}{a_f}$$

$$x_0 = \frac{1}{3} + \frac{0.22}{b} \cdot (b - n)^{1.8}$$

$$a = b \cdot \left(\frac{\sqrt{3}}{2}\right)^{1/n}$$

**Flat (Dogbone) Coupon**

$$n = \ln\left(1 + \frac{\delta_d}{L_0}\right)$$

$$b = \frac{2}{\sqrt{3}} \cdot \ln\frac{t_o}{t_f} + \frac{2 \cdot n}{\sqrt{3}} \cdot \left(\sqrt{3} - 1\right)$$

$$x_0 = \frac{1}{\sqrt{3}} - \frac{2 \cdot n}{3 \cdot b} \cdot \left(\sqrt{3} - 1\right)$$

$$a = b \cdot \left(\frac{\sqrt{3}}{2}\right)^{1/n}$$

For ductile metals in Abaqus, the damage threshold is reached when the ductile criterion (DUCTCRT) reaches a value of 1. The DUCTCRT is calculated by integrating the change in PEEQ divided by the PEEQ where damage initiates as a function of triaxiality (i.e., the B-W envelope) according to Equation F5.

**Equation F5. Calculation of the Ductile Damage Criterion (DUCTCRT) in Abaqus**

$$DUCTCRT = \int \frac{d\varepsilon^{pl}}{\varepsilon_D^{pl}(\eta)}$$

After DUCTCRT reaches a value of 1 the stiffness of the element is degraded according to the damage progression in the material definition. In this report, exponential displacement-based damage progression values are calibrated for each material; however, previous puncture simulations have used linear energy-based damage progressions [11, 12].

## F3. Cryogenic T304 Stainless Steel

The T304 stainless steel stress-strain behavior at 77 K and 0.05 in/in/s presented in the Test 11 report was used to calibrate a material model for the full-scale DOT-113 surrogate with LN2 puncture model [4]. A temperature of 77 K, corresponding to the saturation temperature of

nitrogen at atmospheric pressure, was chosen for the coupon FE model and DOT-113 FE model. This was the closest temperature used in the tensile test series, which was conducted after Test 11, to the estimated temperature of the inner tank in Test 12. The Test 11 T304 material was tested at a temperature of 77 K and strain rates of 0.0005, 0.05, 0.5, 5, and 16 in/in/s. There was very little difference in the measured fracture toughness at 77 K between the strain rates which were above quasi-static strain rate (0.0005 in/in/s). An elevated strain rate of 0.05 in/in/s was chosen from the tensile test series for calibrating the FE model because (1) it was in the range of estimated strain rates which could occur during the test and (2) it resulted in the lowest estimate of fracture toughness.

Figure F3 shows the nominal stress-strain tensile results of the ASTM-E8 subsize (1-inch gage length) rectangular coupons from Test 11. Walking through the nominal stress-strain test results shown from start through break:

1. The coupons yielded at approximately 77 ksi
2. Then quickly reached a nominal stress of 105 ksi at 2 percent nominal strain
3. The nominal stress plateaued at 105 ksi until 15 percent nominal strain
4. The nominal stress smoothly increased to the 178 ksi UTS at 30 percent nominal strain
5. The coupons quickly underwent necking and broke at ~33 percent nominal strain

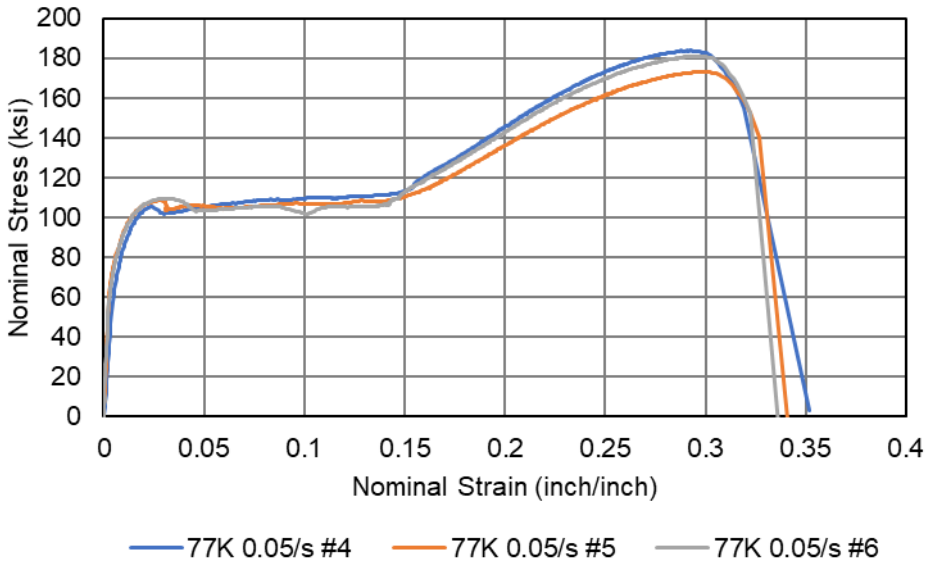


**Figure F3. Nominal Stress-Strain Responses of Test 11 T304 Stainless Steel DB Coupons (1-inch GL) at a Strain Rate of 0.05/s and Temperature of 77 K**

The shape of stress-strain curves for stainless steels tested at cryogenic temperatures are unique in that a phase transformation from face centered cubic (FCC) γ-austenite into α'-martensite occurs and results in a significant increase in strength [31].

To estimate a true stress-PEEQ strain plastic hardening curve for the material, Equation F1 was used up to UTS at 30 percent nominal strain. After reaching its UTS stainless steel quickly necks and breaks, which made it difficult to extrapolate true stress values for high PEEQ strain. This is because it is difficult to tell where the transition between damage and necking occurs. In carbon

steels like TC-128, necking occurs over a much larger range of PEEQ strains before fracture occurs making it easier to locate the transition.

A Voce (saturation) plastic hardening equation was fit onto the calculated true stress-PEEQ strain curve starting after the plateau region at 15 percent nominal strain to the UTS at 30 percent nominal strain. The Voce constants which resulted in the best fit were determined by a least-squares regression similar to Paredes et al. [36]. The Voce curve was used to extrapolate the true stress-PEEQ strain behavior after the UTS occurred (necking) up to PEEQ strains as high as 200 percent. Figure F4 shows the Voce plastic hardening input for cryogenic (77 K) T304 stainless steel at 0.05 in/in/s. The resulting saturation true stress was 235 ksi.

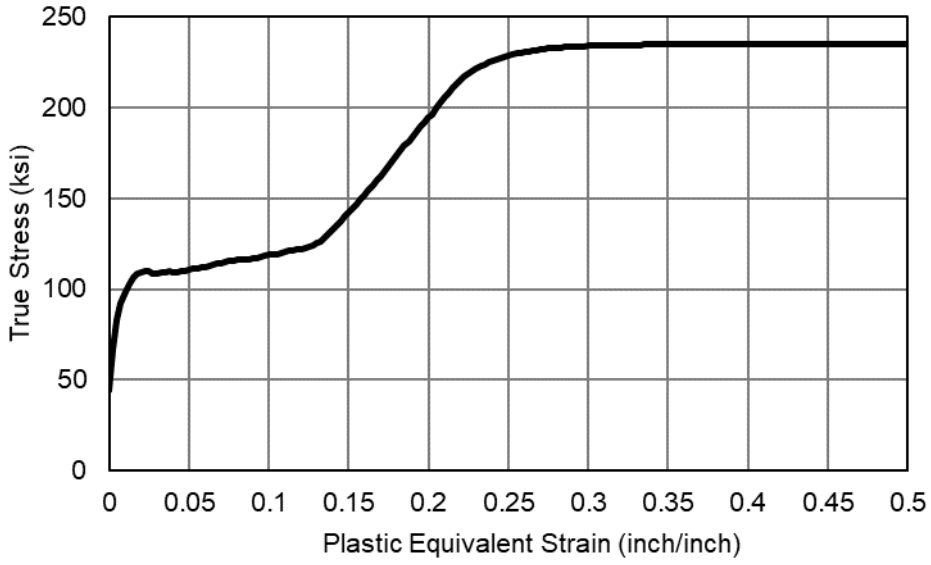


**Figure F4. True Stress-PEEQ Strain FE Input for Test 11 T304 Stainless Steel at 77 K and 0.05/s in Inner Tank FE Model**

The constants for the Voce plastic hardening expression (see Equation F2) are given in Table F1. Note that the Voce plastic hardening expression was only used to extrapolate true stress for PEEQ strains above 0.2 inch/inch. Refer to Table F2 for the true stress-PEEQ strain behavior up to a PEEQ strain of 0.2 inch/inch which was directly calculated using Equation F1 on regularized test data from the sample named "77K 0.05/s #6" in Figure F3.

**Table F1. Constants for Voce Plastic Hardening of T304 Stainless Steel at 77 K and 0.05/s in Inner Tank FE Model**

| $k_0$ | $Q$ | $\beta$ |
|---|---|---|
| *ksi* | *ksi* | - |
| $-1.025 \times 10^5$ | $1.028 \times 10^5$ | $3.890 \times 10^1$ |

**Table F2. Plastic Equivalent Strain versus True Stress Input for T304 Stainless Steel in Inner Tank at 77 K and 0.05/s**

| PEEQ | True Stress | PEEQ | True Stress | PEEQ | True Stress |
|---|---|---|---|---|---|
| *in/in* | *ksi* | *in/in* | *ksi* | *in/in* | *ksi* |
| 0.000E+00 | 4.400E+01 | 6.750E-02 | 1.140E+02 | 1.350E-01 | 1.284E+02 |
| 2.500E-03 | 6.713E+01 | 7.000E-02 | 1.146E+02 | 1.375E-01 | 1.304E+02 |
| 5.000E-03 | 8.317E+01 | 7.250E-02 | 1.150E+02 | 1.400E-01 | 1.329E+02 |
| 7.500E-03 | 9.261E+01 | 7.500E-02 | 1.154E+02 | 1.425E-01 | 1.355E+02 |
| 1.000E-02 | 9.863E+01 | 7.750E-02 | 1.158E+02 | 1.450E-01 | 1.377E+02 |
| 1.250E-02 | 1.029E+02 | 8.000E-02 | 1.161E+02 | 1.475E-01 | 1.401E+02 |
| 1.500E-02 | 1.061E+02 | 8.250E-02 | 1.163E+02 | 1.500E-01 | 1.422E+02 |
| 1.750E-02 | 1.083E+02 | 8.500E-02 | 1.166E+02 | 1.525E-01 | 1.444E+02 |
| 2.000E-02 | 1.096E+02 | 8.750E-02 | 1.166E+02 | 1.550E-01 | 1.468E+02 |
| 2.250E-02 | 1.100E+02 | 9.000E-02 | 1.167E+02 | 1.575E-01 | 1.493E+02 |
| 2.500E-02 | 1.098E+02 | 9.250E-02 | 1.167E+02 | 1.600E-01 | 1.519E+02 |
| 2.750E-02 | 1.086E+02 | 9.500E-02 | 1.174E+02 | 1.625E-01 | 1.542E+02 |
| 3.000E-02 | 1.087E+02 | 9.750E-02 | 1.182E+02 | 1.650E-01 | 1.571E+02 |
| 3.250E-02 | 1.092E+02 | 1.000E-01 | 1.188E+02 | 1.675E-01 | 1.598E+02 |
| 3.500E-02 | 1.095E+02 | 1.025E-01 | 1.194E+02 | 1.700E-01 | 1.625E+02 |
| 3.750E-02 | 1.097E+02 | 1.050E-01 | 1.195E+02 | 1.725E-01 | 1.653E+02 |
| 4.000E-02 | 1.094E+02 | 1.075E-01 | 1.199E+02 | 1.750E-01 | 1.680E+02 |
| 4.250E-02 | 1.095E+02 | 1.100E-01 | 1.205E+02 | 1.775E-01 | 1.708E+02 |
| 4.500E-02 | 1.100E+02 | 1.125E-01 | 1.211E+02 | 1.800E-01 | 1.735E+02 |
| 4.750E-02 | 1.103E+02 | 1.150E-01 | 1.216E+02 | 1.825E-01 | 1.762E+02 |
| 5.000E-02 | 1.106E+02 | 1.175E-01 | 1.220E+02 | 1.850E-01 | 1.789E+02 |
| 5.250E-02 | 1.111E+02 | 1.200E-01 | 1.223E+02 | 1.875E-01 | 1.817E+02 |
| 5.500E-02 | 1.114E+02 | 1.225E-01 | 1.226E+02 | 1.900E-01 | 1.844E+02 |
| 5.750E-02 | 1.120E+02 | 1.250E-01 | 1.234E+02 | 1.925E-01 | 1.870E+02 |
| 6.000E-02 | 1.124E+02 | 1.275E-01 | 1.240E+02 | 1.950E-01 | 1.897E+02 |
| 6.250E-02 | 1.128E+02 | 1.300E-01 | 1.254E+02 | 1.975E-01 | 1.923E+02 |
| 6.500E-02 | 1.135E+02 | 1.325E-01 | 1.264E+02 | 2.000E-01 | 1.949E+02 |

Because final thickness measurements were not taken from the T304 DB tensile coupons before they were discarded, the B-W quick calibration approach [34, 35] could not be directly used. The B-W damage initiation envelope from the T304 inner tank in the post-test model of a previous DOT-113 test in 2019 was used. This damage initiation envelope resulted in a reasonable damage initiation point for the T304 DB coupon models from the Test 11 DOT-113 surrogate.

The constants for the B-W damage envelope are given in Table F3, and the resulting B-W envelope is plotted in Figure F5.

**Table F3. B-W Damage Initiation Envelope Constants for Test 11 T304 Stainless Steel in Inner Tank at 77 K and 0.05/s**

| $a$ | $b$ | $x_0$ |
|---|---|---|
| 0.24475 | 0.42804 | 0.28396 |

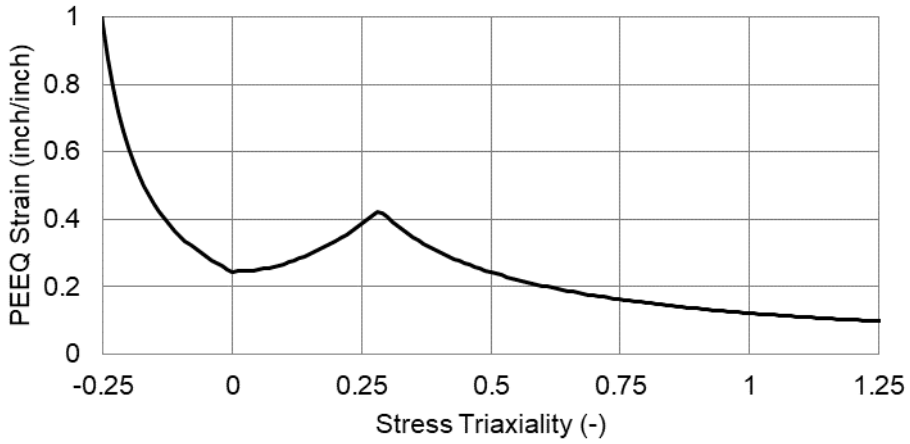


**Figure F5. B-W Damage Initiation Envelope for T304 Stainless Steel in Inner Tank**

Figure F6 shows the resulting nominal stress-strain responses from the T304 DB FE model. A displacement-based exponential damage progression was selected at 0.005 in/in$^2$ with an exponent of -1 because it gave a reasonable nominal stress-strain slope after damage initiation. Qualitatively, the nominal stress-strain response from the FE model matches the overall shape of the T304 DB tensile coupon response below.

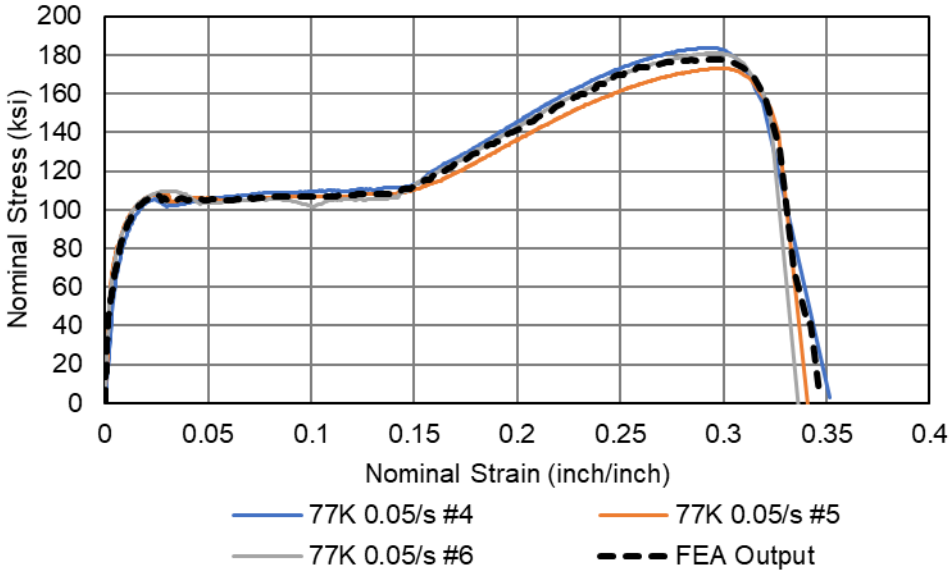


**Figure F6. Nominal Stress-Strain Output of T304 Stainless Steel DB (1-inch GL) FE Model with Test Results Shown for Comparison at 77 K and 0.05/s**

### *F3.1. Mesh Size Scaling*

Because the T304 subsize coupon model (Figure F1) which was used for calibration employed a finer mesh size than the inner tank solid patch (Figure D6) in the full-scale DOT-113 surrogate FE model, a separate FE model of a standard-sized ATSM-E8 smooth round bar (SRB) was used to compare the damage progression response at both mesh sizes. The subsize coupon model for calibration used a mesh size of 0.0084 inches and the full-scale model used a mesh size which was approximately 6 times larger at 0.05 inches.

The TC-128 coupon model from Test 11 [4] used approximately the same mesh size (0.081 inches) as the outer tank solid patch (Figure D8) in the Test 12 full-scale DOT-113 surrogate FE model. The authors determined that it was therefore not necessary to consider scaling the damage progression value for TC-128.

Figure F7 shows the FE model of the SRB coupon with a 2-inch GL at both mesh sizes for the comparison of the calibrated T304 behavior. The damage progression value of 0.005 in/in$^2$ (see Section F3) was used with both mesh sizes. The SRB model did not represent an actual tensile coupon. Such a coupon could not be excised from 1/4-inch-thick tank since the diameter of the specimen gage section was larger at 0.5 inches. Thus, the FE model results are not directly compared against actual test data.

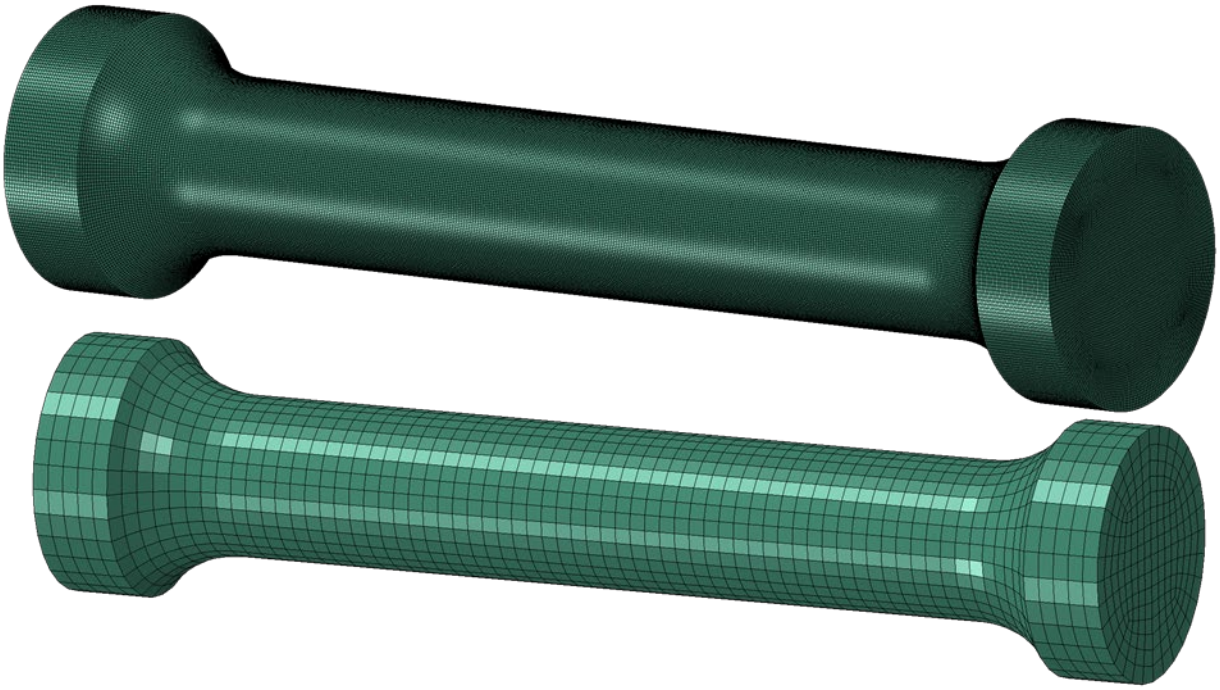

**Figure F7. FE Model of ASTM E8 Smooth Round Bar Coupon with 2-inch Gage Length Used to Compare 0.0084-inch (top) and 0.05-inch (bottom) Mesh Sizes**

Figure F8 compares the nominal stress-strain response from the SRB 2-inch GL model with 0.0084-inch and 0.05-inch mesh sizes. While the GL in the SRB model was twice as large as the 1-inch GL used in the subsize DB model, an EB at approximately 0.35 in/in was observed in both cases. This is attributed to the rapid and highly localized plastic instability (necking) observed in T304 stainless steel.

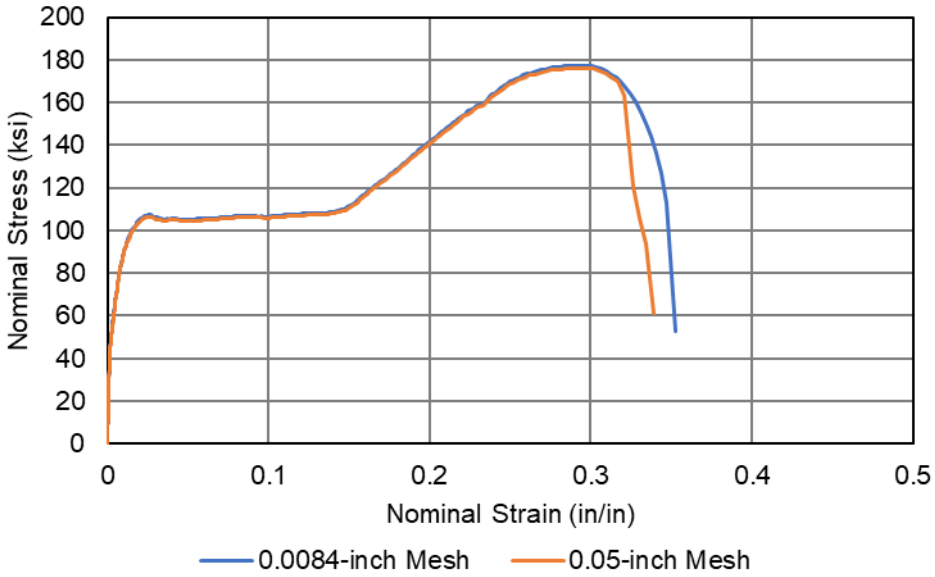


**Figure F8. Nominal Stress-Strain Output of T304 Stainless Steel SRB (2-inch GL) FE Model Comparing Damage Progression at Two Mesh Sizes**

The results of the mesh size comparison indicated that the damage progression determined in Section F3 could be directly applied to the T304 inner tank solid patch in the full-scale DOT-113 surrogate puncture model. No modifications were made to the T304 material behavior calibrated from the subsize coupon model when applying the material behavior to the full-scale puncture model.

# Appendix G.
# Outage Volume and Pressure Calculations

The calculations described in this Appendix are adapted from calculations made by Dr. Phani Raj of FRA's Office of Safety. The original calculations were provided to the test team during the preparation phase of the first DOT-113 tank car test (Test 10) to enable the filling level and pressure for that test to be chosen [3].

## G1. Pre-test Target Outage Volume

The "filling density" is defined as the weight ratio of the cryogenic commodity at its design temperature to water at atmospheric pressure and 60 °F. Based on this definition, using LN2 as the test liquid required additional calculations to determine the volume of LN2 to fill the tank. If the stipulation was that at the PRV's STDP (75 psig) condition the volume of vapor space was to be 2 percent of the tank volume (as is the condition given in the Final Rule [18]) then the mass of LNG in the tank car could be calculated knowing the saturation density of LNG at the PRV's STDP. Previous FRA-sponsored testing and analysis have shown that the height of the outage can have a significant effect on the structural response and puncture behavior of an impacted tank car under the standardized test conditions. Thus, the filling level was chosen to match the approximate filling volume of LNG with an equivalent volume of LN2. Because LN2 has a higher density than LNG, using an equivalent volume of LN2 to LNG would result in an LN2-filled tank that is heavier than an LNG-filled car.

To calculate the volume of the tank car that would be filled with LNG using a filling density of 37.3 percent, the density of the LNG also needed to be known. The density of LNG varies with the pressure at which the LNG is stored. While the DOT-113 tank car is highly-insulated, the lading will gradually heat up. As the lading heats up, it expands within the tank. This expansion simultaneously reduces the outage volume and increases the outage pressure.

This relationship between outage pressure and outage volume had to be considered when choosing either pressure or outage volume as an input to the test plan. Because LNG was not widely-transported via DOT-113 tank cars at the time this test was being planned, there were no data on "typical" service conditions that could be used to select a test pressure and calculate a corresponding filling level that is commonly encountered. The Final Rule stated:

> *In this final rule, PHMSA is adopting a 37.3 percent maximum filling density for LNG, which will allow for approximately 2 percent outage below the inlet of the pressure control valve to prevent the venting of liquid material at start-to-discharge pressure… PHMSA expects that any tank car containing a cryogenic material will be delivered to its destination within 20 days of offering, and requires notification of any car that has not reached its destination within this timeframe. See § 173.319(a)(3). Therefore, PHMSA is adopting a 15 psig maximum offering pressure, as proposed, which is appropriate for the transportation of LNG and is consistent with the level of safety provided to other flammable cryogenic materials. The HMR do not prohibit shippers from offering a tank car of LNG at a lower pressure* [18].

The previously-conducted tests of a DOT-113 tank car and tank car surrogate each used an outage pressure of 50 psig, and an outage volume of approximately 17.6 percent. That outage volume was based on the filling density given in the NPRM, which was 32.5 percent. As the

final rule set a filling density of 37.3 percent, the initial filling volume needed to be recalculated using this new filling density.

Two bounding conditions were identified. At one limit, just prior to activation of the PRV the tank would have a pressure of 75 psig and a 2 percent outage volume. This represents the highest pressure expected to be encountered in normal service and the smallest outage volume. At the other limit, assuming a 15 psig loading pressure and a filling density (by weight) of 37.3 percent would result in an 8.3 percent outage by volume (calculated in this appendix). This set of conditions represents the lowest pressure expected to be encountered in normal service and the largest outage volume.

The calculations made to determine these outage pressure and volume targets used saturated liquid methane properties obtained from and are presented in Table G1 [37].

**Table G1. Assumed Properties Used in Outage Pressure and Volume Calculations**

| Description | Value | Unit |
|---|---|---|
| STDP of the PRV | 75.0 | psig |
| Minimum vapor space volume as a percentage of tank car volume at STDP condition | ~2 | % |
| Maximum liquid volume as a percentage of tank car volume at STDP condition | ~98 | % |
| Maximum tank car pressure at the time of offering the tank car for transportation | 15.0 | psig |
| Liquid filling density by weight[15] | 37.3 | % by weight |

Using the filling density by weight, STDP, and minimum vapor space at STDP condition from the table above, the liquid filling density by volume was calculated for two further pressures of interest. The first pressure of interest was the initial filling pressure of 15 psig. This filling volume would represent the smallest liquid percent (by volume) expected to be encountered during normal service. The second pressure of interest was a pressure of 50 psig, the target pressure for this test. This pressure and corresponding liquid volume would represent a DOT-113 tank car that has been in transit for a period of time, causing it to heat up and for the liquid inside to expand.

One assumption made in these calculations was that for each pressure examined, the LNG remained saturated. Therefore, with the total mass of LNG within the tank remaining constant at each pressure, the volume occupied by the LNG would vary because the saturated liquid density varies with pressure. As the liquid mass remains constant at each pressure, the liquid mass per

[15] Ratio of the weight of saturated liquid at 15 psig and the weight of water occupying the entire tank car volume at 60 °F. The density of water used in these calculations was 997.94 kg/m$^3$.

unit tank volume also remains constant as the volume of the tank is also assumed to remain unchanged at each pressure.

The filling density by weight is calculated as the ratio of the liquid mass per unit tank volume to the density of water at 60 °F, as shown in Equation G1. Since the density of water and the filling density given in the final rule are known, this equation is rearranged to solve for the liquid mass per unit tank volume.

**Equation G1. Filling Density**

$$Filling\ Density = \frac{Liquid\ Mass\ per\ Unit\ Tank\ Volume}{Density\ of\ Water\ (mass\ of\ liquid\ per\ unit\ volume\ of\ liquid)}$$

$$Liquid\ Mass\ per\ Unit\ Tank\ Volume = Density\ of\ Water \cdot Filling\ Density$$

$$Liquid\ Mass\ per\ Unit\ Tank\ Volume = 997.94\ \frac{kg}{m^3} \cdot 37.3\%$$

$$Liquid\ Mass\ per\ Unit\ Tank\ Volume = 372.2\ \frac{kg}{m^3}$$

As a check on this value of liquid mass per unit tank volume, the final rule stated that at the STDP of 75 psig the outage would be approximately 2 percent of the tank's volume. This outage volume fraction corresponds to a liquid volume fraction of 98 percent. Thus, the liquid mass per unit tank volume at the STDP can be used to calculate the liquid volume fraction according to Equation G2.

**Equation G2. Liquid Mass per Unit Tank Volume**

$$Liquid\ Volume\ Fraction = \frac{Liquid\ Mass\ per\ Unit\ Tank\ Volume\ at\ STDP}{Liquid\ Density\ at\ STDP}$$

$$Liquid\ Volume\ Fraction = \frac{372.2\frac{kg}{m^3}}{381.5\frac{kg}{m^3}}$$

$$Liquid\ Volume\ Fraction = 97.6\%$$

$$Outage\ Volume\ Fraction = 100\% - 97.6\%$$

$$Outage\ Volume\ Fraction = 2.4\%$$

As both the liquid mass per unit tank volume and the filling density by weight remain constant across all pressures, the liquid volume fraction at the other pressures of interest are simply the ratio of the liquid mass per unit tank volume to the liquid density at each saturated gage pressure of interest. These calculations are shown in Equation G3.

**Equation G3. Liquid Volume Fraction**

$$Liquid\ Volume\ Fraction = \frac{Liquid\ Mass\ per\ Unit\ Tank\ Volume}{Liquid\ Density}$$

$$\frac{372.2\,\frac{kg}{m^3}}{410.6\,\frac{kg}{m^3}} = 90.7\%\ (at\ 15\ psig)$$

$$\frac{372.2\,\frac{kg}{m^3}}{391.6\,\frac{kg}{m^3}} = 95.0\%\ (at\ 50\ psig)$$

**Table G2. Liquid Volume Fractions at Varied Pressures of Interest**

| Condition | Saturated Gage Pressure (psig) | Liquid Density at Saturated Gage Pressure ($kg/m^3$) [37] | Liquid Volume Fraction at Saturated Gage Pressure (%) |
|---|---|---|---|
| Assumed Loading Pressure, from NPRM | 15 | 410.6 | 90.7 |
| Target Test Pressure | 50 | 391.6 | **95.0** |
| Start-to-discharge Pressure, from NPRM | 75 | 381.5 | 97.6 |

Thus, a liquid volume fraction of 95.0 percent, corresponding to a 5.0 percent outage, was used for the target test pressure of 50 psig. Over the range of gage pressures expected during typical service conditions, the outage volume fraction was expected to range between 9.3 and 2.4 percent.

## G2. Pre- and Post-test Pressures and Temperatures

Test data were recorded from 1 second prior to impact through 30 seconds after impact. Pressure measurements made in the second prior to impact are plotted on the left side of Figure G1 and the pressure measurements recorded from 29 to 30 seconds after impact are plotted on the right side. Both sides of this figure show that the pressure measurement from a given transducer was stable over each one second duration, indicating the pressure was stable at both periods of time. While each transducer's pressure-time history followed a different path during the impact event, each pressure transducer showed a drop in pressure between the start of the test and after the test.

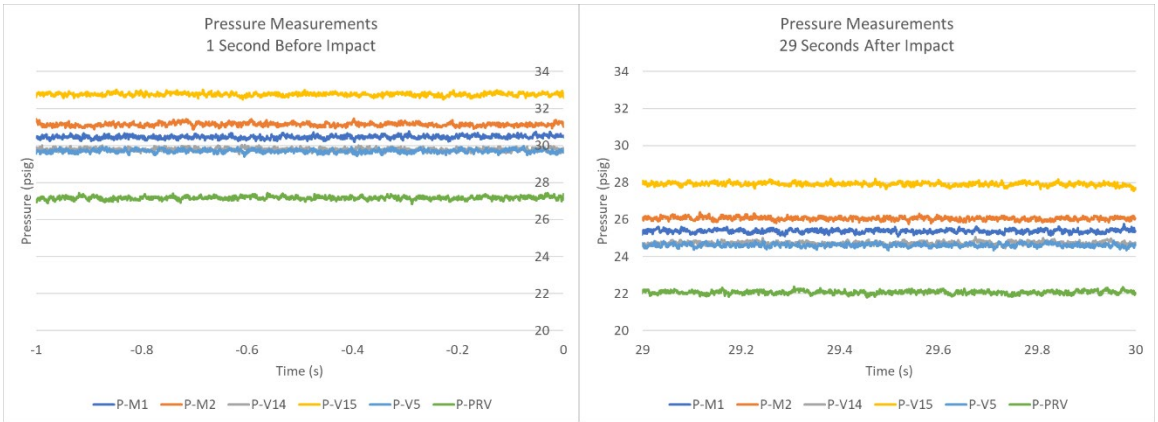


**Figure G1. Pressure Measurements Recorded in the Second Before Impact (left) and 29 Seconds After Impact (right)**

Temperature measurements were recorded on the morning of the test several hours prior to the release of the ram car to assess the initial conditions within the tank. The temperature versus time measurements made using the combination pressure/temperature sensors are plotted in Figure G2. These sensors had an allowable temperature range of -320 to 70 °F (see Table 11). The data collected before the test shows that several of the combination temperature/pressure sensors jumped suddenly between these two limit temperatures without measuring any intermediate values. Two of the sensors recorded a constant temperature near the 70 °F upper limit. This created some uncertainty for these measurements. These sensors were installed in piping external to the inner tank, and thus may have been at a temperature very near or above the upper limit of the sensors' rating. The measurements made by the combination sensors could not be relied upon to determine the initial temperature of the LN2.

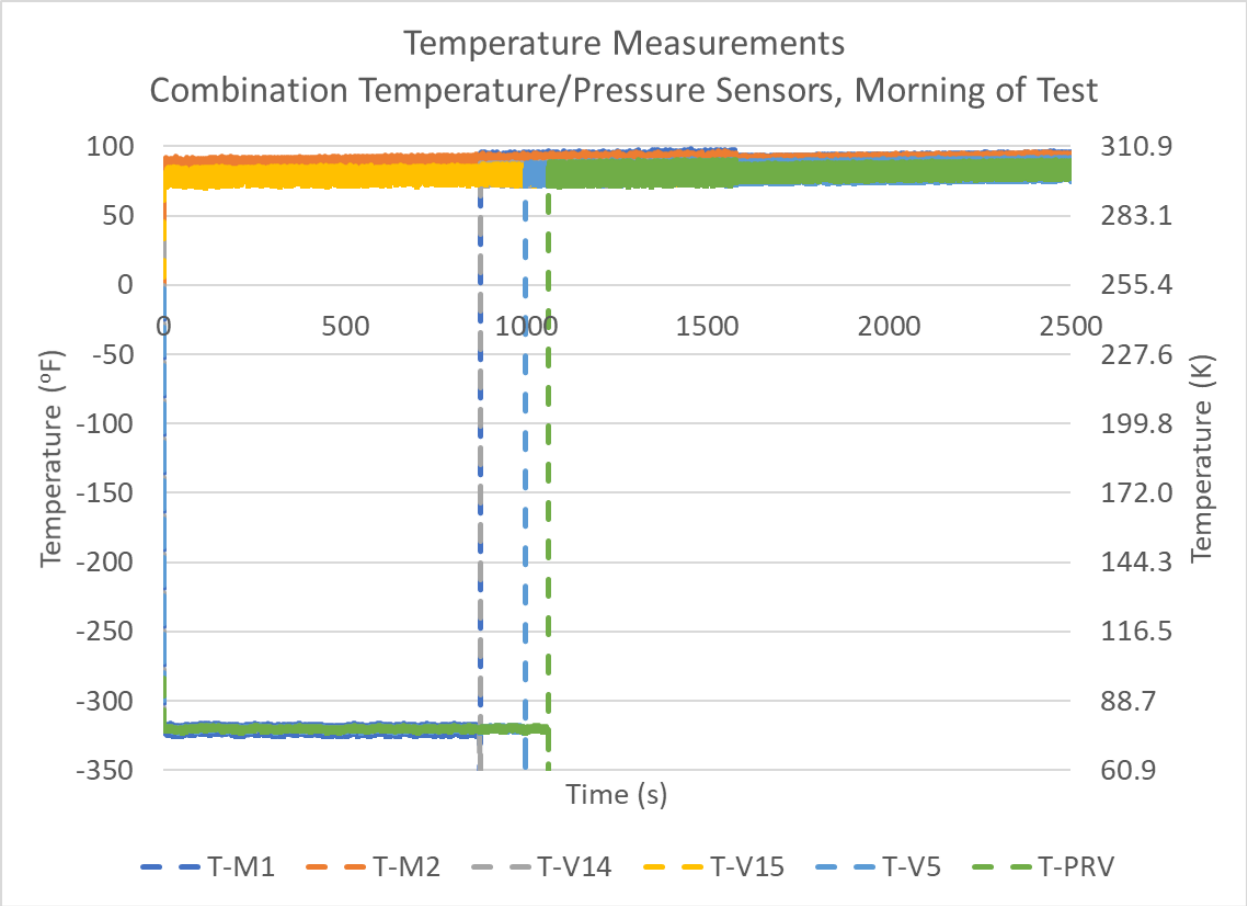


**Figure G2. Temperature Measurements from Combination Temperature/Pressure Sensors Taken on the Morning of the Test**

Similar temperature-time measurements were made on the morning of the test using the five functioning thermocouples within the tank. These measurements are shown in Figure G3. This figure includes a dashed line indicating the saturation temperature of -302 °F for LN2 at a pressure of 42.3 psia (30 psig, the known initial pressure). At 30 psig, LN2 must be kept at or below this temperature to remain in the liquid state, while GN2 must be at or above this temperature. Thermocouples TT2000 and TT3000 were installed in the outage at the top of the tank and were expected to report temperatures above the saturation temperature. The remaining thermocouples were submerged below the liquid-vapor level and were expected to report temperatures below the saturation temperature.

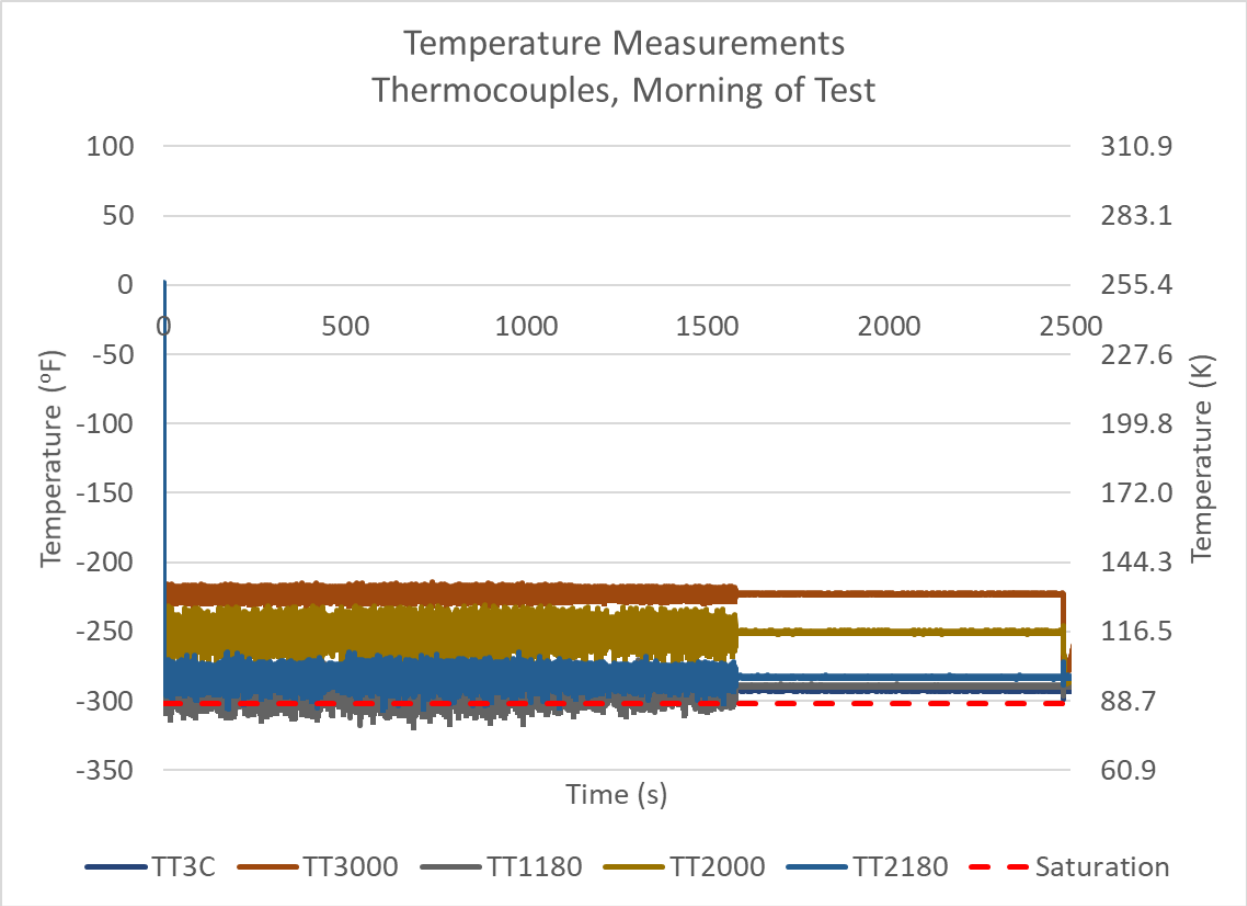


**Figure G3. Temperature Measurements from Thermocouples Taken on the Morning of the Test**

The thermocouple measurements made in the second leading up to impact are shown in Figure G4. While each thermocouple measured a stable temperature at its location, all of the measured temperatures are once again above the saturation temperature at 30 psig. The thermocouple named TT3C (shown in Figure 39) was installed furthest from the surface of the inner tank on a bracket extending 3 feet from the center of the B-end head into the LN2, and it gave the coldest temperature reading prior to the impact (approximately -290 °F). However, this temperature measurement was still above the saturation temperature of LN2 at 30 psig. While a temperature above the saturation temperature is expected for the two thermocouples in the vapor space (i.e., TT3000 and TT2000), the remaining temperature measurements are suspicious since LN2 cannot exist at the measured temperatures and a pressure of 30 psig, but LN2 was known to exist within the tank.

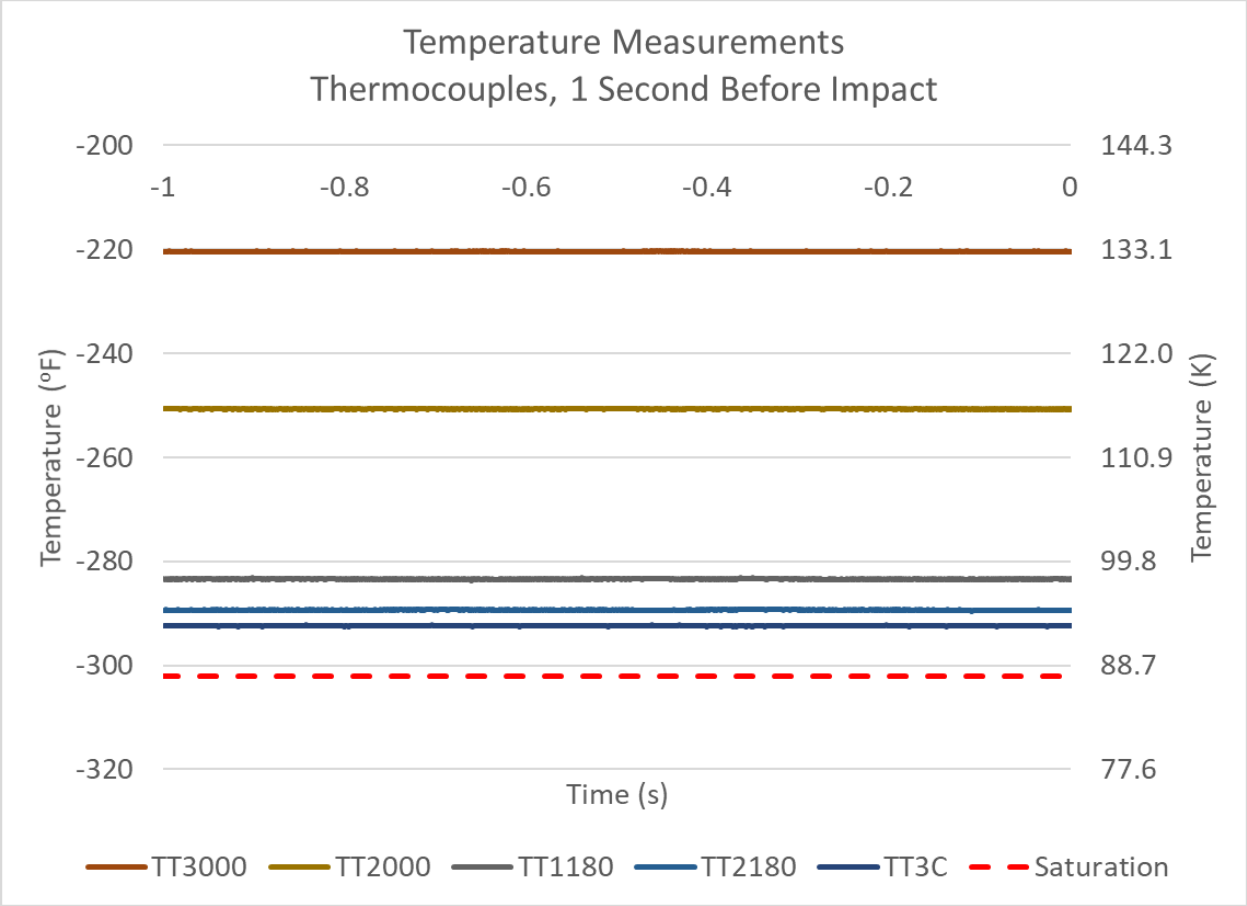


**Figure G4. Temperature Measurements from Thermocouples Measured in the Second Prior to Impact**

## G3. Post-test Estimate of Actual Filling Level

The actual test pressure was known to be 30 psig (see Section 4.5). At that pressure LN2 has a saturated liquid density of 401.4 kg/m$^3$ [37]. Equation G4 shows the calculation of the liquid volume fraction that corresponded to the actual initial test pressure.

**Equation G4. Liquid Volume Fraction, Actual Test Pressure**

$$\frac{372.2\,\frac{kg}{m^3}}{401.4\,\frac{kg}{m^3}} = 92.7\%\ (at\ 30\ psig)$$

The actual outage during the test was estimated to be approximately 9 percent (see Section 4.5), corresponding to a 91 percent liquid volume fraction. The corresponding saturated liquid density for this filling density was back-calculated using Equation G5.

**Equation G5. Liquid Density, Actual Test Liquid Volume Fraction**

$$\frac{\mathbf{372.2}\,\boldsymbol{\frac{kg}{m^3}}}{\boldsymbol{Liquid\ Density}} = \mathbf{91.0\%}$$

$$Liquid\ Density = 409.0\,\frac{kg}{m^3}$$

This value of liquid density was used to estimate the saturation pressure that corresponded to a 91 percent liquid volume fraction. At 15 psig, LN2 has a saturated liquid density of 410.6 kg/m$^3$ and at 20 psig LN2 has a saturated liquid density of 407.2 kg/m$^3$ [37]. Using linear interpolation between these values, the calculated liquid density of 409.0 kg/m$^3$ for a 9 percent outage corresponds to an outage saturation pressure of approximately 18.8 psig.

Table G3 summarizes the liquid volume fraction calculations at actual test conditions. The actual test conditions of a 9 percent outage (i.e., 91 percent liquid volume fraction) at 30 psig differed both from the target test conditions (i.e., a 5 percent outage at 50 psig) and from the saturation conditions at the actual pressure or outage.

**Table G3. Liquid Volume Fractions at Actual Test Conditions**

| Condition | Saturated Gage Pressure (psig) | Liquid Density at Saturated Gage Pressure (kg/m$^3$) [37] | Liquid Volume Fraction at Saturated Gage Pressure (%) |
|---|---|---|---|
| Actual Test Pressure | **30** | 401.4 | 92.7 |
| Actual Test Outage Volume | 18.8 | 409.0 | **91.0** |

# Appendix H.
# Post-Test FEA with Pressure-time Test Data as Input

As a further investigation of the outage modeling techniques, the authors used the pressure-time history data measured by each sensor as a pressure load input to the model instead of using a pneumatic cavity. The authors observed that using each sensor's measured data as a model input resulted in an overestimation of the tank car's global stiffness. The authors used a similar technique in modeling the side impact of a DOT-111 tank car meeting industry-sponsored standard CPC-1232 to investigate the effect of water and air leakage out of the manway [14].

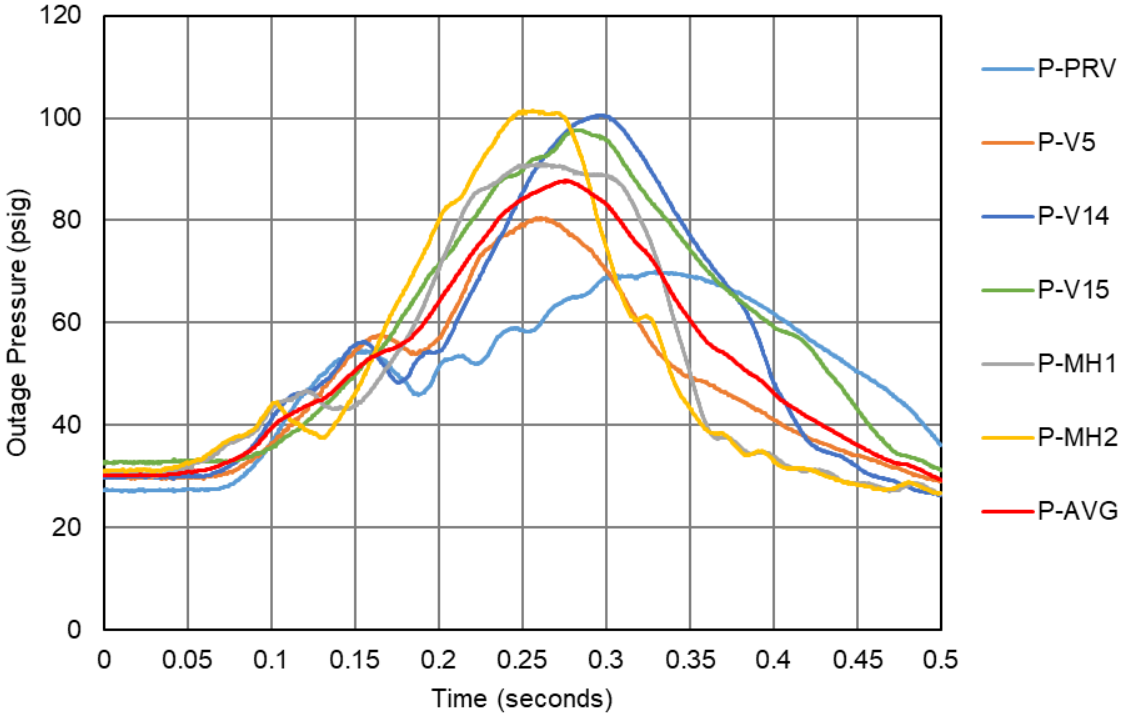


**Figure H1. Pressure-time History Measurements from Outage**

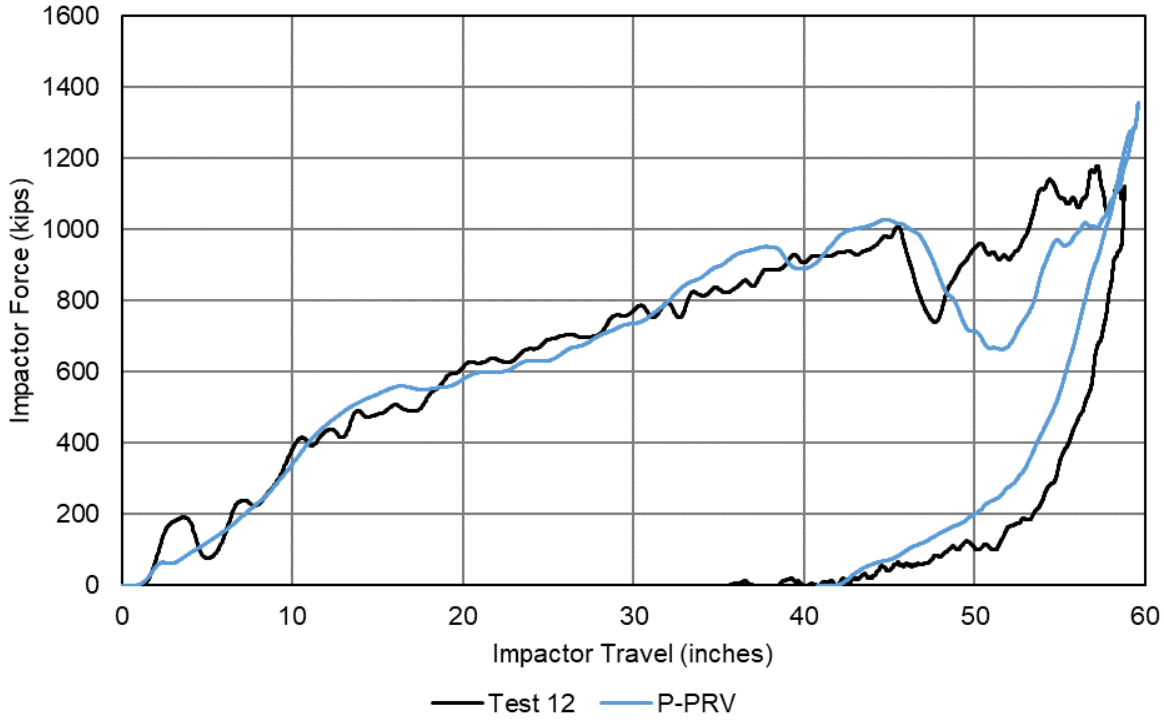


**Figure H2. Non-puncture FE Model Result with PRV Pressure Data as Input**

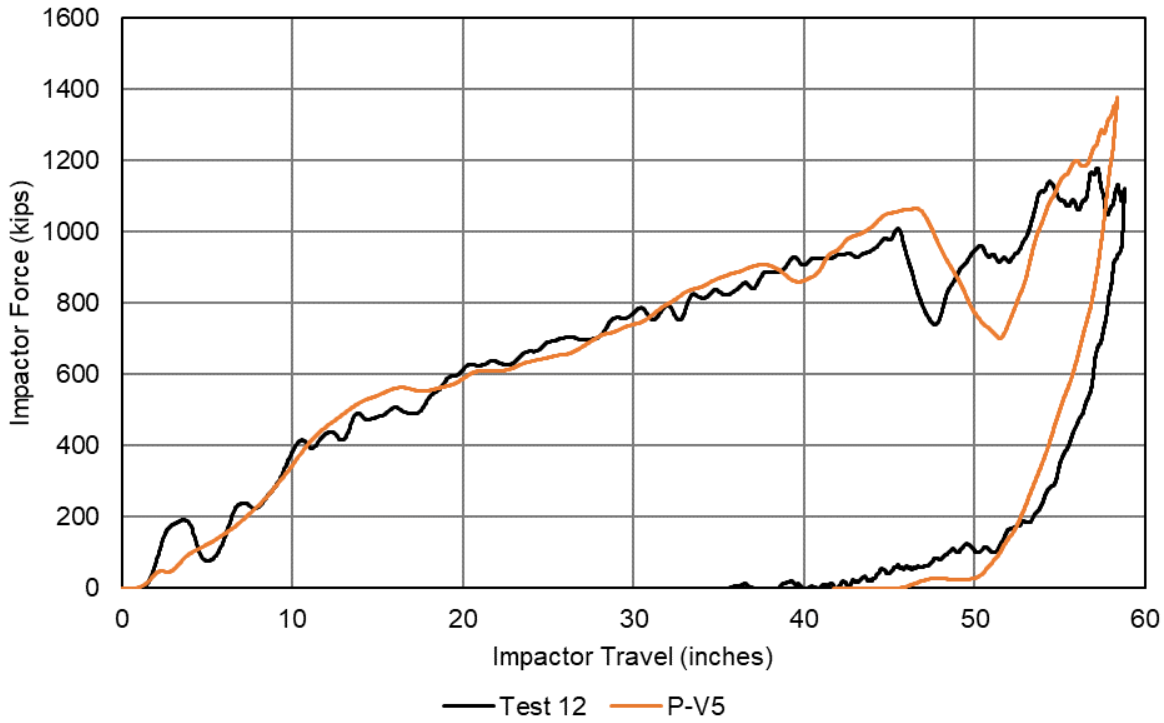


**Figure H3. Non-puncture FE Model Result with V5 Pressure Data as Input**

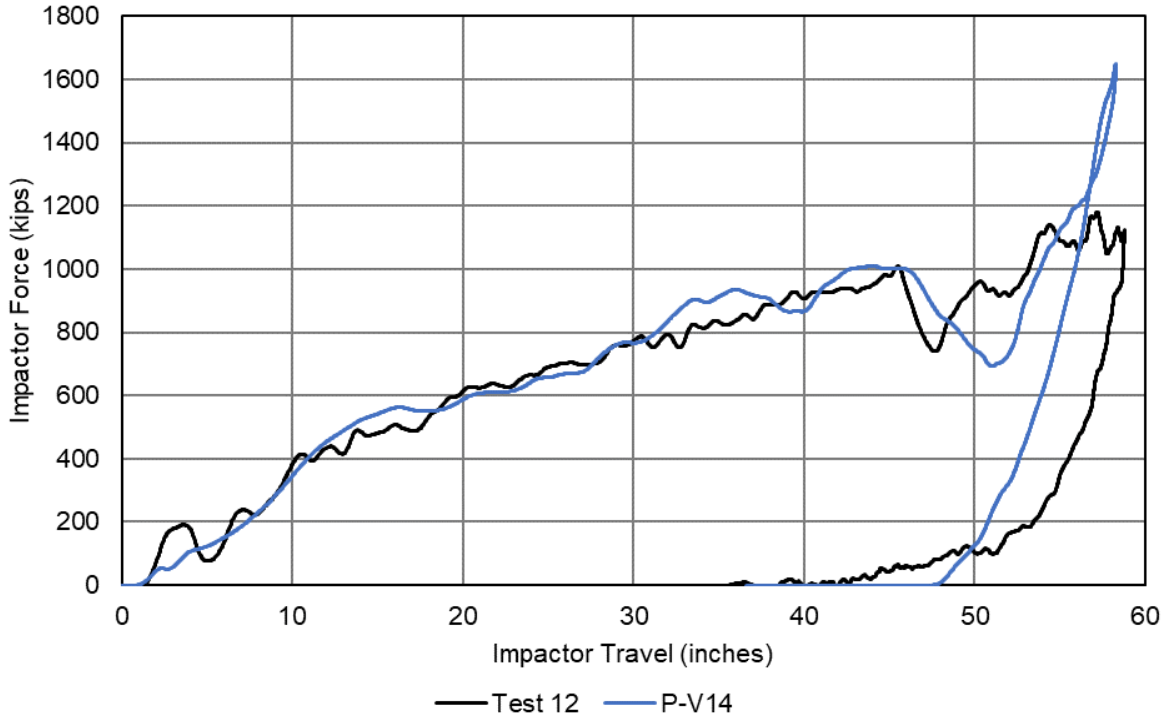


**Figure H4. Non-puncture FE Model Result with V14 Pressure Data as Input**

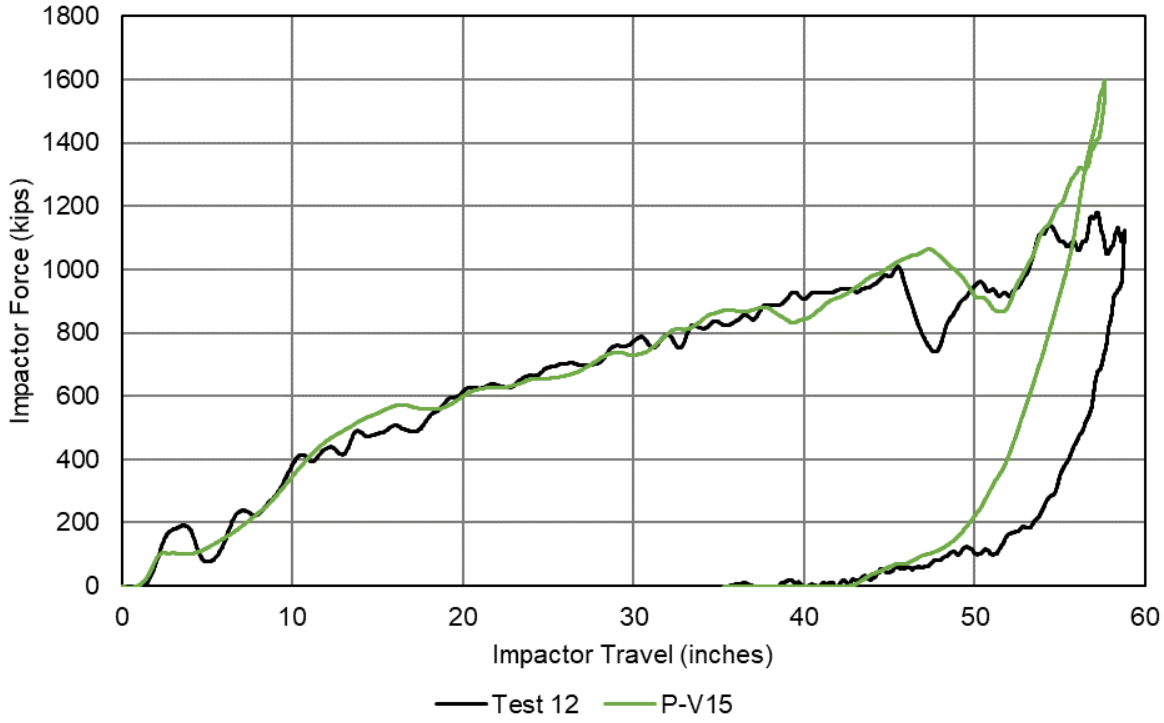


**Figure H5. Non-puncture FE Model Result with V15 Pressure Data as Input**

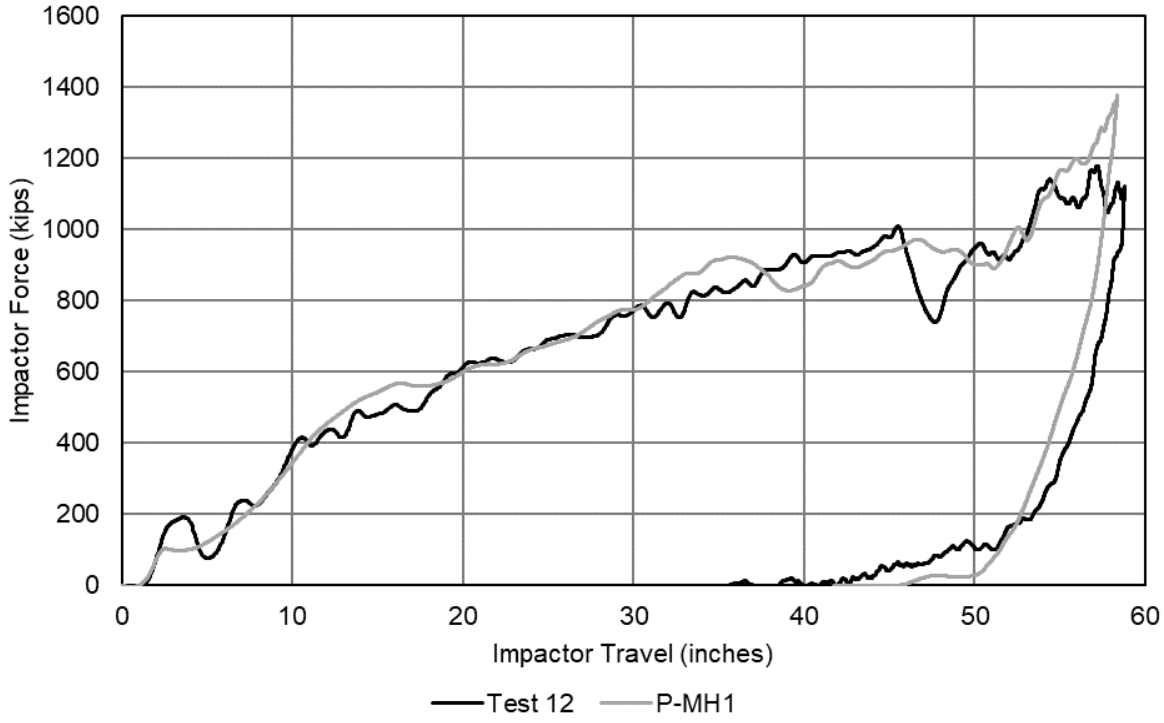


**Figure H6. Non-puncture FE Model Result with MH1 Pressure Data as Input**

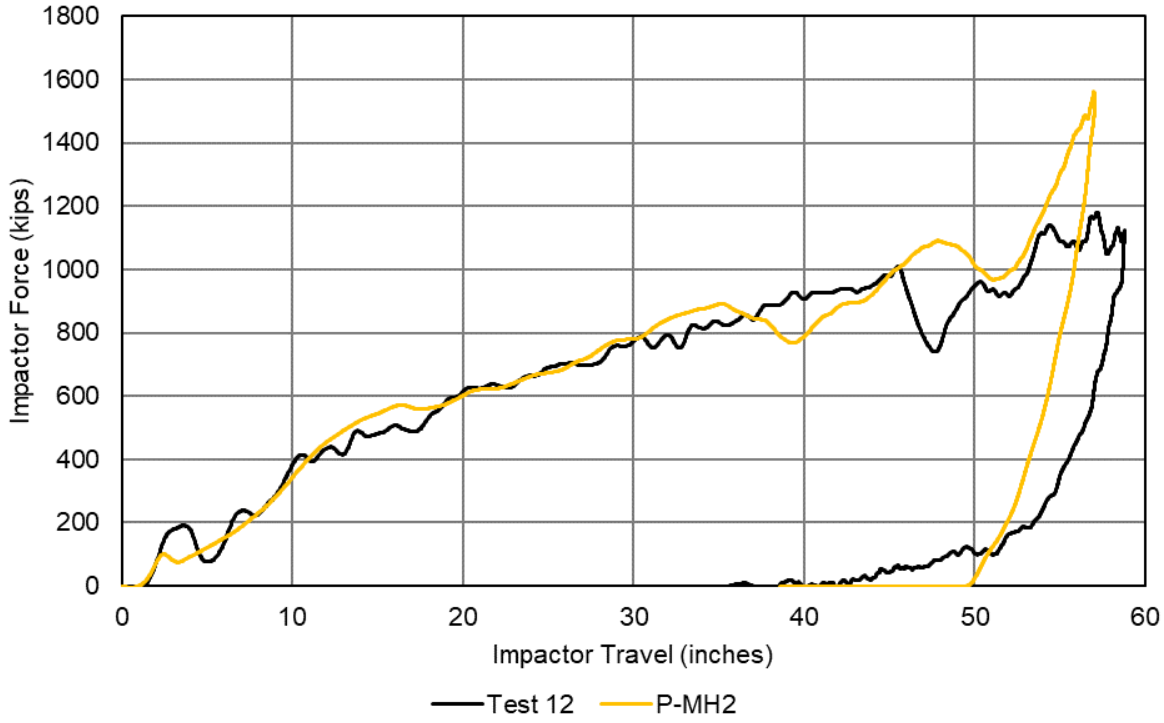


**Figure H7. Non-puncture FE Model Result with MH2 Pressure Data as Input**

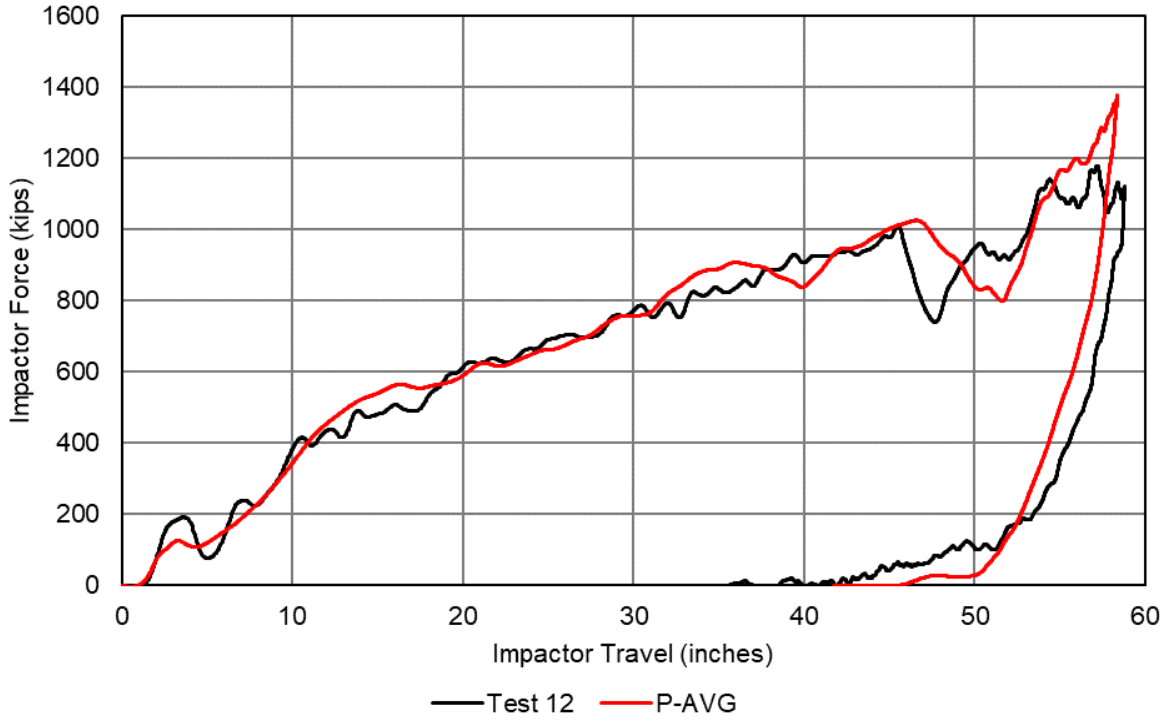


**Figure H8. Non-puncture FE Model Result with Average Outage Pressure Data as Input**

# Appendix I.
# Post-puncture Behaviors of LN2

In a test where the inner and outer tanks of the DOT-113 surrogate are both punctured, there was concern expressed in the pre-test discussions that such a situation could lead to a pressure building inside the inner tank. This pressure rise was hypothesized to come about due to two distinct thermodynamic processes. Considerable discussion and simplified pre-test calculations were performed to attempt to estimate the amount of LN2 that would convert to GN2 due to two phenomena: *superheated* LN2 undergoing a rapid phase transition when pressure quickly dropped to 1 atmosphere following puncture, and LN2 boiling off as a result of the "hot" impactor continuing to move forward after puncturing the inner tank. Regardless of the phenomena responsible for causing LN2 to vaporize, if the vapor could not escape the tank as quickly as it was being created pressure would build within the inner tank. Additionally, both rapid vaporization due to a pressure reduction and vaporization of LN2 due to heat transfer from the impactor could occur simultaneously under particular initial conditions (i.e., pressure and temperature of the LN2) and test outcome (i.e., puncture with impactor continuing forward).

This appendix includes simplified calculations and discussion of the potential concerns. One important limitation common to both the calculations and the discussion presented in this appendix is the difficulty in determining the rate over which particular behaviors occur. In general, pressure building within the tank is a function of the amount of LN2 converted into vapor, the rate at which the LN2 is converted into vapor, and the rate at which the tank allows the vapor to escape. If only a small mass of LN2 is converted to GN2, the pressure rise is expected to be small. If a large mass of LN2 is converted to GN2 over a long period of time, then the pressure rise is expected to be small as the GN2 will be able to escape the tank before significant pressure buildup can occur. However, if a large quantity of LN2 is converted to GN2 in a short period of time, there was the possibility that GN2 would build up within the inner tank more quickly than it could escape to atmosphere. Estimating the mass of LN2 that would be converted to GN2 under different conditions was relatively straightforward. However, estimating the rates of phase change and vapor venting, particularly through a puncture hole of unknown size and shape, were highly-complex prospects that were not undertaken.

Table I1 contains a list of the symbols used throughout this appendix with a description and value for each one. The values in this table have been grouped by three categories. The first category is *constant values*. These values remained the same throughout the calculations. The second category is *calculated values*. These values are calculated in this appendix, with the equation used to calculate each value noted in this table. The third category is *values that depend on other values*. These values, such as saturated liquid density, depend on the pressure (and corresponding temperature) of the liquid. These values were typically obtained from tables of published values, with the appropriate source noted.

## Table I1. Symbols Used in Appendix I Calculations

| Symbol | Description | Value |
|---|---|---|
| *Constant Values* | | |
| $A_H(t)$ | Area of puncture hole as a function of time | Not determined |
| $C_d$ | Coefficient of discharge for the puncture hole | Not determined |
| $C_{psteel}$ | Specific heat of steel | 502.416 J/(kg-K) [38] |
| d | Inside diameter of inner tank | 106 inch (Table 30) |
| E | Welded joint efficiency | 0.9 [39] |
| $\mu_{N2}$ | Molar mass of N2 | 28 grams/mol [26] |
| $m_{impactor}$ | Mass of impactor head | 1,014 kg |
| $P_{atm}$ | Final pressure of the liquid after depressurization (1 atmosphere) | 12.3 psia [29] |
| $Pct_{outage}$ | Outage (vapor space) as a percentage | 9% |
| $\rho_{liquid\text{-}atm\text{-}sat}$ | Density of saturated LN2 at atmospheric pressure | 814.1 kg/m$^3$ [40] |
| $R_U$ | Universal Gas Constant | 8.3145 J/(mol-K) [26] |
| S | Minimum tensile strength of the plate material | 75,000 psi<br>(minimum, room temperature [16])<br>OR<br>179,300 psi<br>(0.05/s, 77K from Test 11 car [Table B3]) |
| $T_{atm\text{-}saturation}$ | Saturation temperature of N2 at atmospheric pressure | 75.9 K [40] |
| $T_{impactor}$ | Temperature of impactor head | 291 K [assumed value] |
| $t_{plate}$ | Minimum thickness of plate, after forming, in inches | 0.25 inch (Table 30) |
| $V_{tank}$ | Volume of inner tank | 67.8 m$^3$ (17,900 gal) [Table 30] |
| Z | Vapor compressibility factor at elevated pressure | 0.9 (See Page VI-C-1 of [41]) |
| *Calculated Values* | | |
| $\Delta m_{1,L}$ | Incremental mass of liquid vaporized | Calculated in Equation I25 |
| $\Delta T_{impactor}$ | Change in impactor temperature | Calculated in Equation I13 |
| f | Mass fraction of the liquid that vaporizes when released from pressure $P_i$ to $P_{atm}$ | Calculated in Equation I1 |
| $f_{quench}$ | Mass fraction of the liquid that vaporizes when impactor is quenched in saturated LN2 | Calculated in Equation I16 |
| $m_{liquid1}$ | Initial mass of LN2 inside tank car | Calculated in Equation I3 |
| $m_{liquid2}$ | Post-flash or post-quench mass of LN2 inside tank car | Calculated in Equation I5 (flash)<br>Calculated in Equation I17 (quench) |
| $m_{liquidquench}$ | Mass of liquid vaporized by quenching impactor | Calculated in Equation I15 |
| $m_{vapor1}$ | Initial mass of vapor in vapor space | Calculated in Equation I4 |
| $m_{vaporflash}$ | Mass of vapor produced by flash | Calculated in Equation I6 |
| $m_{vaportotal}$ | Total mass of vapor in vapor space after flash | Calculated in Equation I9 |
| $\dot{m}_{1,L}(t)$ | Mass rate of liquid flow out through the puncture hole at any instant of time | Calculated in Equation I1 |
| $P_{burst}$ | Burst pressure of inner | Calculated in Equation I22 and Equation I23 |
| $P_{tank}$ | Theoretical maximum pressure for isothermal accumulation of gas in the vapor space | Calculated in Equation I11 (flash)<br>Calculated in Equation I19 (quench) |
| $q_{impactor}$ | Heat of impactor released to LN2 | Calculated in Equation I12 |
| $\rho_{vapor2}$ | Vapor density in vapor space after flash, assuming no outflow of gases | Calculated in Equation I10 |
| $V_{liquid2}$ | Volume of liquid at atmospheric pressure after flash | Calculated in Equation I7 |
| $V_{vapor2}$ | Vapor space volume after flash, assuming incompressible liquid | Calculated in Equation I8 |

| Symbol | Description | Value |
|---|---|---|
| *Values that Depend on Other Values* | | |
| $c_{pLN2}$ | Specific heat of LN2 at the pressure indicated | Varies with pressure<br>Date obtained from [21] |
| $h_L^{sat}$ | Enthalpy of the saturated liquid at the pressure indicated | Varies with pressure<br>Data obtained from [40] |
| $h_v^{sat}$ | Enthalpy of the saturated vapor at the pressure indicated | Varies with pressure<br>Data obtained from [40] |
| $\lambda_{L\text{-}V}$ | Heat of vaporization of saturated liquid to saturated vapor at the pressure indicated | Varies with pressure<br>Data obtained from [40] |
| P | A given value of pressure. | Hypothetical value of pressure. |
| $P_1$ | Initial (saturation) pressure of the liquid | Varied for this study |
| $\rho_{liquid1}$ | Density of saturated LN2 at initial pressure | Varies with pressure<br>Data obtained from [40] |
| $\rho_{vapor1}$ | Density of saturated GN2 at initial pressure | Varies with pressure<br>Data obtained from [40] |
| $T_{sat}$ | Saturation temperature for N2 | Varies with pressure<br>Correlation calculation parameters from [42] |

## I1. Analysis of Phenomena Occurring After Puncture of a Tank Car Containing a Pressurized Cryogenic Liquid

The purpose of this appendix is to discuss the possible outcomes of subjecting a cryogenic tank car to an impact test and describe the various physical phenomena that could occur, primarily due to the potential for very rapid vaporization of a part of the liquid mass due to rapid depressurization.[16] A second objective is to determine the optimal initial pressure of the lading commensurate with a successful test but also ensuring safety of personnel and test equipment.

The appendix provides a description of the following phenomena and modeling approaches to evaluate the tank car pressure as a function of time. Discussions of the physics of these phenomena are also provided.

- Flash vaporization of a liquid that is initially pressurized and in a superheated state (relative to the condition of liquid at the final pressure), and rapidly depressurized.
- Description of the physical behavior of the liquid-vapor system in the tank car when the depressurization rate varies from very low (pressure drop in minutes) to very high rate (pressure drop in fractions of seconds)
- Model to estimate the maximum pressure realized in the tank car if there is absolutely no venting.
- An approach to modeling the behavior of the liquid-vapor system under different rates of depressurization and venting of the tank car.

[16] This appendix was contributed by Dr. Phani Raj of FRA's Office of Railroad Safety.

## I2. Flash Vaporization of a Liquid

When a liquid in equilibrium with its vapor (i.e., in a saturated condition) is heated (or alternately, is pressurized) the heat added manifests itself as increased internal energy of the liquid and of the vapor. The liquid is said to be in a *superheated* condition relative to its "normal" condition at, for example, the atmospheric pressure. If this superheated (and also pressurized relative to atmospheric pressure) liquid is suddenly depressurized back to the atmospheric pressure, the extra heat (i.e., *superheat*) stored in the liquid is used to vaporize a part of the liquid and leave the rest of the vaporized liquid at a state (i.e., temperature) corresponding to the lower pressure. This phenomenon of auto-vaporization due to depressurization is termed liquid *flashing*.

The mass fraction of flash (i.e., the fraction of the mass of the liquid that vaporizes due to depressurization) can be calculated from the difference between the saturated enthalpy of LN2 at the initial pressure $[h_L^{sat}(P_1)]$ and atmospheric pressure, $[h_L^{sat}(P_{atm})]$ divided by the heat of vaporization at atmospheric pressure [$\lambda_{L\text{-}V}(P_{atm})$]. This is shown in Equation I1. Examination of this equation shows that if the initial pressure is equal to atmospheric pressure, the numerator is zero and no flash vaporization will occur.

**Equation I1. Mass Fraction of Flash Due to Depressurization**

$$f = \frac{\{h_L^{sat}(P_1) - h_L^{sat}(P_{atm})\}}{\lambda_{L-V}(P_{atm})}$$

The heat of vaporization at a given pressure (P) is the difference between the saturated enthalpy of the vapor $(h_v^{sat})$ and the liquid $(h_L^{sat})$ states at that pressure, as shown in Equation I2. The heat of vaporization at atmospheric pressure [$\lambda_{L\text{-}V}(P_{atm})$] can be calculated using this equation for conditions at atmospheric pressure.

**Equation I2. Heat of Vaporization**

$$\lambda_{L-V}(P) = h_v^{sat}(P) - h_L^{sat}(P)$$

The calculated mass fraction of liquid that forms vapor formed due to a sudden pressure reduction to 1 atmosphere was calculated for numerous initial pressures. The results are shown in Table I2. The practical range of initial test pressures spanned from atmospheric pressure (12.3 psia) to the STDP of the PRV (87.3 psia). The saturation pressures and temperatures were calculated using equations and parameters for LN2 from a published source [42].

**Table I2. Saturation Thermodynamic Properties of Nitrogen and Flash Mass Fractions**

| $P_{sat}$ | $P_{sat}$ | $T_{sat}$ | $\rho_{liquid1}$ | $\rho_{vapor1}$ | $h_L^{sat}$ | $h_v^{sat}$ | $\lambda_{L\text{-}V}(P_{sat})$ | $f$ |
|---|---|---|---|---|---|---|---|---|
| - | [42] | [42] | [40] | [40] | [40] | [40] | Equation I2 | Equation I1 |
| (psia) | (kPa) | (K) | (kg/m$^3$) | (kg/m$^3$) | (kJ/kg) | (kJ/kg) | (kJ/kg) | % |
| 12.30 | 84.8 | 75.89 | 814.1 | 3.91 | 26.2949 | 227.4961 | 201.201 | 0.00 |
| 12.46 | 85.9 | 76.00 | 813.6 | 3.96 | 26.516 | 227.585 | 201.069 | 0.11 |
| 14.06 | 97.0 | 77.00 | 809.1 | 4.42 | 28.644 | 228.374 | 199.730 | 1.17 |
| 14.70 | 101.4 | 77.37 | 807.4 | 4.60 | 29.397 | 228.657 | 199.260 | 1.54 |
| 15.81 | 109.0 | 78.00 | 804.4 | 4.93 | 30.712 | 229.144 | 198.432 | 2.20 |
| 17.73 | 122.2 | 79.00 | 799.8 | 5.48 | 32.119 | 229.893 | 197.774 | 2.89 |

| $P_{sat}$ | $P_{sat}$ | $T_{sat}$ | $\rho_{liquid1}$ | $\rho_{vapor1}$ | $h_L^{sat}$ | $h_v^{sat}$ | $\lambda_{L\text{-}V}(P_{sat})$ | $f$ |
|---|---|---|---|---|---|---|---|---|
| - | [42] | [42] | [40] | [40] | [40] | [40] | Equation I2 | Equation I1 |
| (psia) | (kPa) | (K) | (kg/m$^3$) | (kg/m$^3$) | (kJ/kg) | (kJ/kg) | (kJ/kg) | % |
| 19.81 | 136.6 | 80.00 | 798.9 | 6.07 | 34.845 | 230.621 | 195.776 | 4.25 |
| 22.07 | 152.2 | 81.00 | 790.4 | 6.71 | 36.912 | 231.328 | 194.416 | 5.28 |
| 24.53 | 169.1 | 82.00 | 785.6 | 7.40 | 38.980 | 232.011 | 193.031 | 6.30 |
| 27.18 | 187.4 | 83.00 | 780.8 | 8.14 | 41.050 | 232.671 | 191.621 | 7.33 |
| 30.04 | 207.1 | 84.00 | 776.3 | 8.94 | 43.122 | 233.301 | 190.179 | 8.36 |
| 33.12 | 228.4 | 85.00 | 771.0 | 9.79 | 45.198 | 233.917 | 188.719 | 9.40 |
| 36.43 | 251.2 | 86.00 | 766.0 | 10.70 | 47.279 | 234.500 | 187.221 | 10.43 |
| 39.98 | 275.7 | 87.00 | 761.0 | 11.68 | 49.366 | 235.051 | 185.685 | 11.47 |
| 42.30[17] | 291.7 | 87.62 | 757.9 | 11.06 | 50.6603 | 235.3809 | 184.721 | 12.11 |
| 43.78 | 301.9 | 88.00 | 756.0 | 10.70 | 51.461 | 235.585 | 184.124 | 12.51 |
| 47.84 | 329.8 | 89.00 | 750.9 | 13.84 | 53.564 | 236.084 | 182.520 | 13.55 |
| 52.17 | 359.7 | 90.00 | 745.7 | 15.03 | 55.617 | 236.553 | 180.936 | 14.57 |
| 56.78 | 391.5 | 91.00 | 740.4 | 16.29 | 57.802 | 236.991 | 179.189 | 15.66 |
| 61.68 | 425.3 | 92.00 | 735.1 | 17.64 | 59.540 | 231.396 | 171.856 | 16.52 |
| 66.88 | 461.1 | 93.00 | 729.7 | 19.07 | 62.092 | 237.161 | 175.069 | 17.79 |
| 72.39 | 499.1 | 94.00 | 724.2 | 20.59 | 64.261 | 238.104 | 173.843 | 18.87 |
| 78.23 | 539.4 | 95.00 | 718.6 | 22.21 | 66.449 | 238.405 | 171.956 | 19.96 |
| 84.40 | 581.9 | 96.00 | 713.1 | 24.27 | 68.656 | 238.669 | 170.013 | 21.05 |
| 87.30[18] | 601.9 | 96.45 | 710.5 | 24.92 | 69.662 | 238.770 | 169.108 | 21.55 |

## I3. Theoretical Maximum Tank Car Pressure Due to Flash

If all the vapor produced by flash vaporization of the liquid in a tank car is assumed to remain within the inner tank, a calculation can be made of the maximum pressure attained within the tank car under the following assumptions

a) The flash vaporization is triggered by the sudden depressurization in the tank car due to the puncture.

b) The time scale for flash vaporization is very short (milliseconds) compared to the time to initiate any pressure relief due to PRV or the liquid flow through the puncture hole (fractions of seconds due to liquid and mechanical parts inertia).

c) Rapid build-up of pressure within the tank car does not suppress flashing.[19]

[17] Initial pressure (30 psig) from test

[18] STDP (75 psig) from PRV used in test

[19] This is a very dubious assumption since vaporization stops when the pressure rises to above the initial temperature of the liquid – that is pressurization of the tank car makes the liquid subcooled with respect to the instantaneous pressure.

d) The tank car walls are strong and do not burst open due to pressurization of tank car beyond the burst pressure.[20]

e) The gas pressure increases isothermally (i.e., the gas in the tank car is at the saturation temperature corresponding to the final saturation pressure attained by the liquid of 1 atmosphere).

The following calculations were used to estimate the maximum theoretical pressure that could be reached within the tank, subject to the above assumptions. During the flash event, the volume of liquid decreases due to evaporation and this liquid yielded volume becomes occupied by the vapor. As the time scale for the flash event is much smaller than the time scale for venting of the tank (Assumption b) the total mass of N2 within the tank remains constant before and after the flash event. A simplified set of calculations based on the above assumptions are presented in this appendix. As noted above, these calculations are a highly-simplified representation of a complex thermodynamic event. As the initial pressure within the tank was considered a variable parameter prior to the test, the effect of different assumed initial pressures (and consequent saturation properties) was examined using this approach.

Initially, the tank car is partially-filled with LN2 having a mass of $m_{liquid1}$. The mass of LN2 initially within the tank depends on the volume of the tank, the outage percentage (i.e., the amount of vapor within the tank), and the density of the LN2 according to Equation I3.

**Equation I3. Initial Mass of LN2 in Tank Car**

$$m_{liquid_1} = \frac{(100 - Pct_{outage})}{100} \cdot V_{tank} \cdot \rho_{liquid_1}$$

The remaining volume of the tank car is filled with GN2 having a mass of $m_{vapor1}$ according to Equation I4.

**Equation I4. Initial Mass of GN2 in Tank Car**

$$m_{vapor_1} = \frac{Pct_{outage}}{100} \cdot V_{tank} \cdot \rho_{vapor_1}$$

The mass of LN2 that remains after the flash (i.e., the mass of liquid that does not flash, $m_{liquid2}$) is found according to Equation I5. The value of $f$, the mass fraction of liquid that flashes due to depressurization, was previously calculated using Equation I1.

**Equation I5. Mass of Liquid After Flash**

$$m_{liquid2} = m_{liquid1} \cdot \frac{(100 - f)}{100}$$

The mass of vapor produced during the flash event is equal to the difference between the initial mass of LN2 in the tank car ($m_{liquid1}$) and the post-flash mass of LN2 in the tank car ($m_{liquid2}$), as

[20] Again, this is a very dubious assumption. However, a primary reason for exploring the potential pressure buildup within the tank car is examining likelihood of sudden burst. A calculated maximum theoretical pressure exceeding the burst pressure of the tank would be cause for concern, since this implies the tank could burst before the maximum theoretical pressure was reached.

shown in Equation I6. This mass relationship is only applicable if no venting of either LN2 or GN2 takes place during the flash event (i.e., total mass within the tank is constant).

**Equation I6. Mass of Vapor Produced by Flash**

$$m_{vapor_{produced}} = m_{liquid_1} - m_{liquid_2}$$

The volume of LN2 that remains in the tank at atmospheric pressure after the flash is the post-flash mass of LN2 in the tank car ($m_{liquid2}$) divided by the saturated density of LN2 at atmospheric pressure ($\rho_{liquid\text{-}atm\text{-}sat}$), as shown in Equation I7.

**Equation I7. Volume of LN2 Remaining After Flash**

$$V_{liquid2} = \frac{m_{liquid_2}}{\rho_{liquid-atm-sat}}$$

The post-flash volume of vapor ($V_{vapor2}$) is the difference between the initial volume of the tank car[21] ($V_{tank}$) and the post-flash volume of liquid that was calculated in Equation I7. Equation I8 shows this calculation, which assumes that the LN2 is incompressible.

**Equation I8. Post-flash Vapor Space Volume**

$$V_{vapor_2} = V_{tank} - V_{liquid_2}$$

As shown in Equation I9, the total mass of vapor after the flash ($m_{vaportotal}$) is equal to the pre-flash mass of vapor in the tank ($m_{vapor1}$) plus the mass of vapor produced by the flash (Equation I6).

**Equation I9. Total Mass of Vapor After Flash**

$$m_{vapor_{total}} = m_{vapor_1} + m_{vapor_{produced}}$$

The density of vapor in the tank following the flash event ($\rho_{vapor2}$) is obtained by dividing the total mass of vapor calculated in Equation I8 with the volume occupied by post-flash vapor calculated in Equation I9. The resulting equation is shown in Equation I10.

**Equation I10. Density of Vapor After Flash**

$$\rho_{vapor_2} = \frac{m_{vapor_{total}}}{V_{vapor_2}}$$

The theoretical maximum pressure that can develop within the inner tank for the isothermal accumulation of gas in the vapor space can be calculated according to Equation I11.

**Equation I11. Maximum Theoretical Pressure Within Tank After Flash**

$$\boldsymbol{P_{tank} = Z\frac{R_U}{\mu_{N_2}}\rho_{vapor_2} \cdot T_{atm-saturation}}$$

[21] This calculation assumes the volume of the tank car does not reduce due to impact. The validity and conservatism of this assumption requires further examination, as the decrease in inner tank volume prior to puncture may result in additional energy stored within the LN2 or GN2 at the time of a flash.

The theoretical maximum pressures that can develop inside the tank for each saturation condition examined are shown in Table I3.

**Table I3. Theoretical Maximum Tank Car Pressure After Liquid Flash for Different Initial LN2 Saturation Temperature Conditions**

| $P_{sat}$ | $P_{sat}$ | $T_{sat}$ | $f$ | $m_{liquid1}$ | $m_{liquid2}$ | $V_{liquid2}$ | $V_{vapor2}$ | $m_{vapor1}$ | $m_{vaporproduced}$ | $m_{vaportotal}$ | $\rho_{vapor2}$ | $P_{tank}$ | $P_{tank}$ |
|---|---|---|---|---|---|---|---|---|---|---|---|---|---|
| - | [42] | [42] | Equation I2 | Equation I3 | Equation I5 | Equation I7 | Equation I8 | Equation I4 | Equation I6 | Equation I9 | Equation I10 | Equation I11 | - |
| (psia) | (kPa) | (K) | % | (kg) | (kg) | ($m^3$) | ($m^3$) | (kg) | (kg) | (kg) | ($kg/m^3$) | (kPa) | (psia) |
| 12.30 | 84.8 | 75.89 | 0.00 | 50197.8 | 50197.8 | 61.7 | 6.1 | 23.8 | 0.0 | 23.8 | 3.9 | 79.3 | 11.5[22] |
| 12.46 | 85.9 | 76.00 | 0.11 | 50167.3 | 50112.1 | 61.6 | 6.2 | 24.1 | 55.1 | 79.3 | 12.8 | 259.2 | 37.6 |
| 14.06 | 97.0 | 77.00 | 1.17 | 49887.2 | 49304.8 | 60.6 | 7.2 | 27.0 | 582.5 | 609.4 | 84.7 | 1717.8 | 249.2 |
| 14.70 | 101.4 | 77.37 | 1.54 | 49782.5 | 49014.9 | 60.2 | 7.6 | 28.1 | 767.5 | 795.6 | 105.4 | 2136.9 | 309.9 |
| 15.81 | 109.0 | 78.00 | 2.20 | 49602.3 | 48513.3 | 59.6 | 8.2 | 30.1 | 1089.0 | 1119.0 | 137.0 | 2778.8 | 403.0 |
| 17.73 | 122.2 | 79.00 | 2.89 | 49316.6 | 47889.1 | 58.8 | 8.9 | 33.4 | 1427.6 | 1461.0 | 163.5 | 3316.5 | 481.0 |
| 19.81 | 136.6 | 80.00 | 4.25 | 49261.5 | 47168.1 | 57.9 | 9.8 | 37.0 | 2093.4 | 2130.4 | 216.9 | 4400.1 | 638.2 |
| 22.07 | 152.2 | 81.00 | 5.28 | 48735.8 | 46164.1 | 56.7 | 11.1 | 40.9 | 2571.7 | 2612.6 | 236.4 | 4794.0 | 695.3 |
| 24.53 | 169.1 | 82.00 | 6.30 | 48441.0 | 45387.0 | 55.8 | 12.0 | 45.1 | 3054.1 | 3099.2 | 258.1 | 5234.7 | 759.2 |
| 27.18 | 187.4 | 83.00 | 7.33 | 48146.0 | 44615.2 | 54.8 | 13.0 | 49.6 | 3530.8 | 3580.4 | 276.4 | 5605.1 | 812.9 |
| 30.04 | 207.1 | 84.00 | 8.36 | 47869.4 | 43865.9 | 53.9 | 13.9 | 54.5 | 4003.5 | 4058.0 | 292.4 | 5931.3 | 860.3 |
| 33.12 | 228.4 | 85.00 | 9.40 | 47540.9 | 43074.4 | 52.9 | 14.8 | 59.7 | 4466.5 | 4526.2 | 304.8 | 6182.5 | 896.7 |
| 36.43 | 251.2 | 86.00 | 10.43 | 47235.0 | 42308.7 | 52.0 | 15.8 | 65.3 | 4926.3 | 4991.6 | 316.1 | 6412.0 | 930.0 |
| 39.98 | 275.7 | 87.00 | 11.47 | 46925.9 | 41545.0 | 51.0 | 16.7 | 71.2 | 5380.8 | 5452.1 | 325.9 | 6610.7 | 958.8 |
| 42.30 | 291.7 | 87.62 | 12.11 | 46732.5 | 41073.2 | 50.5 | 17.3 | 67.4 | 5659.3 | 5726.7 | 330.9 | 6711.2 | 973.4 |
| 43.78 | 301.9 | 88.00 | 12.51 | 46613.7 | 40783.3 | 50.1 | 17.7 | 65.3 | 5830.4 | 5895.7 | 333.8 | 6769.9 | 981.9 |
| 47.84 | 329.8 | 89.00 | 13.55 | 46298.7 | 40023.8 | 49.2 | 18.6 | 84.4 | 6274.9 | 6359.3 | 342.0 | 6935.9 | 1006.0 |
| 52.17 | 359.7 | 90.00 | 14.57 | 45977.6 | 39277.1 | 48.2 | 19.5 | 91.6 | 6700.6 | 6792.2 | 348.1 | 7059.8 | 1023.9 |
| 56.78 | 391.5 | 91.00 | 15.66 | 45654.2 | 38505.0 | 47.3 | 20.5 | 99.4 | 7149.2 | 7248.6 | 354.3 | 7185.0 | 1042.1 |
| 61.68 | 425.3 | 92.00 | 16.52 | 45325.3 | 37836.1 | 46.5 | 21.3 | 107.6 | 7489.2 | 7596.8 | 356.9 | 7239.5 | 1050.0 |
| 66.88 | 461.1 | 93.00 | 17.79 | 44991.3 | 36986.6 | 45.4 | 22.3 | 116.3 | 8004.7 | 8121.0 | 363.7 | 7377.3 | 1070.0 |
| 72.39 | 499.1 | 94.00 | 18.87 | 44655.7 | 36229.3 | 44.5 | 23.3 | 125.6 | 8426.4 | 8552.0 | 367.7 | 7458.1 | 1081.7 |
| 78.23 | 539.4 | 95.00 | 19.96 | 44312.3 | 35468.8 | 43.6 | 24.2 | 135.4 | 8843.5 | 8978.9 | 371.2 | 7528.0 | 1091.8 |
| 84.40 | 581.9 | 96.00 | 21.05 | 43967.9 | 34710.9 | 42.6 | 25.1 | 148.0 | 9257.0 | 9405.1 | 374.4 | 7593.1 | 1101.3 |
| 87.30 | 601.9 | 96.45 | 21.55 | 43809.9 | 34367.1 | 42.2 | 25.5 | 152.0 | 9442.8 | 9594.8 | 375.6 | 7618.2 | 1104.9 |

## I4. Quenching a "Hot" Impactor with LN2

Using a similar approach as used in the previous section, the effects of quenching a "hot" impactor in LN2 could be estimated. If the impactor punctured both the outer and inner tanks and continued to move forward, the impactor head would become submerged in the LN2 within the inner tank. Because the impactor was at ambient temperature when it entered the tank, heat from the impactor would be transferred into the pool of LN2 until both the LN2 and the impactor were

[22] The expected internal pressure calculated for this condition (i.e., saturated LN2 at atmospheric pressure) would also be atmospheric pressure, or 12.3 psia. The value of *Z*, used in Equation I11 to calculate maximum theoretical tank pressure, will affect the calculated pressure.

at the same temperature. Transferring heat from the high-temperature steel impactor to the low-temperature LN2 could have two effects on the LN2, depending on the LN2's condition at the time the impactor was submerged. If the LN2 was unsaturated (i.e., the temperature of the LN2 was lower than the boiling point for its current pressure), the heat removed from the impactor would simply increase the temperature of the LN2 without causing a phase change. If the LN2 heated up to its saturation temperature because of the impactor's heat, or if the LN2 was initially at its saturation temperature when the impactor plunged into it then the heat from the impactor would cause some of the LN2 to change phases into GN2.

The initial temperature of the impactor ($T_{impactor}$) was not typically measured in tests, but could be estimated for ambient conditions. Similarly, at the time these calculations were made (i.e., pre-test), the exact temperature and pressure of the LN2 at the time of the test were not known. The calculations were performed over a range of temperatures for both the impactor and the LN2, since these two parameters were independent of one another. This approach is similar to that used in the flash calculations presented in the previous section.

A combination of heating of LN2 and changing the LN2's phase into GN2 would likely occur. As a means of bookending the possibilities, the effects of quenching the impactor in LN2 were calculated two separate ways. First, the LN2 was assumed to be capable of absorbing the impactor's heat without undergoing a phase change. This calculation gives the maximum value of estimated temperature increase in the bulk temperature of the LN2, since all of the impactor's heat ($q_{impactor}$) goes into raising the LN2's temperature. The second calculation assumed that the LN2 was at its saturation temperature at the instant the impactor entered the LN2. Thus, the second calculation assumed that all of the impactor's heat would be used to vaporize LN2 into GN2. This second calculation gives the maximum value of the estimated mass of LN2 that would convert into GN2. For the second set of calculations, the mass of LN2 converted to GN2 could also be used to estimate the resulting pressure rise within the tank assuming that no leakage could occur. Again, this approach and its limiting assumptions are similar to that used in the flashing calculations presented in the previous section.

For both sets of calculations, the LN2 was assumed to be saturated. This is accurate for the calculations assuming all of the LN2 vaporizes but is a simplification for the calculations that has the capability to increase in temperature without undergoing a phase change. These calculations also assume the properties remain constant throughout the duration of the calculation, which is a simplification. For example, the specific heat of LN2 will change as the temperature and/or pressure of the LN2 changes, but that effect is not considered in these simplified calculations.

For both assumptions, the heat transferred to the LN2 was limited to the heat contained in the impactor when it was first submerged. Sustained heat transfer from the ram car through the ram arm and into the impactor was not considered in these calculations. The heat energy in the impactor was calculated according to Equation I12. This calculation assumes that the temperature increase of the LN2 will be negligible, and the initial LN2 temperature can be used as a conservative estimate of the total heat to be transferred out of the impactor head.

**Equation I12. Heat Energy to be Removed from Impactor**

$$\boldsymbol{q_{impactor} = m_{impactor} \cdot Cp_{steel} \cdot \Delta T_{impactor}}$$

The change in temperature of the impactor ($\Delta T_{impactor}$) is the difference between the initial temperature of the impactor ($T_{impactor}$) and the assumed temperature of the LN2 ($T_{sat}$). As the LN2

was assumed to be saturated at a range of temperatures for these calculations, the amount of heat to be removed from the impactor would also vary with the saturation temperature of the LN2.

**Equation I13. Change in Impactor Temperature**

$$\Delta T_{impactor} = T_{sat} - T_{impactor}$$

### *I4.1 Assumption 1 – Temperature Increase without Phase Change*

The first assumption examined was that the heat transferred to the LN2 only increased the LN2's temperature without changing its phase. The heat transferred out of the impactor is assumed to be equal to the heat transferred into the LN2 (i.e., no heat is transferred into the tank, the GN2, or from the impactor to the environment outside of the tank). The average increase in temperature across the entire volume of LN2 is calculated according to Equation I14 assuming that the heat transferred from the impactor to the LN2 causes the LN2 to increase its temperature but remain liquid. This equation is a rearrangement of Equation I12, using values for the properties of LN2 rather than steel, as appropriate. Note that the negative sign indicates heat transferring out of the impactor and into the LN2.

**Equation I14. Temperature Increase of LN2 Without Phase Change**

$$\Delta T_{LN2} = \frac{-q_{impactor}}{m_{liquid1} \cdot C_{pLN2}}$$

The results of this calculation for the same range of saturation conditions examined in the previous flash calculations are shown in Table I4. These calculations did not attempt to estimate the amount of time necessary for the LN2 to mix and reach a uniform temperature. While the assumption that saturated liquid can increase its temperature without undergoing a phase change is a dubious one, the results shows that for all initial LN2 temperatures examined the increase in bulk temperature is approximately 1 K.

**Table I4. Results of Temperature Increase of LN2 without Phase Change Calculations**

| $P_{sat}$ | $P_{sat}$ | $T_{sat}$ | $m_{liquid1}$ | $\Delta T_{impactor}$ | $q_{impactor}$ | $C_{pLN2}$ | $\Delta T_{LN2}$ |
|---|---|---|---|---|---|---|---|
| - | [42] | [42] | Equation I3 | Equation I13 | Equation I12 | [21] | Equation I14 |
| (psia) | (kPa) | (K) | (kg) | (K) | (kJ) | J/(gram-K) | (K) |
| 12.30 | 84.8 | 75.89 | 50197.8 | -215.11 | -1.10E+05 | **2.035** | 1.1 |
| 12.46 | 85.9 | 76.00 | 50167.3 | -215.00 | -1.10E+05 | 2.0353 | 1.1 |
| 14.06 | 97.0 | 77.00 | 49887.2 | -214.00 | -1.09E+05 | 2.0398 | 1.1 |
| 14.70 | 101.4 | 77.37 | 49782.5 | -213.63 | -1.09E+05 | 2.042 | 1.1 |
| 15.81 | 109.0 | 78.00 | 49602.3 | -213.00 | -1.09E+05 | 2.0447 | 1.1 |
| 17.73 | 122.2 | 79.00 | 49316.6 | -212.00 | -1.08E+05 | 2.0499 | 1.1 |
| 19.81 | 136.6 | 80.00 | 49261.5 | -211.00 | -1.07E+05 | 2.0555 | 1.1 |
| 22.07 | 152.2 | 81.00 | 48735.8 | -210.00 | -1.07E+05 | 2.0616 | 1.1 |
| 24.53 | 169.1 | 82.00 | 48441.0 | -209.00 | -1.06E+05 | 2.0681 | 1.1 |
| 27.18 | 187.4 | 83.00 | 48146.0 | -208.00 | -1.06E+05 | 2.0751 | 1.1 |
| 30.04 | 207.1 | 84.00 | 47869.4 | -207.00 | -1.05E+05 | 2.0826 | 1.1 |
| 33.12 | 228.4 | 85.00 | 47540.9 | -206.00 | -1.05E+05 | 2.0906 | 1.1 |
| 36.43 | 251.2 | 86.00 | 47235.0 | -205.00 | -1.04E+05 | 2.0993 | 1.1 |

| $P_{sat}$ | $P_{sat}$ | $T_{sat}$ | $m_{liquid1}$ | $\Delta T_{impactor}$ | $q_{impactor}$ | $C_{pLN2}$ | $\Delta T_{LN2}$ |
|---|---|---|---|---|---|---|---|
| - | [42] | [42] | Equation I3 | Equation I13 | Equation I12 | [21] | Equation I14 |
| (psia) | (kPa) | (K) | (kg) | (K) | (kJ) | J/(gram-K) | (K) |
| 39.98 | 275.7 | 87.00 | 46925.9 | -204.00 | -1.04E+05 | 2.1086 | 1.1 |
| 42.30 | 291.7 | 87.62 | 46732.5 | -203.38 | -1.04E+05 | 2.115 | 1.0 |
| 43.78 | 301.9 | 88.00 | 46613.7 | -203.00 | -1.03E+05 | 2.1185 | 1.0 |
| 47.84 | 329.8 | 89.00 | 46298.7 | -202.00 | -1.03E+05 | 2.1292 | 1.0 |
| 52.17 | 359.7 | 90.00 | 45977.6 | -201.00 | -1.02E+05 | 2.1407 | 1.0 |
| 56.78 | 391.5 | 91.00 | 45654.2 | -200.00 | -1.02E+05 | 2.1531 | 1.0 |
| 61.68 | 425.3 | 92.00 | 45325.3 | -199.00 | -1.01E+05 | 2.1664 | 1.0 |
| 66.88 | 461.1 | 93.00 | 44991.3 | -198.00 | -1.01E+05 | 2.1807 | 1.0 |
| 72.39 | 499.1 | 94.00 | 44655.7 | -197.00 | -1.00E+05 | 2.196 | 1.0 |
| 78.23 | 539.4 | 95.00 | 44312.3 | -196.00 | -9.99E+04 | 2.2126 | 1.0 |
| 84.40 | 581.9 | 96.00 | 43967.9 | -195.00 | -9.93E+04 | 2.2305 | 1.0 |
| 87.30 | 601.9 | 96.45 | 43809.9 | -194.55 | -9.91E+04 | 2.2690 | 1.0 |

### *I4.2 Assumption 2 – Phase Change without Temperature Increase*

The second assumption examined was that the LN2 was initially at its saturation temperature at the assumed initial pressure. If all the heat transferred out of the quenched impactor caused LN2 to vaporize to GN2, the mass of LN2 to undergo phase change can be calculated according to Equation I15. This approach assumes that no increase in temperature is necessary before phase change occurs (i.e., all of the LN2 is at its saturation temperature when the impactor plunges into it). This approach uses $\lambda_{L\text{-}V}(P_{sat})$ of the initial saturation condition, effectively assuming that the internal pressure at the time the impactor enters the LN2 is the same as at the time of impact. Note again that the negative sign in this equation indicates heat removed from the impactor by the LN2.

**Equation I15. Mass of LN2 That Can Undergo Phase Change Using Heat from Impactor**

$$m_{liquidquench} = \frac{-q_{impactor}}{\lambda_{L-V}(P_{sat})}$$

The percentage of the initial mass of LN2 that could potentially undergo a phase change using the heat removed from the impactor was calculated according to Equation I16. The initial mass of LN2 ($m_{liquid1}$) was previously calculated using Equation I3.

**Equation I16. Percentage of LN2 That Can Undergo Phase Change using Heat from Impactor**

$$f_{quench} = \frac{m_{liquidquench}}{m_{liquid1}} \cdot 100$$

The calculated mass fraction of vapor formed due to a heat transfer from the impactor to the LN2 was calculated for numerous initial pressures. The results are shown in Table I5. Note that values for Psat, Tsat, and $\lambda_{L\text{-}V}$ are the same as previously shown in Table I2. The values shown in this table for $\Delta T_{impactor}$ and $q_{impactor}$ are the same as previously shown in Table I4.

**Table I5. Saturation Thermodynamic Properties of Nitrogen and Post-quench Mass Fractions**

| $P_{sat}$ | $P_{sat}$ | $T_{sat}$ | $\Delta_{Timpactor}$ | $q_{impactor}$ | $\lambda_{L-V}$ | $m_{liquidquench}$ | $f_{quench}$ |
|---|---|---|---|---|---|---|---|
| - | [42] | [42] | Equation I13 | Equation I12 | Equation I2 | Equation I115 | Equation I16 |
| (psia) | (kPa) | (K) | (K) | (kJ) | (kJ/kg) | (kg) | % |
| 12.30 | 84.8 | 75.89 | -215.11 | -1.10E+05 | 201.201 | 544.7 | 1.09 |
| 12.46 | 85.9 | 76.00 | -215.00 | -1.10E+05 | 201.069 | 544.7 | 1.09 |
| 14.06 | 97.0 | 77.00 | -214.00 | -1.09E+05 | 199.730 | 545.8 | 1.09 |
| 14.70 | 101.4 | 77.37 | -213.63 | -1.09E+05 | 199.260 | 546.2 | 1.10 |
| 15.81 | 109.0 | 78.00 | -213.00 | -1.09E+05 | 198.432 | 546.9 | 1.10 |
| 17.73 | 122.2 | 79.00 | -212.00 | -1.08E+05 | 197.774 | 546.1 | 1.11 |
| 19.81 | 136.6 | 80.00 | -211.00 | -1.07E+05 | 195.776 | 549.1 | 1.11 |
| 22.07 | 152.2 | 81.00 | -210.00 | -1.07E+05 | 194.416 | 550.3 | 1.13 |
| 24.53 | 169.1 | 82.00 | -209.00 | -1.06E+05 | 193.031 | 551.6 | 1.14 |
| 27.18 | 187.4 | 83.00 | -208.00 | -1.06E+05 | 191.621 | 553.0 | 1.15 |
| 30.04 | 207.1 | 84.00 | -207.00 | -1.05E+05 | 190.179 | 554.5 | 1.16 |
| 33.12 | 228.4 | 85.00 | -206.00 | -1.05E+05 | 188.719 | 556.1 | 1.17 |
| 36.43 | 251.2 | 86.00 | -205.00 | -1.04E+05 | 187.221 | 557.8 | 1.18 |
| 39.98 | 275.7 | 87.00 | -204.00 | -1.04E+05 | 185.685 | 559.7 | 1.19 |
| 42.30 | 291.7 | 87.62 | -203.38 | -1.04E+05 | 184.721 | 560.9 | 1.20 |
| 43.78 | 301.9 | 88.00 | -203.00 | -1.03E+05 | 184.124 | 561.7 | 1.20 |
| 47.84 | 329.8 | 89.00 | -202.00 | -1.03E+05 | 182.520 | 563.8 | 1.22 |
| 52.17 | 359.7 | 90.00 | -201.00 | -1.02E+05 | 180.936 | 565.9 | 1.23 |
| 56.78 | 391.5 | 91.00 | -200.00 | -1.02E+05 | 179.189 | 568.6 | 1.25 |
| 61.68 | 425.3 | 92.00 | -199.00 | -1.01E+05 | 171.856 | 589.9 | 1.30 |
| 66.88 | 461.1 | 93.00 | -198.00 | -1.01E+05 | 175.069 | 576.2 | 1.28 |
| 72.39 | 499.1 | 94.00 | -197.00 | -1.00E+05 | 173.843 | 577.3 | 1.29 |
| 78.23 | 539.4 | 95.00 | -196.00 | -9.99E+04 | 171.956 | 580.7 | 1.31 |
| 84.40 | 581.9 | 96.00 | -195.00 | -9.93E+04 | 170.013 | 584.3 | 1.33 |
| 87.30 | 601.9 | 96.45 | -194.55 | -9.91E+04 | 169.108 | 586.091 | 1.34 |

## I5. Theoretical Maximum Tank Car Pressure Due to "Hot" Impactor Vaporizing LN2

The potential increase in outage pressure caused by each mass of LN2 vaporizing within the tank was calculated. While the approach used to calculate the pressure rise inside the tank due to vaporizing LN2 with the impactor's added heat is fundamentally the same as was used to calculate the rise in pressure due to flash vaporization due to a pressure drop, there are several important differences to note.

The mass of liquid remaining after the impactor is quenched ($m_{liquid2}$) is the difference between the initial mass of liquid in the tank ($m_{liquid1}$) and the mass that underwent phase change using the heat from the impactor ($m_{liquidquench}$).

**Equation I17. Mass of Liquid Remaining in Tank After Impactor Quench**

$$m_{liquid_2} = m_{liquid_1} - m_{liquid_{quench}}$$

In the flash vaporization calculations, Equation I7 was used to calculate the volume of LN2 that would occupy the tank at atmospheric pressure. The current calculations instead calculate the volume of LN2 that would occupy the tank at the *saturation* pressure. The volume of LN2 that remains in the tank at saturation pressure after the quench is the post-quench mass of LN2 in the tank car ($m_{liquid2}$) divided by the density of LN2 at the saturation pressure ($\rho_{liquid1}$), as shown in Equation I18.

**Equation I18. Volume of LN2 Remaining After Impactor Quenching**

$$V_{liquid2} = \frac{m_{liquid_2}}{\rho_{liquid1}}$$

The post-quench volume of vapor ($V_{vapor2}$) can be calculated according to Equation I8. The total mass of vapor produced during the phase change ($m_{vaporproduced}$) is equal to the mass of liquid that underwent phase change ($m_{liquidquench}$). The total mass of vapor in the tank after the impactor is quenched can be calculated using Equation I9 with the appropriate values for $m_{vaporproduced}$ associated with impactor quenching. The density of the vapor after quenching the impactor ($\rho_{vapor2}$) can be calculated according to Equation I10.

The theoretical maximum pressure that can develop within the inner tank for the isothermal accumulation of gas in the vapor space can be calculated according to Equation I19. This equation is slightly different from Equation I11, which was used to calculate the maximum theoretical pressure within the tank after a flash event. In the flash event calculation, the saturation temperature at 1 atmosphere of pressure ($T_{atm\text{-}saturation}$) was used. In the impactor quenching calculation the saturation temperature at the assumed saturation pressure ($T_{sat}$) is used.

**Equation I19. Maximum Theoretical Pressure Within Tank After Impactor Quenching**

$$P_{tank} = Z\frac{R_U}{\mu_{N_2}}\rho_{vapor_2} \cdot T_{sat}$$

**Table I6. Theoretical Maximum Tank Car Pressure After Impactor Quench for Different Initial LN2 Saturation Temperature Conditions**

| $P_{sat}$ | $P_{sat}$ | $T_{sat}$ | $f_{quench}$ | $m_{liquid2}$ | $V_{liquid2}$ | $V_{vapor2}$ | $m_{vaporproduced}$ | $m_{vaportotal}$ | $\rho_{vapor2}$ | $P_{tank}$ | $P_{tank}$ |
|---|---|---|---|---|---|---|---|---|---|---|---|
| - | [42] | [42] | Equation I16 | Equation I17 | Equation I18 | Equation I8 | Equation I15 | Equation I9 | Equation I10 | Equation I19 | - |
| (psia) | (kPa) | (K) | % | (kg) | ($m^3$) | ($m^3$) | (kg) | (kg) | ($kg/m^3$) | (kPa) | (psia) |
| 12.30 | 84.8 | 75.89 | 1.09 | 49653.1 | 61.0 | 6.8 | 544.7 | 568.5 | 84.0 | 1703.8 | 247.1 |
| 12.46 | 85.9 | 76.00 | 1.09 | 49622.5 | 61.0 | 6.8 | 544.7 | 568.9 | 84.1 | 1707.3 | 247.6 |
| 14.06 | 97.0 | 77.00 | 1.09 | 49341.4 | 61.0 | 6.8 | 545.8 | 572.8 | 84.6 | 1740.4 | 252.4 |
| 14.70 | 101.4 | 77.37 | 1.10 | 49236.3 | 61.0 | 6.8 | 546.2 | 574.3 | 84.8 | 1752.8 | 254.2 |
| 15.81 | 109.0 | 78.00 | 1.10 | 49055.4 | 61.0 | 6.8 | 546.9 | 576.9 | 85.1 | 1774.3 | 257.3 |
| 17.73 | 122.2 | 79.00 | 1.11 | 48770.5 | 61.0 | 6.8 | 546.1 | 579.5 | 85.5 | 1804.3 | 261.7 |
| 19.81 | 136.6 | 80.00 | 1.11 | 48712.4 | 61.0 | 6.8 | 549.1 | 586.1 | 86.4 | 1846.7 | 267.8 |
| 22.07 | 152.2 | 81.00 | 1.13 | 48185.6 | 61.0 | 6.8 | 550.3 | 591.2 | 87.0 | 1883.6 | 273.2 |

| $P_{sat}$ | $P_{sat}$ | $T_{sat}$ | $f_{quench}$ | $m_{liquid2}$ | $V_{liquid2}$ | $V_{vapor2}$ | $m_{vaporproduced}$ | $m_{vaportotal}$ | $\rho_{vapor2}$ | $P_{tank}$ | $P_{tank}$ |
|---|---|---|---|---|---|---|---|---|---|---|---|
| - | [42] | [42] | Equation I16 | Equation I17 | Equation I18 | Equation I8 | Equation I15 | Equation I9 | Equation I10 | Equation I19 | - |
| (psia) | (kPa) | (K) | % | (kg) | ($m^3$) | ($m^3$) | (kg) | (kg) | ($kg/m^3$) | (kPa) | (psia) |
| 24.53 | 169.1 | 82.00 | 1.14 | 47889.4 | 61.0 | 6.8 | 551.6 | 596.7 | 87.7 | 1922.9 | 278.9 |
| 27.18 | 187.4 | 83.00 | 1.15 | 47593.0 | 61.0 | 6.8 | 553.0 | 602.6 | 88.5 | 1963.9 | 284.8 |
| 30.04 | 207.1 | 84.00 | 1.16 | 47314.9 | 60.9 | 6.8 | 554.5 | 609.0 | 89.4 | 2006.8 | 291.1 |
| 33.12 | 228.4 | 85.00 | 1.17 | 46984.8 | 60.9 | 6.8 | 556.1 | 615.8 | 90.3 | 2051.3 | 297.5 |
| 36.43 | 251.2 | 86.00 | 1.18 | 46677.2 | 60.9 | 6.8 | 557.8 | 623.1 | 91.3 | 2097.9 | 304.3 |
| 39.98 | 275.7 | 87.00 | 1.19 | 46366.2 | 60.9 | 6.8 | 559.7 | 630.9 | 92.3 | 2146.7 | 311.3 |
| 42.30 | 291.7 | 87.62 | 1.20 | 46171.6 | 60.9 | 6.8 | 560.9 | 628.3 | 91.9 | 2151.6 | 312.1 |
| 43.78 | 301.9 | 88.00 | 1.20 | 46052.0 | 60.9 | 6.8 | 561.7 | 626.9 | 91.6 | 2155.3 | 312.6 |
| 47.84 | 329.8 | 89.00 | 1.22 | 45734.9 | 60.9 | 6.8 | 563.8 | 648.2 | 94.6 | 2251.1 | 326.5 |
| 52.17 | 359.7 | 90.00 | 1.23 | 45411.7 | 60.9 | 6.9 | 565.9 | 657.6 | 95.9 | 2306.5 | 334.5 |
| 56.78 | 391.5 | 91.00 | 1.25 | 45085.6 | 60.9 | 6.9 | 568.6 | 668.0 | 97.3 | 2365.9 | 343.1 |
| 61.68 | 425.3 | 92.00 | 1.30 | 44735.4 | 60.9 | 6.9 | 589.9 | 697.5 | 101.1 | 2485.1 | 360.4 |
| 66.88 | 461.1 | 93.00 | 1.28 | 44415.1 | 60.9 | 6.9 | 576.2 | 692.5 | 100.5 | 2498.7 | 362.4 |
| 72.39 | 499.1 | 94.00 | 1.29 | 44078.4 | 60.9 | 6.9 | 577.3 | 702.9 | 101.9 | 2560.8 | 371.4 |
| 78.23 | 539.4 | 95.00 | 1.31 | 43731.6 | 60.9 | 6.9 | 580.7 | 716.1 | 103.7 | 2632.6 | 381.8 |
| 84.40 | 581.9 | 96.00 | 1.33 | 43383.6 | 60.8 | 6.9 | 584.3 | 732.4 | 105.9 | 2716.1 | 393.9 |
| 87.30 | 601.9 | 96.45 | 1.34 | 43223.8 | 60.8 | 6.9 | 586.1 | 738.0 | 106.6 | 2747.9 | 398.6 |

## I6. Estimated Burst Pressure of Inner Tank

The burst pressure of the DOT-113's inner tank was estimated to provide some context to the calculated pressure results in Table I3 and Table I6. The minimum required thickness of the inner tank of a DOT-113 tank car can be calculated according to the formula given in 49 CFR § 179.400–8 [39]. This formula is reproduced below as Equation I20. The terms used in this equation were included in Table I1.

**Equation I20. Minimum Wall Thickness for DOT-113's Inner Tank**

$$t = \frac{P_{burst} \cdot d}{2 \cdot S \cdot E}$$

Equation I20 can be rearranged to solve for the burst pressure of a tank car with known design parameters. The rearranged equation is shown in Equation I21.

**Equation I21. Burst Pressure for DOT-113's Inner Tank**

$$P_{burst} = \frac{2 \cdot S \cdot E \cdot t}{d}$$

Within the CFR, this equation is to be used to determine the minimum thickness of plate used to form the tank. The minimum allowable tensile strength of the material of construction must be used in the design calculation, as that will result in a greater plate thickness for a given burst

pressure.[23] This minimum tensile strength is typically defined for room temperature and quasi-static conditions. However, to estimate the expected burst pressure of the tank under test conditions, the tensile strength of the plate at the target temperature can be used. Further, as the assumptions in this appendix assume that flash vaporization occurs very rapidly, the tank can be assumed to be loaded at an elevated rate. Therefore, the burst pressure calculations were performed twice: once using the quasi-static, room temperature minimum strength of T304 stainless steel (Equation I22) and a second time using the 0.05 /s, 77K tensile strength of the Test 11 T304 stainless steel described in Table B3 (Equation I23).

**Equation I22. Burst Pressure Using Minimum Tensile Strength at Room Temperature**

$$P_{burst} = \frac{2 \cdot 7500psi \cdot 0.9 \cdot 0.25in}{106in}$$

$$P_{burst} = 318\ psi$$

**Equation I23. Burst Pressure Using 77K, Elevated Strain Rate Tensile Strength**

$$P_{burst} = \frac{2 \cdot 179300psi \cdot 0.9 \cdot 0.25in}{106in}$$

$$P_{burst} = 761\ psi$$

It is important to note that these two burst pressures are, at best, rough estimates of the actual burst pressure of a tank car due to a rapid buildup of pressure when a tank is at cryogenic temperature. In particular, these estimated burst pressures do not take into account the damage to the tank caused by the impact event, or how that impact damage could negatively affect the structural integrity of the tank.

While the calculations of maximum theoretical pressure are conservative for several reasons stated in this appendix, at a saturated pressure of 30 psig the theoretical post-flash pressure was 973.4 psia. This pressure exceeded the estimated burst pressure of the inner tank, even when the burst pressure calculation is made using the increased tensile strength of T304 at 77 K. Additionally, the theoretical pressure that could be developed from vaporization caused by impactor quenching was 312.1 psia. While an actual puncture test would result in some leakage through the puncture hole or PRVs, some minimum flow rate of LN2 and/or GN2 out of the tank would be necessary to prevent pressure from building up to a level sufficient to burst the tank car.

## I7. Description of the Physics of Depressurization of a Tank Car and its Effects

Figure I1 shows, schematically, the conditions within the tank car at the instant of puncture of inner tank wall. The various phenomena that occur are described, with emphasis on explanation of the physics. An attempt is made to mathematically model the simultaneous high vapor release rate due to rapid phase transition of a fraction of liquid mass, pressure build up in the tank car, and the leak of liquid through the puncture hole.

[23] A minimum bursting pressure of 300 psig is required for a DOT-113C120W tank car (49 CFR § 179.401–11).

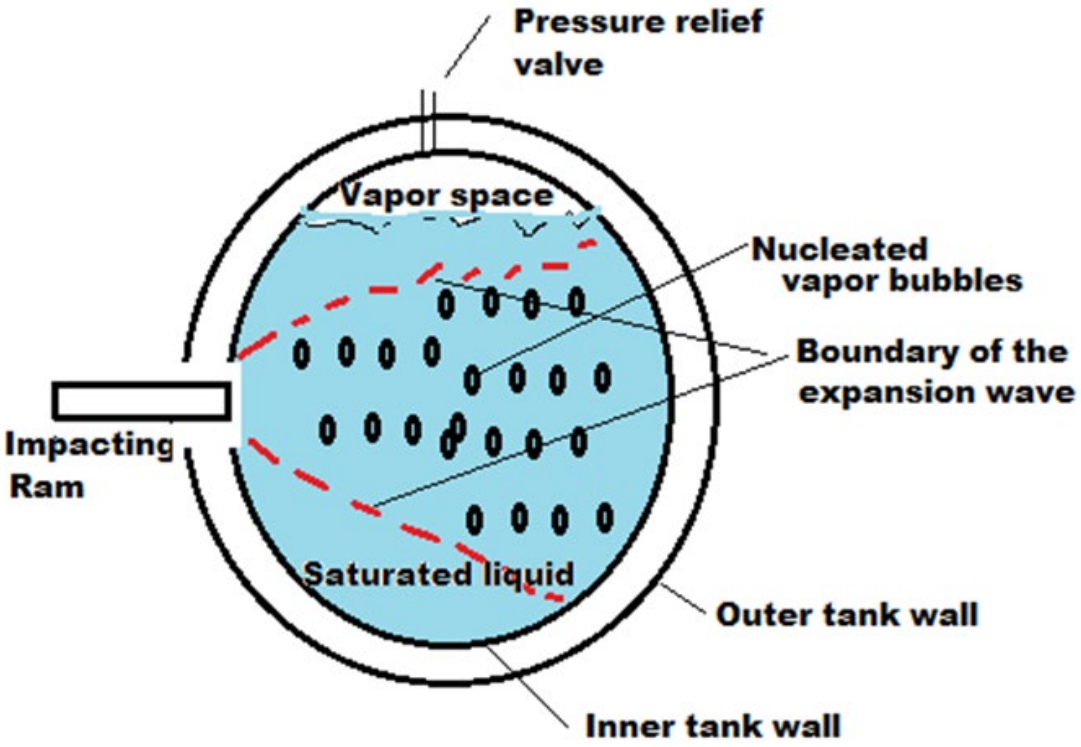


**Figure I1. Schematic Representation of Conditions at the Instant of Breach of Inner Tank Wall**

The rapidity of vaporization depends on the rate of formation of the puncture hole (i.e., hole-size as a function of time). The effect of such rapid vaporization can lead to different outcomes, depending upon a number of factors, many of which are difficult to quantify.

At the instant the inner tank wall punctures (with a very small annular hole-area surrounding the ram) an expansion pressure wave will sweep across the liquid (communicating the outside atmospheric pressure to the liquid). This wave travels at a speed of about 1,500 m/s, thus making the liquid "feel" the depressurization in a matter of about 2 ms. This depressurization initiates the flash vaporization of a fraction of the liquid resulting in the formation of vapor bubbles in the body of the liquid, as shown schematically in Figure I1. This "rapid phase transition" phenomenon occurs in time scales from microseconds to milliseconds. The accumulation rate of the vapor thus generated in the (small) vapor space is very fast (again, on a millisecond time scale).

Activation of the PRV takes time as the pressure wave must travel through the piping connecting the PRV to the vapor space of the tank, and overcome the inertia of the PRV components (fractions of seconds). Once the PRV has opened, it may not have sufficient capacity to relieve all of the vapor generated, resulting in a high pressure pulse within the vapor space. The liquid's own significant inertia means it will take a matter of fractions of second to one second for the initiation of the liquid flow through the hole. The liquid behavior is made more complex by the fluid dynamics (e.g., sloshing) that were initiated by the initial stages of the impact prior to puncture. The rate of liquid flow out of the hole is a balance between being pushed by the increased pressure in the tank and being resisted by the impactor potentially obstructing some

portion of the puncture. In essence, the net area available for the liquid to escape is the difference between the total area of the puncture of the inner tank and the area of the puncture obstructed by the impactor or deformed portion of the outer tank shell.

The increased tank pressure may result in one of several outcomes:

> (1) Nothing may happen to the tank car wall following initial puncture if the rate of hole creation is slow. In this situation, the initially increased pressure suppresses further flashing or produces vapor at rate that the pressure relief valve and liquid venting can keep up with, or;
>
> (2) The tank wall bursts if the built-up pressure is higher than the burst pressure of the tank. This situation could develop if venting is inhibited (e.g., crushed or obstructed piping leading to the PRV, impactor plugging the puncture hole, etc.). This situation could also develop in spite of effective venting if the rate of vapor production exceeds the rate of venting through PRVs and/or puncture hole,[24] or;
>
> (3) The rapid pressure increase suppresses further vaporization of the liquid once the pressure is significantly higher than the saturated vapor pressure corresponding to the liquid temperature, but is not high enough to burst the tank wall. In this case it is entirely possible that the in-transit bubbles rising through the liquid column will be "crushed" by the high pressure, in a process similar to *cavitation.* The collapse of the bubbles induces a shock wave in the liquid. The combined shock wave produced by individual shockwave produced by each collapsed vapor bubble in the liquid can be very large and its impact on the vessel wall resulting in the shattering of the wall and sudden release of the entire tank car contents into the open. This scenario will hurl two phase contents to considerable horizontal and vertical distance.

The above physical scenarios are very difficult to model mathematically, there are no known controlled laboratory test data against which any model results can be tested for different parameter values. However, the data from real railroad accidents in which hydrocarbon liquid tank cars were exposed to fires and the resulting multitude of ways in which tank cars have failed provide a clue to the occurrence of the above-described phenomena.[25]

## I8. A Mathematical Model to Predict Tank Car Pressure Variation with Time

It is assumed that the formation of a very small area of the puncture hole initiates an expansion wave into the liquid. Let the initial tank pressure before puncture be $P_1$ and the corresponding

---

[24] An incident was investigated by NTSB (NTSB/HZM-04/02) in which rapid vapor production led to catastrophic rupture of a tank car. In this incident the PRV was venting continuously until the point of catastrophic rupture. This situation illustrates a scenario in which vapor was generated at a rate that exceeded the available venting capacity, leading to pressure buildup.

[25] In many accidents the portion of tank car wall that is wetted by vapor is exposed to fire, fails by a thermal tear, releases a very rapid boiling liquid, and results in a fireball. In these cases, there is considerable damage to the tank car and many times partial loss of tank wall. However, in some accidents the same thermal tear seems to have induced detonation waves in the liquid–this is evidenced by the fact that the tank car cylindrical wall opens up and ends up as a flat plate of metal [sometimes referred to as the "dance floor"]. It is postulated that such an opening up is possible only if the thermal crack propagates along the length of the tank car at speeds of sound in metal (5,800 m/s), resulting in massive flash vaporization and very high pressure build up inside the shell.

saturated liquid temperature be $T_1$. It is further assumed that the hole size is sufficiently small; therefore, the expansion wave induced pressure drop ($\Delta P_1$) is small and far below the full drop to atmospheric pressure. The new pressure following the incremental pressure drop is calculated according to Equation I24.

**Equation I24. New Pressure after Incremental Pressure Drop**

$$P_1^* = P_1 - \Delta P_1$$

Following this incremental pressure drop, the liquid is now superheated at temperature $T_1$ with respect to the new pressure $(P_1^*)$. This results in the formation of a flash vaporization of a small mass of liquid ($\Delta m_{1,L}$) given by Equation I25.

**Equation I25 Flash Vaporization of a Small Mass of Liquid due to Incremental Pressure Drop**

$$\Delta m_{1,L} = m_{liquid1} \frac{\{h_L^{sat}(P_1) - h_L^{sat}(P_1^*)\}}{\lambda_{L-V}(P_1^*)}$$

Assuming that this flashing results in the accumulation of vapor in the vapor space the new pressure in the vapor space can be calculated. The following calculations are made assuming an isothermal accumulation of vapor at a temperature ($T_2$) corresponding to the new saturated liquid pressure $(P_1^*)$. The total mass of vapor in the tank car ($m_{vaportotal}$) after the incremental pressure drop is the mass of the initial vapor ($m_{1,V}$) plus the small mass of liquid that flashed ($\Delta m_{1,L}$), as shown in Equation I26.

**Equation I26. Total Mass of Vapor in Tank After Flash Vaporization of a Small Mass of Liquid**

$$m_{vaportotal} = m_{1,V} + \Delta m_{1,L}$$

The total volume of vapor in the tank car ($V_{vaportotal}$) after the incremental pressure drop is the volume of the initial vapor ($V_{1,v}$) plus the mass of liquid that flashed ($\Delta m_{1,L}$) divided by the saturated vapor density at the new saturation temperature ($T_2$), as shown in Equation I27.

**Equation I27. Total Volume of Vapor in Tank After Flash Vaporization of a Small Mass of Liquid**

$$V_{vaportotal} = V_{1,V} + \frac{\Delta m_{1,L}}{\rho_{L,2}}$$

The new density of vapor ($\rho_{2,v}$) is equal to the sum of the initial mass of vapor ($m_{1,v}$) plus the mass of newly-created vapor ($\Delta m_{1,L}$) divided by the initial volume of vapor ($V_{1,v}$) plus the mass of newly-created vapor ($\Delta m_{1,L}$).

**Equation I28. Vapor Density After Flash Vaporization of a Small Mass of Liquid**

$$\rho_{2,V} = \frac{m_{vaportotal}}{V_{vaportotal}}$$

The new pressure in the vapor space ($P_{1,V}$) following flash vaporization of a small mass of liquid is calculated according to Equation I29.

**Equation I29. Pressure in Vapor Space After Flash Vaporization of a Small Mass of Liquid**

$$P_{1,V} = Z(P_1,T_1) \cdot \rho_{2,V} \cdot \frac{R_u}{\mu_{N2}} \cdot T_2$$

It is assumed that due to this new higher pressure ($P_{1,V}$) in the vapor space further vaporization of liquid is terminated. $P_{1,V}$ drives a leak of liquid through the hole that was created in the tank shell. The pressure driving the flow is time dependent and equal to the difference between the pressure in the vapor space at a given instant of time and the atmospheric pressure, as shown in Equation I30.

**Equation I30. Flow Pressure**

$$P_{flow}(t) = P_{1,V}(t) - P_{atm}$$

The rate of mass flow of liquid thru the hole is given by Equation I31.

**Equation I1. Mass Flow Rate of Liquid Through Puncture Hole**

$$\dot{m}_{1,L}(t) = C_d A_H(t) \sqrt{\rho_{2,V} \cdot P_{flow}(t)}$$

No gas is assumed to be released through the puncture hole or the PRV. As liquid leaks out of the tank, the pressure in the vapor space decreases due to expansion of the vapor space's volume. The expansion of the gas in the vapor volume can be assumed to be adiabatic. This expansion is continued, mathematically, until the gas pressure is slightly lower than the saturation pressure $(P_1^*)$ corresponding to liquid temperature *T2*.

The total mass of liquid expelled over the time that the pressure is decreasing in the vapor space can be calculated. Subsequent to this calculation the entire calculation (starting at Equation I25) is repeated with new conditions and another assumed small pressure drop in the liquid leads to yet another flash vaporization. The pressure-time history associated with this cycle is illustrated, schematically, in Figure I2. Note that as a schematic illustration the relative heights and durations of the peaks on this figure are not drawn to scale.

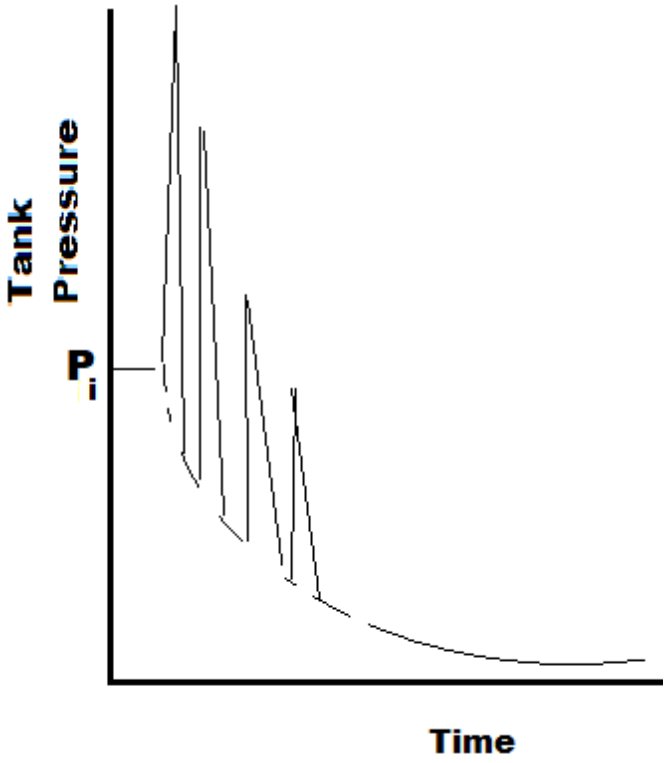


**Figure I2. Schematic Representation of the Pressure Variation Within a Tank Car Containing a Cryogenic Liquid after Puncture of the Tank Car Wall**

## I9. Rapid Phase Transition Due to Pressure Drop

Initial plans for this test included a target outage pressure of 50 psig, to be consistent with the outage pressures in the two previous tests of DOT-113 cars and surrogates. While attaining a target outage pressure is straightforward when the fluids in the tank are water and air, increasing the pressure in an LN2-GN2 tank is more complex. If the LN2-GN2 system inside the tank were kept saturated during the pressurization of the GN2, the LN2 would have a temperature of approximately 92 K at a pressure of 50 psig. If the bulk temperature of the LN2 was lower than 92 K, then the GN2 would cool down and the pressure would drop. The bulk temperature of the LN2 could not be any higher than 92K at 50 psig, as then the LN2 would boil into GN2.

While the saturated LN2-GN2 system would be stable within the tank at 50 psig prior to the test, concerns were raised about the possibility of a rapid phase transition following puncture of the inner tank. At sea level, LN2 has a saturation temperature of approximately 77 K under 1 atmosphere of pressure.[26] If the bulk temperature of the LN2 within the tank was above 77 K at the time of puncture, this LN2 would be superheated once exposed to atmosphere. Superheated LN2 cannot exist as a liquid at this lower pressure and would rapidly change phase to GN2. As N2 changes phase from a liquid to a vapor, heat is pulled from the surroundings in an endothermic process. In this case, heat would be removed from the remaining bulk LN2,

[26] At Pueblo, CO's, elevation LN2 has a saturation temperature of approximately 76 K under 1 atmosphere of pressure.

bringing its temperature down. This rapid phase transition of LN2 exposed to atmospheric pressure and consequential reduction in the remaining LN2's temperature would continue until the bulk temperature of the remaining LN2 was reduced to its saturation temperature at atmospheric pressure. At that point, the remaining LN2 would continue to boil as ambient heat entered the tank, but this boiling would be slow compared to the rapid phase transition and would not pose a concern for pressure buildup.

One of the challenges facing the test team in assessing the likelihood and consequences of a rapid phase transition was in trying to understand how rapidly such a phase transition could practically occur compared to how quickly the tank would allow pressure to escape. Logically, if the puncture in the inner tank allowed LN2 to contact atmospheric air and vaporize, then a path existed for the newly-created vapor to escape to atmosphere. At the same time, even if 99 percent of the vapor that was rapidly-created was able to escape the tank, the 1 percent that remained could lead to a substantial increase in pressure if a large enough mass of LN2 were to undergo rapid phase transition, since a given mass of GN2 occupies a substantially-larger volume within the tank than the same mass of LN2.

Several different potential combinations of initial pressure, GN2 temperature, LN2 temperature were considered during the test planning phase. Each of these combinations of initial conditions offered different practical and safety considerations. The ability to safely conduct the test with minimum risk to test personnel and facilities and equipment was the first priority. The second priority was ensuring that the test conditions were measured and that all test data were successfully captured.

Four different concerns were considered for each condition as summarized in Table I7. This table also shows the desired (target) behavior sought for the test, and the parameters that would lead to the target behavior during the test.

**Table I7. Summary of LN2-GN2 Situations and Test Targets**

| Concern | Target Behavior for Test | Parameters for Target Behavior |
|---|---|---|
| Stability of the LN2-GN2 system within the tank | Stable pressures and temperatures in both LN2 and GN2 prior to impact. | LN2 and GN2 at same temperature |
| Representative of realistic in-service conditions | LN2 and GN2 conditions representative of a situation that could occur in service. | Outage, pressure, and temperature chosen based on in-service conditions |
| Potential for GN2 to condense to LN2 due to sloshing | Minimize the likelihood of GN2 condensation to simplify modeling | LN2 not substantially colder than GN2 |
| Potential for flashing of LN2 to GN2 following a puncture | Minimize potential for flashing due to potential safety concerns. | LN2 temperature kept close to saturation temperature at 1 atmosphere |

This table represented targets that the test team sought to control. However, in practice, the test team had relatively little control over the first and third concerns. Essentially, both of these concerns would have been addressed by ensuring that the LN2 and GN2 were at the same temperature. This would have ensured that the LN2-GN2 system was stable since neither fluid would be warmer than the other. Similarly, if both the LN2 and GN2 were at the same temperature, there would be no "cold" LN2 to suddenly condense "warm" GN2. As the test team did not have a means to mix the fluids prior to the test, they did not attempt to ensure the GN2 and LN2 were at the same temperature before the test.

### *I9.1 LN2 and GN2 Condition 1*

Condition 1 assumed the LN2 and GN2 could both be maintained at the saturation temperature for the chosen initial pressure. The initial pressure was assumed to be 50 psig (62.3 psia), the same pressure as in the previous two tests. The initial temperature of the LN2 and GN2 were both assumed to be 92 K. Condition 1 is schematically illustrated in Figure I3.

There were several advantages identified if the test were run at Condition 1. At Condition 1, the temperatures and pressures within the tank are both stable. Without a pressure or temperature difference, there would be no liquid-gas heat transfer, initially. Condition 1 could be thought to be representative of service conditions if a DOT-113 slowly heated up over many days in transit, where equilibrium between the two phases was maintained. Finally, since the temperatures are initially the same there was a decreased chance of cold LN2 collapsing outage pressure during the test due to sloshing.

There were several disadvantages identified if the test were run at Condition 1. Since the LN2 was initially at the saturation temperature corresponding to 50 psig, flash boiling was possible if the inner tank punctured and the LN2 was suddenly exposed to atmosphere. Additionally, if the GN2 was initially at its saturation temperature and pressure any reduction in volume caused by the impact would result in condensation of the GN2 to LN2, which was a behavior not well-represented by the pre-test FE models.

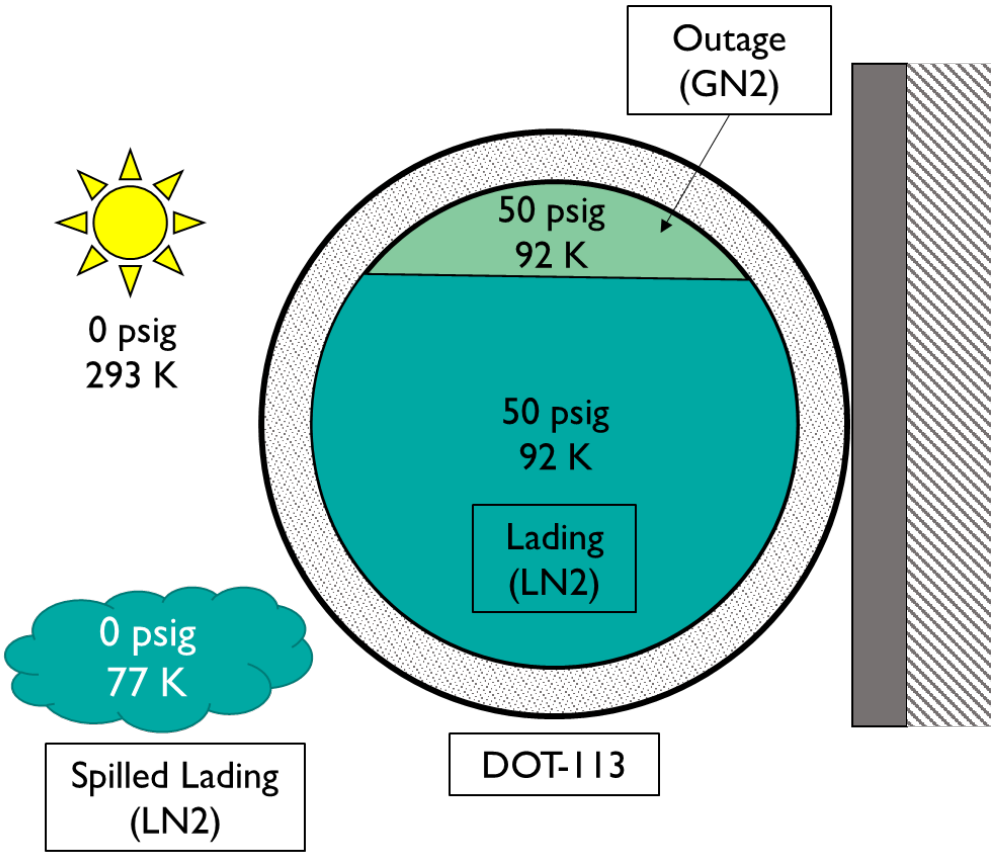


**Figure I3. Condition 1**

### *I9.2 LN2 and GN2 Condition 2*

Condition 2 assumed the LN2 and GN2 would be at different temperatures. The initial pressure was assumed to be 50 psig (62.3 psia), the same pressure as in the previous two tests. The initial temperature of the LN2 was assumed to be 77 K, the saturation temperature of LN2 at 1 atmosphere. The initial temperature of the GN2 was assumed to be 92K, the saturation temperature at 62.3 psia. Condition 2 is schematically illustrated in Figure I4.

There were several advantages identified if the test could be run at Condition 2. At Condition 2, the LN2 would be less likely to flash boil if the tank punctured since the LN2 was not superheated relative to its atmospheric pressure saturation temperature. Condition 2 also used an outage pressure that was directly comparable to the pressures used in the previous two tests.

There were several disadvantages identified if the test were run at Condition 2. Since the LN2 and GN2 were at different temperatures, the conditions within the tank were not stable. The temperatures would change until equilibrium was reached or until the time of impact. Since the LN2 was colder than the GN2, sloshing during the test could cause the outage pressure to collapse. Additionally, if the GN2 was initially at its saturation temperature and pressure any reduction in volume caused by the impact would result in condensation of the GN2 to LN2, which was a behavior not well-represented by the pre-test FE models. Finally, this condition did not represent transportation conditions, as constant motion of a tank car would tend to mix the fluid species.

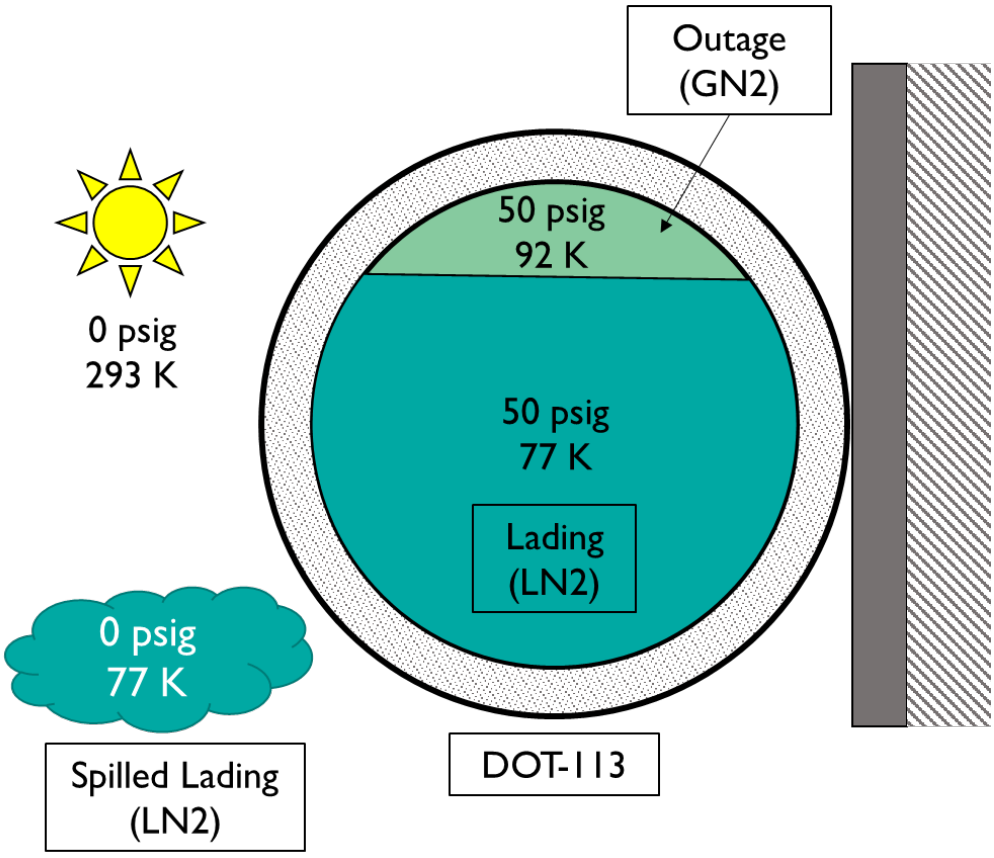


**Figure I4. Condition 2**

### *I9.3 LN2 and GN2 Condition 3*

Condition 3 assumed the LN2 and GN2 could both be maintained at the saturation temperature for the chosen initial pressure. The initial pressure was assumed to be 15–25 psig (27.3–37.3 psia), a lower pressure than in the previous two tests. The initial temperature of the LN2 and GN2 were both assumed to be 83–86 K. Condition 3 is schematically illustrated in Figure I6. Ultimately, the test team chose Condition 3 to guide the targets for the test.

There were several advantages identified if the test were run at Condition 3. At Condition 3, the temperatures and pressures within the tank are both stable. Without a pressure or temperature difference, there would be no liquid-gas heat transfer, initially. Condition 3 could be thought to be representative of service conditions if a DOT-113 slowly heated up over many days in transit, where equilibrium between the two phases was maintained. Using a temperature and pressure combination that was less than the 50 psig considered in Condition 1 was thought to lead to a less energetic flash boiling event if the inner tank was punctured. Finally, since the temperatures are initially the same there was a decreased chance of cold LN2 collapsing outage pressure during the test due to sloshing.

There were several disadvantages identified if the test were run at Condition 3. Since the LN2 was initially at the saturation temperature corresponding to 15–25 psig, flash boiling was still possible if the inner tank punctured and the LN2 was suddenly exposed to atmosphere. Additionally, if the GN2 was initially at its saturation temperature and pressure any reduction in

volume caused by the impact would result in condensation of the GN2 to LN2, which was a behavior not well-represented by the pre-test FE models. Finally, Condition 3 used a different initial pressure than the previous two tests, preventing a direct comparison of the results.

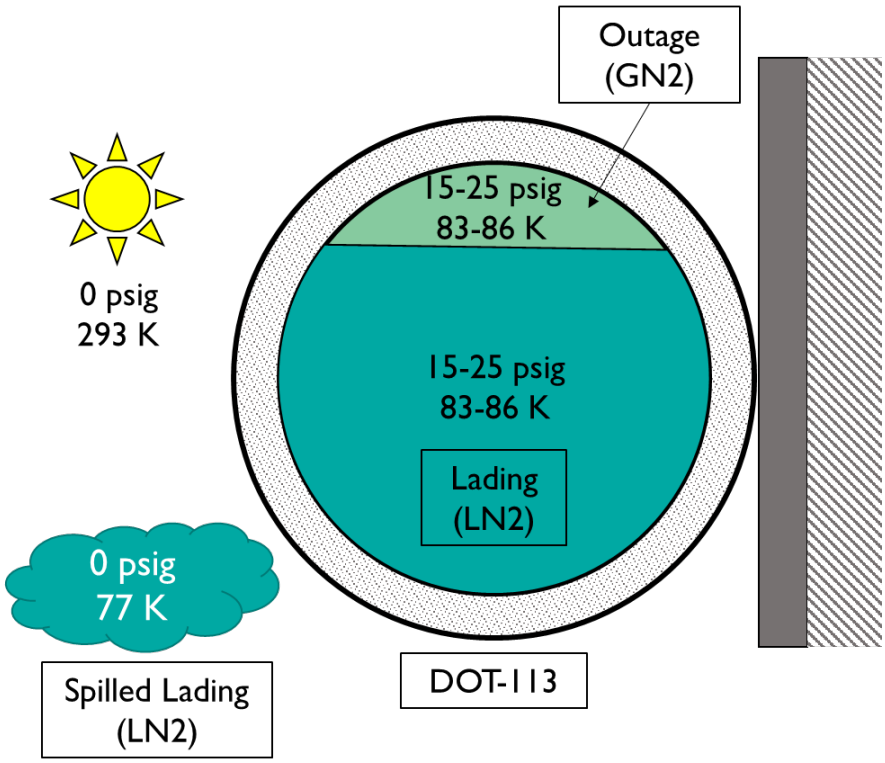


**Figure I5. Condition 3**

### *I9.4 LN2 and GN2 Condition 4*

Condition 4 assumed the LN2 and GN2 could both be maintained at the saturation temperature for the chosen initial pressure. The initial pressure was assumed to be 1 atmosphere (0 psig) The initial temperature of the LN2 and GN2 were both assumed to be 77 K. Condition 4 is schematically illustrated in Figure I6.

There were several advantages identified if the test were run at Condition 4. At Condition 4, the temperatures and pressures within the tank are both stable. Without a pressure or temperature difference, there would be no liquid-gas heat transfer, initially. Flash boiling would not occur in the event of a puncture since the initial conditions within the tank were the same as atmospheric conditions outside the tank. Finally, since the GN2 and LN2 were initially at the same temperatures there was a decreased chance of cold LN2 collapsing outage pressure during the test due to sloshing.

There were several disadvantages identified if the test were run at Condition 4. If the GN2 was initially at its saturation temperature and pressure any reduction in volume caused by the impact would result in condensation of the GN2 to LN2, which was a behavior not well-represented by the pre-test FE models. Condition 4 used a different initial pressure than the previous two tests, preventing a direct comparison of the results. Finally, Condition 4 was not considered representative of service conditions.

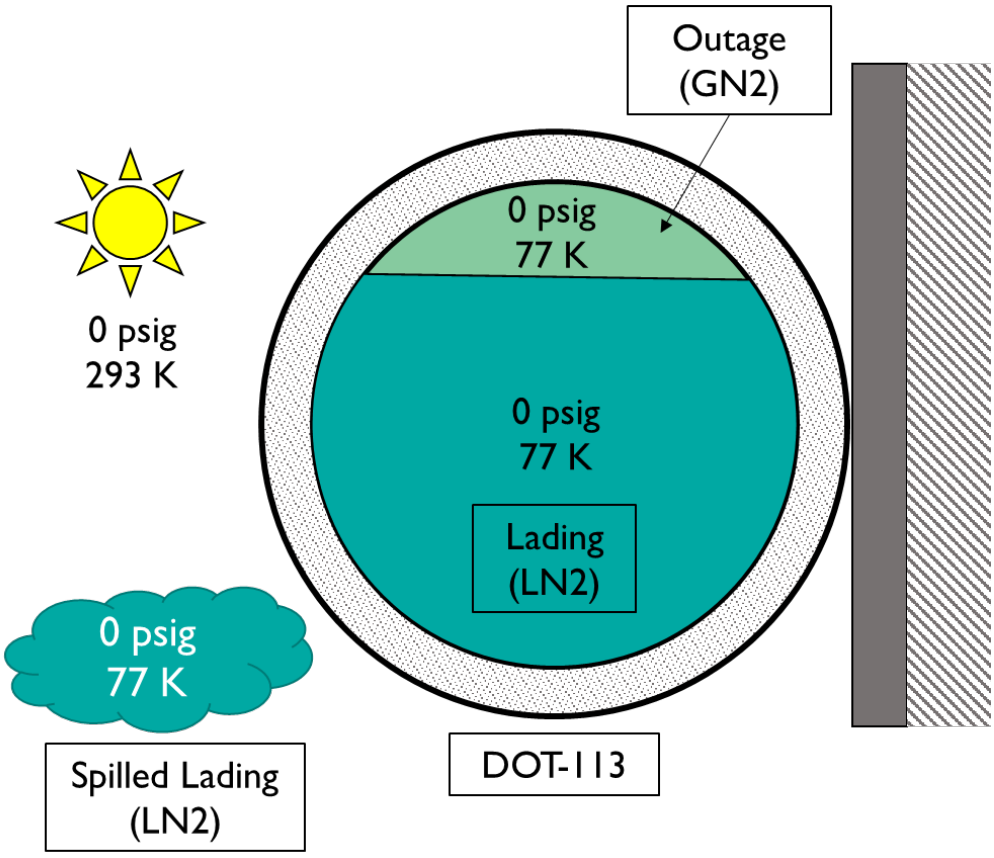


**Figure I6. Condition 4**

## Abbreviations and Acronyms

| ACRONYMS | EXPLANATION |
|---|---|
| ASTM | American Society for Testing and Materials |
| AAR | Association of American Railroads |
| B-W | Bao-Wierzbicki |
| CFC | Channel Frequency Class |
| DOF | Degrees-of-Freedom |
| DOT | Department of Transportation |
| DB | Dogbone |
| EOS | Equations of State |
| FE | Finite Element |
| FEA | Finite Element Analysis |
| FRA | Federal Railroad Administration |
| HD | High Definition |
| HHFT | High-hazard Flammable Trains |
| LIDAR | Light Detection and Ranging |
| LNG | Liquefied Natural Gas |
| MLI | Multi-layer Insulation |
| MMC | Modified Mohr Coulomb |
| PHMSA | Pipeline and Hazardous Materials Safety Administration |
| PEEQ | Plastic Equivalent |
| PWHT | Post-weld Heat Treated |
| PRV | Pressure Relief Valve |
| RA | Reduction in Area |
| SSC | Shell-to-solid Coupling |
| SPH | Smoothed Particle Hydrodynamics |
| SRB | Smooth Round Bar |
| SAE | Society of Automotive Engineers |
| SCFM | Standard Cubic Feet per Minute |
| TRIAX | Stress Triaxiality |
| TC | Transport Canada |
| TTC | Transportation Technology Center (the site) |

| ACRONYMS | EXPLANATION |
|---|---|
| TTCI | Transportation Technology Center, Inc. (the company) |
| UTS | Ultimate Tensile Strength |
| Volpe | Volpe National Transportation Systems Center |
| YS | Yield Strength |